

# GROUND MOTION MODELS CONSIDERING DIVERSE GROUND MOTION INTENSITY MEASURE PARAMETERS FOR THE PERUVIAN SUBDUCTION ZONE

by

Jorge Luis Paredes Estacio

A dissertation Submitted to the University of Bristol in Accordance with the  
Requirements for Award of the Degree of  
Master of Science in Earthquake Engineering and Infrastructure Resilience  
in the Faculty of Engineering, Department of Civil Engineering

24 September 2020

**Word count:**

## Author Declaration

I declare that the work in this dissertation was carried out in accordance with the Regulations of the University of Bristol. The work is original except where indicated by special reference in the text and no part of the dissertation has been submitted for any other degree.

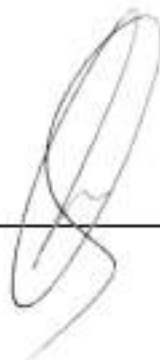
Any views expressed in the dissertation are those of the author and in no way represent those of the University of Bristol.

The dissertation has not been presented to any other University for examination either in the United Kingdom or overseas.

The copyright of this dissertation rests with the author. Information derived from it should be acknowledged.

Commercial confidentiality of research funders will be respected at all times.

Signature

A handwritten signature in black ink, consisting of several overlapping loops and a long horizontal stroke at the bottom.

Date

24 September 2020

## Ground motion models considering diverse ground motion intensity measure parameters for the Peruvian subduction zone

**Author:** Jorge Paredes, *postgraduate in MSc Earthquake Engineering and Infrastructure Resilience, University of Bristol*

**ABSTRACT:** This dissertation is written for the purpose of developing a Ground-Motion Prediction Equation (GMPE) for the Peruvian subduction zone, which relies on foreign GMPEs for Probabilistic Seismic Hazard Assessment (PSHA) from which is base the current Peruvian seismic code (E030). The proposed GMPE model not only predict common Intensity Measures (IM) for both horizontal and vertical components like peak ground acceleration (PGA) and Spectral accelerations ( $S_a$ ) between 0.2 and 5.0s, but also covers other IMs such as the mean period ( $T_m$ ), the  $PGA/PGV$  ratio, the  $PGA/PGVT_m$  ratio and the  $PGA/(PGVf_m)$  ratio. The latter two parameter relates PGA, peak ground velocity (PGV) and mean frequency ( $f_m$ ), which is the inverse of the  $T_m$ . To do so, a compiled dataset of 2803 events were collected mainly from Peru, Chile and Ecuador between 4.0 and 8.5  $M_w$  from 1951 to 2020. The current Slab2 three-dimensional geometry of the South America subduction zone as well as other 18 sections derived from different studies were used to define the Peru, Ecuador and Chile subduction zone. This enabled to identify interface, inslab and crustal earthquakes, which represent the 45%, 33% and 22% considering the entire dataset, respectively. So, only 453 interface events were selected with 3750 ground motion records from 533 stations, which comprise six different networks from Peru, Chile and Ecuador. The aforementioned IMs were used as regressor parameters for both horizontal and vertical components to derive GMPEs applicable to a range of 4.0 to 8.5  $M_w$ , and a range up to rupture distances ( $R_{rup}$ ) of 1000km by assessing the two-step maximum likelihood. The new GMPE for PGA and  $S_a$  performs better than commonly used foreign GMPEs, which tend to underestimate ground motions at  $M_w$  higher than 7.0 at a specific  $R_{rup}$  range. This implies the E030 is currently providing lower PGA at lower  $R_{rup}$  distances for interface events which exclusively harbours the strongest events higher than 8.0  $M_w$  for the entire dataset used in this study. Also, a new soil classification and site coefficient are suggested which are quite similar to the Chilean Seismic code (NCh 433). These proposed site coefficients do not underestimate PGA values for soil classes  $S_0$ ,  $S_2$  and  $S_3$  as the Peruvian Seismic code (E030) does for soils under inelastic behavior caused by strong earthquakes. Besides, the  $T_m$ , the  $PGA/PGV$  ratio, and the  $PGA/PGVf_m$  provide less residuals compared to PGA,  $S_a$ , and the  $PGA/PGVT_m$  ratio. Meanwhile, the  $PGA/PGVf_m$  is an innovate ratio parameter proposed in this study that has the lowest uncertainty compared to the other IMs. Also, this new IM may contribute to generate reliable synthetic motions with the same proxy applicability range as previous stated when a strong dataset is not available. In addition, the  $PGA/PGV$  ratio indicates that ground motions (GMs) can be classified as high and intermediate range for the South America subduction zone. Besides, the  $T_m$  variations indicate that both structures and soils with fundamental periods between 0.1 and 0.70s are more vulnerable to resonate to critical scenarios for both horizontal and vertical motions. Finally, the vertical to horizontal PGA ratio of 2/3 suggested in the Peruvian Seismic code (E030) may overestimate the PGA for vertical ground motions. This study found that this ratio depends strongly on moment magnitude, rupture distances and shear wave velocity ( $V_{S30}$ ) and for critical scenarios this ratio may be up to 0.55.

**KEY WORDS:** Ground-motion prediction equations, Peruvian Subduction zone, Site effect, PGA, response spectra,  $PGA/(PGVf_m)$  ratio, mean period  $T_m$ .

## **ACKNOWLEDGEMENTS**

I would like to sincerely thank my supervisor Dr Raffaele De Risi for his support and guidance throughout this dissertation and for being my supervisor to study the Civil Engineering (Ph.D.) at the University of Bristol. I am also grateful to Prof. Anastasios Sextos who supported me to take this dissertation into a more complex research field by getting a full scholarship from the Peruvian government for the Ph.D. program.

I also would like to thank Prof. George Mylonakis, and all lectures of this MSc for their support and experiences shared during this year.

I would like to thank my fellow postgraduate students in Bristol for their encouragement and support during the summer.

I would like to specially thank my parents, Florencio Paredes Narvaez and Antonia Estacio Barba. I dedicate this achievement specially to them, who despite not having completed a degree, were my earthly angels who inspired me to have constant fight left in me and humility to continue their wishes.

Thank you God for lighting every step I take.

## TABLE OF CONTENTS

ABSTRACT .....	iii
ACKNOWLEDGEMENTS .....	iv
TABLE OF CONTENTS .....	v
LIST OF FIGURES .....	vii
LIST OF TABLES .....	x
1. INTRODUCTION .....	1
2. PERU, CHILE AND ECUADOR DATASET .....	6
2.1. Instrumentation .....	8
2.2 Selection of Interface Events from the Catalogue .....	10
2.3 Processing of Raw Data .....	15
2.4 Estimation of IM parameters for the horizontal and vertical motion: $PGA/PGV$ , $(S_{ai})$ , $T_m$ ..	17
2.5 Magnitude homogenization and distance to source .....	18
3. DEVELOPMENT OF A NEW GMPEW FOR THE $PGA$ AND $S_a$ INTENSITY MEASURES FROM SUBDUCTION EVENTS CONSIDERING THE HORIZONTAL AND THE VERTICAL GROUND MOTION RECORDS.....	30
3.1. GMPE: General Form.....	31
3.2. Two-step Maximum-likelihood method.....	32
3.3. Functional Form of the median GMPE for the Horizontal and Vertical IMs .....	36
4. THE MEAN PERIOD $T_m$ , THE $PGA/PGV$ RATIO, THE $PGA/(PGVT_m)$ RATIO, AND THE $PGA/(PGVf_m)$ RATIO GMPE REGRESSION FOR THE HORIZONTAL AND VERTICAL GROUND MOTION RECORDS.....	43
5. COMPARING THE PROPOSED GMPE FOR INTERFACE EVENTS WITH PREVIOUS MODELS.....	49
6. DISCUSSION .....	51
7. CONCLUSIONS .....	57
8. RECOMMENDATIONS .....	59
REFERENCES .....	60
APPENDIX .....	73
A.1. LIST OF STATIONS.....	73
A.2. LIST OF EVENTS .....	81
A.3. RESIDUAL PLOTS FOR THE HORIZONTAL GMs .....	88
A.4. RESIDUAL PLOTS FOR THE VERTICAL GMs:.....	90
A.5. COMPARINSON BETWEEN MODEL FITTED WITH ALL DATA CONSIDERING DIFFERENT MOMENT MAGNITUDES AND DIFFERENT IMs FOR HORIZONTAL GMs: .....	92

A.6. COMPARINSON BETWEEN MODEL FITTED WITH ALL DATA CONSIDERING DIFFERENT MOMENT MAGNITUDES AND DIFFERENT IMs FOR VERTICAL GMs: .....	99
A.7. RESIDUAL PLOTS FOR THE <b><i>Tm</i></b> FOR BOTH HORIZONTAL AND VERTICAL GMs: .....	106
A.8. RESIDUAL PLOTS FOR THE <b><i>PGA/PGV</i></b> FOR BOTH HORIZONTAL AND VERTICAL GMs: .....	108
A.9. RESIDUAL PLOTS FOR THE <b><i>PGA/(PGVfm)</i></b> FOR BOTH HORIZONTAL AND VERTICAL GMs: .....	110
A.10. COMPARINSON BETWEEN MODEL FITTED WITH ALL DATA CONSIDERING DIFFERENT MOMENT MAGNITUDES AND <b><i>Tm</i></b> FOR HORIZONTAL GMs: .....	112
A.11. COMPARINSON BETWEEN MODEL FITTED WITH ALL DATA CONSIDERING DIFFERENT MOMENT MAGNITUDES AND <b><i>PGA/PGV</i></b> FOR HORIZONTAL GMs: .....	113
A.12. COMPARINSON BETWEEN MODEL FITTED WITH ALL DATA CONSIDERING DIFFERENT MOMENT MAGNITUDES AND <b><i>PGA/(PGVfm)</i></b> FOR HORIZONTAL GMs: .....	114
A.13. COMPARINSON BETWEEN MODEL FITTED WITH ALL DATA CONSIDERING DIFFERENT MOMENT MAGNITUDES AND <b><i>Tm</i></b> FOR VERTICAL GMs: .....	115
A.14. COMPARINSON BETWEEN MODEL FITTED WITH ALL DATA CONSIDERING DIFFERENT MOMENT MAGNITUDES AND <b><i>PGA/PGV</i></b> FOR VERTICAL GMs: .....	116
A.15. COMPARINSON BETWEEN MODEL FITTED WITH ALL DATA CONSIDERING DIFFERENT MOMENT MAGNITUDES AND <b><i>PGA/(PGVfm)</i></b> FOR VERTICAL GMs: .....	117

## LIST OF FIGURES

<b>Figure 1:</b> The compiled data set used in this study that comprises interface, intraslab and crustal earthquakes ( $M_w \geq 4.0$ ), 1951-2020. ....	7
<b>Figure 2:</b> Location map of: (a) the six networks from Peru, Chile and Ecuador utilized in this study, and (b) the six networks from Peru, Chile and Ecuador and the Arc Volcanic Front of the subduction zone.....	9
<b>Figure 3:</b> Model construction of the plan shape of the Peruvian, Chile, Ecuador, Brazil, Bolivia and Argentina Subduction Zone Geometry with contour lines and sections .....	11
<b>Figure 4:</b> Interface Events from the compiled dataset used in this study. ....	12
<b>Figure 5:</b> Intraslab Events from the compiled dataset used in this study. ....	13
<b>Figure 6:</b> Crustal Events from the compiled dataset used in this study. ....	14
<b>Figure 7:</b> Graphs showing: (a) a low-cut Butterworth filter with low-cut corner of $f_{IC} = 0.1\text{Hz}$ , and (b) a high-cut Butterworth filter with a high-cut corner of $f_{hc} = 20\text{Hz}$ . [108]. ....	16
<b>Figure 8:</b> Squamatisation the Tukey Window with various taper lengths which indicated what flatten portion of the Tukey window has a value of zero. Siemens, 2019 [109]. ....	17
<b>Figure 9:</b> $R_{jb}$ and $R_{rup}$ distances for the selected 454 interface events used for the GMPE regression.....	24
<b>Figure 10:</b> Interface Dataset plots of Moment Magnitude versus: (a) Hypocentral Distance ( $H_{hyp}$ ), and (b) Focal Depth ( $D$ ). ....	24
<b>Figure 11:</b> Interface Dataset plots of Moment Magnitude versus: (a) Joyner-Boore Distance ( $R_{jb}$ ), and (b) Rupture Distance ( $R_{rup}$ ). ....	25
<b>Figure 12:</b> Peak Ground Acceleration (PGA) versus Moment Magnitude ( $M_w$ ) and Rupture Distance ( $R_{rup}$ ) considering the: (a) Geometric mean of the two horizontal Ground Motion Records, and (b) Vertical Ground Motion Records. ....	25
<b>Figure 13:</b> PGA/PGV ratio versus Moment Magnitude ( $M_w$ ) and Rupture Distance ( $R_{rup}$ ) considering the: (a) Geometric mean of the two horizontal Ground Motion Records, and (b) Vertical Ground Motion Records. ....	26
<b>Figure 14:</b> Mean Period ( $T_m$ ) versus Moment Magnitude ( $M_w$ ) and Rupture Distance ( $R_{rup}$ ) considering the: (a) Geometric mean of the two horizontal Ground Motion Records, and (b) Vertical Ground Motion Records.....	26
<b>Figure 15:</b> Spectral Acceleration with 5% damping ratio at 0.2s ( $SA(0.2\text{sec})$ ) versus Moment Magnitude ( $M_w$ ) and Rupture Distance ( $R_{rup}$ ) considering the: (a) Geometric mean of the two horizontal Ground Motion Records, and (b) Vertical Ground Motion Records. ....	26
<b>Figure 16:</b> Spectral Acceleration with 5% damping ratio at 0.3s ( $SA(0.3\text{s})$ ) versus Moment Magnitude ( $M_w$ ) and Rupture Distance ( $R_{rup}$ ) considering the: (a) Geometric mean of the two horizontal Ground Motion Records, and (b) Vertical Ground Motion Records. ....	27
<b>Figure 17:</b> Spectral Acceleration with 5% damping ratio at 0.6s ( $SA(0.6\text{s})$ ) versus Moment Magnitude ( $M_w$ ) and Rupture Distance ( $R_{rup}$ ) considering the: (a) Geometric mean of the two horizontal Ground Motion Records, and (b) Vertical Ground Motion Records. ....	27
<b>Figure 18:</b> Spectral Acceleration with 5% damping ratio at 1.0s ( $SA(1.0\text{s})$ ) versus Moment Magnitude ( $M_w$ ) and Rupture Distance ( $R_{rup}$ ) considering the: (a) Geometric mean of the two horizontal Ground Motion Records, and (b) Vertical Ground Motion Records. ....	27
<b>Figure 19:</b> Spectral Acceleration with 5% damping ratio at 2.0s ( $SA(2.0\text{s})$ ) versus Moment Magnitude ( $M_w$ ) and Rupture Distance ( $R_{rup}$ ) considering the: (a) Geometric mean of the two horizontal Ground Motion Records, and (b) Vertical Ground Motion Records. ....	28
<b>Figure 20:</b> Spectral Acceleration with 5% damping ratio at 3.0s ( $SA(3.0\text{s})$ ) versus Moment Magnitude ( $M_w$ ) and Rupture Distance ( $R_{rup}$ ) considering the: (a) Geometric mean of the two horizontal Ground Motion Records, and (b) Vertical Ground Motion Records. ....	28

---

<b>Figure 21:</b> Spectral Acceleration with 5% damping ratio at 4.0s ( $SA(4.0s)$ ) versus Moment Magnitude ( $M_w$ ) and Rupture Distance ( $Rrup$ ) considering the: (a) Geometric mean of the two horizontal Ground Motion Records, and (b) Vertical Ground Motion Records. ....	28
<b>Figure 22:</b> Spectral Acceleration with 5% damping ratio at 5.0s ( $SA(5.0s)$ ) versus Moment Magnitude ( $M_w$ ) and Rupture Distance ( $Rrup$ ) considering the: (a) Geometric mean of the two horizontal Ground Motion Records, and (b) Vertical Ground Motion Records. ....	29
<b>Figure 23:</b> Comparison of the median predictions calculated from horizontal ground models derived through different Shear wave velocities ( $VS30$ ) of 1200, 700, 437, 270 and 140m/s that correspond soil classes A, B, C, D and E, respectively. These GMPEs are obtained from different IMs that for this case only resemble 8.5 $M_w$ earthquakes.....	38
<b>Figure 24:</b> Comparison of the median predictions calculated from vertical ground models derived through different Shear wave velocities ( $VS30$ ) of 1200, 700, 437, 270 and 140m/s that correspond soil classes A, B, C, D and E, respectively. These GMPEs are obtained from different IMs that for this case only resemble 8.5 $M_w$ earthquakes.....	39
<b>Figure 25:</b> Response spectra with 5% damping ratio predicted for horizontal ground motions with different moment magnitudes ( $M_w$ ) and rupture distances ( $Rrup$ ) for a reference rock site that presents a $VS30$ of 1200 m/s.....	40
<b>Figure 26:</b> Response spectra with 5% damping ratio predicted for vertical ground motions with different moment magnitudes ( $M_w$ ) and rupture distances ( $Rrup$ ) for a reference rock site that presents a $VS30$ of 1200 m/s. .	40
<b>Figure 27:</b> Response spectra predicted for horizontal ground motions with 8.5 $M_w$ and different rupture distances ( $Rrup$ ) for site classes A, B, C, D and E that correspond Shear wave velocities ( $VS30$ ) of 1200, 700, 437, 270 and 140m/s, respectively. ....	41
<b>Figure 28:</b> Response spectra predicted for horizontal ground motions with 8.5 $M_w$ and different rupture distances ( $Rrup$ ) for site classes A, B, C, D and E that correspond Shear wave velocities ( $VS30$ ) of 1200, 700, 437, 270 and 140m/s, respectively. ....	41
<b>Figure 29:</b> Average Site Effects Coefficients computed for soil classes A, B,C, D and E that correspond Shear wave velocities ( $VS30$ ) of 1200, 700, 437, 270 and 140m/s, respectively for: (a) horizontal ground Motions, and (b) vertical ground motions. ....	42
<b>Figure 30:</b> PGA/PGV ratio versus $Tm$ and Moment Magnitude ( $M_w$ ) for: (a) horizontal ground motion records, and (b) vertical ground motion records.....	44
<b>Figure 31:</b> PGA/PGV ratio versus $Tm$ and Rupture Distance ( $Rrup$ ) for: (a) horizontal ground motion records, and (b) vertical ground motion records.....	44
<b>Figure 32:</b> PGA/PGV ratio versus $Tm$ for: (a) horizontal ground motion records, and (b) vertical ground motion records. ....	44
<b>Figure 33:</b> Mean Period ( $Tm$ ) predicted for different moment magnitude for a reference rock site ( $VS30 = 1200 m/s$ ). (a) Horizontal ground motions and (b) Vertical ground motions. ....	46
<b>Figure 34:</b> PGA/PGV ratio predicted for different moment magnitude for a reference rock site ( $VS30 = 1200 m/s$ ). (a) Horizontal ground motions and (b) Vertical ground motions. ....	47
<b>Figure 35:</b> PGA/(PGVfm) ratio predicted for different moment magnitude for a reference rock site ( $VS30 = 1200 m/s$ ). (a) Horizontal ground motions and (b) Vertical ground motions. ....	47
<b>Figure 36:</b> Comparison of the $Tm$ median prediction derived through different Shear wave velocities ( $VS30$ ) of 1200, 700, 437, 270 and 140m/s that correspond soil classes A, B, C, D and E, respectively. These GMPEs only resemble a 8.5 $M_w$ earthquake calculated from: (a) horizontal ground motions, and (b) vertical ground motions. ....	47
<b>Figure 37:</b> Comparison of the PGA/PGV ratio median prediction derived through different Shear wave velocities ( $VS30$ ) of 1200, 700, 437, 270 and 140m/s that correspond soil classes A, B, C, D and E, respectively. These GMPEs only resemble a 8.5 $M_w$ earthquake calculated from: (a) horizontal ground motions, and (b) vertical ground motions. ....	48



**Figure 38:** Comparison of the  $PGA/(PGVfm)$  ratio median prediction derived through different Shear wave velocities ( $VS30$ ) of 1200, 700, 437, 270 and 140m/s that correspond soil classes A, B, C, D and E, respectively. These GMPEs only resemble a 8.5  $M_w$  earthquake calculated from: (a) horizontal ground motions, and (b) vertical ground motions. .... 48

**Figure 39:** Original record data of important events versus predicted PGA using new GMPE and previous GMPEs for subduction zones. (a) the 23 June 2001  $M_w$  8.4 Atico - Peru earthquake, (b) the 15 August 2007  $M_w$  7.9 Pisco - Peru earthquake, (c) the 16 September 2015  $M_w$  8.4 Cochimbo - Chile earthquake, (d) the 16 April 2016  $M_w$  7.53 Manabi - Ecuador earthquake, (e) the 14 January 2018  $M_w$  6.95 Arequipa - Peru earthquake, and (f) the 26 May 2019  $M_w$  8.00 Loreto - Peru earthquake. .... 50

**Figure 40:** Comparison of the vertical to horizontal PGA ratio median prediction derived through: (a) different Shear wave velocities ( $VS30$ ) of 1200, 700, 437, 270 and 140m/s that correspond soil classes A, B, C, D and E, respectively. These median ratios only resemble a 8.5  $M_w$  earthquake, and (b) different moment magnitude that correspond soil Class A with  $VS30$  of 1200m/s..... 53

**Figure 41:** Comparison of the vertical to horizontal spectral acceleration ratios at 0.2, 0.3, 0.6, 1.0, 2.0, 3.0, 4.0, and 5.0s through different shear wave velocities ( $VS30$ ) of 1200, 700, 437, 270 and 140m/s that correspond soil classes A, B, C, D, and E, respectively. These median ratios only resemble a 8.5  $M_w$  earthquake..... 56

## LIST OF TABLES

<b>Table 1:</b> Site Classification based on the Resulting Average S-Wave Velocity of the Upper 30 m ( $V_{s30}$ ), based in the average values from Leyton et al. (2018) and Aguilar et al. (2019). .....	10
<b>Table 2:</b> Mean Converted Rhyp distances respect to $R_{jb}$ and $M_w$ for 40° dip reverse fault. Tavakoli et al. (2018) [127]. .....	22
<b>Table 3:</b> Coefficients of the Finite-Fault Depth versus Magnitude and its uncertainty. Tavakoli et al. (2018) [127]. .....	23
Table 4: Magnitude-dependent limit to distance in the selection of the GMPE data subset. Abrahamson et al. (2016) [58]. .....	23
<b>Table 5:</b> Regression model coefficients for the median GMPE and standard deviations for different IM parameters considering horizontal GMs. ....	37
<b>Table 6:</b> Regression model coefficients for the median GMPE and standard deviations for different IM parameters considering vertical GMs. ....	37
<b>Table 7:</b> Regression model coefficients for the median GMPE and standard deviations for the $T_m$ , the $PGA/PGV$ ratio, the $PGA/(PGVT_m)$ ratio, and the $PGA/(PGVfm)$ ratio considering horizontal GMs.....	45
<b>Table 8:</b> Regression model coefficients for the median GMPE and standard deviations for the $T_m$ , the $PGA/PGV$ ratio, the $PGA/(PGVT_m)$ ratio, and the $PGA/(PGVfm)$ ratio considering vertical GMs. ....	46
<b>Table 9:</b> Applicability range of the new GMPE for the Peruvian subduction zone according to Moment magnitude $M_w$ , rupture distance ( $R_{rup}$ ), and focal depth ( $D$ ). .....	52
<b>Table 10:</b> Comparison of the Site effect coefficients between the current seismic code from Peru (E030) and the present study for both horizontal and vertical GMs. ....	54
<b>Table 11:</b> Comparison of site effect coefficients between the current seismic code from Peru (E030), the current seismic code from Chile (NCh 433), and the present study for both horizontal and vertical GMs. ....	54

## INTRODUCTION

Peru is located in the ring of fire where the Nazca plate is being subducted under the westward-moving South America Plate at a converge range of 7-9cm/year in N78° E direction [1] causing upper plate deformation, earthquake and volcanism [2]. A special significant subduction zone complexity in Southern Peru (from 14°S to 20°S) has been attributed to the marked difference in size between the Nazca Ridge (approximately 200 km x 18km) and the flat slab segment (~1500 km wide) [3], [4], which is considered the largest in the world. Two seismic regions in Peru are located in the north or south direction of the Nazca Ridge. The latter is coincident with a region of low coupling where the Nazca plate subducts aseismically [5]. The dominant mechanism of interface type earthquakes corresponds thrust faulting on shallow dipping planes that are oriented nearly parallel to the trench axis. At depths greater than the coupled interface, the stress system goes from compression to tension, and as a result, normal faulting prevails. These normal mechanism earthquakes are related to intraslab behaviour that occurs within the subducted Nazca plate, at some distance down-dip from the seismically coupled interface. In intermediate depths, two types of intraslab events have been recognized: (a) slab-push, and (b) slab-pull. These intraslab events are associated with down-plate compression and extension, respectively [6]. The manifestation of slab-pull earthquakes is quite common. However, some slab-push events have occurred in the Central part of Peru in the 5 and 29 April 1991 [7]. Also, crustal earthquakes along the Andean cordillera may trigger events up to  $M_w$  7.5 [8]–[11].

During the last century, destructive earthquakes larger than  $M_w$  8.0 have happened for the rupture of the Peruvian subduction zone. Many of these earthquakes have been thrust-faulting that occurred in the interface between the Nazca and South American Plates [7]. The strong 1868 earthquake generated the destructive tsunami in Pisco City that may have been the unique known exception that suggests a fault model rupturing along the ridge from south to north [12]. The central part of Peru which conforms the north of the Nazca ridge has been frequently affected by strong earthquakes like the  $M_w$  8.6-9.2 28/10/1976 subduction event that experienced Lima City accompanied by a tsunami event [13]. This earthquake was followed by the 7-8  $M_w$  1940, 1966, 1974 and 2007 events [14]. Several previous studies have identified a long-standing seismic gap in this area, which could trigger an earthquake higher than  $M_w$  8.8 in the future [5].

Seismic hazard assessment is critical for developing rules for seismic hazard mitigation and risk reduction such as land-use planning, building regulations, insurance, and emergency preparedness [15]–[17]. Most seismic hazard estimations are focused on the application of Probabilistic Seismic Hazard Assessment (PSHA) in different parts around the globe, and new methodologies changes came up during its development [15], [18] and with it, the implementation of either deterministic or non-deterministic seismic hazard methods [19]–[21]. Nevertheless, many conventional PSHA studies were performed in the Peruvian Subduction

zone [22]–[24] without considering a temporal variation of the parameter “b” (that is assumed to be a constant value) [25] that may increase potential bias in ground motion parameters [26]. Moreover, it is a bad practice not to perform a proper ground motion selection that considers wide bounds on casual parameters (e.g. magnitude, source to site distance, and site conditions bound) [27], as well as considering epistemic uncertainties within a logic tree framework that have been converted as the actual important procedure. Though, the selection of branch models and weights is most often still treated in an informal way such as the Peruvian case [28]. So, this ended in potential tricks concerning the elaboration and use of logic trees and also in huge uncertainties on the results of hazard assessments [29].

Selecting a proper Ground Motion Prediction Equation (GMPE) has a vast impact when applying a PSHA because the selected GMPEs relate to a ground motion intensity measure (IM) such as peak ground acceleration (PGA), spectral accelerations ( $S_a$ ), mean period ( $T_m$ ), to a set of explanatory variables which describe the earthquake source, wave propagation path, and local site conditions [30]. Certain recent models also account for the factors affecting earthquake ground motions such as hanging wall effects [31], ground motion directionality [32], and topographic effects [33]–[36]. However, further investigation calls for adopting the true static stress drop ( $\Delta\tau_s$ ) in order to account the between event variability of the Ground Motion Models (GMMs) [37], [38]. The GMMs are usually obtained from Global GMPEs developed in the United States, which have some important variations for PSHA applications that depend on the annual exceedance rate and seismicity. Therefore, identification of appropriate GMPEs partly relies on assembling test-bed databases from the strong motion recordings of the region of interest. For this reason, there is a permanent effort among the countries and research community to excel a quality technological infrastructure and to get a huge accelerometric data base [39].

On the other hand, prediction equations have gained more attention for the horizontal component than those for the vertical. So, there is an engineering need to predict vertical ground motion for specific structures such as long-span bridges, nuclear plants, dams, etc. [40]. Also, the vertical motion may amplify and potentially cause a reversal of bending moment in longitudinal bridge girders [41]. In addition, the vertical acceleration may increase the axial column force, the moment and shear demand, and plastic deformation. This will enable hinge deformation and finally diminish the overall ductility of the structure [42]. As a consequence of that, the vertical acceleration is assumed to be 2/3 times the horizontal acceleration for designing purposes as stated in the Peruvian Seismic Code (E030) [43]. This is a consequence of not having any developed GMPE for the vertical PGA and spectral accelerations so far.

Some studies indicated that the high-frequency of the input ground motion is related to peak ground acceleration (PGA). Meanwhile, the moderate or low-frequency wave are well correlated to peak ground velocity (PGV) [44]. This means that transient excitations of earthquakes and a single intensity measure (IM) such as PGA cannot provide a proper characteristic of ground motion. On the other hand, many studies suggested that PGA/PGV can be a representative parameter for the appropriate selection ground motion for a wide range of structures as well as probabilistic hazard analysis (PSHA) [45]. Also, the PGA/PGV can be a representative parameter to classify ground motion (GM) into high, medium and weak ranges [44], [46]. This classification indicates that  $PGA/PGV > 1.2g/m/s$  is in the high range,  $PGA/PGV < 0.8g/m/s$  is in the low range, and  $0.8g/m/s \leq PGA/PGV \leq 1.2g/m/s$  is in the intermediate range. Some regression analysis indicates that the  $PGA/PGV$  ratio presents a

good correlation with the mean period ( $T_m$ ) of ground motions compared to the predominant spectral period ( $T_p$ ) [47], [48]. Besides, the  $T_m$  is the best representative parameter that can be correlated to earthquake magnitude, site-to-source distance, site conditions, and rupture directivity [49], [50]. However, only two dimensional (2D) plots have correlated both the  $PGA/PGV$  ratio and the ( $T_m$ ) using twenty-two pairs of far-source and twenty-seven pair of horizontal near-source ground motion records identified by FEMA P695 (2009) [48]. So, no investigation was performed so far at all to develop a GMPE utilizing these two parameters represented by one single IM for both horizontal and vertical GMs records. So, these GMPEs relationships can be very useful for many applications such as vector-IM seismic hazard or ground-motion selection process to generate synthetic motions [51]. Therefore, establishing correlations between  $PGA/PGV$  and  $T_m$  will be very useful for the Peruvian subduction zone considering the reduced amount of data from earthquakes higher than  $M_w$  7.

In 2010, accelerograms were compiled and processed as well as the information on the source parameters of the causative earthquakes, fault-plane geometrics and local site conditions at 59 different site stations in Peru and Chile between 1966 and 2007. However, this data base is not satisfactory for the derivation of a new GMPE for subduction events in Peru [52]. As a consequence of that, only two GMPEs were derived from local data available 14 years ago. The first proposed GMPE only used ten records which raise concerns for its application [53]. Meanwhile, the second attempt only gave results for site class C, and the number of records performed in their regression was about 300, which is still very little compared to the number of motions used to obtain modern GMPEs [54]. Therefore, these GMPEs are not acceptable according to the preselection criteria for adjusting ground-motion models [55].

Because of the insufficient amount of record data in Peru, it is a common practice to adopt foreign GMPEs. Thus, its selection process is the major challenge for predicting ground motion. In 2019, Charca et al. [56] performed the average log-likelihood method (LLH) of Scherbaum et al. (2004) [57] in order to assess the goodness of fit of different GMPEs from global earthquakes and foreign countries such as New Zealand and Japan. Consequently, Charca suggested that the GMPE proposed by Abrahamson et al. (2016) [58], Zhao et al. [59], [60], and Youngs et al. [61] perform better than other foreign GMPEs. However, this lately attempt performed by Charca et al. (2019) is based on an old goodness of fit version that has not clear advantages over Kullback-Leiber distance method [57], [62]–[66] proposed by Scherbaum et al. (2009) [28]. Besides, the suggested GMPEs are based on foreign ground motion data that consider several casual parameters (e.g. moment magnitude and its scaling effect [67], event type, epicentral location and depth, either aftershock or foreshock events, station location, site classification, forearc or backarc classification, distance metrics, and the shear wave velocity over the top 30m ( $V_{s30}$ )) that may not certainly represent the Peruvian Subduction zone scenario. Also, these casual parameters are considered error free when the maximum log likelihood (MLL) is performed as a common regression method. Meanwhile, the Bayesian measurement error (BME) model allows to consider measurements uncertainties in the predictor variables and reduces the values of the between-event standard deviation ( $\tau$ ) and the within-event/within station standard deviation ( $\phi_{s2s}$ ) depending on the spectral period. This implies that GMMs based on BME performs better than MLL when selecting foreign GMPEs. Consequently, adopted GMPEs has important impact on PSHA applications for the Peruvian Territory if the site terms are used in a partially nonergodic PSHA [68].

Above all, apart from the compiled data gathered from 1966 to 2015 (which includes 484 ground motion records from 118 subduction type events with moment magnitude ranging from 5.0 to 8.4, which were recorded in Peru and northern Chile) [52], a robust ground motion data have been gathered in Peru after 2015. This is the result of the implementation of more seismometers in seven networks that are operated by the Geophysical Institute of Peru (IGP), the Japan- Peru Centre for Seismic Research and Disaster Mitigation (CISMID), the National Training Service for the Construction Industry (SENCICO), the Graduate Faculty of Civil Engineering of the National University of Engineering (FIC-UNI), the Peruvian Association of Engineers (CIP), the South American Regional Seismological Centre (CERESIS), the Peruvian State Water Company (SEDAPAL). The total number of seismometers that have been implemented so far is around 236 from which 66 stations only have information on proper soil classification. The remaining site stations are classified from rigid, intermediate and soft soil [69]. The lack of geophysical information from some stations can be supplied by the  $V_{S30}$  data provided by the United States Geological Survey (USGS). Meanwhile, a new  $V_{S3}$  site classification has been proposed to modify the current Peruvian Earthquake Resistant Design Code (E030) [70]. This new classification is very similar to the neighbouring country of Chile, from which Peru shares the same subduction zone [71]. Furthermore, geophysical surveys were performed in some stations located in Lima City [72], [73], Ica [74], Atico 2001 [75] and Tacna City [76]. Moreover, a strong ground motion data is available from the National Accelerometer Network of the Department of Civil Engineering (RENADIC), the Chilean National Seismological Centre (CSN) and Integrated Plate Boundary Observatory (IPOC) from Chile. For stations located in Northern Chile, geophysical surveys are presented by Leyton et al. [71], [77], [78] which can be used to allocate site class to the majority of stations. Furthermore, there are 21 records from the 7.5 Mw 16/04/2016 subduction event earthquake that occurred in Manabí, Ecuador. These were measured by the Geophysical Institute of the National Polytechnic School (IG) from the RENAC network that corresponds to an interface event [79], [80]. However, its empirical site classification maintains similar conditions than the ASCE7-16, which cannot be representative to predict site amplification compared to Chile [81].

This study aims to develop a GMPE for interface events for the PGA and Spectral accelerations ( $S_a$ ) between 0.2s and 5.0s for both horizontal and vertical components using the aforementioned strong compiled dataset from Peru, Chile and Ecuador. This new GMPE will be compared to other attenuation relationships developed for interface earthquakes such as the Abrahamson's model [58], the Youngs's equation [61], the Zhao's model [59], the Atkinson & Boore's equation [82], and the Chilean GMM [83]. Likewise, empirical correlations of the mean period ( $T_m$ ), PGA/PGV ratio,  $PGA/(PGVT_m)$  ratio, and the  $PGA/(PGVf_m)$  will be performed for the horizontal and vertical component to characterize the motions of the Peruvian subduction zone. It is expected to identify lower residuals compared to the PGA and  $S_a$  as previous investigations cited. Moreover, the vertical to horizontal PGA and  $S_a$  ratios, and the site coefficients for soil classes A, B, C, D and E for the selected data set will be studied. These results will be compared to the current Peruvian Seismic Code (E030).



**For the present study, the limit length is set under 20,000 words without considering the References and Appendix Sections. This higher length is because the explanation of the methods employed and of the collected data is particularly hard. Also, this dissertation is linked to my current MSc. scholarship and to my future Ph.D. scholarship; in fact, I will be a Ph.D. student here in Bristol under the sponsor of the Peruvian Government.**

#### Dissertation Structure:

- Chapter 2 contains the description of how the compiled dataset from Peru, Chile and Ecuador were processed in order to obtain the IM parameters for the GMPE regression analysis. To do so, the description of the instrumentation and stations that were used are given. Next, an explanation of how these dataset was classified into interface, inslab and crustal events is stated. Then, only the interface dataset is selected for the present study in order to process all the raw records ground motions considering the two horizontal and one vertical components. After that, a general explanation of which methodology was used to estimate the IM parameters is presented. Finally, the procedure of magnitude homogenization is described.
- Chapter 3 incorporates an explanation of the methodology chosen for GMPE regression analysis for both horizontal and vertical IM parameters. First, the General form of the GMPE is presented. Second, the two-step Maximum-likelihood is explained. Finally, the functional form of the median GMPE, the regression coefficients and standard deviation of the PGA and spectral acceleration of the predictor variables are given.
- Chapter 4 refers to the regression analysis of the mean period ( $T_m$ ), the  $PGA/PGV$  ratio, the  $PGA/PGVT_m$  ratio, and the  $PGA/PGVf_m$  ratio in order to develop the GMPE for each IM.
- Chapter 5 contains the comparison of the new GMPE for interface events with previous existing models.
- Chapter 6 gives the discussion
- Chapter 7 concludes the findings of this study
- Chapter 8 refers to the recommendations for future work

## PERU, CHILE AND ECUADOR DATASET

Motion records between 4 and 8.5 magnitudes were compiled from the Geophysical Institute of Peru (IGP), The Japan- Peru Centre for Seismic Research and Disaster Mitigation (CISMID), the National Training Service for the Construction Industry (SENCICO), the Graduate Faculty of Civil Engineering of the National University of Engineering (FIC-UNI), the Peruvian Association of Engineers (CIP), the South American Regional Seismological Centre (CERESIS), the Peruvian State Water Company (SEDAPAL). Moreover, records from National CNS and RENADIC network from Chile were selected considering the same range of magnitude. Also, 21 records from the 7.5  $M_w$  16/04/2016 subduction event earthquake that occurred in Manabí, Ecuador was considered. Two-thousands eight-hundred and three (2803) events were collected mainly from Peru, Chile and Ecuador between 4.0 and 8.5  $M_w$  from 1951 to 2020. These events comprise nearly eighteen-thousands (18,000) records from these sources that harbours interface, intraslab and crustal events. All the events are plotted in [Figure 01](#).

In order to develop a GMPE for interface events, a new subset of motion must be selected. To do so, it is important to identify the geometry of the Peruvian, Chilean and Ecuadorian subduction zone as they will be described in [section 2.2](#). Then, another group of records was taken apart using signal processing criteria as it will be presented in [section 2.3](#). Finally, magnitude homogenization to moment magnitude was carried out considering the different types of magnitudes presented from the different sources and restrained the events applying magnitude-dependent limits to distance in order to diminish any bias produced by the trigger threshold of accelerometers [\[58\]](#) as they will be presented in [section 2.4](#).



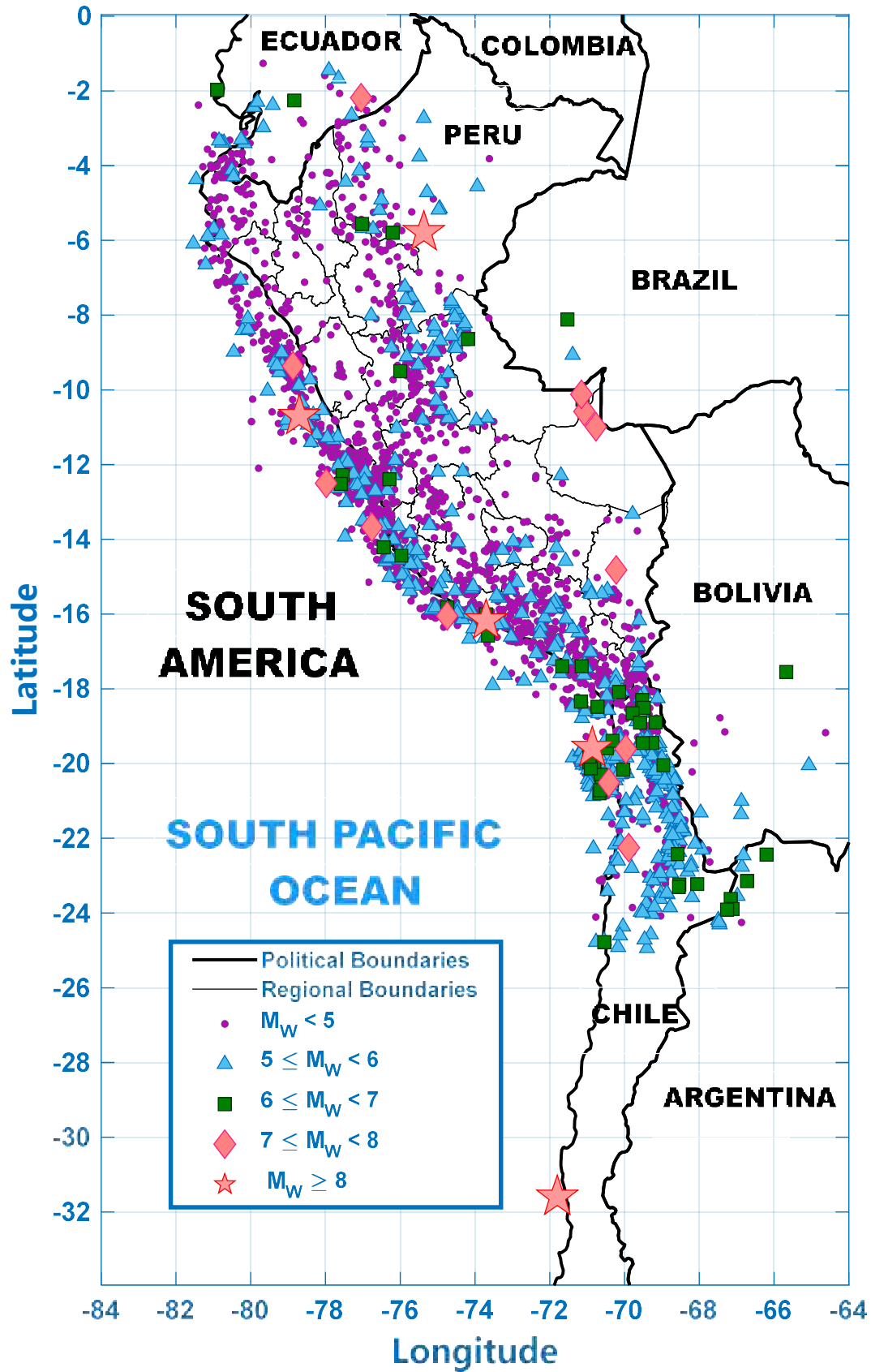


**Figure 1:** The compiled data set used in this study that comprises interface, intraslab and crustal earthquakes ( $M_W \geq 4.0$ ), 1951-2020.

## 2.1. Instrumentation

**Fig. 02(a)** shows the location of the 523 stations used in this study from six different Networks of Peru, Chile and Ecuador. The stations from the National Training Service for the Construction Industry (SENCICO) and the Peruvian State Water Company (SEDAPAL) are monitored and available from the IGP and CISMID website. All the records from the compiled data shown in **Fig. 01** were downloaded from their network operator website [IGP, UNI-FIC, CISMID, RENADIC, CNS, and RENAC]. The largest density of instruments is placed in the capital of Peru (Lima) where the CISMID network operates with 72 stations. It is worth mentioning that almost all the stations are located in the forearc region (between the subduction trench axis and the axis of the volcanic front) as shown in **Fig.02(b)**. The stations that are located in the backarc region (as some station located in the Peruvian southern part from the IGP and FIC-UNI networks) may have a possible dissimilarity in the rate and characteristics of ground motion attenuation [58]. However, the volcanic activity in Peru is not as much active as in the past. For instance, the Coropuna, Chacani, El Misti, Huaynaputina, Tutupaca, Yucumane, and Casiri volcanoes have erupted during the last 10,000 years. Meanwhile, the Ubinas and the Sabancaya located in Moquegua and Arequipa respectively presented eruptions in the last 200 years [84], [85]. Nowadays, the Ubinas volcano has presented explosions releasing ash within a radius of 25km (16 miles) in 2019 in the southern part of Peru [86]. Therefore, ground motion attenuation due to the volcanic activity will be neglected for the present study, and these few stations will be treated as well as backarc GM records.

The National Seismological Centre of the University of Chile (CNS, Centro Sismológico Nacional) harbours more than 100 multiparametric stations. These are composed of broadband seismometers, accelerometers and Global Navigation Satellite System instruments [71], [87]. For the present study 177 stations were utilized from this network as described in **Appendix A.1**. Meanwhile, the National Accelerometer Network of the Department of Civil Engineering (RENADIC) from Chile consist of 20 analogue and 15 digital stations installed in Northern and Central Chile [52]. For this study, 19 stations were utilized as presented in **Appendix A.1**. The Peruvian networks from CISMID, IGP, and FIC-UNI are mainly composed by digital accelerometers from which some of them were at the beginning analogue accelerometers before they were replaced [69]. For the present study, 72, 160, and 74 stations were used from the CISMID, IGP and FIC-UNI networks respectively as cited in **Appendix A.1**. Finally, the 21 stations from the National Accelerometer Network (RENAC) from Ecuador are digital accelerometers and broadband seismometers (as shown in **Appendix A.1**) [79], [88]. The  $V_{s30}$  profiles considered for all the 523 stations are described in the introduction and these values are cited in column 07 of the table presented in **Appendix A.1**. However, the site classification based on the resulting average S-Wave velocity of the upper 30m ( $V_{s30}$ ) was based in the average classification values proposed by Leyton et al. (2018) [71] and Aguilar et al. (2019) [70] for their similarities. Therefore, the site classification for the present study based on  $V_{s30}$  are cited in **Table 01**. As a result, site classification considered for all the stations are cited in column 09 of the table shown in **Appendix A.1** where AB, BC, CD and DE are the limit values of 875, 525, 350 and 190 m/s for the stations that have  $V_{s30}$  between an upper and a lower bound range of  $\pm 50$  m/s respect those limit values. Meanwhile, the soil classes A, B, C, D and E correspond the stations that have  $V_{s30}$  between the range established in **Table 01** whose values are 1150, 700,

437.5, 270 and 180m/s respectively as described in Column 10 of the tables given in Appendix A.1.

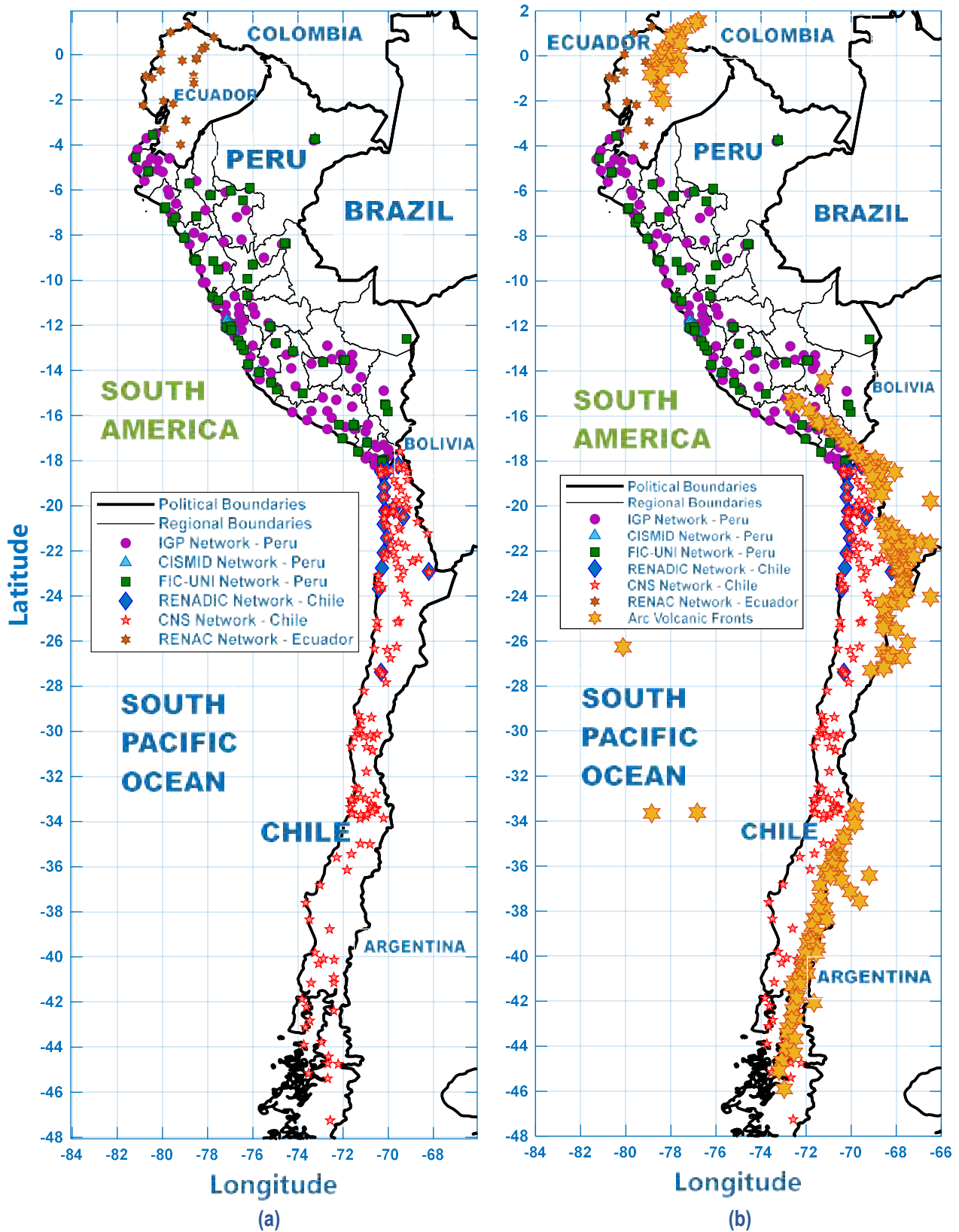


**Figure 2:** Location map of: (a) the six networks from Peru, Chile and Ecuador utilized in this study, and (b) the six networks from Peru, Chile and Ecuador and the Arc Volcanic Front of the subduction zone.

**Table 1:** Site Classification based on the Resulting Average S-Wave Velocity of the Upper 30 m ( $V_{s30}$ ), based in the average values from Leyton et al. (2018) and Aguilar et al. (2019).

Classification	$V_{s30}$	Range (m/s)
A	875	$< V_{s30}$
B	525	$< V_{s30} \leq 875$
C	350	$< V_{s30} \leq 525$
D	190	$\leq V_{s30} \leq 350$
E		$V_{s30} < 190$

## 2.2 Selection of Interface Events from the Catalogue

Many studies have been performed in order to identify the geometry of the subduction zone [89]–[93]. However, 18 sections have been selected and they were derived from the evaluation and discussion of the geodynamic evolution mechanism of the Peruvian subduction zone [94], from the calculation of receiver functions (RFs) of broadband seismic data and common conversion point (CCP) stacking [95], from PULSE studies [96], and from P- and S-wave tomography inversions [97]. Then, these depth locations of the subduction zone were compared to the Slab2 three-dimensional geometry [98] in order to estimate a depth variability of the subduction interface. Now, the location of the interface will be matched to the focal depth ( $D$ ) of each event between a specific range that defines its variability. A value of  $\pm 16$  km was determined after calculating the standard deviation of the absolute difference between the 18 sections and the Slab2 geometry as shown in Fig. 03. This value will be taken as the variability range to identify interface, inslab and crustal earthquakes. The events that are under that range will be classified as inslab and the events that are over that range will be classified as crustal. At that point, MATLAB software was utilized to interpolate the points respect to the trench axis (epicentral coordinates and focal depth) considering the 2803 events, which will enable to classify the events considering the aforementioned estimation of the standard deviation. As a result, the earthquake classifications are shown in Fig. 04, Fig. 05, and Fig. 06 for interface, inslab and crustal events, respectively. Considering the complied dataset in this study, 45% corresponds interface events, 33% corresponds inslab events, and 22% corresponds crustal earthquakes. Almost all the events are located in the forearc region and few events are located in the backarc region where the volcanic arc was represented in the previous figures. From Fig. 04 Interface events comprise events up to  $M_w$  8.5. Meanwhile, events up to  $M_w$  8.0 and  $M_w$  7.0 correspond intraslab and crustal events as shown in Fig. 05 and Fig. 06, respectively. For the present study, only interface earthquakes will be utilized to generate the GMPE for the Peruvian Subduction Zone.

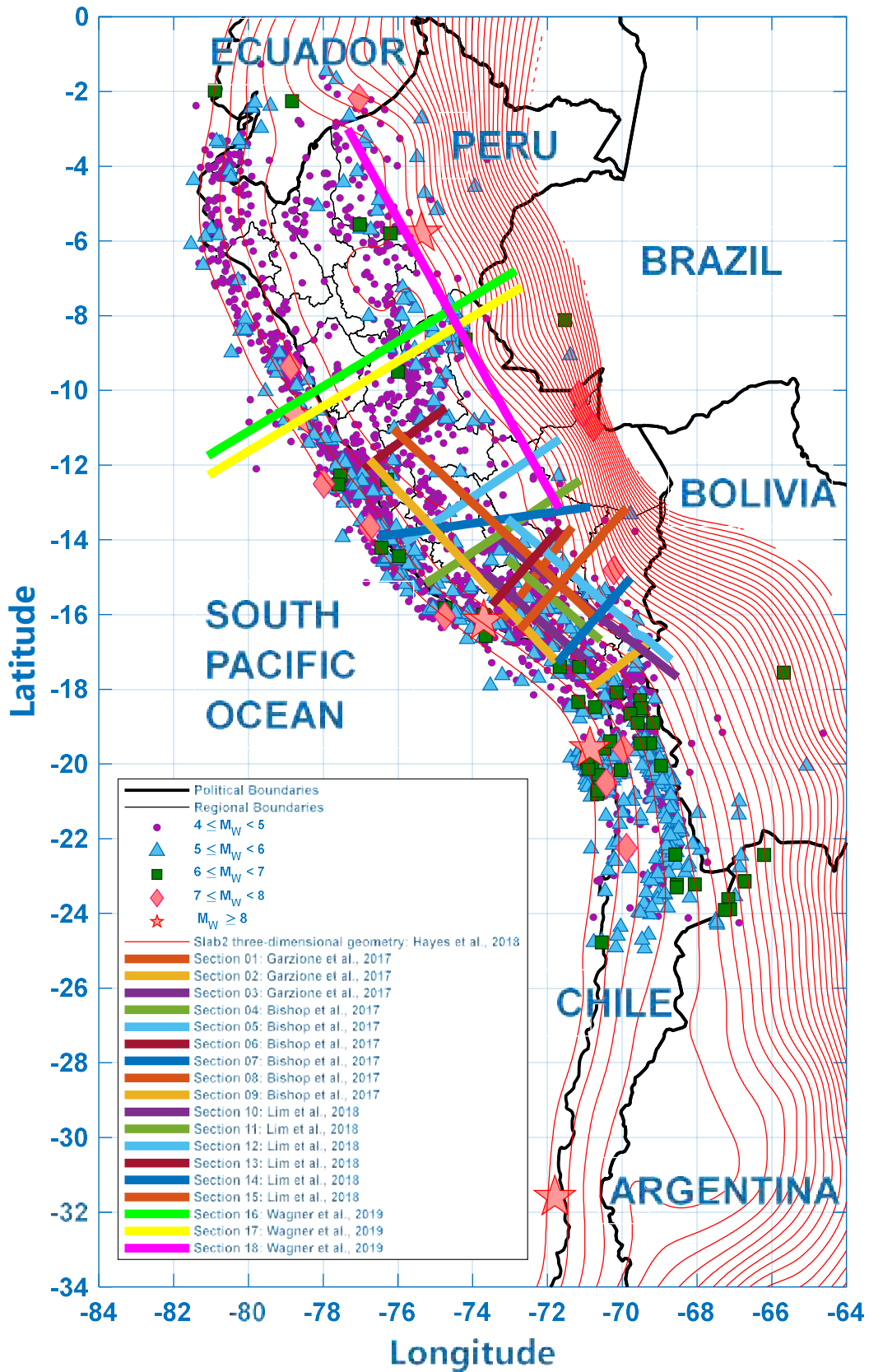


*Figure 3: Model construction of the plan shape of the Peruvian, Chile, Ecuador, Brazil, Bolivia and Argentina Subduction Zone Geometry with contour lines and sections*



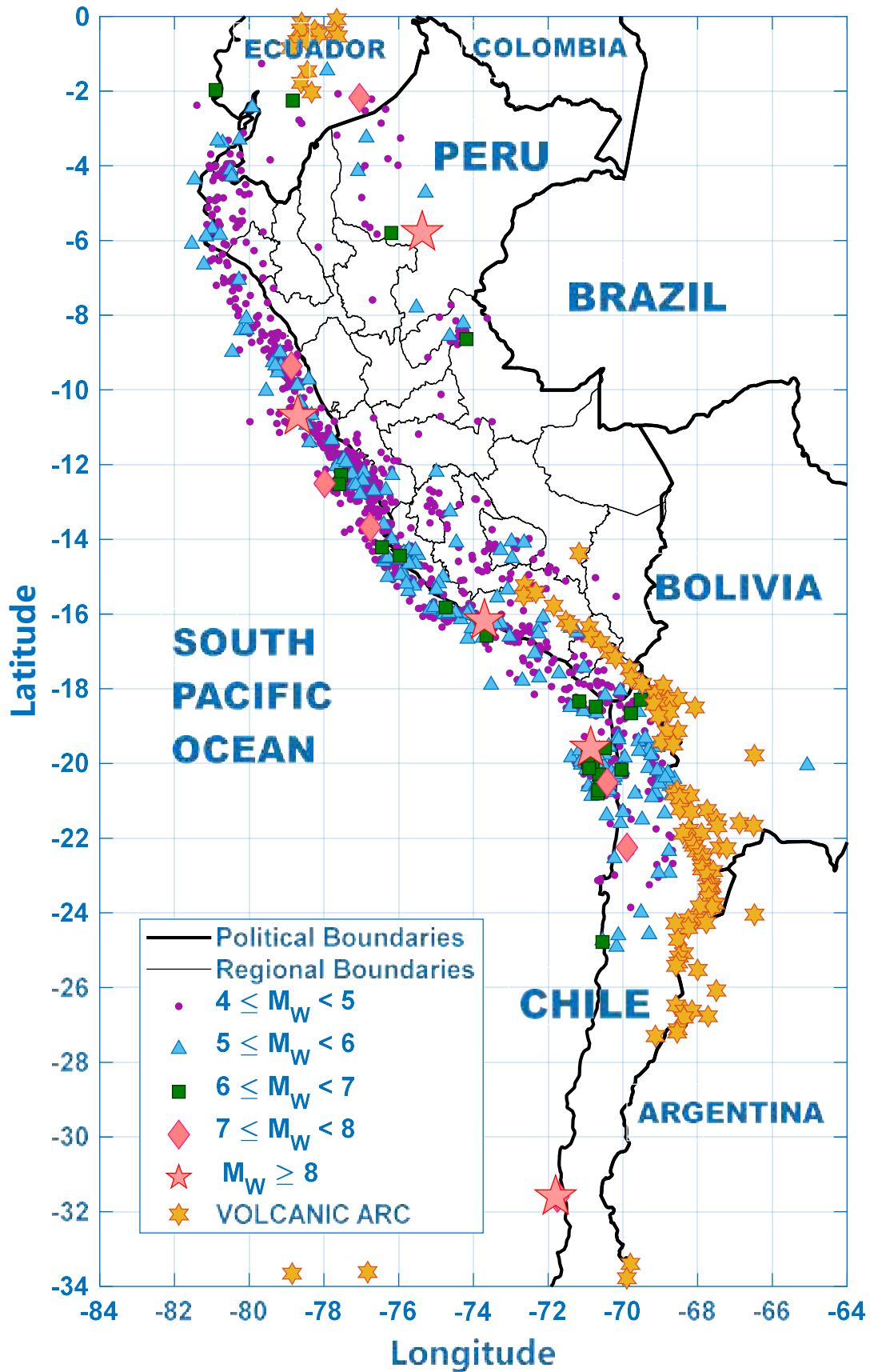


Figure 4: Interface Events from the compiled dataset used in this study.

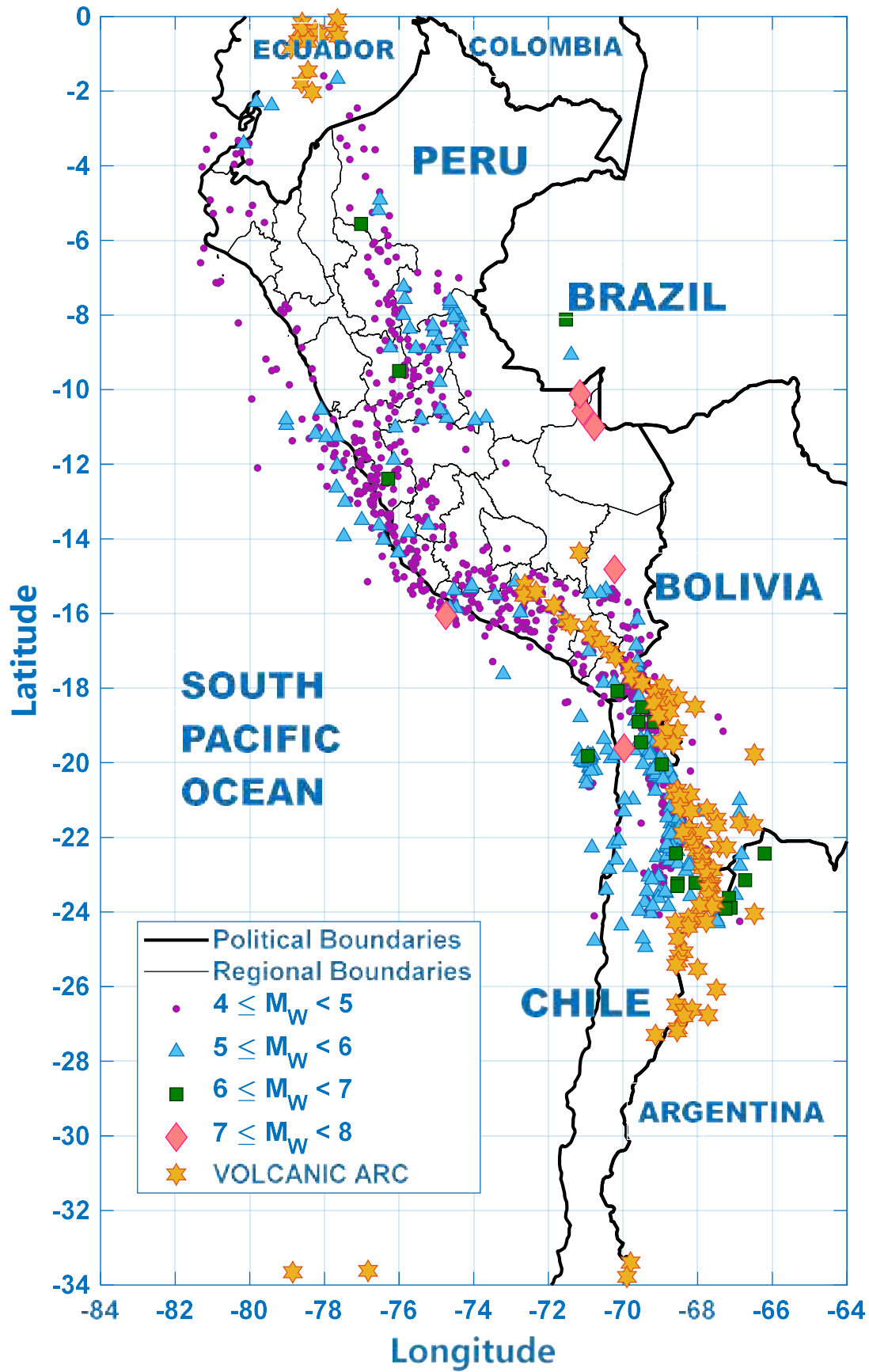


Figure 5: Intraslab Events from the compiled dataset used in this study.

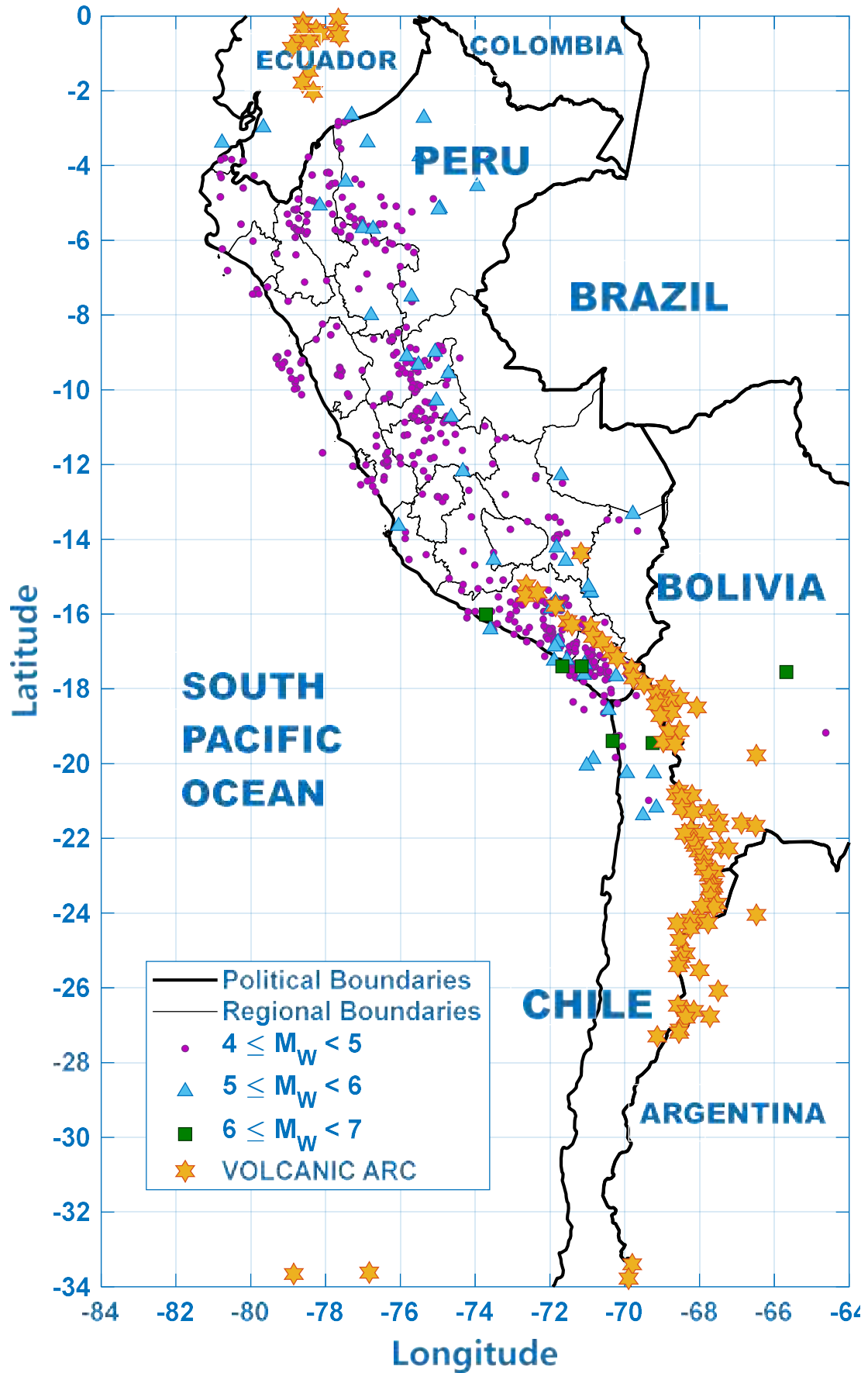


Figure 6: Crustal Events from the compiled dataset used in this study.



## 2.3 Processing of Raw Data

The dynamic response of the structure depends on the characteristics of the ground motion [99]. Therefore, the variability of the structural output relies on the signal processing that plays an important role in the variability of structural analysis [100], [101]. The processing of ground motion presents two important steps [102]: (1) reduction of arbitrary noise that alters ground motion signals, and (2) response correction due to strong movement of the instrument itself. However, it does not exist an ideal method for processing that takes into account the unknown random noise and known noise of recorded motions. So, many methods have been proposed [101]–[104] to obtain the cut-off low frequency or high-pass corner frequency and also to eliminate the baseline drift. The main goal of high pass filtering is to maintain the complete nature of the records by minimizing the removal of seismic signal. As a result, selecting the lowest quantity of the high-pass corner frequency maintains the actual earthquake time series. Nevertheless, the latter does not necessarily imply that it is appropriate. So, the choice of the filter parameters may not offer proper signal processing [105]. However, the selection of a specific filter type is not very sensitive for a particular ground motion. Therefore, the Butterworth filter is utilized by the California Strong Motion Instrumentation Program (CSMIP), the United States Geological Survey (USGS), and the University of Bristol. Meanwhile, the Ormsby filter is assessed by the University of Southern California (USC), and the elliptical filter is used by the Imperial College London [106]. For the present study, the Butterworth filter is utilized for the high-pass filtering, which is governed by the following transfer function:

$$|H_n(\omega)| = \frac{(\omega/\omega_c)^n}{\sqrt{1+(\omega/\omega_c)^{2n}}} \quad 1.$$

Where  $n$  indicates the order of filter that defines the slope of the transition band (as shown in Fig. 7), and  $\omega_c$  is the high-pass corner frequency.

Three factors may be considered when performing a filter type with a specific high-pass corner frequency: (1) choosing lower values of the filter order ( $n < 8$ ) can recover portions of the low-frequency components and as the same time it can remove part of the high-frequency components; (2) picking out lower values of the filter order can lead to the reduction of the interval of the usable frequency of the earthquake motion; and (3) an adequate wave signal of the velocity and displacements. The first two reasons for selecting higher filter order values can be more appropriate. However, lower-frequency can be neglected. In addition, neglecting lower frequencies values can be prejudicial to long-period structures such as long-span bridges, tall buildings and based isolated structures. Therefore, if the lower value of the prevailing frequency range of the structural response is higher than the minimum usable frequency ( $f_{use}^{min}$ ), it is suggested using a filter order equal to 8 in order to assess the filtering process. The prevailing frequency range for a structure can consider this range  $[f_n - \xi f_n, f_n + \xi f_n]$  in the static analysis and the  $[0.8f_n, 1.2f_n]$  range in the nonlinear analysis ( $f_n$  in the fundamental frequency of the building and  $\xi$  is the damping ratio) [107]. This implies that  $f_n - \xi f_n$  and  $0.8f_n$  must be higher than  $f_{use}^{min}$  for linear and nonlinear analysis respectively. For the present study, the spectral periods with 5% damping ratio chosen for the GMPE regression are 0.2, 0.3, 0.6, 1.0, 2.0, 3.0, 4.0 and 5.0sec. The critical value is 3.0sec because it refers to structures with a fundamental frequency of 0.33Hz and

damping ratio of 5%. This implies that  $f_n - \xi f_n$  and  $0.8f_n$  are 0.317Hz and 0.27Hz which are higher than  $f_{use}^{min}$  that is set to 0.25 for the static and nonlinear analysis respectively neglecting the effect for spectral periods larger than 3.0s for the present study. Likewise, it can be justified to use a filter order equal to 4 for simplicity [108] as presented in Fig.7. Furthermore, the selection of  $f_{use}^{min}$  can be insensitive to filter motion records when earthquakes present moment magnitudes larger than Mw 7, have epicentral distances (R) larger than 30 km, are released in specific soil shear velocity (except for  $V_{s30} = 100m/s$ ). Therefore, for the other cases  $f_{use}^{min}$  can be calculated by minimizing the cumulative energy content of seismic signals in order to establish the high-pass corner frequency (which can be higher than 0.25). The latter definitely influence on PGA, PGV and PGD estimations from raw ground motion records and making decision of which filter order value can be used. Then, this decision may safeguard the lower frequency content of a ground motion for design purposes [106].

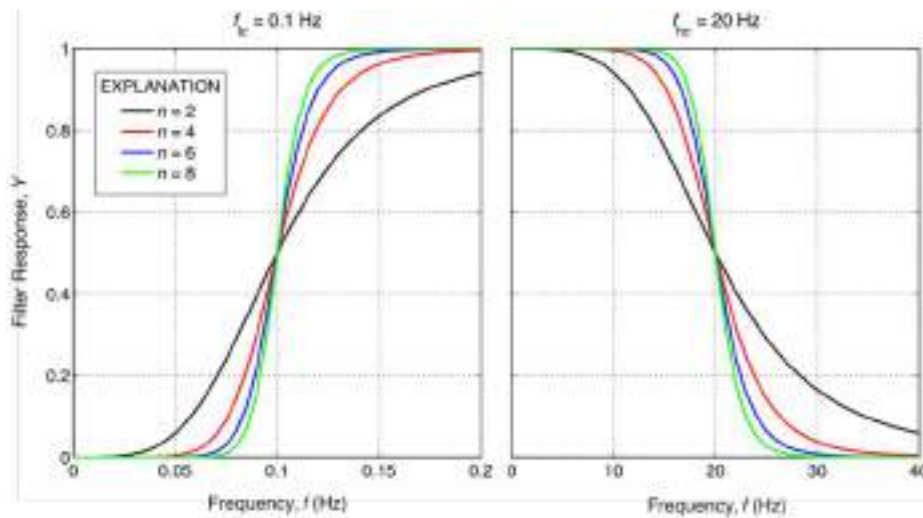


**Figure 7:** Graphs showing: (a) a low-cut Butterworth filter with low-cut corner of  $f_{IC} = 0.1\text{Hz}$ , and (b) a high-cut Butterworth filter with a high-cut corner of  $f_{HC} = 20\text{Hz}$ . [108].

Furthermore, the correct use of windowing leads to reduce spectral leakage when turning time data into the frequency domain when assessing the Fourier Transform. There are different types of windows such as Hanning, Flattop, Uniform, Tukey and Exponential. Ground motion is mostly aperiodic in all its time history. Therefore, a window is needed in order to capture the acceleration in a non-periodic manner so that leakage is minimized. This action will recreate the original sine wave by avoiding broadband transient events or leakage. On the other hand, windowing is not necessary for periodic time series because it may modify the Fourier Transform and creates spectral leakage where no leakage would have been presented.

Tukey window is usually used for transient data and offers a flat time domain with a close value of one for the whole window. This offers better advantages of not affecting the amplitude of transients rather than other types of windows (e.g. hanning or flattop). Therefore, the length of this flatness can be specified by assigning a specific value known as the taper length which can be expressed as a percentage. The Taper percentage of 10% will be used for the present study to perform the Butterworth method. This means that 80% of the taper length will have a value of one and the remaining

20% distance will be distributed equally at both sides to generate the transition from one to zero as shown in **Fig.8** [109].

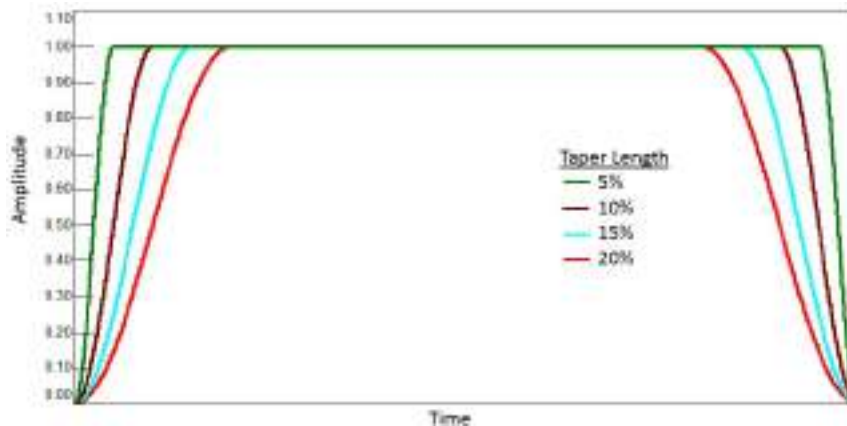


**Figure 8:** Squamation the Tukey Window with various taper lengths which indicated what flatten portion of the Tukey window has a value of zero. Siemens, 2019 [109].

Finally, a MATLAB code was prepared to assess these procedures for each ground motion record for the two horizontal and one vertical components.

## 2.4 Estimation of IM parameters for the horizontal and vertical motion: PGA/PGV, ( $S_{ai}$ ), $T_m$

After all the ground motion data are filtered from interface events, the Peak Ground Acceleration (PGA), the Peak Ground Velocity (PGV), the spectral acceleration ( $S_{ai}$ ) with 5% damping ratio for the periods of 0.20, 0.30, 0.60, 1.0, 2.0, 3.0, 4.0 and 5.0 sec and the Mean period ( $T_m$ ) for the two components of the horizontal motion and one component of the vertical acceleration can be obtained. In order to safeguard accurate parameters of the PGA and PGV, some explanation was given in **section 2.3**. Meanwhile, the proper numerical method should be chosen to obtain the  $S_{ai}$  and the  $T_m$ . For the present study they will be described as follows.

Concerning to  $S_{ai}$ , the applicability of algorithms for earthquake response estimation depends on the variability of the time history of strong ground motions. This can be restricted especially for structures with a short vibration period. Therefore, the methods for estimating the structural response of a single degree of freedom (SDOF) can be evaluated by two methods: (1) Frequency-domain method, and (2) Time-domain method. The two methods are equivalents when performing linear elastic problems. However, time-domain is only applicable when nonlinear behaviour of structures is evaluated [110]. There are many time-domain methods such as the Newmark method [111], the Duhamel Integration method [112], the Z-transform method [113], the Central Difference Method [114] and the Jin Xing method [110]. The Duhamel method and the Z-Transform method offer an amplitude error of less than 10% when this condition  $0 \leq \Delta t/T_0 < 1/10$  is met ( $T_0$  is the natural period of the SDOF system and  $\Delta t$  the time step of the ground motion). On the other hand, the Central and the Newmark method offer the same error when the upper bound is increased to 1/20. This implies that the Newmark method and the Central method present more error in structure with periods less than 0.2 sec compared to the other methods with lower bound when the time step is 0.01sec (or

the sample rate is 100 Hz) for common ground motion records. In addition, the Duhamel method and the Jin Xing method provide better advantages compared to the other methods [110]. Nevertheless, the improved Jin Xing method can offer less than 5% error for spectral acceleration as well as the Duhamel Method. This is true for frequency band between 0.01 and 50 Hz assessed to a structure that has a natural period and damping ratio of 0.2s and 0.05, respectively [115]. For the present, the Duhamel method is used so each motion should meet this condition  $0 \leq \Delta t/T_o < 1/10$  to reduce the error.

On the other hand, the mean period ( $T_m$ ) can be computed from the Fourier Amplitude Spectrum of each ground motion by using the following equation [49], [116]:

$$T_m = \frac{\sum_i c_i^2 (1/f_i)}{\sum_i c_i^2} \text{ for } 0.25 \text{ Hz} \leq f_i \leq 20 \text{ Hz, with } \Delta f \leq 0.05 \text{ Hz} \quad (2)$$

Where,  $C_i$  are the Fourier amplitude coefficients,  $f_i$  are the discrete fast Fourier transform (FFT) frequencies, and  $\Delta f$  is the frequency interval used in the FFT calculation given in equation (3).

$$\Delta f = 1/(N \cdot \Delta t) \quad (3)$$

Where,  $N$  is the number of point in a time series, and  $\Delta t$  is the time step that is usually between 0.01s and 0.005s for the recorded motions analysed in this study.

For the present study, only the motions that meet the condition of the frequency interval ( $\Delta f$ ) as indicated in **equation 2** will be selected for the regression. Then, a MATLAB code was prepared to obtained the  $S_{ai}$  with 5% damping ratio and the mean period ( $T_m$ ) for the two horizontal and one vertical components for each GM record.

## 2.5 Magnitude homogenization and distance to source

The local Magnitude ( $M_L$ ) [117], [118] and the body-wave magnitude ( $m_b$ ) are common measures to estimate energy released from earthquakes in Peru. However, it may lead to an incorrect energy estimation of strong ground motion. The moment magnitude ( $M_w$ ) is commonly used as a proxy value for the generation of GMPEs because does not saturate and gives a most robust estimate of large earthquakes. This parameter is derived from seismic moment utilizing seismic waves with much longer periods [119], [120]. However,  $M_w$  is suitable to simulate the variability of ground motion for frequencies below 2Hz. On the other hand, the high frequency magnitude performs better for higher frequencies motions [121]. Nevertheless, if the peak ground velocity increases with increasing stress drop ( $\Delta\sigma$ ), the local and energy magnitude perform better than the  $M_w$  as predictors for potential shaking [122]. Therefore, avoiding the concern of the variability of the  $M_w$  on the spectral periods larger than 0.5sec, it is important to homogenize the diverse magnitudes into  $M_w$ . To do so, the  $M_w - M_L$  and  $M_w - m_b$  conversions proposed by Tang et al. (2016) [123] will be used for having lower standard deviations. The latter is because the general orthogonal regression (GOR) method was performed and provided better advantages than the ordinary least-squares (OLS) regression. Then, these equations are described as follows:

$$M_w = 1.48 + 0.71M_L \quad (4)$$

$$M_w = -0.55 + 1.16m_b \quad (5)$$

On the other hand, the conversion of distance metric can generate uncertainties of the selected and developed GMM to establish a magnitude and distance-dependent. This means that point-source models cannot be appropriate for larger events at short distances. So, the reduction of ground motion cannot be defined as a simple function of a point-source distance measure. Therefore, several distance metrics have been proposed for extended sources [124], [125]. As a consequence of that, there are many reasons when comparing the GMPE resulted from commonly used attenuation relationships [126]. The same problem occurs when PSHA has been performed using different attenuation relationships with different branches of a logic tree.

The Joyne-Boore distance (the nearest distance to the surface projection of an extended fault,  $R_{jB}$ ) or rupture distance (the nearest distance to an extended fault,  $R_{rup}$ ) are the most commonly used parameters to relate ground motion attenuation over distance. These distances will enable to capture the effect of finite fault ruptures, in special for near-source recordings. Particularly, the spatial distribution of earthquakes (where traces of fault are unknown) is evaluated as point-source models in PSHA applications. Thus, it is mandatory to convert the epicentral ( $R_{epi}$ ) or hypocentral ( $R_{hyp}$ ) point-sourced based distances into the extended fault-based distance measure defined in GMMs [127]. This is because seismic energy is released from the entire extended-fault rupture during a strong earthquake. Therefore,  $R_{jB}$  and  $R_{rup}$  can be well correlated to the geometric-mean ground motion intensity measure. The simplest relation between the extended source and a point source are the Joyner-Boore distance ( $R_{jB}$ ) and the epicentre distance ( $R_{epi}$ ), respectively. Both distances neglect any depth information because they are measured along the surface distance. However, a linear regression is not sufficient to capture the relationship between the hypocentral and Joyner-Boore distance. The Joyner-Boore distance is always lower than the epicentral distance ( $R_{jB} \leq R_{epi}$ ) and this difference depends on source size, fault dip, and site orientation [128]. Therefore, for the present study the epicentral distance ( $R_{epi}$ ) can be calculated for each event as stated as follows:

$$R_{epi} = [ST(Lat, Long) - EV(Lat, Long)] \quad (6)$$

where,  $ST(Lat, Long)$  are the latitude and longitude coordinates of each station that corresponds to each event,  $EV(Lat, Long)$  are the latitude and longitude hypocentral coordinates of each event, and  $R_{epi}$  is the epicentral distance in km.

Besides, the depth distribution of hypocentres ( $D$ ) can be grouped into two categories: (1) indirect approach, and (2) direct approach. The first one is based on rupture initiation based on stress/strength distribution inside the Earth where the high-frequency phases are used for its location [129], [130]. Meanwhile, the second approach is modelled directly that results from a moment tensor inversion closely related to the centre of moment release [128]. Some considerable differences may arise between these two categories for large earthquakes because the description of the hypocentral distance coordinates from earthquakes catalogues will be based on the location method. The hypocentral distance ( $R_{hy}$ ) strongly depends on hypocentre depth ( $D$ ) for closer events and small events as stated in the following equation:



$$R_{hyp} = \sqrt{R_{epi}^2 + D^2} \quad (7)$$

where,  $D$  is the focal depth in Km,  $R_{epi}$  is the epicentral distance in km, and  $R_{hyp}$  is the hypocentral distance for each station in km.

As previously stated, the epicentral coordinates  $EV(Lat, Long)$  and the depth ( $D$ ) can vary according to the indirect and direct approach. These were the case when comparing the data from earthquakes catalogues among the different sources (eg. USGS, IGP, CNS, FIC-UNI, CISMID, RENADIC) for events larger than  $M_w$  5. As a consequence of that, it was assumed that all the events were based on rupture initiation and were located in the centre of the extended fault source (with a width ( $W$ ), a length ( $L$ ), and a dip angle ( $\delta$ )) for the present study. So, the geometric mean was taken for each event in order to unify one value of  $EV(Lat, Long)$  and  $D$  when  $R_{epi}$  and  $R_{hyp}$  were calculated. Meanwhile, the  $D$  influence on  $R_{hyp}$  is negligible with increasing distance and magnitude [128].

Now, the general analytical-based distance conversion used for this study is based on the uniform weighted average of the distance from virtual sites, and they are modified to include the geometrical spreading decay function ( $G$ ), the shear wave velocity ( $V_s$ ), the quality factor ( $Q$ ) and the reference frequency in the attenuation function and attenuations. Tavakoli et al. (2018) [127] proposed the following equation to convert the effective point source based distance metric ( $R_{EFF}$ ) based on either  $R_{hyp}$  or  $R_{epi}$  into  $R_{jb}$  distance by using the following equation:

$$G(R_{EFF}) \exp\left(\frac{-\pi f R_{EFF}}{Q(f) V_s}\right) = \left[ \int_{Z_{TOR}}^{Z_{TOR}+W \sin(\delta)} \int_0^{W \cos(\delta)} \int_{-L/2}^{L/2} \left\{ \left[ G(\lambda) \exp\left(\frac{-\pi \lambda f}{Q(f) V_s}\right) \right]^2 p(x) p(y) p(z) dx dy dz \right\}^{0.5} \right] \quad (8)$$

where,  $Z_{TOR}$  is the depth of the top of the fault rupture as defined in [equation 9](#),  $\lambda$  is the distance between the observation point and possible epicentre or hypocentre location on the fault as defined in [equation 10](#),  $p(x)$ ,  $p(y)$ , and  $p(z)$  are the probability distribution functions which can be uniform or exponential depending on the azimuth as proposed by Tavakoli et al. (2018), and  $W$  and  $L$  are the rupture width and the rupture length in km respectively that can be calculated using [equation 11](#) and [equation 12](#) for subduction events as proposed by Strasser et al. (2010) [131]:

$$Z_{TOR} = h_{center} - W/2 \quad (9)$$

$$\lambda = \sqrt{[(R_c^2 + x^2 - 2xR_c \cos(\theta)) + z^2]} \quad (10)$$

$$\log_{10}(W) = -0.882 + 0.351M_w \quad (11)$$

$$\log_{10}(L) = -2.477 + 0.585M_w \quad (12)$$

Where,  $h_{center}$  is the distance from the ground surface to the centre of the fault plane, which is assumed to be equal to  $D$  as stated before,  $R_c$  is the auxiliary distance as presented in [equation 13](#),  $\theta$  is the particular azimuth angle for each observation point between  $R_{jb}$  distance and  $R_{hyp}$  distance.

$$R_c = \begin{cases} \sqrt{(L/2)^2 + R_{jb}^2 - 2(L/2)R_{jb} \cos \left[ 180 - \left( \theta + \arcsin \left( \frac{\sin(\theta)L/2}{R_{jb}} \right) \right) \right]} & \text{if } 0 \leq \theta < \theta_0 \\ R_{jb}/\sin(\theta) & \text{if } \theta_0 \leq \theta < 90 \end{cases} \quad (13)$$

Some quality factor values ( $Q$ ) were proposed by Jang et al. (2019) [132] beneath the Nazca-South America subduction from 11°S to 15°S, the Central Andean Plateau (which is related to the subducting Nazca Plate) from ~13°S to 18°S and the Brazilian mantle lithosphere considering shallow and intermediate-depth earthquakes. Five important features were identified for P and S phase arrivals denoted by  $Q_p$  and  $Q_s$ , respectively. These values can provide accurate estimations for site amplification [132]. Furthermore, the south part region of Peru presents normal subduction dipping angle of 30° with maximum depths of 300 km [97], [133]. However, the central to the north part of Peru (flat subduction zone) present dipping angles between 0° and 16° for depths up to 100km and then increases to dipping angles of about 50° for higher depths [96], [98]. For simplicity purposes in this study, the mean converted  $R_{hyp}$  distances respect to  $R_{jb}$  distances up to 1000km for 40° dip reverse fault proposed by Tavakoli et al. (2018) [127] is used as presented in **Table 02**.

These effective hypocentral distances ( $R_{EFF}$ ) distances for the different  $R_{jb}$  and  $M_w$  values (as presented in **Table 02**) were estimated for Eastern North America. The values used such as the quality factor ( $Q$ ), the surface geometrical spreading functions ( $G$ ), and the shear velocity ( $V_s$ ) can be assumed as the same values for the Peruvian subduction zone. Meanwhile, the distance conversion is very insensitive to frequency ( $f$ ) value that was employed [134]. Therefore, an interpolation MATLAB coding was performed considering the  $R_{hy}$  distance for each station and each event. However, some arrangement were assumed for the events that have  $R_{hyp}$  distances higher than 1,040km and moment magnitudes lower or higher than 4.5 and 8, respectively. For  $R_{jb}$  distances higher than 1,000km, there is a tendency of being equal to  $R_{hy}$  as previous stated (as indicated in **Table 02**). Also, an exponential trend exists in the values and they were estimated from moment magnitudes higher and lower than 4.5 and 8, respectively in order to cover the gap range for the interpolation.

**Table 2:** Mean Converted Rhyb distances respect to Rjb and Mw for 40° dip reverse fault. Tavakoli et al. (2018) [127].

$R_{jb}$ (km)	Moment Magnitude (Mw)							
	4.50	5.00	5.50	6.00	6.50	7.00	7.50	8.00
1.00	10.60	10.61	10.69	11.05	12.12	13.61	14.34	18.60
2.00	11.09	11.10	11.30	11.39	12.50	14.39	17.39	26.79
3.00	11.20	11.26	11.28	11.97	13.24	15.45	19.21	31.29
5.00	12.11	12.17	12.48	13.35	14.34	17.28	22.12	36.64
7.00	12.69	13.30	13.59	14.76	16.29	19.11	24.47	40.23
10.00	15.00	15.41	15.99	16.78	18.64	22.03	27.98	44.44
12.00	16.60	16.77	17.13	18.28	20.74	24.04	30.35	46.92
15.00	19.20	19.47	19.95	21.28	23.35	27.11	33.41	50.33
20.00	23.38	23.78	24.49	25.78	28.32	32.18	38.93	55.40
30.00	32.53	32.88	33.89	35.31	38.09	42.59	49.19	63.97
40.00	42.04	42.54	43.59	45.14	48.00	52.63	58.64	83.29
50.00	51.82	52.38	53.24	54.94	57.88	62.04	66.29	113.96
60.00	61.66	62.20	63.19	64.85	67.05	68.87	80.61	130.78
70.00	71.52	72.07	73.05	74.91	78.42	84.89	97.21	138.73
80.00	81.43	81.95	82.92	84.84	88.24	94.74	107.43	145.48
100.00	101.30	101.85	102.83	104.64	108.08	114.48	130.14	158.54
120.00	121.22	121.78	122.74	124.54	127.99	136.67	146.99	173.30
150.00	151.13	151.68	152.66	154.45	157.78	163.82	174.51	202.67
200.00	201.03	201.58	202.60	204.37	207.74	213.86	224.81	253.89
250.00	251.00	251.53	252.50	254.34	257.68	263.88	274.96	304.88
300.00	300.95	301.49	302.48	304.30	307.66	313.88	325.09	355.68
400.00	400.90	401.46	402.42	404.25	407.63	413.89	425.23	456.87
500.00	500.89	501.41	502.40	504.24	507.62	513.89	525.35	557.70
600.00	600.87	601.40	602.40	604.21	607.60	613.89	625.41	658.32
700.00	700.85	701.38	702.38	704.20	707.59	713.89	725.46	758.78
800.00	800.83	801.38	802.38	804.19	807.57	813.89	825.49	859.15
1,000.00	1,000.82	1,001.38	1,002.36	1,004.18	1,007.57	1,013.89	1,025.53	1,059.70

In order to estimate the rupture distance ( $R_{rup}$ ), the following equation that correlates the closest distance from the rupture and the effective hypocentral distance ( $R_{EFF}$ ) proposed by Tavakoli et al. (2018) [127] is utilized:

$$R_{EFF} = \sqrt{R_{rup}^2 + h^2} \quad (14)$$

Where,  $R_{EFF}$  is set equal to the  $R_{hy}$  for each station and each event, and  $h$  is the finite fault factor [135] known as the equivalent point-source depth, or fictitious depth [136], [137]. Different relationships have been proposed to obtain the finite-fault depth at closest distances [134], [136], [138]. The fictitious depth ( $h$ ) can be calculated by **equation 15** and the regression coefficient for a diverse  $R_{jb}$  distances up to 50 km as proposed by Tavakoli et al. (2018) [127] are listed in **Table 3**. Nevertheless, these input parameters can be extended for any arbitrary input parameters and functions.

$$\log(h) = a + bM \quad (15)$$

Where,  $a$  and  $b$  are listed in **Table 03**, and  $M$  is the moment magnitude for each event and respective station.



**Table 3:** Coefficients of the Finite-Fault Depth versus Magnitude and its uncertainty. Tavakoli et al. (2018) [127].

$R_{jb}$	$a$	$b$	$\sigma$
1	0.1075	0.1275	0.0210
2	0.0062	0.1513	0.0149
3	-0.0255	0.1600	0.0357
5	-0.1342	0.1825	0.0320
7	-0.1513	0.1901	0.0343
10	-0.2206	0.2076	0.0189
12	-0.2828	0.2198	0.0135
15	-0.2475	0.2197	0.0198
20	-0.2638	0.2287	0.0191
30	-0.3195	0.2468	0.0143
40	-0.3730	0.2643	0.0223
50	-0.3730	0.2706	0.0405

From **Table 3**,  $a$  and  $b$  were calculated using the MATLAB interpolation function for each station and each event. Then, the  $R_{rup}$  distances were calculated using **equation 15** and **equation 14**. Now, that  $R_{rup}$  and  $R_{jb}$  distances are calculated (as presented in **Fig. 9**) it is necessary to define the magnitude-dependent limits to distance because the selected ground motion records may increase the bias produced by the trigger threshold of accelerometers. Abrahamson et al. (2016) [58] recommended to utilize the magnitude dependence limits, as shown in **Table 4**. However, because of the limited amount of data for developing the GMPE, they will be restricted to the  $R_{jb}$  distances up to 1000 km for the regression analysis [51], [139] as presented in **Fig. 09** and **Fig. 11(a)**.

**Table 4:** Magnitude-dependent limit to distance in the selection of the GMPE data subset. Abrahamson et al. (2016) [58].

$M_w$ Range	Interface R Limit (Km)
$5.5 \leq M_w \leq 6.0$	$R \leq 100$
$6.0 < M_w \leq 6.5$	$R \leq 150$
$6.5 < M_w \leq 7.5$	$R \leq 300$
$M_w > 7.5$	$R \leq 400$

Then, 454 events were selected for the GMPE regression (as depicted in **Fig. 04**) that comprises 3750 ground motion records. The detailed description of the events and the number of motions for each event are presented in **Appendix A.2**. The hypocentral distances ( $R_{hy}$ ) and the Focal Depths (D) of the aforementioned events are depicted in **Fig. 10**. Also, the magnitude versus distance distribution of the records in the selected dataset is presented in **Fig. 11**. Finally, the IM parameters that were obtained assessing **section 2.3**, **section 2.4** and **section 2.5** are summarized from **Fig. 11** to **Fig. 22**. These plots represent all the 3750 Interface records utilized for the development of the GMPE for the Peruvian subduction zone as it will be described in the next section. It is worth mentioning that each recording comprises two horizontal and one vertical ground motions (GMs). For this study, the geometric mean was just calculated to unify one value for each GM that comprises two horizontal components. This also was the case for the spectral values ( $S_a$ ), the mean period ( $T_m$ ), the PGA/PGV ratio, the  $PGA/PGVT_m$  ratio, and the  $PGA/PGVf_m$  ratio derived for each horizontal components. Meanwhile, the IMs for the vertical GMs maintain their single value for the GMPE regression.

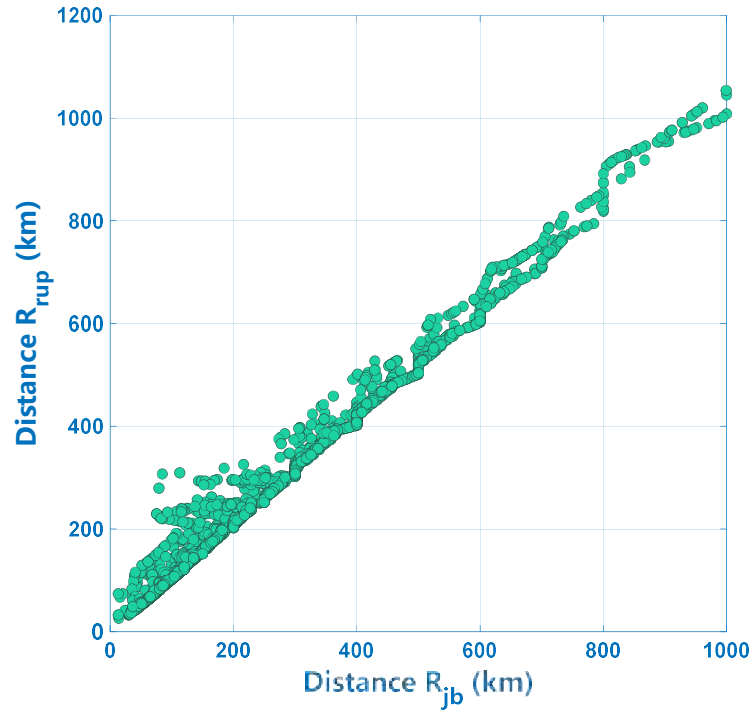


**Figure 9:**  $R_{jb}$  and  $R_{rup}$  distances for the selected 454 interface events used for the GMPE regression.

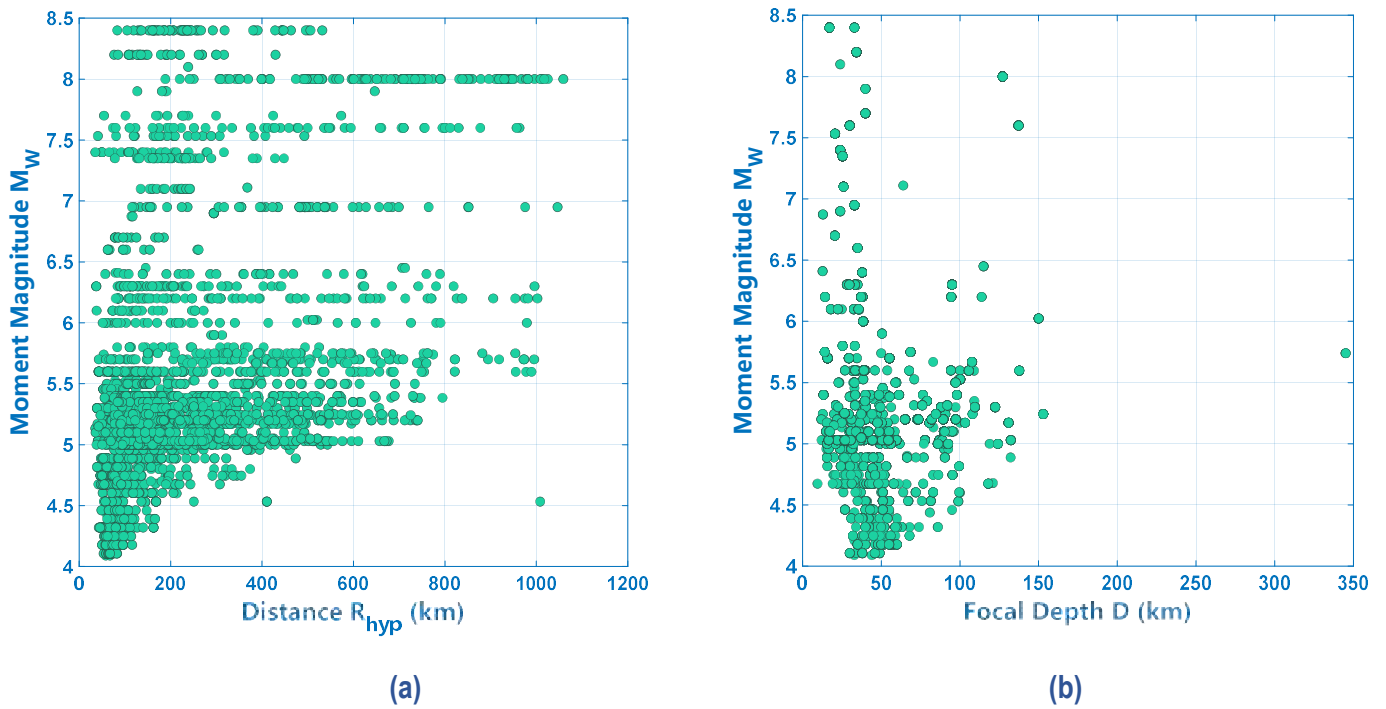
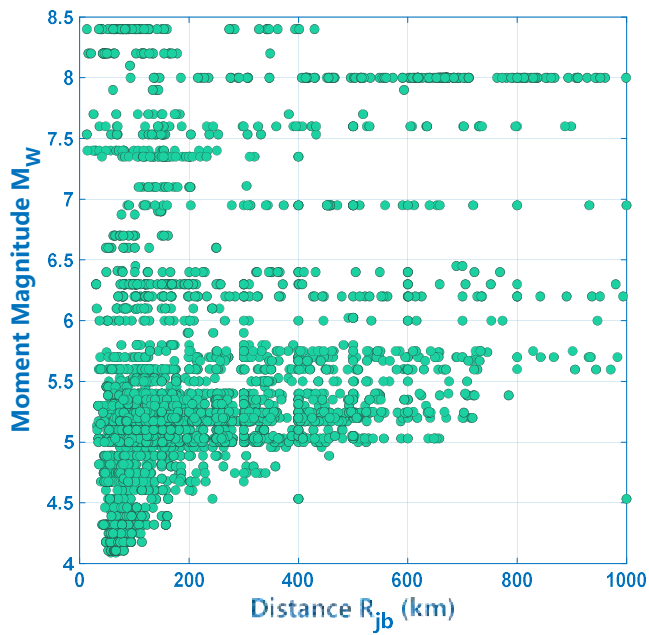
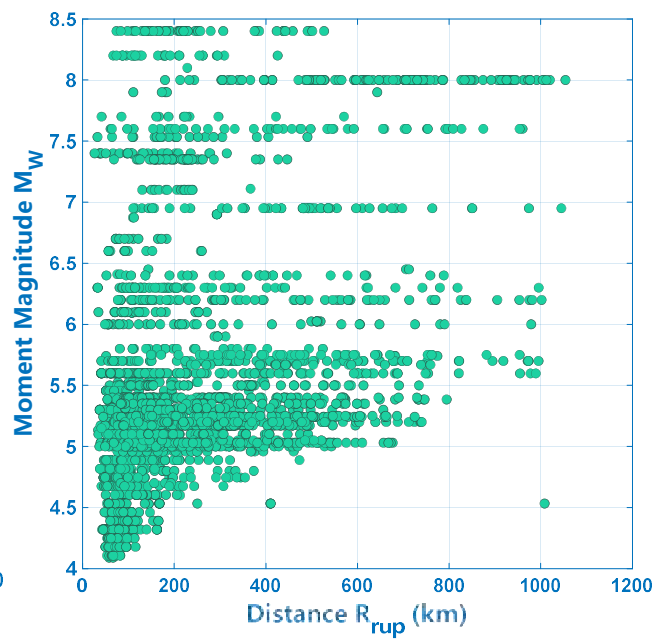


**Figure 10:** Interface Dataset plots of Moment Magnitude versus: (a) Hypocentral Distance ( $H_{hyp}$ ), and (b) Focal Depth ( $D$ ).

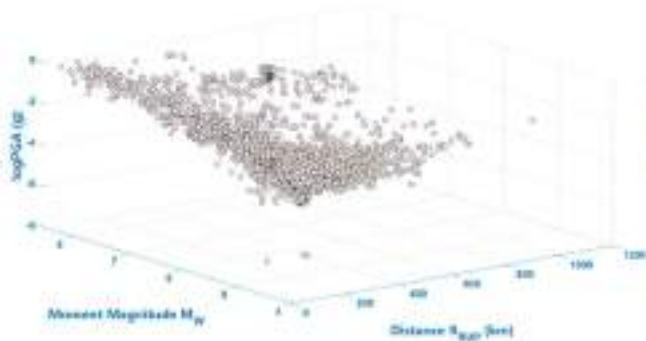


(a)

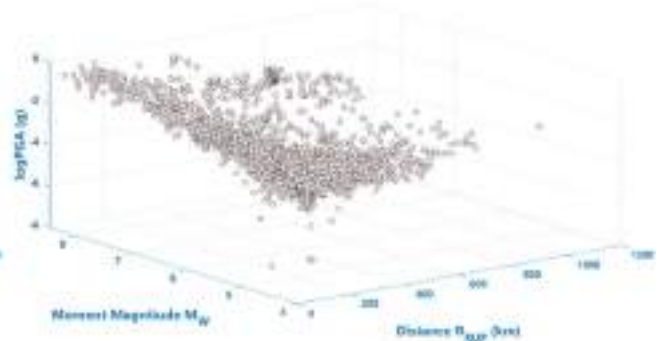


(b)

**Figure 11:** Interface Dataset plots of Moment Magnitude versus: (a) Joyner-Boore Distance ( $R_{jb}$ ), and (b) Rupture Distance ( $R_{rup}$ ).



(a)



(b)

**Figure 12:** Peak Ground Acceleration (PGA) versus Moment Magnitude ( $M_w$ ) and Rupture Distance ( $R_{rup}$ ) considering the: (a) Geometric mean of the two horizontal Ground Motion Records, and (b) Vertical Ground Motion Records.

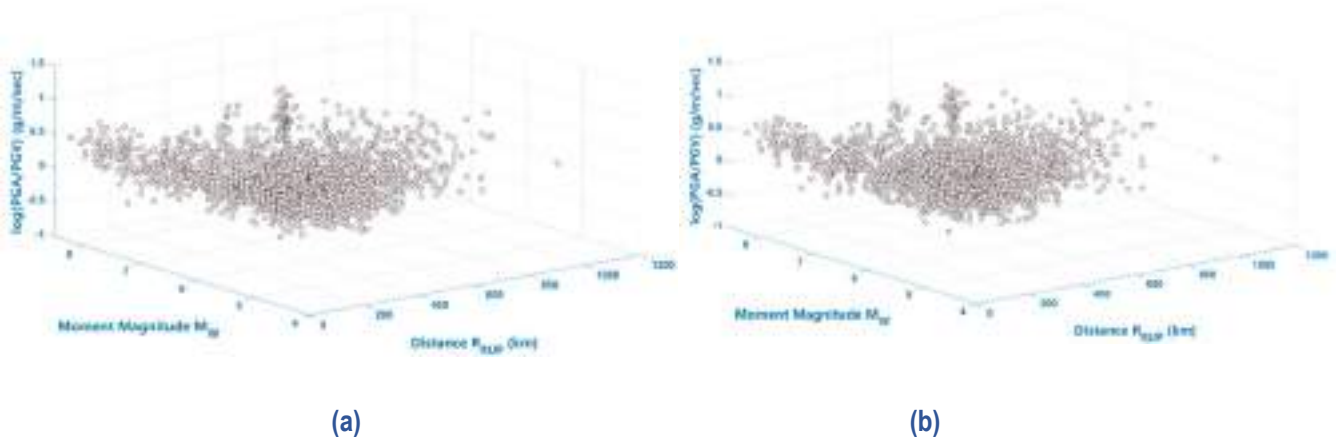


**Figure 13:** PGA/PGV ratio versus Moment Magnitude ( $M_w$ ) and Rupture Distance ( $R_{rup}$ ) considering the: (a) Geometric mean of the two horizontal Ground Motion Records, and (b) Vertical Ground Motion Records.

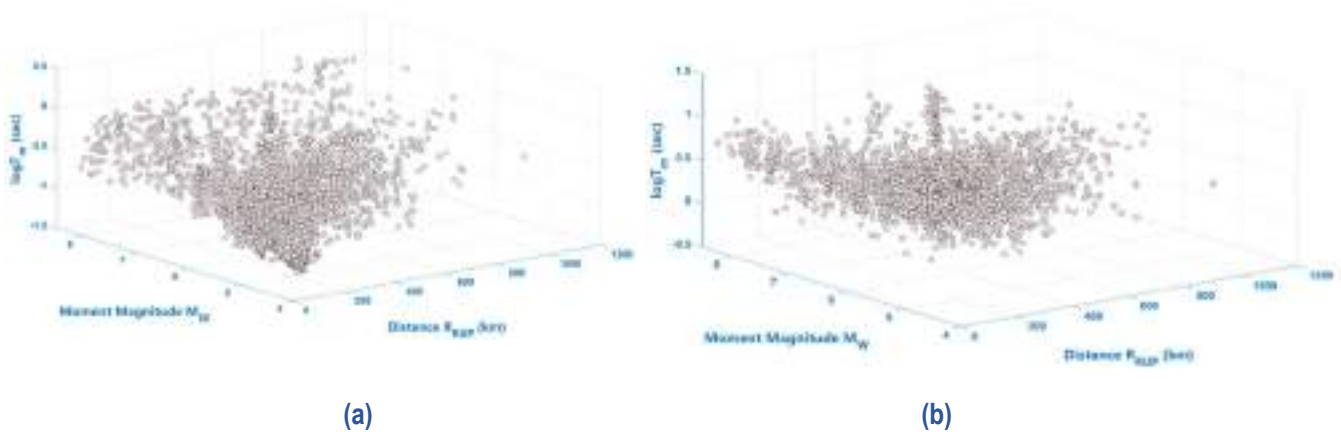


**Figure 14:** Mean Period ( $T_m$ ) versus Moment Magnitude ( $M_w$ ) and Rupture Distance ( $R_{rup}$ ) considering the: (a) Geometric mean of the two horizontal Ground Motion Records, and (b) Vertical Ground Motion Records.

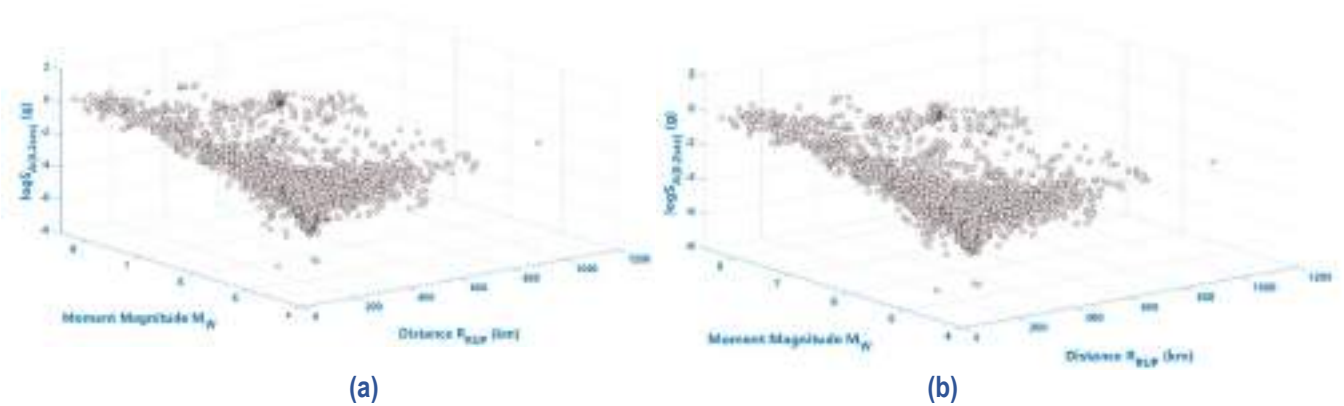


**Figure 15:** Spectral Acceleration with 5% damping ratio at 0.2s ( $S_{A(0.2sec)}$ ) versus Moment Magnitude ( $M_w$ ) and Rupture Distance ( $R_{rup}$ ) considering the: (a) Geometric mean of the two horizontal Ground Motion Records, and (b) Vertical Ground Motion Records.

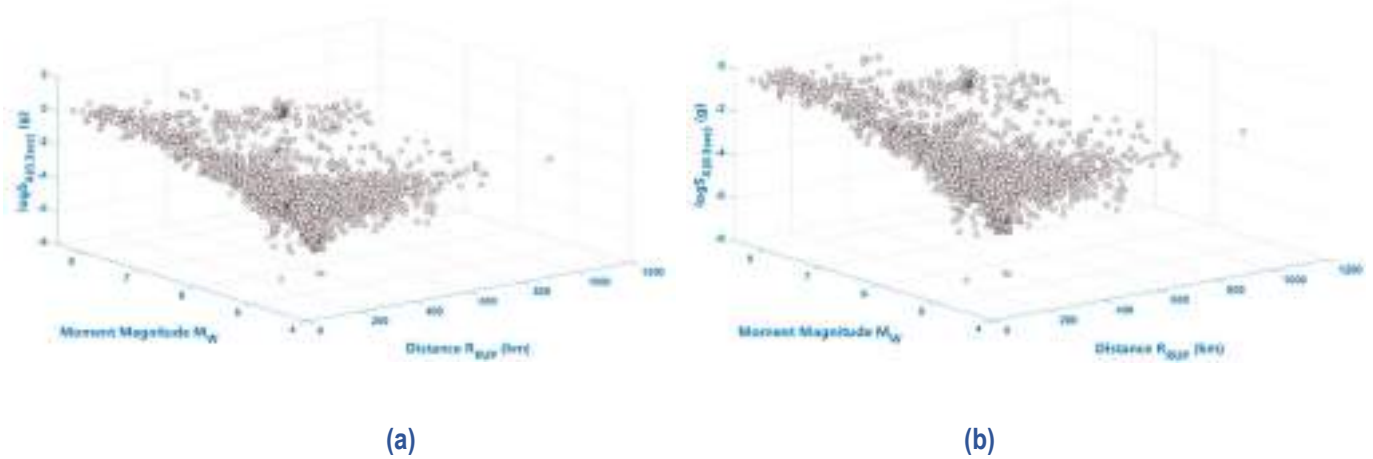


**Figure 16:** Spectral Acceleration with 5% damping ratio at 0.3s ( $S_{A(0.3s)}$ ) versus Moment Magnitude ( $M_w$ ) and Rupture Distance ( $R_{rup}$ ) considering the: (a) Geometric mean of the two horizontal Ground Motion Records, and (b) Vertical Ground Motion Records.

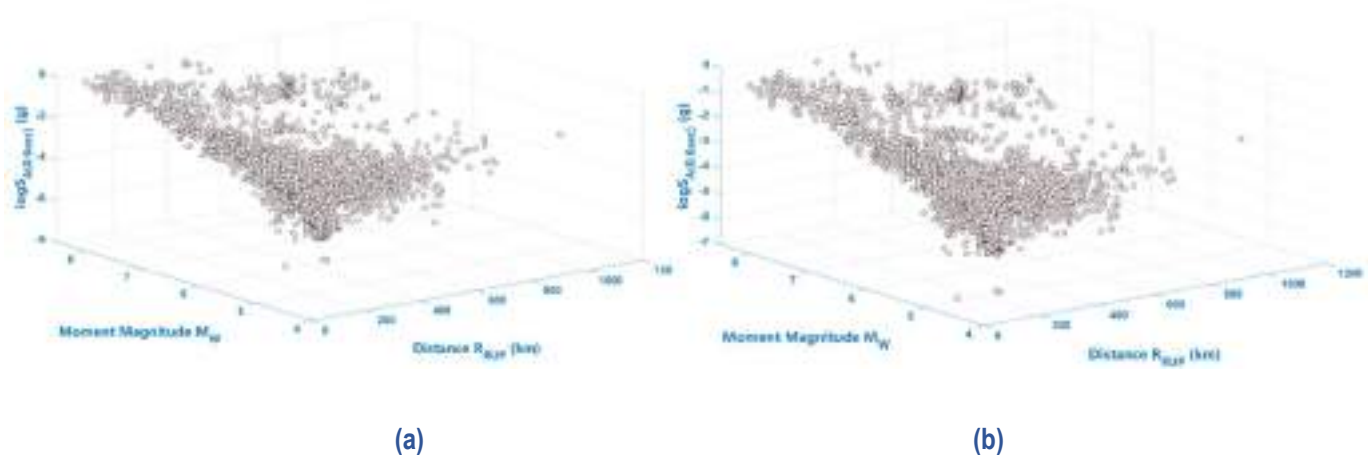


**Figure 17:** Spectral Acceleration with 5% damping ratio at 0.6s ( $S_{A(0.6s)}$ ) versus Moment Magnitude ( $M_w$ ) and Rupture Distance ( $R_{rup}$ ) considering the: (a) Geometric mean of the two horizontal Ground Motion Records, and (b) Vertical Ground Motion Records.

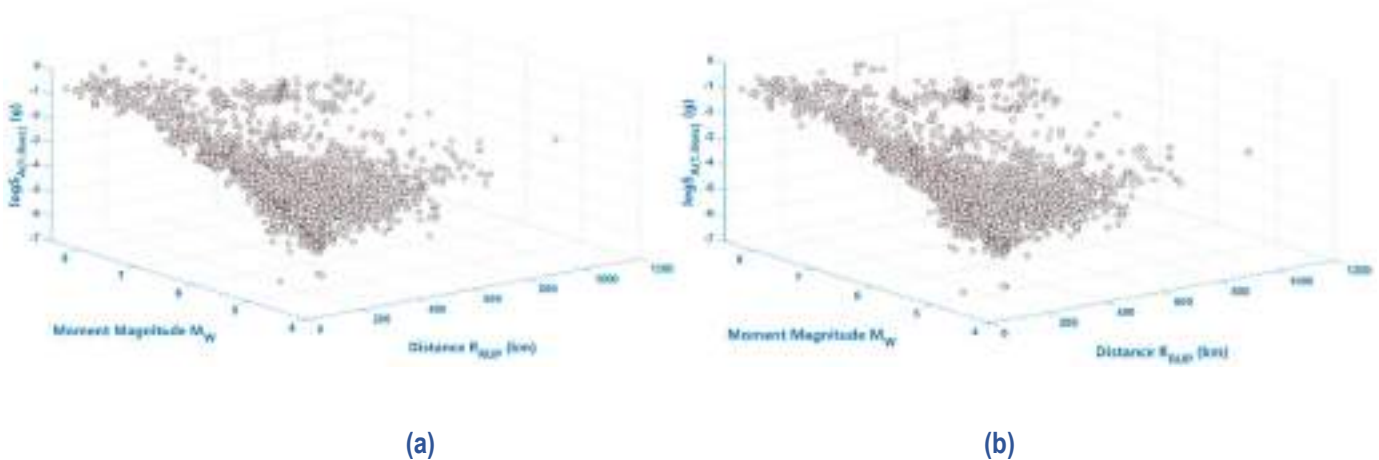


**Figure 18:** Spectral Acceleration with 5% damping ratio at 1.0s ( $S_{A(1.0s)}$ ) versus Moment Magnitude ( $M_w$ ) and Rupture Distance ( $R_{rup}$ ) considering the: (a) Geometric mean of the two horizontal Ground Motion Records, and (b) Vertical Ground Motion Records.



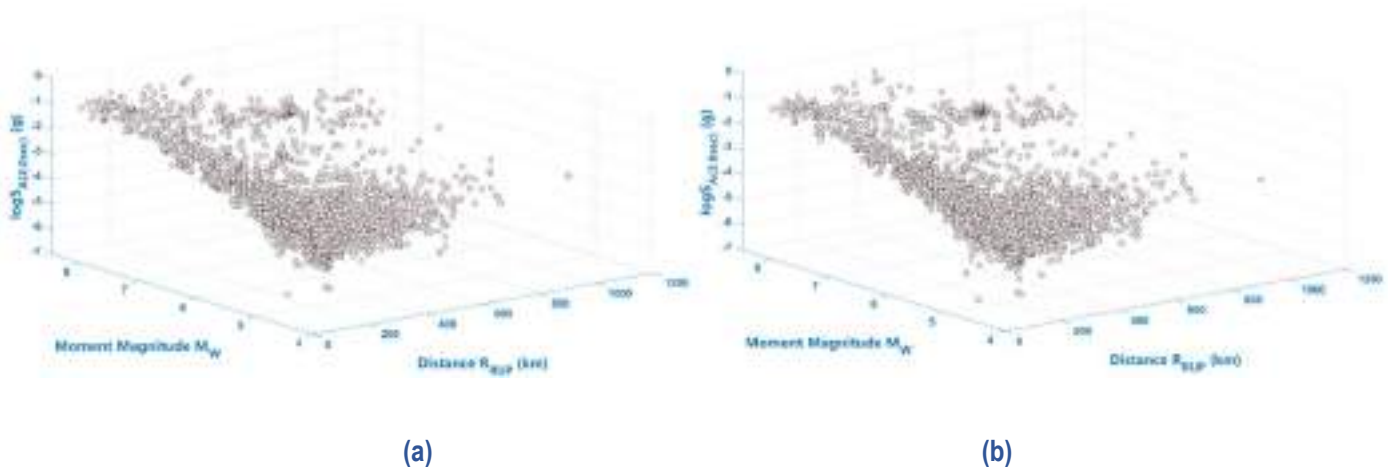


**Figure 19:** Spectral Acceleration with 5% damping ratio at 2.0s ( $S_{A(2.0s)}$ ) versus Moment Magnitude ( $M_w$ ) and Rupture Distance ( $R_{rup}$ ) considering the: (a) Geometric mean of the two horizontal Ground Motion Records, and (b) Vertical Ground Motion Records.

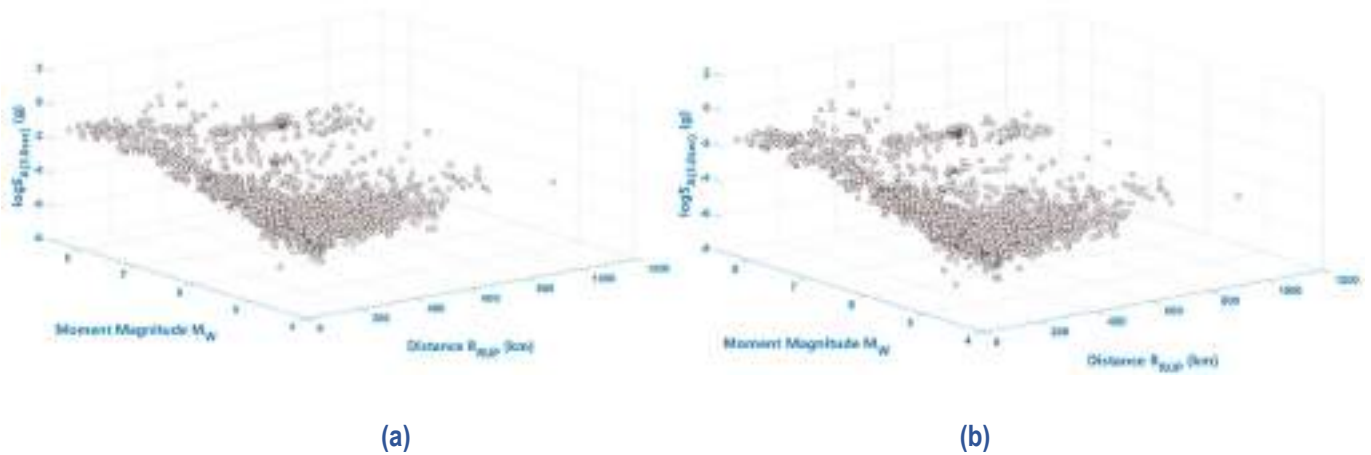


**Figure 20:** Spectral Acceleration with 5% damping ratio at 3.0s ( $S_{A(3.0s)}$ ) versus Moment Magnitude ( $M_w$ ) and Rupture Distance ( $R_{rup}$ ) considering the: (a) Geometric mean of the two horizontal Ground Motion Records, and (b) Vertical Ground Motion Records.

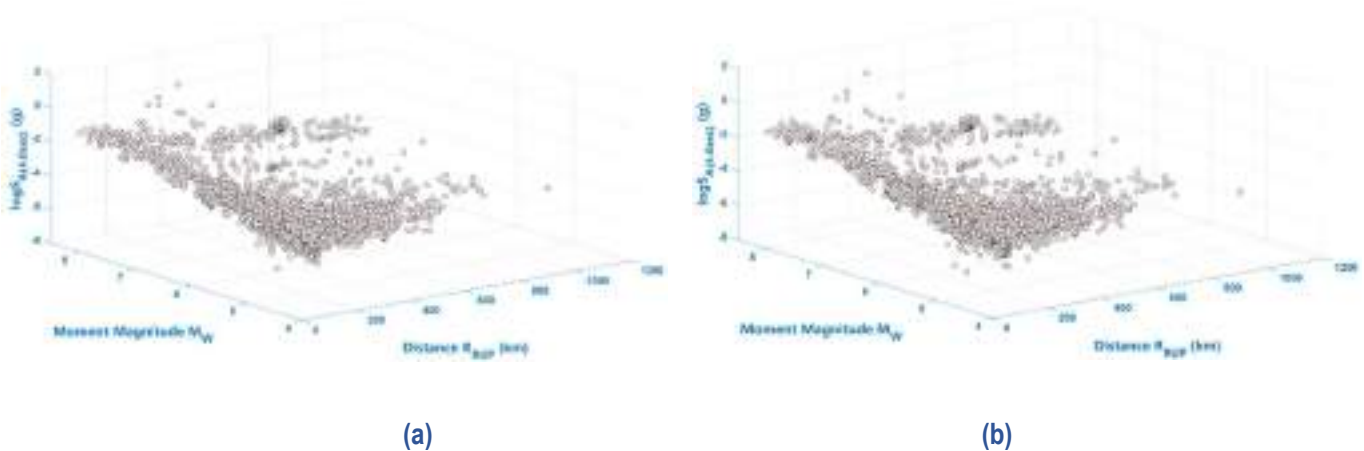


**Figure 21:** Spectral Acceleration with 5% damping ratio at 4.0s ( $S_{A(4.0s)}$ ) versus Moment Magnitude ( $M_w$ ) and Rupture Distance ( $R_{rup}$ ) considering the: (a) Geometric mean of the two horizontal Ground Motion Records, and (b) Vertical Ground Motion Records.

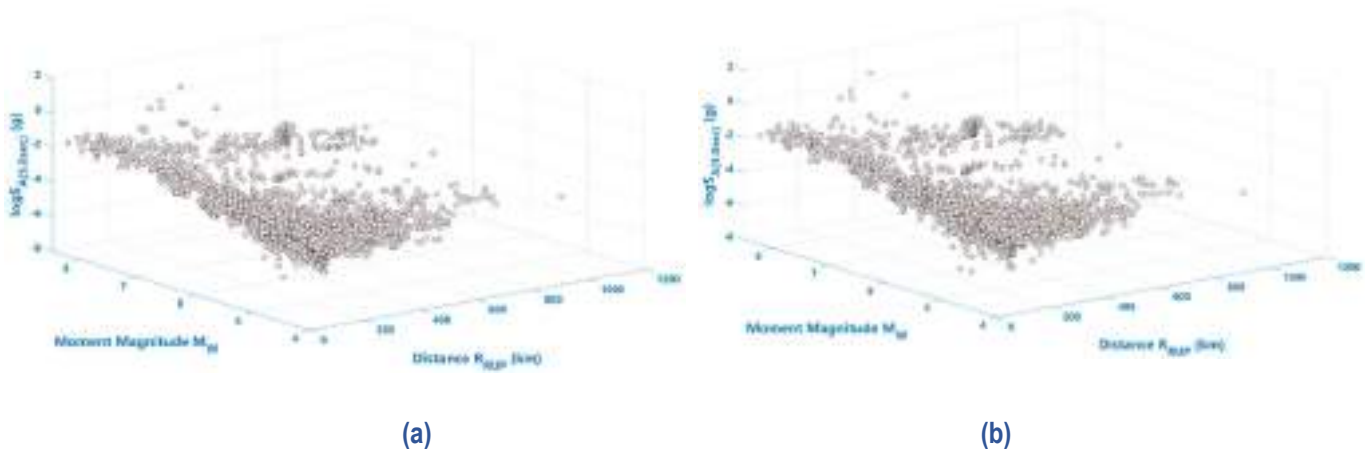


**Figure 22:** Spectral Acceleration with 5% damping ratio at 5.0s ( $S_{A(5.0s)}$ ) versus Moment Magnitude ( $M_w$ ) and Rupture Distance ( $R_{rup}$ ) considering the: (a) Geometric mean of the two horizontal Ground Motion Records, and (b) Vertical Ground Motion Records.

## DEVELOPMENT OF A NEW GMPEW FOR THE PGA AND $S_a$ INTENSITY MEASURES FROM SUBDUCTION EVENTS CONSIDERING THE HORIZONTAL AND THE VERTICAL GROUND MOTION RECORDS

Ground motion prediction equation (GMPE) is used to evaluate the probability of the ground motion intensity measure (IM). The latter can evaluate the log values of peak ground acceleration (PGA), spectral acceleration of different periods ( $S_{a(T_i)}$ ), mean period ( $T_m$ ), PGA/PGV ratio, etc. These IMs parameters are obtained for a given ground motion scenario that has specific source, path, and site condition. Therefore, they are described by several predictor variables like magnitude, distance from the source, fault geometry, and others, which are useful when performing probability or deterministic hazard assessments. Many GMPEs have been proposed so far [140]. Most of the developed GMPEs are based on the regression analysis of the recorded ground motion data. Therefore, both the regression analysis and the observed ground motion presents a strong influence on the development of the Ground Motion Model (GMM) [141]. Furthermore, regression methods can be nonlinear or linear. Nonlinear regression can be performed by Simulated Annealing and Stochastic Search (SASS) [142], [143]. However, SASS can be used as linear regressor [144]. Meanwhile, linear regression models are achieved by the application of Least Square (LSQ) methods and Artificial Neural Networks (ANN) [145]–[147].

On the other hand, ground motion records are random variables subjected to a certain ground motion scenario. As a consequence of that, GMPEs are statistical models that are based on the probability density function of ground motion. So, model coefficients of GMM can be obtained through regression methods. The most common method is the least-square (LSQ) error method because of its ease application approach. This method tends to minimize the sum of the square error of each motion. Nevertheless, it cannot be used to derive accurate analysis results considering the correlation among all ground motion signals [148]. This means that the LSQ method will bias towards the events and the stations when having a huge amount of data. Then, the main purpose of the Maximum-likelihood (MLL) method is to find a solution that maximizes the likelihood and correlation between each motion by considering covariance matrix of the residuals [144], [149]. The principal assumption of the MLL method is that the log value of the observed ground motion is a normally distributed random variable. Meanwhile, this is not always true when ground motion intensity is lower than the triggering threshold of the strong-motion instrument. Only ground motion intensities that are larger than the threshold value is recorded along the time history signal. Then, these strong values for the selected dataset are used for developing GMPEs. In addition, the measured ground motion for some long-distances scenarios may have probability density functions that are not normally distributed because the data tend to be biased at motions higher than the triggering threshold of instruments.



This is true not only for long-distances scenarios but also for short-distances prediction results [150]. These negative aspects can be diminished if the data truncation effect on the probability density function is assessed on the observed ground motion during the regression analysis. The data truncation effects on developed GMPEs were studied by some researchers [151]–[155]. However, a magnitude-dependent limit to distance is suggested (as shown in **Table 04**) to avoid these effects and to approximate all the scenarios as normally distributed when developing a GMPE [151], [153], [154].

So, the correlation and data truncation on the ground motion records can be treated by applying the new two-step maximum likelihood method proposed by Chao et al. (2019) [150]. This new algorithm is developed based on the two-step maximum likelihood method proposed by Joyner and Boore (1993) [149] and the probability density function of the truncated ground motion data proposed by Bragato (2004) [152]. Unfortunately, time limitations to apply this new algorithm forces the present study to assess the two-step maximum likelihood method proposed by Joyner and Boore (1993). Despite  $R_{jb}$  distances from ground motion records up to 1,000 km exceed the recommendations previous stated, they are utilized. This means that if the application of the magnitude-dependent limit to distance (cited in **Table 04**) is adopted, it will require this study to just use 82 events and 564 ground motion records. This amount of data will not be enough to develop a new GMPE for subduction events. This is the reason why the magnitude-dependent to limit distances are considered up to 1000 km for  $R_{jb}$  distances in order to use the 454 events and 3750 ground motion records ( $n_r$ ). This condition is convenient for the limited amount of data available so that the GMPE can be developed with less uncertainty.

### 3.1. GMPE: General Form

The functional form of the GMPE adopted for the present study has the same form as most previous studies in the past [148], [154], [156]–[162].

$$\log Y = f_1(M) + f_1(r, E) + f_3(r, M, E) + f_4(F) + \varepsilon \quad (16)$$

Where  $Y$  is the horizontal or vertical peak ground acceleration and  $f_1$  to  $f_4$  are the functions of the properties that are stated in the brackets.  $M$  is the moment magnitude,  $r$  is the rupture distance from the event to the recording station,  $E$  is the tectonic properties,  $F$  is the fault mechanism, and  $\varepsilon$  is the random variable that represents the uncertainty of the  $\log Y$ . For the present study, the function  $f_4$  and variable  $F$  are not evaluated because all the records only belong to interface events. So, 424 events and 3750 records are considered for the regression analysis as previously stated. The list of earthquakes (from column 1 to 8) and the number of records for each event (column 9) are cited in the table of **Appendix A.2**. Furthermore, it is worth reminding that 533 stations from six different networks are utilized as detailed in **Appendix A.1**.

Moreover, the mathematical expression of the GMPE can be stated as follows:

$$y_i = u_i + \delta_i = \mathbf{x}_i \mathbf{c} + \delta_i \quad (17)$$

Where  $y_i$  is the random variable such as the observed ground motion intensity of the  $i$ th motion scenario from the  $i$ th record generally measured in natural log of the spectral acceleration.;  $u_i$  is the model prediction of media ground motion intensity of the  $i$ th ground motion scenario and it is a constant value;  $\delta_i$  is the residual of the model prediction of the  $i$ th ground motion scenario and it is a zero-mean normal random

variable;  $\mathbf{c}$  is a vector that harbours the model coefficients that describe the median ground motion intensity with dimensions  $n_p \times 1$ , where  $n_p$  is the number of model coefficients; and  $\mathbf{x}_i$  is a matrix with dimensions  $1 \times n_p$  that harbours each term in the median model for the  $i$ th ground motion scenario. When the number of ground motion records ( $n_r$ ) are considered, [equation 17](#) can be rewritten in the following form:

$$\mathbf{Y} = \mathbf{X}\mathbf{c} + \boldsymbol{\delta} \quad (18)$$

where,  $\mathbf{Y}$  is a vector with dimensions  $n_r \times 1$  that harbours all  $y_i$  values from all records;  $\mathbf{X}$  is a matrix with dimensions  $n_r \times n_p$  that harbours all  $\mathbf{x}_i$  values from all records; and  $\boldsymbol{\delta}$  is a vector with dimensions  $n_r \times 1$  that harbours all  $\delta_i$  values from all records.

The main purpose of the regression analysis is to obtain the model coefficient vector  $\mathbf{c}$  of the median model and the coefficients to define the probability density function of vector  $\boldsymbol{\delta}$ . This will allow estimating the median value and uncertainty of the Intensity Measure (IM). So, assuming that the observed IM of each record is a normal distributed random variable and also the residual is a zero-mean normal-distributed random variable, [equation 18](#) can be converted as follows [163]:

$$\ln L = -0.5n_r \ln(2\pi) - 0.5 \ln(|\mathbf{V}|) - 0.5(\mathbf{Y} - \mathbf{X}\mathbf{c})^T \mathbf{V}^{-1} (\mathbf{Y} - \mathbf{X}\mathbf{c}) \quad (19)$$

Where  $L$  is the likelihood value, and  $\mathbf{V}$  is the covariance matrix of residual vector  $\boldsymbol{\delta}$ . When no correlation is found between each record, the covariance matrix  $\mathbf{V}$  of residual vector  $\boldsymbol{\delta}$  is a diagonal matrix with zero non-diagonal elements that can be stated as follows:

$$\mathbf{V} = \boldsymbol{\delta}^T \boldsymbol{\delta} = \text{diag}\{\sigma^2\} = \text{diag}\{\sigma_1^2 \sigma_2^2 \dots \sigma_{n_r}^2\} \quad (20)$$

Where  $\text{diag}\{\dots\}$  is a matrix with diagonal elements  $\{\dots\}$  and zero non-diagonal elements;  $\sigma_i^2$  is the variance of the residual for  $i$ th ground motion scenario.; and  $\sigma_i$  is the variance of the residual for  $i$ th ground motion scenario.

Then, if the model coefficient vector  $\mathbf{c}$  that maximizes the likelihood values is set equal to the solution of the LSQ error method [163], it can be expressed as follows:

$$\hat{\mathbf{c}} = (\mathbf{X}^T \mathbf{X})^{-1} \mathbf{X}^T \mathbf{Y} \quad (21)$$

Also, if the standard deviation of the residual for each ground motion scenario is set equal to  $\sigma$ , the estimation can be obtained as follows:

$$\mathbf{H}_{\hat{\mathbf{c}}} = \mathbf{V}_{\hat{\mathbf{c}}}^{-1} = \frac{\mathbf{X}^T \mathbf{X}}{\sigma^2} \quad (22)$$

Where,  $\mathbf{H}_{\hat{\mathbf{c}}}$  is the Hessian matrix of the estimated model coefficient  $\hat{\mathbf{c}}$ , and  $\mathbf{V}_{\hat{\mathbf{c}}}$  is the covariance matrix of the estimated model coefficient  $\hat{\mathbf{c}}$ . [Equation 21](#) is utilized to obtain the standard error in step 1 of the two-step maximum-likelihood method.

Meanwhile, the one-step or two-step method maximum likelihood method [149] can be utilized to decipher the model with correlated normal-distributed residuals.

### 3.2. Two-step Maximum-likelihood method

Herein, the median form is separated into an event-specific term, station-specific term, and record-specific term that corresponds to the event-specific coefficients ( $c_e$ ), station-specific coefficients ( $c_s$ ), and record-specific coefficients ( $c_r$ ), respectively. Furthermore,

the residual is separated into an event-specific residual ( $\delta_{e,j}$ ), station-specific residual ( $\delta_{s,k}$ ), and record-specific residual ( $\delta_{r,i}$ ) for each  $j$ th event,  $k$ th station, and  $i$ th record, respectively. Therefore, the GMPE mathematical expression can be expressed as follows:

$$y_{i,jk} = x_{i,jk}c + \delta_{e,j} + \delta_{s,k} + \delta_{r,i} = [x_{r,i} \quad x_{e,j} \quad x_{s,k}] \begin{bmatrix} c_r \\ c_e \\ c_s \end{bmatrix} + \delta_{e,j} + \delta_{s,k} + \delta_{r,i} \quad (23)$$

Where  $c_r$ ,  $c_e$  and  $c_s$  are vector with dimensions  $n_{pr} \times 1$ ,  $n_{pe} \times 1$ , and  $n_{ps} \times 1$ , respectively, and  $n_{pr}$ ,  $n_{pe}$ ,  $n_{ps}$  are the number of record-specific, event-specific, and station-specific coefficients, respectively, and  $x_{r,i}$ ,  $x_{e,j}$  and  $x_{s,k}$  are submatrices of  $x_i$  that comprises the path-specific, source specific, and site specific terms in the median model for the  $i$ th ground motion scenario. **Equation 23** can be rewritten the following matrix form when  $n_r$  ground motion records are considered:

$$Y = Xc + \delta = [X_r \quad B_e X_e \quad B_s X_s] \begin{bmatrix} c_r \\ c_e \\ c_s \end{bmatrix} + B_e \delta_e + B_s \delta_s + \delta_r \quad (24)$$

Where  $B_e$  and  $B_s$  are the transformation matrices with dimensions  $n_r \times n_e$  and  $n_r \times n_s$  that include elements 0 to 1 to assign event-specific and station-specific terms to the corresponding records, where  $n_e$  and  $n_s$  are the event number and station number of the selected records, respectively;  $B_e$  and  $B_s$  can be assembled considering the event and station that belong to each record;  $X_r$ ,  $X_e$  and  $X_s$  matrices with dimensions  $n_r \times n_{pr}$ ,  $n_e \times n_{pe}$ , and  $n_s \times n_{ps}$  that correspond the record-specific, event-specific, and station-specific term of the median model, respectively;  $\delta_e$ ,  $\delta_s$ , and  $\delta_r$  are vectors with dimensions  $n_e \times 1$ ,  $n_s \times 1$ ,  $n_r \times 1$  that are related to the event-specific residual of each event, stations-specific residual of each station, and record-specific residual of each record, respectively. Then, the covariance matrix of each residual term can be formulated as follows:

$$V_r = \delta_r^T \delta_r = \text{diag}\{\phi_{ss}^2\} = \text{diag}\{\phi_{ss,1}^2 \quad \phi_{ss,2}^2 \dots \phi_{ss,n_r}^2\} \quad (25)$$

$$V_e = \delta_e^T \delta_e = \text{diag}\{\tau^2\} = \text{diag}\{\tau_1^2 \quad \tau_2^2 \dots \tau_{n_e}^2\} \quad (26)$$

$$V_s = \delta_s^T \delta_s = \text{diag}\{\phi_{s2s}^2\} = \text{diag}\{\phi_{s2s,1}^2 \quad \phi_{s2s,2}^2 \dots \phi_{s2s,n_s}^2\} \quad (27)$$

Where  $\phi_{ss,i}$  is the standard deviation of the record-specific residual of the  $i$ th record,  $\phi_{s2s,k}$  is the standard deviation of the station-specific residual of the  $k$ th station, and  $\tau_i$  is the standard deviation of the event-specific residual of  $j$ th event. The covariance matrices  $V_r$ ,  $V_e$ , and  $V_s$  are diagonal because the event-specific residual of each event, the station-specific residual of each station, and the record-specific residual of each record are not interconnected to each other.

Now, the GMPE is restructured from the step 1 to the two-step maximum-likelihood method as follows:

$$y_{i,jk} = x_{1i,jk}c_1 + \delta_{r,i} = [x_{r,i} \quad 1 \quad 1] \begin{bmatrix} c_r \\ E_{e,j} \\ S_{s,k} \end{bmatrix} + \delta_{r,i} \quad (28)$$

Where

$$E_{e,j} = x_{e,j}c_e + \delta_{e,j} \quad (29)$$

$$S_{s,k} = x_{s,j}c_s + \delta_{s,k} \quad (30)$$

Where  $E_{e,j}$  is the event term of the  $i$ th event that defines its contribution to the IM, and  $S_{s,k}$  is the station term of the  $k$ th station that defines its contribution to the IM. Therefore, **equation 30** can be restructured if the  $n_r$  ground motion records are presented as follows:

$$Y = X_r c_r + B_e E_e + B_s S_s + \delta_r \quad (31)$$

Where

$$E_e = X_e c_e + \delta_e \quad (32)$$

$$S_s = X_s c_s + \delta_s \quad (33)$$

$$X_1 = [X_r \quad B_e \quad B_s] \quad (34)$$

$$c_1 = [c_r \quad E_e \quad S_s]^T \quad (35)$$

Where  $E_e$  is a vector with dimensions  $n_e \times 1$  that harbours the event term of each event, and  $S_s$  is a vector with dimensions  $n_s \times 1$  that harbours the station term of each station.

From **equation 31**, the unknown variables are  $\phi_{ss}$  that is the standard deviation of  $\delta_r$  and vector  $c_1$ . These variables are involved with the path-specific model coefficients  $c_r$ , the event term of each event  $E_e$  and the station term of each station  $S_s$ . Considering that the record-specific residual of each record presents no correlation to each other with a zero-mean normal random variable and equal standard deviation  $\phi_{ss}$ . Then, this problem can be solved using the LSQ error method as follows:

$$\hat{c}_1 = (X_1^T X_1)^{-1} X_1^T Y = [\hat{c}_r \quad \hat{E}_e \quad \hat{S}_s]^T \quad (36)$$

$$\hat{\phi}_{ss}^2 = \frac{(Y - X_1 \hat{c}_1)^T (Y - X_1 \hat{c}_1)}{n_r - n_{pr} - n_e - n_s - 1} \quad (37)$$

Then, the standard error of the model coefficients  $\hat{c}_1$  can be obtained from its covariance matrix  $V_{\hat{c}_1}$  that is calculated by the inverse of its Hessian matrix  $H_{\hat{c}_1}$  as follows:

$$H_{\hat{c}_1} = V_{\hat{c}_1}^{-1} = X_1^T X_1 / \hat{\phi}_{ss}^2 \quad (38)$$

Herein, the covariance matrix  $V_{\hat{c}_1}$  is obtained by the inverse of the matrix  $H_{\hat{c}_1}$  in the step-two regression [149]. The Hessian matrices of  $\hat{c}_r$ ,  $\hat{E}_e$ , and  $\hat{S}_s$  are  $H_{\hat{c}_r}$ ,  $H_{\hat{E}_e}$ , and  $H_{\hat{S}_s}$ , respectively. These matrices can be obtained from the Hessian matrix  $H_{\hat{c}_1}$  as follows:

$$H_{\hat{c}_r} = \{H_{\hat{c}_1}\}_{1:n_{pr}, 1:n_{pr}} \quad (39)$$

$$H_{\hat{E}_e} = \{H_{\hat{c}_1}\}_{n_{pr}+1:n_{pr}+n_e, n_{pr}+1:n_{pr}+n_e} \quad (40)$$

$$H_{\hat{S}_s} = \{H_{\hat{c}_1}\}_{n_{pr+n_e+1:n_{pr+n_e+n_s}, n_{pr+n_e+1:n_{pr+n_e+n_s}}} \quad (41)$$

Where  $\{\dots\}_{i,j,k:l}$  is the extracted submatrix from the  $i$ th row to  $j$ th row and  $k$ th column to the  $l$ th column of matrix  $\{\dots\}$ .

From step 2 of the two-step maximum likelihood method, the estimated event term vector  $\hat{E}_e$ , and the estimated station term vector  $\hat{S}_s$  can be calculated as follows:

$$\hat{E}_e = X_e c_e + \delta_{e2} = X_e c_e + \delta_e + \delta_{\hat{E}_e} \quad (42)$$

$$\hat{S}_s = X_s c_s + \delta_{s2} = X_s c_s + \delta_s + \delta_{\hat{S}_s} \quad (43)$$

Where  $\delta_e$  is the event specific residual,  $\delta_s$  is the station specific residual,  $\delta_{\hat{E}_e}$  is the prediction error of the event term as stated in [equation 44](#),  $\delta_{\hat{S}_s}$  is the prediction error term of the station as stated in [equation 45](#).

$$\delta_{\hat{E}_e} = \hat{E}_e - E_e \quad (44)$$

$$\delta_{\hat{S}_s} = \hat{S}_s - S_s \quad (45)$$

The covariance matrices of the residual term  $\delta_e + \delta_{\hat{E}_e}$  and residual term  $\delta_s + \delta_{\hat{S}_s}$  can be calculated as follows:

$$V_{e2} = V_e + H_{\hat{E}_e}^{-1} \quad (46)$$

$$V_{s2} = V_s + H_{\hat{S}_s}^{-1} \quad (47)$$

Where,  $V_e$  and  $V_s$  represents the residual terms of equations 42 and 43.

Considering the maximum likelihood method to derive unbiased regression results can be expressed as follows:

$$\ln L_e = -0.5n_e \ln(2\pi) - 0.5 \ln(|V_{e2}|) - 0.5(\hat{E}_e - X_e c_e)^T H_{e2} (\hat{E}_e - X_e c_e) \quad (48)$$

$$\ln L_s = -0.5n_s \ln(2\pi) - 0.5 \ln(|V_{s2}|) - 0.5(\hat{S}_s - X_s c_s)^T H_{s2} (\hat{S}_s - X_s c_s) \quad (49)$$

where  $L_e$  and  $L_s$  are the likelihood, and Hessian matrices  $H_{e2}$  and  $H_{s2}$  can be calculated as follows:

$$H_{e2} = H_{\hat{E}_e} - (I + H_{\hat{E}_e} V_e)^{-1} H_{\hat{E}_e} V_e H_{\hat{E}_e} \quad (50)$$

$$H_{s2} = H_{\hat{S}_s} - (I + H_{\hat{S}_s} V_s)^{-1} H_{\hat{S}_s} V_s H_{\hat{S}_s} \quad (51)$$

Then, the log values of  $|V_{e2}|$  and  $|V_{s2}|$  can be obtained from these equations:

$$\begin{aligned} \ln(|V_{e2}|) &= \ln(|(V_e + H_{\hat{E}_e}^{-1})|) = \ln(|H_{\hat{E}_e}^{-1}(H_{\hat{E}_e} V_e + I)|) = \\ &= -\ln(|H_{\hat{E}_e}|) + \ln(H_{\hat{E}_e} V_e + I) \end{aligned} \quad (52)$$

$$\begin{aligned} \ln(|V_{s2}|) &= \ln(|(V_s + H_{\hat{S}_s}^{-1})|) = \ln(|H_{\hat{S}_s}^{-1}(H_{\hat{S}_s} V_s + I)|) = \\ &= -\ln(|H_{\hat{S}_s}|) + \ln(H_{\hat{S}_s} V_s + I) \end{aligned} \quad (53)$$

Meanwhile, this method assumed the observed ground motion intensity to be normally distributed. The truncation effect is diminished as well as its influence on the probability density function of the IM.

### 3.3. Functional Form of the median GMPE for the Horizontal and Vertical IMs

The following functional form of the median GMPE was used in order to minimize the residuals of the median model for the horizontal and vertical intensity Measures (IMs) parameters by performing a genetic algorithm in MATLAB [164]:

$$\ln y = b_1 + b_2(M_w) + b_3(M_w)^2 + b_4 \ln(R_{rup}^2 + h^2)^{0.5} + b_5 \ln(V_{S30} / 760) \quad (53)$$

where  $y$  is the Intensity Measure (IM) such as PGA,  $S_a$ ,  $T_m$ , PGA/PGV ratio,  $PGA/PGVT_m$  ratio,  $PGA/PGVf_m$  ratio;  $M_w$  is the moment magnitude for each event and IM for each station;  $R_{rup}$  is the rupture distance for each IM recorded at each station;  $h$  is the fictitious depth that is set to a 50 km as the best fit constant value for all the  $y$  regression parameters utilized in this study;  $V_{S30}$  is the Shear Wave Velocity of the upper 30m for each station; and  $b_1$ ,  $b_2$ ,  $b_3$ ,  $b_4$  and  $b_5$  are the regression coefficients calculated for each IM when applying the two-step Maximum-Likelihood method [149].

This functional form includes magnitude-dependent geometrical spreading term defined by the variables  $M_w$  and  $R_{rup}$ , and the coefficients  $b_1$ ,  $b_2$ ,  $b_3$ , and  $b_4$ . The anelastic attenuation is not included in this study. Also, it includes a linear and quadratic scaling  $M_w$  higher or equal than 4. The regressions are performed applying the Two-step Maximum-Likelihood method. Herein, the residuals are separated into their between-event ( $\delta_e B_e$ ) and within-event ( $\delta_s B_s$ ) components. Meanwhile, the  $\delta_e B_e$  quantifies the average deviation of the observed ground motion of any individual event from the model median prediction, the  $\delta_s B_s$  quantifies the variance between an individual observation at any station respect to the event-specific median prediction that is corrected by  $\delta_e B_e$ . Therefore, the standard deviation of the between-events ( $\tau$ ) and the within-event ( $\emptyset$ ) define the total sigma ( $\sigma$ ) of each GMPE as follows:

$$\sigma = \sqrt{\tau^2 + \emptyset^2} \quad (54)$$

As stated in [Section 2.5](#), the geometric mean was performed for each IM for the horizontal Ground Motions (GMs). This was not the case for the vertical GMs for having a single value for each recording. Hence, [Table 5](#) and [Table 6](#) summarize the results obtained from the regression analysis performed in MATLAB (as stated in [Section 3.2](#) and [Section 3.3](#)) for each IM for the horizontal and vertical GMs, respectively. The between-event ( $\delta_e B_e$ ) and within-event ( $\delta_s B_s$ ) residual plots for each IM for both horizontal and vertical GMs are presented in [Appendix A.3](#) and [Appendix A.4](#), respectively. Furthermore, the main model mean of the GMPEs and their standard deviations for each IM are plotted considering the compiled dataset for different magnitudes used for their regression. These plots are shown in [Appendix A.5](#) and [Appendix A.6](#) for the horizontal and vertical GMs respectively to provide a view of the characterization of the data used for each GMPE. The latter shows good agreement with the observations overall except for some scatter events.



**Table 5:** Regression model coefficients for the median GMPE and standard deviations for different IM parameters considering horizontal GMs.

<i>IM</i>	$b_1$	$b_2$	$b_3$	$b_4$	$b_5$	$\tau$	$\phi$	$\sigma$
<i>PGA</i>	-8.6862	3.9071	-0.2005	-2.3033	-0.1837	0.500	0.700	0.8602
$S_{a(0.20s)}$	-18.2348	7.1477	-0.4494	-2.3032	-0.3084	0.500	0.700	0.8602
$S_{a(0.30s)}$	-23.6562	8.4882	-0.5464	-2.1550	-0.3287	0.500	0.700	0.8602
$S_{a(0.60s)}$	-25.2684	8.1074	-0.5018	-1.8662	-0.3590	0.500	0.700	0.8602
$S_{a(1.00s)}$	-20.2671	5.9054	-0.3187	-1.7354	-0.1821	0.500	0.700	0.8602
$S_{a(2.00s)}$	-11.6956	2.8792	-0.0762	-1.8207	-0.1125	0.500	0.700	0.8602
$S_{a(3.00s)}$	-6.9873	1.4297	0.0342	-1.9453	-0.0837	0.500	0.700	0.8602
$S_{a(4.00s)}$	-4.6925	0.8439	0.0726	-2.0487	-0.0420	0.500	0.700	0.8602
$S_{a(5.00s)}$	-3.5385	0.6886	0.0769	-2.1664	-0.0189	0.500	0.700	0.8602

**Table 6:** Regression model coefficients for the median GMPE and standard deviations for different IM parameters considering vertical GMs.

<i>IM</i>	$b_1$	$b_2$	$b_3$	$b_4$	$b_5$	$\tau$	$\phi$	$\sigma$
<i>PGA</i>	-9.6179	3.9550	-0.2068	-2.2430	-0.2430	0.500	0.700	0.8602
$S_{a(0.20s)}$	-17.7731	6.6455	-0.4114	-2.2056	-0.3791	0.500	0.700	0.8602
$S_{a(0.30s)}$	-23.3519	8.0270	-0.5120	-2.0515	-0.2857	0.500	0.700	0.8602
$S_{a(0.60s)}$	-24.1082	7.3998	-0.4464	-1.7799	-0.1573	0.500	0.700	0.8602
$S_{a(1.00s)}$	-19.7905	5.5195	-0.2896	-1.6900	-0.1055	0.500	0.700	0.8602
$S_{a(2.00s)}$	-12.7809	3.0659	-0.0910	-1.7959	-0.1077	0.500	0.700	0.8602
$S_{a(3.00s)}$	-9.0445	1.9436	-0.0058	-1.9170	-0.1064	0.500	0.700	0.8602
$S_{a(4.00s)}$	-7.1844	1.5496	0.0164	-2.0438	-0.1110	0.500	0.700	0.8602
$S_{a(5.00s)}$	-6.3063	1.4919	0.0137	-2.1676	-0.1194	0.500	0.700	0.8602

Then, the valuation of ground motion prediction equations for different site conditions such as classes A, B, C, D and E, according to **Table 01** are presented in **Fig. 23**, and **Fig. 24** for horizontal and vertical GMs, respectively. Herein, the strongest earthquake scenario of  $8.5 M_w$  was considered. Furthermore, the response spectra with 5% damping ratio of ground motion predictions are presented in **Fig. 25** and **Fig. 26** for horizontal and vertical GMs, respectively. Different moment magnitudes and rupture distances are evaluated for a reference rock site with  $V_{S3}$  sets to 1200 m/s. A Smooth shape and consistent scaling with moment magnitude are observed for all the response spectra from 0.01 to 5s. Meanwhile, the response spectra of ground motion predictions considering a  $8.5 M_w$  earthquake with different rupture distances and different site conditions are presented in **Fig. 27** and **Fig. 28**. Herein, consistent soil amplification can be observed for all spectral periods. However, higher amplification factors are obtained from horizontal GMs compared to vertical GMs, as shown in **Fig. 29** for soil classes B, C, D and E. Furthermore, the highest amplification factors are obtained at spectral periods of 0.6 and 0.2s for horizontal and vertical GMs respectively.

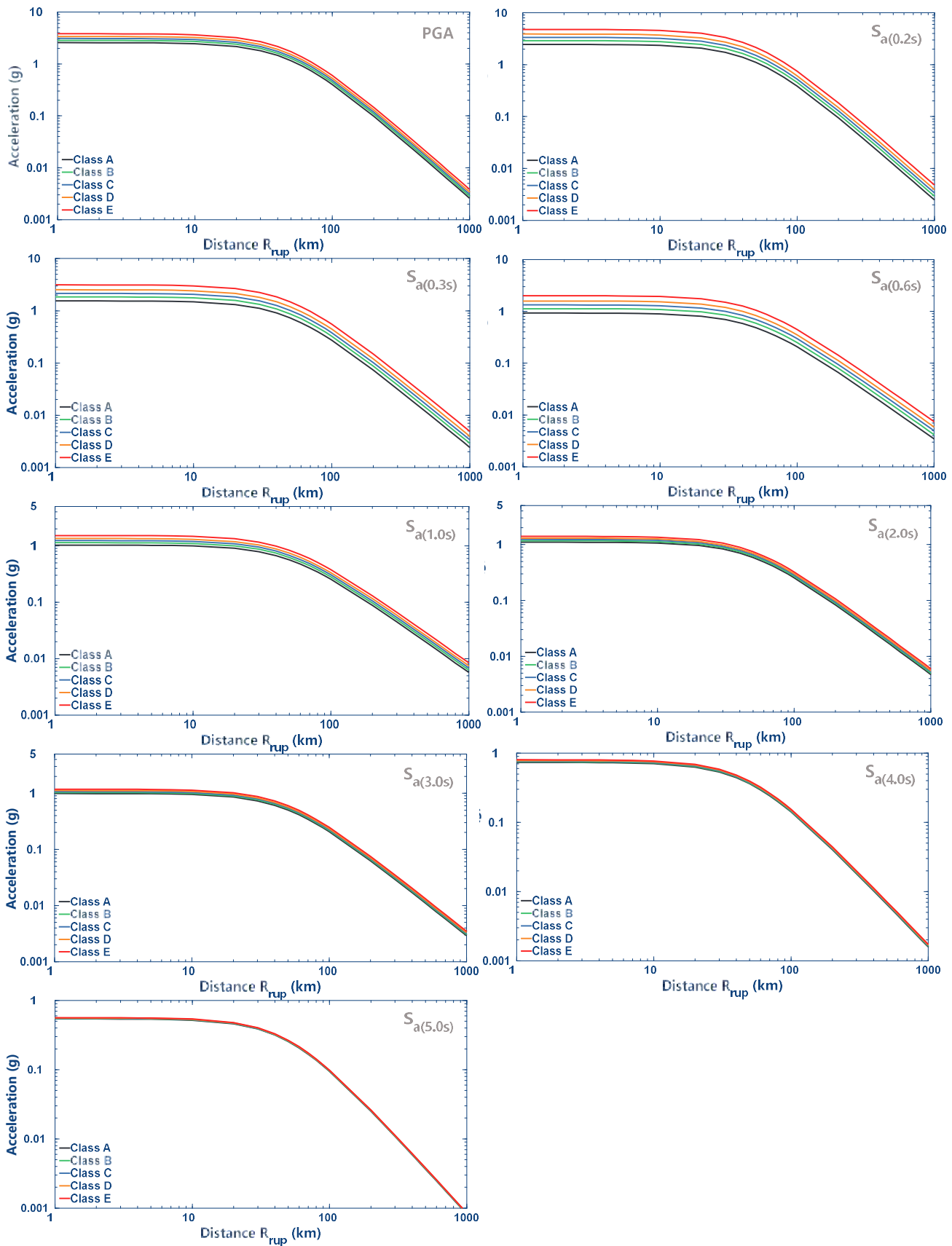


**Figure 23:** Comparison of the median predictions calculated from horizontal ground models derived through different Shear wave velocities ( $V_{S3}$ ) of 1200, 700, 437, 270 and 140m/s that correspond soil classes A, B, C, D and E, respectively. These GMPEs are obtained from different IMs that for this case only resemble 8.5  $M_w$  earthquakes.

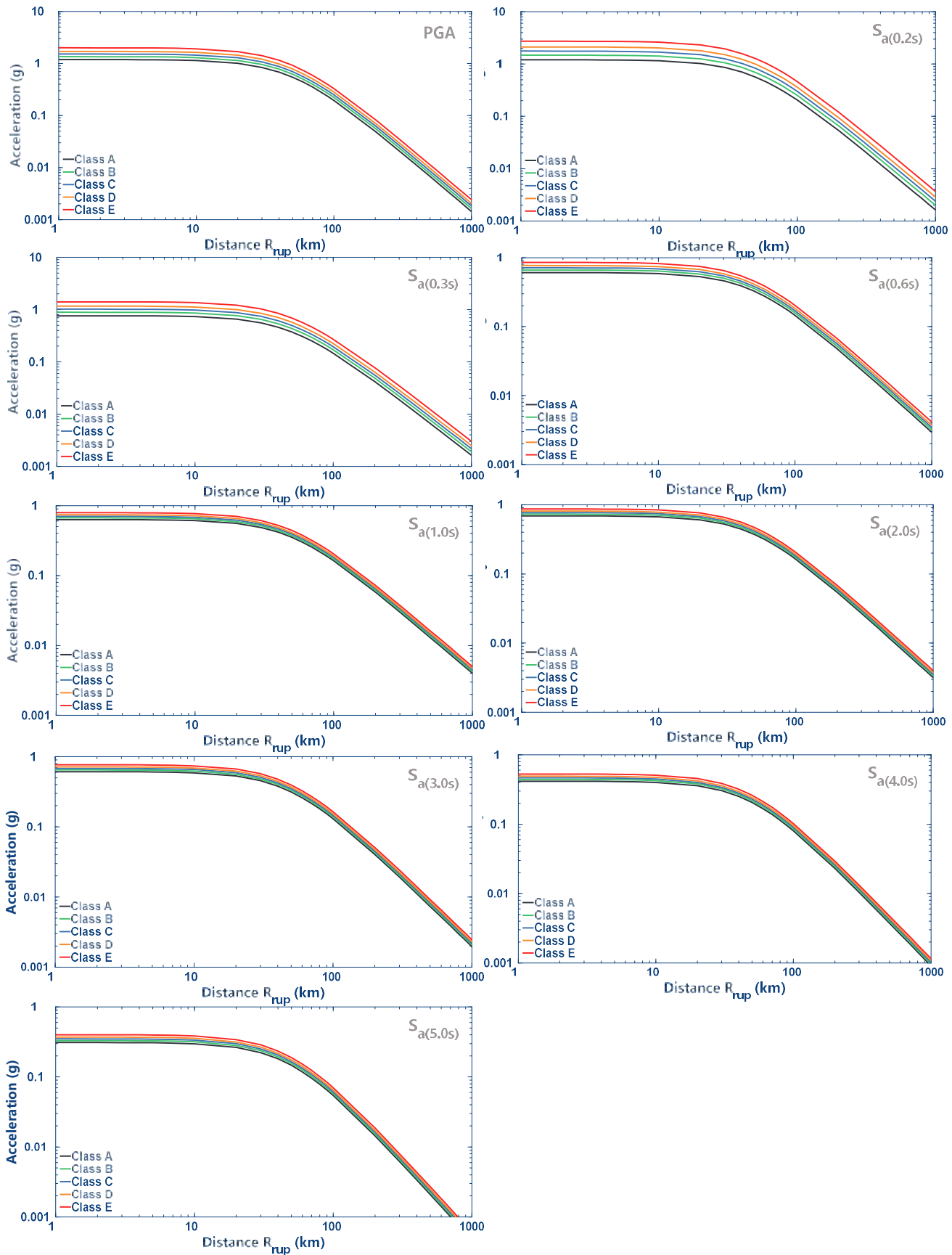


**Figure 24:** Comparison of the median predictions calculated from vertical ground models derived through different Shear wave velocities ( $V_{S3}$ ) of 1200, 700, 437, 270 and 140m/s that correspond soil classes A, B, C, D and E, respectively. These GMPEs are obtained from different IMs that for this case only resemble 8.5  $M_w$  earthquakes.

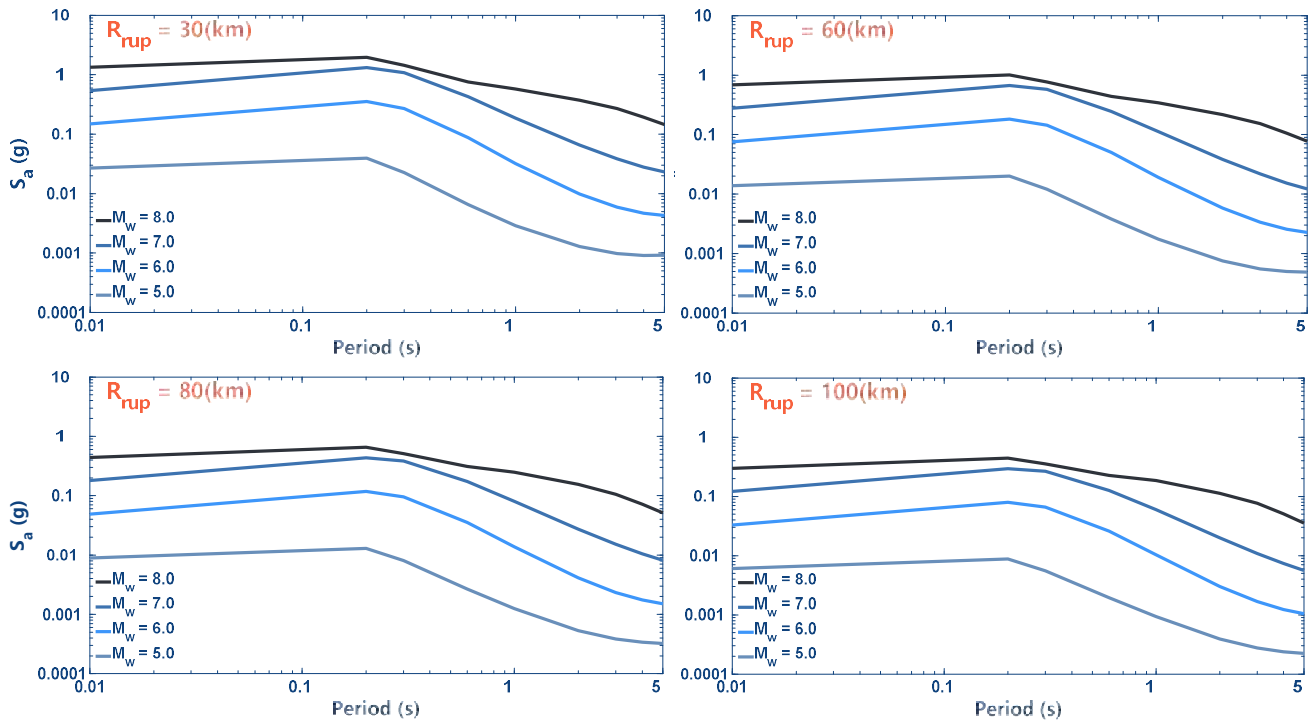


**Figure 25:** Response spectra with 5% damping ratio predicted for horizontal ground motions with different moment magnitudes ( $M_w$ ) and rupture distances ( $R_{rup}$ ) for a reference rock site that presents a  $V_{S30}$  of 1200 m/s.

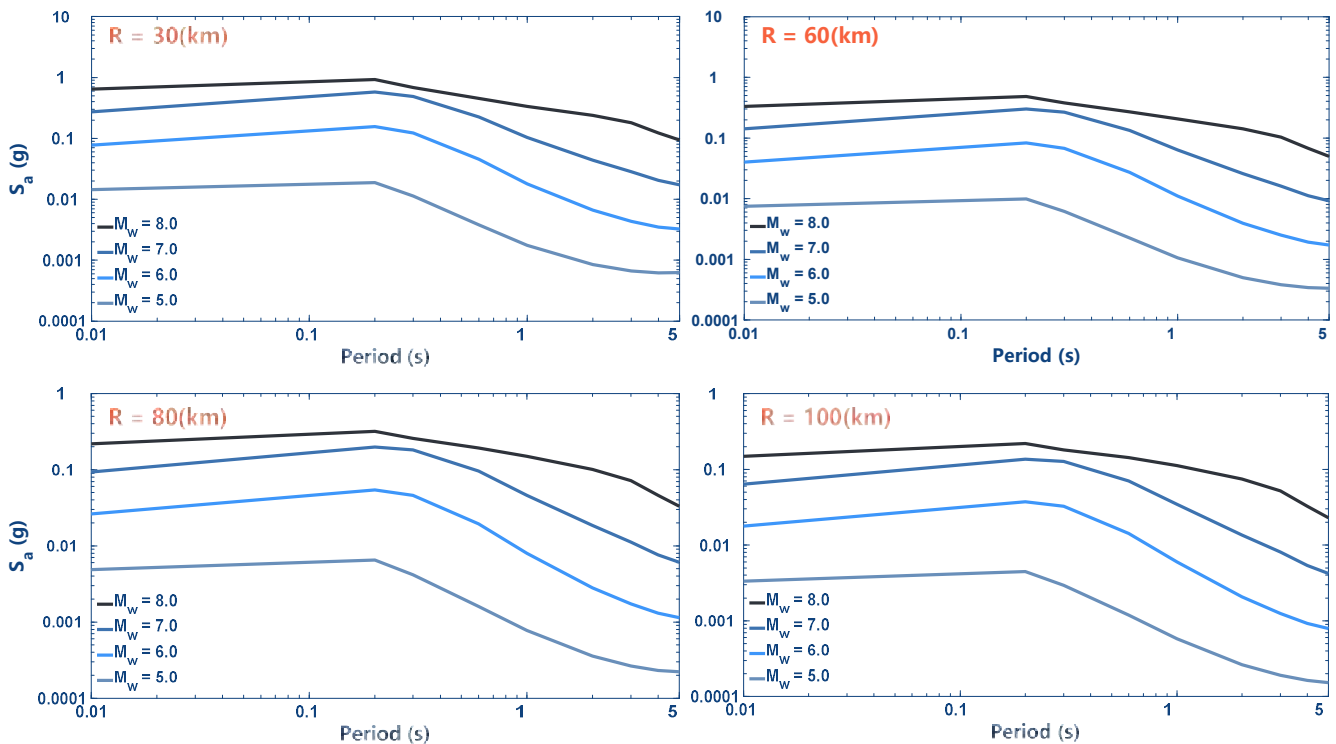


**Figure 26:** Response spectra with 5% damping ratio predicted for vertical ground motions with different moment magnitudes ( $M_w$ ) and rupture distances ( $R_{rup}$ ) for a reference rock site that presents a  $V_{S30}$  of 1200 m/s.

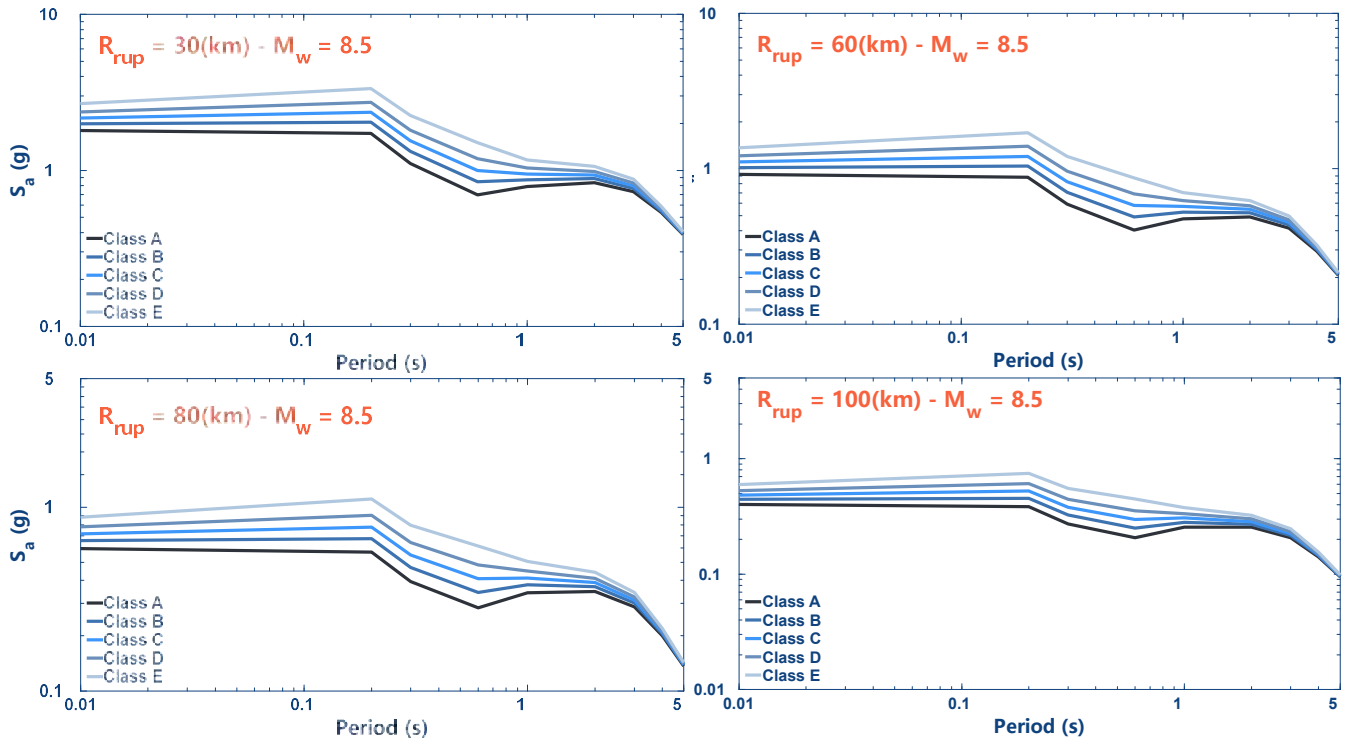


**Figure 27:** Response spectra predicted for horizontal ground motions with  $8.5 M_w$  and different rupture distances ( $R_{rup}$ ) for site classes A, B, C, D and E that correspond Shear wave velocities ( $V_{S30}$ ) of 1200, 700, 437, 270 and 140m/s, respectively.

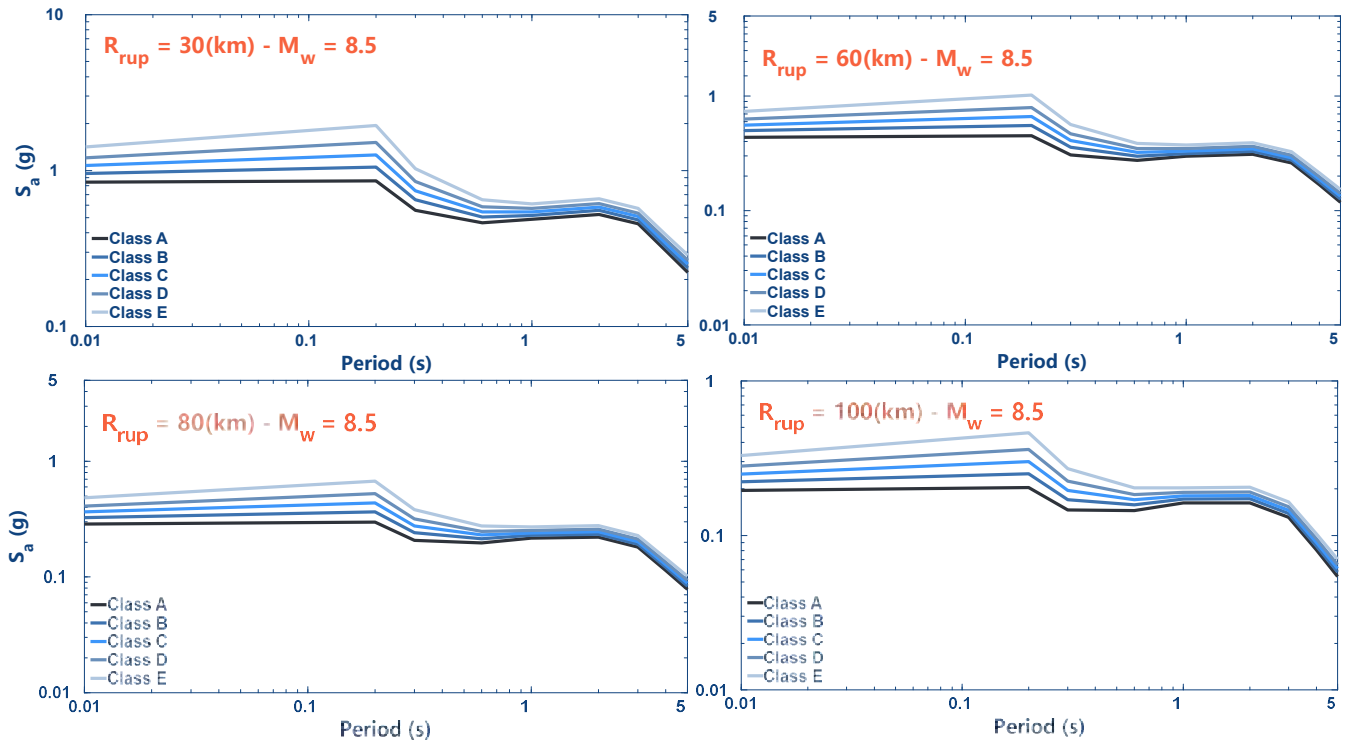


**Figure 28:** Response spectra predicted for horizontal ground motions with  $8.5 M_w$  and different rupture distances ( $R_{rup}$ ) for site classes A, B, C, D and E that correspond Shear wave velocities ( $V_{S30}$ ) of 1200, 700, 437, 270 and 140m/s, respectively.

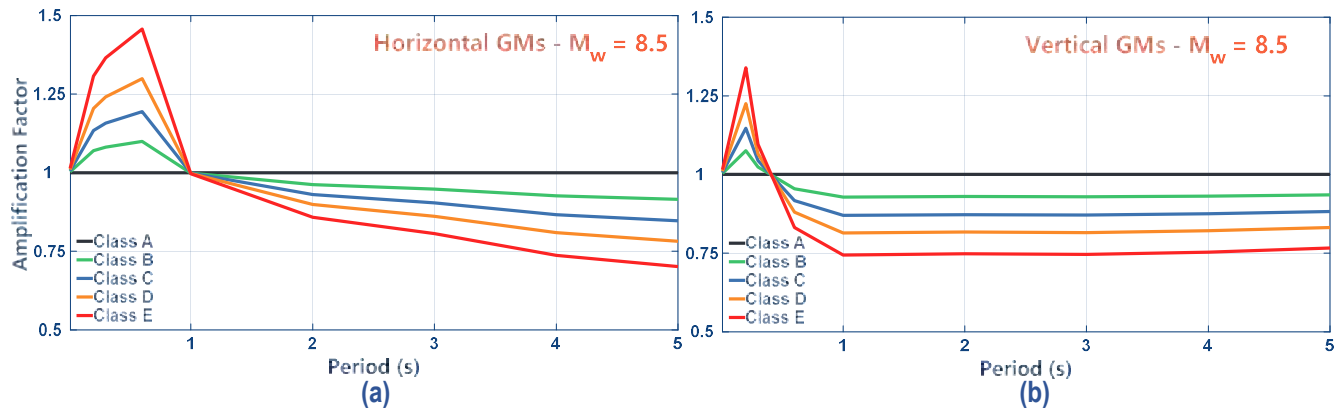


**Figure 29:** Average Site Effects Coefficients computed for soil classes A, B, C, D and E that correspond Shear wave velocities ( $V_{S30}$ ) of 1200, 700, 437, 270 and 140m/s, respectively for: (a) horizontal ground Motions, and (b) vertical ground motions.



## THE MEAN PERIOD $T_m$ , THE $PGA/PGV$ RATIO, THE $PGA/(PGVT_m)$ RATIO, AND THE $PGA/(PGVf_m)$ RATIO GMPE REGRESSION FOR THE HORIZONTAL AND VERTICAL GROUND MOTION RECORDS

The frequency content of an earthquake ground motion (GM) is important because it influences the dynamic response of earth and structural systems. This means when the frequency content of an event equates the natural period of the ground environment (such as soil deposit, earth dam) or structural systems (such as building or any civil structure), the dynamic response is increased, higher inertial forces are applied on the system, and considerable damage may occur [165], [166]. Therefore, it is important to acknowledge the frequency content of an earthquake and its effect on the dynamic response of any structure. Various parameters have been used to characterize the frequency content of an event such as the mean period ( $T_m$ ), the average spectral period ( $T_{avg}$ ), the smooth spectral period ( $T_o$ ), and the predominant spectral period ( $T_p$ ). However, the  $T_m$  has shown better precise capabilities to represent the time acceleration history among all the parameters. The  $T_m$  provides less scatter of seismic response when it is used as a normalization parameter [49], [116]. The methodology calculation of  $T_m$  for the two horizontal and one vertical components for each record was given in [Section 2.4](#). For the present study, 3750 records from 454 events were used for the regression as described in [Appendix A.2](#).

On the other hand, usually, the peak ground acceleration (PGA) and the peak ground velocity (PGV) are important IM parameters for carrying out nonlinear time history analysis of structures as well as for being an empirical parameter to predict ground motion frequency content. As a consequence of that,  $PGA/PGV$  ratio presents the best correlation with the  $T_m$  for both near- and far-source earthquakes [48]. For the present study, also  $PGA/PGV$  ratio is evaluated considering the 3750 records from the 454 subduction interface events that mostly comprises records from Peru, Chile and Ecuador. The PGA and PGV procedures applied in this study are cited in [Section 2.3](#) and [Section 2.4](#). Then, [Fig. 30](#), [Fig. 31](#) and [Fig. 32](#) show three different perspectives of how both the  $T_m$  and the  $PGA/PGV$  ratio well correlate in terms of moment magnitude ( $M_w$ ), rupture distance ( $R_{rup}$ ), and shear wave velocity ( $V_{S30}$ ) for both horizontal and vertical GM records. It is worth mentioning that the two dimensional plots (as shown in [Fig. 32](#)) confirm the good correlation between the  $PGA/PGV$  ratio and the  $T_m$  as it was presented by Elhout (2020) [48]. However, two datasets were used from this last study attempt that comprises twenty-two far-source and twenty-seven near-source ground motion records and their correlations were found separately. This study confirms their correlation using a strong dataset from both far-source and near-source ground motion

records as presented in Fig. 31 for horizontal and vertical GM records. These plots apart from being the first information ever presented so far for the South America Subduction zone suggest less scatter compared to the other IMs parameters (as presented from Fig.12 to Fig. 22) described in Section 3.3. These results bring the opportunity to study the  $T_m$ ,  $PGA/PGV$  ratio, and the  $PGA/(PGVT_m)$  ratio as independent IM parameters to develop ground motion prediction equations, and compare their residuals respect to the GMPE median model for each case.

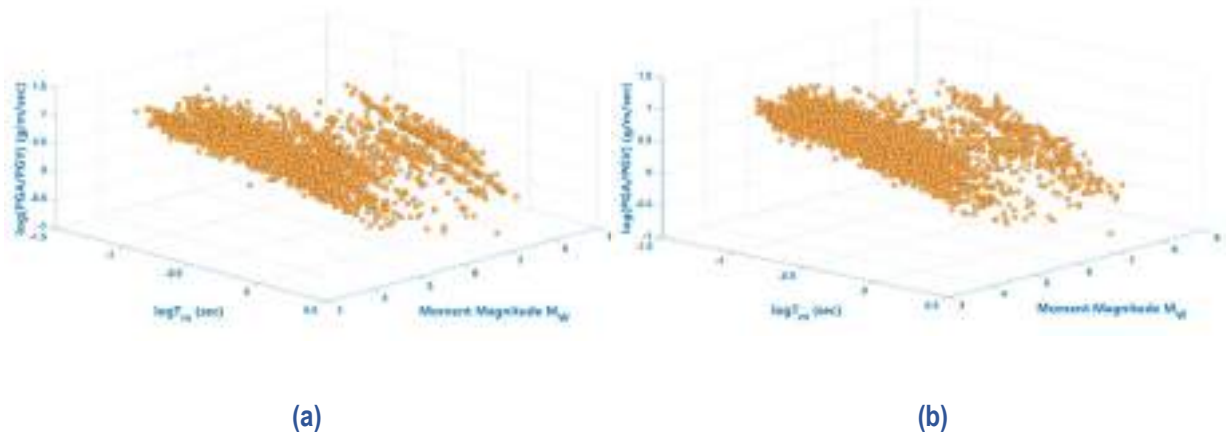


**Figure 30:**  $PGA/PGV$  ratio versus  $T_m$  and Moment Magnitude ( $M_w$ ) for: (a) horizontal ground motion records, and (b) vertical ground motion records.

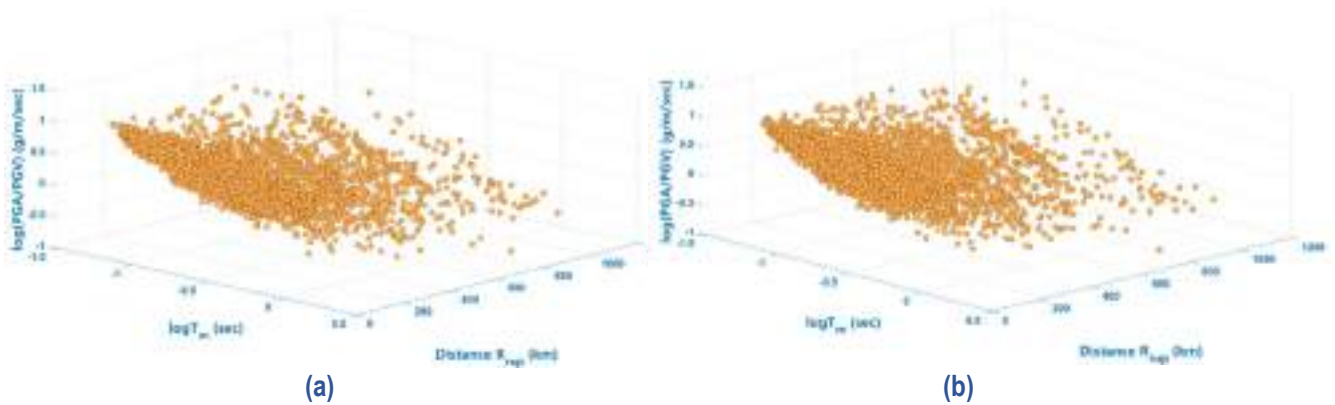


**Figure 31:**  $PGA/PGV$  ratio versus  $T_m$  and Rupture Distance ( $M_{rup}$ ) for: (a) horizontal ground motion records, and (b) vertical ground motion records.

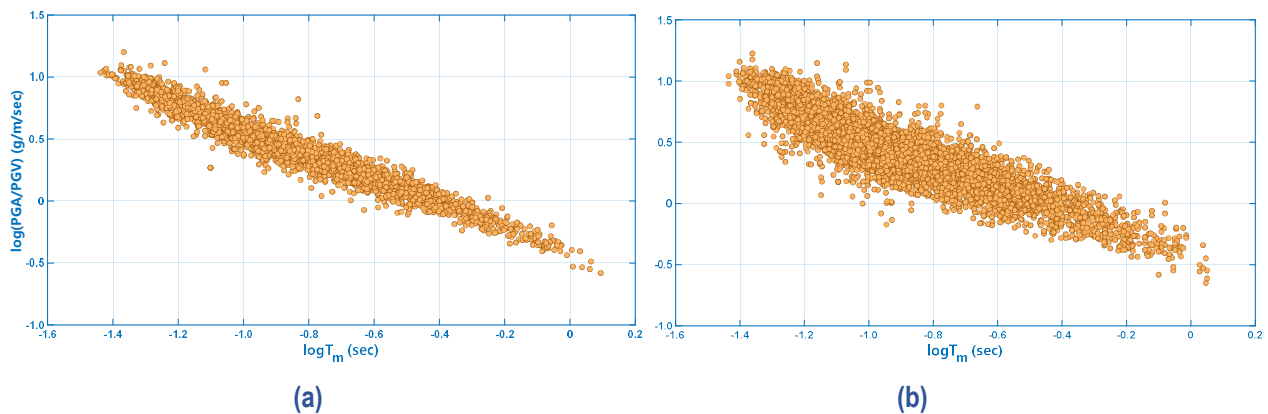


**Figure 32:**  $PGA/PGV$  ratio versus  $T_m$  for: (a) horizontal ground motion records, and (b) vertical ground motion records.

The regression method performed for these three IM parameters were described in [Section 3.1](#), [Section 3.2](#) and [Section 3.3](#). Hence, [Table 7](#) and [Table 8](#) summarize the results obtained from the regression analysis performed in MATLAB for each IM for the horizontal and vertical GM records, respectively. Herein, the same function form of the median GMPE presented in [Equation 53](#) was utilized. However,  $PGA/(PGVT_m)$  ratio presents the highest variability for the between-event ( $\tau$ ) and the within-event ( $\emptyset$ ) as it was expected. This is because the  $PGA/PGV$  ratio attenuates differently than the  $T_m$  over distance. The value of the first variable decrease at larger rupture distances (as it will be presented in [Fig. 34](#) and [Fig. 37](#)). Meanwhile,  $T_m$  increases at larger rupture distances [49], [116]. Therefore, it would be appropriate to use the mean frequency ( $f_m$ ) instead of the  $T_m$ . This is because the inverse of the mean period ( $f_m = 1/T_m$ ) will attenuate over larger rupture distances as the same manner the  $PGA/PGV$  ratio does. Now, the  $PGA/(PGVf_m)$  ratio is analyzed as a new regressor variable in MATLAB for both the horizontal and vertical GMs. The results of the residuals are also shown in [Table 7](#) and [Table 8](#). Now, these residuals are in good agreement with the correlations found in [Fig. 30](#), [Fig. 31](#) and [Fig. 32](#). So, this confirms that the  $PGA/(PGVT_m)$  ratio is not a good regressor variable for the reasons previous stated and it is discarded for the present study. Then, the between-event ( $\delta_e B_e$ ) and within-event ( $\delta_s B_s$ ) residual plots for the  $T_m$ , the  $PGA/PGV$  ratio, and the  $PGA/(PGVf_m)$  ratio for both horizontal and vertical GMs are presented in [Appendix A.7](#), [Appendix A.8](#), and [Appendix A.9](#), respectively. Furthermore, the main model mean of the GMPEs and their standard deviations for the  $T_m$ , the  $PGA/PGV$  ratio, and the  $PGA/(PGVf_m)$  ratio are plotted considering the compiled dataset for different magnitudes used for their regression. For Horizontal GMs, these plots are presented in [Appendix A.10](#), [Appendix A.11](#), and [Appendix A.12](#) for the same IMs, respectively. Meanwhile, concerning vertical GMs for the same IMs, these are displayed in [Appendix A.13](#), [Appendix A.14](#), and [Appendix A.15](#), respectively. Herein, those figures provide a view of the characterization of the data used for each GMPE regression. It is worth mentioning that the residuals of the  $T_m$ , the  $PGA/PGV$  ratio, and the  $PGA/(PGVf_m)$  ratio for both horizontal and vertical GMs are lower than the PGA and Spectral acceleration values at 0.2, 0.3, 0.6, 1.0, 2.0, 3.0, 4.0 and 5.0s. However, the  $PGA/(PGVf_m)$  ratio exhibits the lowest level of uncertainty ( $\sigma$ ) and almost all the data is inside the upper and lower bound delimited by its the standard deviation (as shown in [Appendix A.11](#) and [Appendix A.15](#)).

**Table 7:** Regression model coefficients for the median GMPE and standard deviations for the  $T_m$ , the  $PGA/PGV$  ratio, the  $PGA/(PGVT_m)$  ratio, and the  $PGA/(PGVf_m)$  ratio considering horizontal GMs.

<i>IM</i>	$b_1$	$b_2$	$b_3$	$b_4$	$b_5$	$\tau$	$\emptyset$	$\sigma$
$T_m$	-9.5106	1.9610	-0.1358	0.2803	-0.0656	0.250	0.450	0.5148
$PGA/PGV$	9.5902	-2.1549	0.1484	-0.267	0.0567	0.250	0.460	0.5235
$PGA/(PGVT_m)$	17.5774	-3.5171	0.2376	-0.5973	0.0172	0.500	0.700	0.8602
$PGA/(PGVf_m)$	0.1208	-0.176	0.0115	-0.0097	-0.0161	0.000	0.300	0.3000

**Table 8:** Regression model coefficients for the median GMPE and standard deviations for the  $T_m$ , the  $PGA/PGV$  ratio, the  $PGA/(PGV T_m)$  ratio, and the  $PGA/(PGV f_m)$  ratio considering vertical GMs.

IM	$b_1$	$b_2$	$b_3$	$b_4$	$b_5$	$\tau$	$\phi$	$\sigma$
$T_m$	-7.7295	1.3249	-0.0855	0.2961	0.0496	0.260	0.440	0.5711
$PGA/PGV$	8.1623	-1.5898	0.1028	-0.3103	-0.0599	0.280	0.470	0.5471
$PGA/(PGV T_m)$	15.9261	-2.9091	0.1884	-0.6213	-0.1126	0.500	0.700	0.8602
$PGA/(PGV f_m)$	0.3031	-0.224	0.0146	-0.0161	-0.0157	0.000	0.300	0.3000

Then, the valuation of the  $T_m$ , the  $PGA/PGV$  ratio, and the  $PGA/(PGV f_m)$  ratio prediction equations for different moment magnitudes and rupture distances are presented in Fig 33, Fig. 34 and Fig 35. From these plots, these IM parameters tend to have similar values at both 7.0 and 8.0  $M_w$ . Although, the predicted values of the  $PGA/PGV$  ratio and the  $PGA/(PGV f_m)$  ratio tend to increase exponentially at values lower than  $M_w$  7, the  $T_m$  reduces exponentially at values lower than  $M_w$  7. Besides, the  $T_m$ , the  $PGA/PGV$  ratio, and the  $PGA/(PGV f_m)$  ratio prediction equations for different site conditions such as class A, B, C, D and E are presented in Fig. 36, Fig. 37, and Fig. 38 according Table 01. Herein, the strongest earthquake scenario of 8.5  $M_w$  was considered. Fig. 36a shows that the predicted  $T_m$  increases at lower  $V_{S30}$  for horizontal motions. Conversely, Fig. 36b shows that the predicted  $T_m$  increases at higher  $V_{S30}$  for vertical motions. On the other hand, the predicted  $PGA/PGV$  ratio tends to reduce at lower  $V_{S30}$  when horizontal ground motions are regressor IMs as presented in Fig. 37(a). Nevertheless, the predicted  $PGA/PGV$  ratio increases at lower  $V_{S30}$  for vertical ground motions as shown in Fig. 37(b). Moreover, the predicted  $PGA/(PGV f_m)$  ratio increases at lower  $V_{S30}$  as depicted in Fig. 38 for both horizontal and vertical GMs.

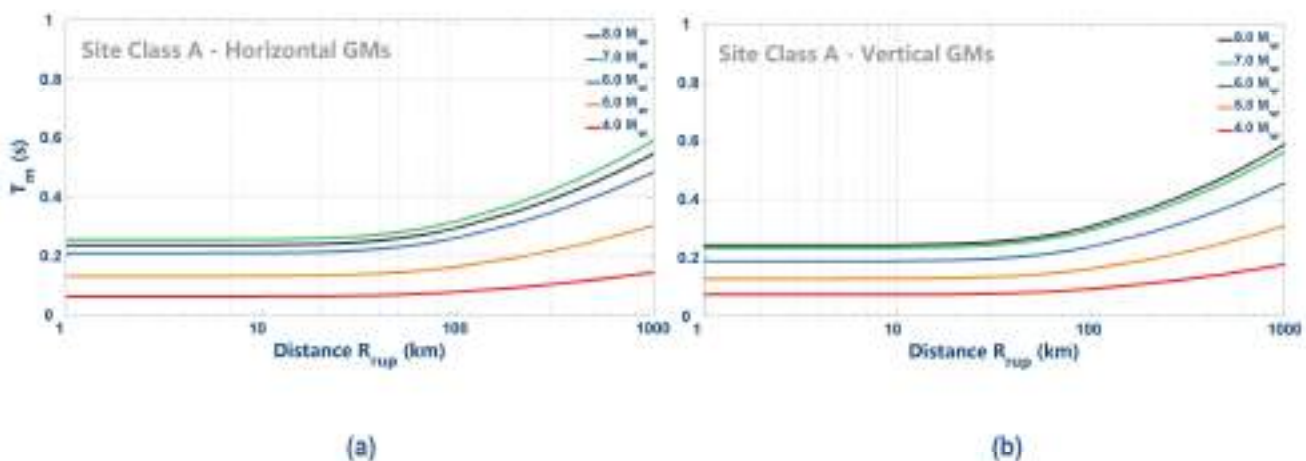


**Figure 33:** Mean Period ( $T_m$ ) predicted for different moment magnitude for a reference rock site ( $V_{S30} = 1200$  m/s). (a) Horizontal ground motions and (b) Vertical ground motions.



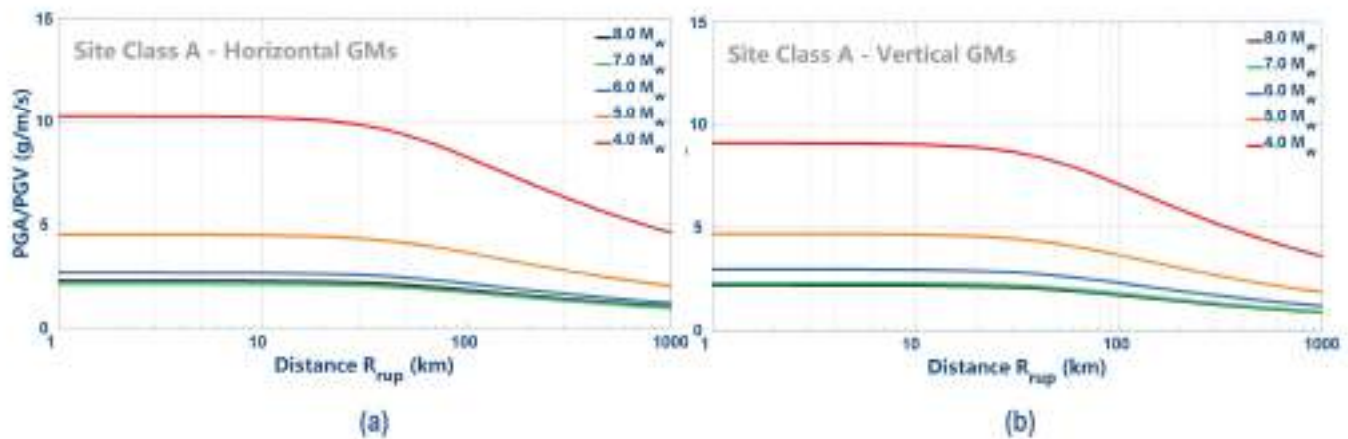


**Figure 34:**  $PGA/PGV$  ratio predicted for different moment magnitude for a reference rock site ( $V_{s30} = 1200$  m/s). (a) Horizontal ground motions and (b) Vertical ground motions.

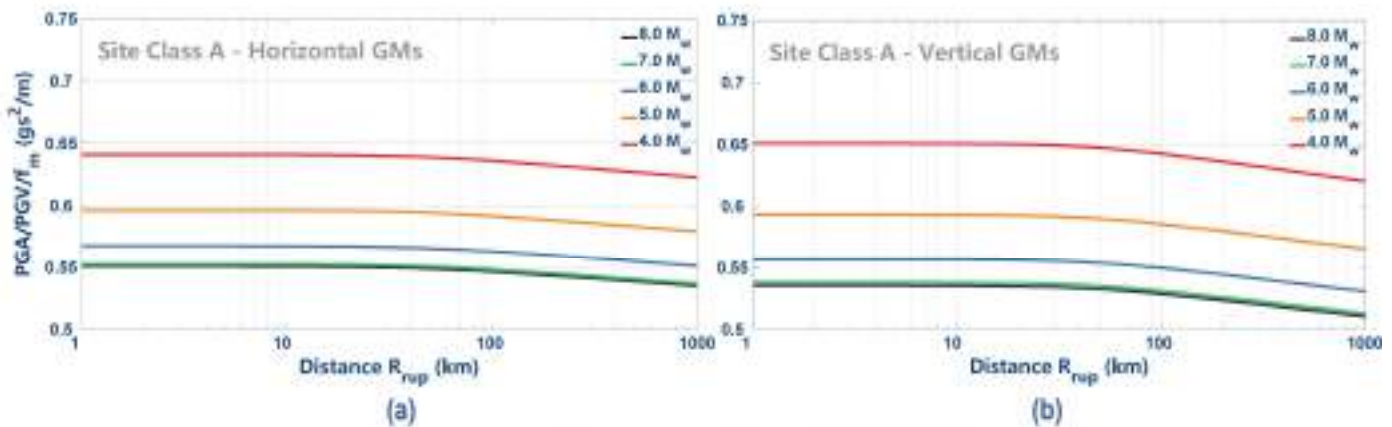


**Figure 35:**  $PGA/(PGV f_m)$  ratio predicted for different moment magnitude for a reference rock site ( $V_{s30} = 1200$  m/s). (a) Horizontal ground motions and (b) Vertical ground motions.

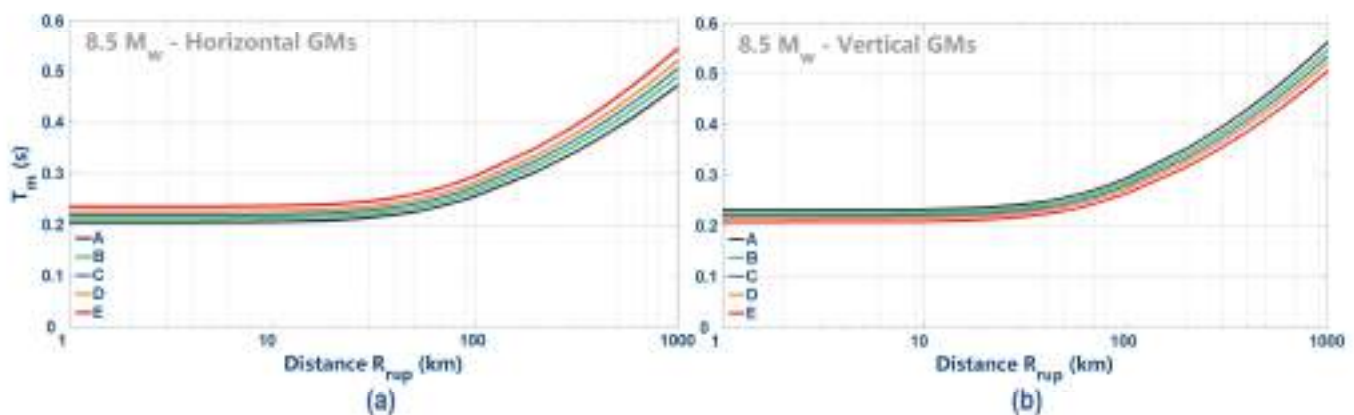


**Figure 36:** Comparison of the  $T_m$  median prediction derived through different Shear wave velocities ( $V_{s30}$ ) of 1200, 700, 437, 270 and 140m/s that correspond soil classes A, B, C, D and E, respectively. These GMPEs only resemble a 8.5  $M_w$  earthquake calculated from: (a) horizontal ground motions, and (b) vertical ground motions.

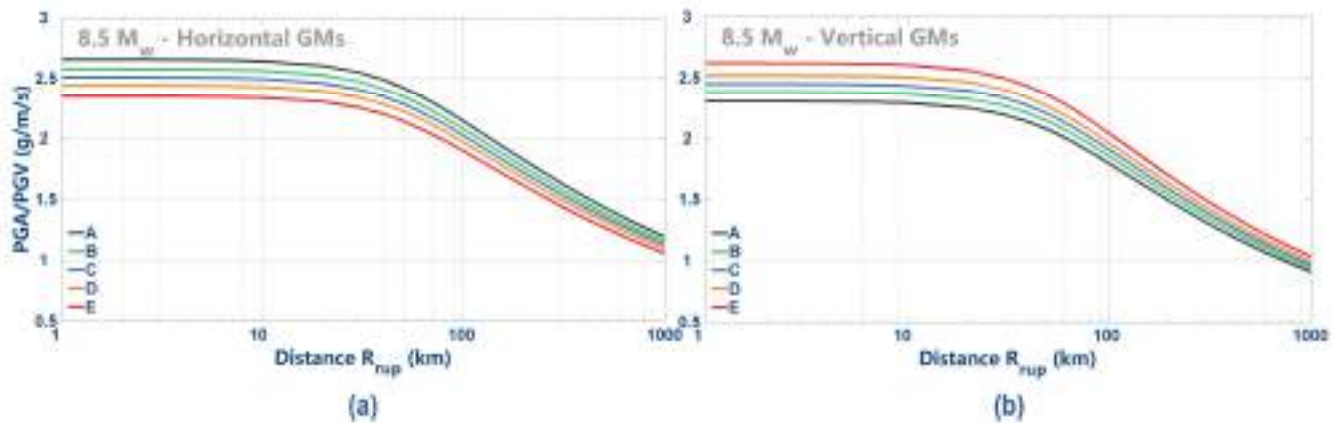


**Figure 37:** Comparison of the  $PGA/PGV$  ratio median prediction derived through different Shear wave velocities ( $V_{S30}$ ) of 1200, 700, 437, 270 and 140m/s that correspond soil classes A, B, C, D and E, respectively. These GMPEs only resemble a 8.5  $M_w$  earthquake calculated from: (a) horizontal ground motions, and (b) vertical ground motions.

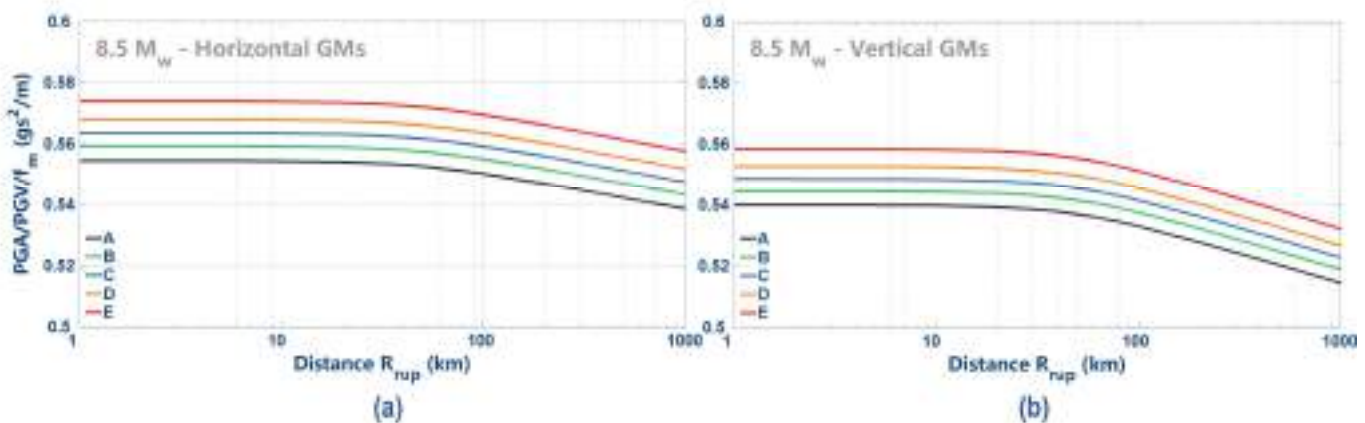


**Figure 38:** Comparison of the  $PGA/(PGV f_m)$  ratio median prediction derived through different Shear wave velocities ( $V_{S30}$ ) of 1200, 700, 437, 270 and 140m/s that correspond soil classes A, B, C, D and E, respectively. These GMPEs only resemble a 8.5  $M_w$  earthquake calculated from: (a) horizontal ground motions, and (b) vertical ground motions.



## COMPARING THE PROPOSED GMPE FOR INTERFACE EVENTS WITH PREVIOUS MODELS

**Fig. 38** presents the predicted PGA for some important interface earthquakes that occurred in Peru, Chile and Ecuador. This new GMPE can predict PGAs for higher longer distance range (up to  $R_{rup}$  a distance of 1000km) when it is compared to previous GMPEs. To do so, a  $V_{s3}$  of 525m/s was considered for all the GMPEs because it represents the intermediate value between soil classes A and Class E. This new GMPE has a better fit when it is contrasted to foreign GMPEs over a large range of hypocentral distances. However, some events such as the 23 June 2001  $M_w$  8.4 Atico, Arequipa, Peru Earthquake (**Fig. 38(a)**) presents higher PGA than this new GMPE and previous GMPEs between  $R_{rup}$  of 300 and 500 km. This may be due to the triggering threshold of accelerometers. Herein, just the Pisagua station from Chile is inside the upper bound of the median model compared to the other stations located near the border of Peru and Chile.

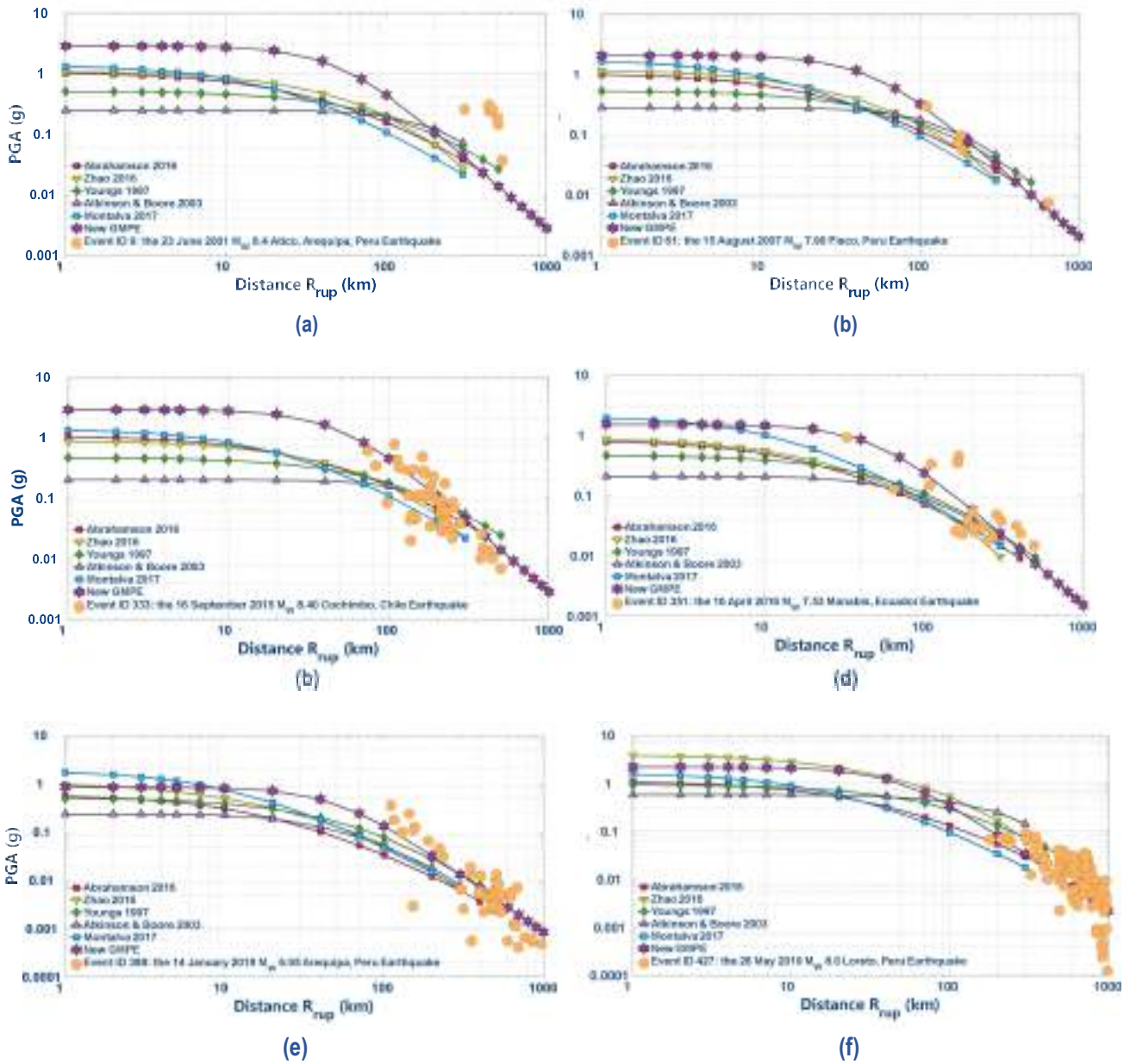


**Figure 39:** Original record data of important events versus predicted PGA using new GMPE and previous GMPEs for subduction zones. (a) the 23 June 2001  $M_w$  8.4 Atico - Peru earthquake, (b) the 15 August 2007  $M_w$  7.9 Pisco - Peru earthquake, (c) the 16 September 2015  $M_w$  8.4 Cochimbo - Chile earthquake, (d) the 16 April 2016  $M_w$  7.53 Manabi - Ecuador earthquake, (e) the 14 January 2018  $M_w$  6.95 Arequipa - Peru earthquake, and (f) the 26 May 2019  $M_w$  8.00 Loreto - Peru earthquake.

## DISCUSSION

The final within-events residuals ( $\delta_e B_e$ ) versus moment magnitude ( $M_w$ ), the single-station residual ( $\delta_r$ ) versus source to site distance ( $R_{rup}$ ), and the site-to-site residual ( $\delta_s B_s$ ) versus  $V_{S30}$  are presented in [Appendix A.3](#) and [Appendix A.4](#) for the PGA and spectral accelerations at 0.2, 0.3, 0.6, 1.0, 2.0, 3.0, 4.0 and 5.0s for both horizontal and vertical GM records, respectively. These residuals show no specific trend, which leads to conclude the regression procedure is robust and reliable. However, it can be improved during the regression analysis by evaluating the truncation effect on the probability density function of the observed ground motions at long-distance scenarios [150]. On the other hand, these residuals tend to decrease when the  $T_m$ , the  $PGA/PGV$  ratio and the  $PGA/PGV f_m$  ratio are the regressor variables for the GMPE as presented in [Appendix A.7](#), [Appendix A.8](#), and [Appendix A.9](#), respectively. This trend confirmed previous investigations performed for the first two parameters ( $T_m$ , and  $PGA/PGV$  ratio) using different foreign sources and different faulting mechanisms [48], [49], [51], [116]. It is worth mentioning that the  $PGA/PGV f_m$  ratio can be described as the best IM parameter for presenting the lowest residuals and standard deviations ( $\sigma$ ). Besides to this, the truncation effect of ground motion is diminished using this innovate ratio at higher distances. Also, the uncertainty due to the lack of geophysical characterization of many stations from Peru, Chile and Ecuador are reduced. Therefore, the GMPE developed for the  $PGA/PGV f_m$  ratio can be employed to generate synthetic motion with more accuracy to fill the gap where a strong dataset is not available such as the Peruvian case. Moreover, this new IM parameter may just provide a characterization of interface typology events. This can be confirmed when inslab and crustal events are also investigated to find a distinguishable ratio among them. This can be supported because a lower amount of IMs from some events tend not to fit the lower and upper bound standard deviation as presented in [Appendix A.12](#) and [Appendix A.15](#). Besides, this parameter could help identifying different earthquakes sources and typologies if it is further investigated.

Meanwhile, magnitude homogenization from local magnitude ( $M_L$ ) and body wave magnitude ( $m_b$ ) to moment magnitude ( $M_w$ ) [123] seem suitable as presented in [Section 2.5](#). The residual plots show quite same residuals between 4.0 and 8.5  $M_w$  and no trends were found. Moreover, variations of  $V_{S30}$  influence site effects and in the amplitude of intensity measures (IMs). Higher  $V_{S30}$  values indicate lower predicted accelerations for any predominant period and lower ( $PGA/PGV f_m$ ) ratios for both horizontal and vertical GMs as presented in [Fig. 23](#), [Fig. 24](#) and [Fig. 38](#). Besides, [Fig. 36](#) indicates that higher  $V_{S30}$  values implies lower  $T_m$  values and higher  $PGA/PGV$  ratios for horizontal GMs. Meanwhile, [Fig. 37](#) shows that higher  $V_{S30}$  values implies higher  $T_m$  values and lower  $PGA/PGV$  ratios for vertical GMs. Although it is important to fully complete geophysical characterization of stations to better understand the dynamic behavior of soils during earthquakes and provide relevant information of site conditions. This will reduce the site-to site-residual versus  $V_{S30}$  for future investigations.

The regression coefficients presented in **Table 5**, **Table 6**, **Table 7** and **Table 8** can be applied in **equation 53** for each predicted IM for interface events. However, the  $PGA/PGVT_m$  ratio is not recommended as a predictor variable as previously stated. Then, these GMPEs are suitable to predict the IMs for events subjected to the applicability range presented in **Table 9** that is based on **Fig. 10** and **Fig 11**.

**Table 9:** Applicability range of the new GMPE for the Peruvian subduction zone according to Moment magnitude  $M_w$ , rupture distance ( $R_{rup}$ ), and focal depth ( $D$ ).

MOMENT MAGNITUDE $M_w$	RUPTURE DISTANCE $R_{rup}$ (km)	FOCAL DEPTH $D$ (km)
4.0 - 4.5	0 - 180	0 - 80
4.5 - 5.0	0 - 400	0 - 130
5.0 - 5.5	0 - 700	0 - 150
5.5 - 6.0	0 - 1000	0 - 150
6.0 - 6.5	0 - 1000	0 - 150
6.5 - 7.0	0 - 1000	0 - 40
7.0 - 7.5	0 - 400	0 - 60
7.5 - 8.0	0 - 1000	0 - 140
8.0 - 8.5	0 - 400	0 - 40

The prediction capabilities of this new GMPE shows better performances than the interface GMPEs proposed by Abrahamson et al. (2016) [58], Zhao et al. (2016) [59], Youngs et al. (1997) [61], Atkinson & Boore (2003) [82], and Montalva et al. (2017) [83]. Meanwhile, the Abrahamson's, Zhao's, and Youngs's GMPE models were suggested and adopted for probabilistic hazard assessment in Peru from which the seismic design code (E030) are based on predicting PGA [22], [24], [56]. This new GMM suggested in this study presents higher predicted PGA at rupture distances up to 300km for earthquakes with  $M_w$  higher than 7.0 compared to previous GMPEs (as shown in **Fig. 39**). This implies the current Peruvian seismic code may underestimate the predicted PGA considering that 45% of the earthquakes correspond to interface events for the compiled dataset used in this study. Also, **Fig. 4**, **Fig. 5** and **Fig. 6** indicate that only interface events present events with moment magnitudes higher than 8.0 and they may influence more on the application of logic trees for PSHA applications. However, the prediction capabilities of this new GMPE should be improved by considering the truncation effect of ground motion over larger rupture distances [150]. Also, considering the low dataset of events higher than 7  $M_w$  performed in this study, it should be appropriate to collect more strong data along the Chile, Peru, Ecuadorian subduction zone. This will reduce the uncertainty and standard deviation ( $\sigma$ ) of the predicted PGA. Finally, the standard deviation for the predicted PGA and spectral acceleration IMs is around 0.86, which is quite high due to the variability of the observed IMs. So, performing the Bayesian measurement error (BME) could reduce the  $\sigma$  value to obtain better predictor variables. The BME method performs better than the common maximum likelihood regression method that has been applied on several GMPEs so far [68].



Based on the Peruvian Seismic code (E030), the vertical to horizontal PGA ratio is set to  $2/3$  ( $\approx 0.67$ ) to estimate the vertical PGA for design purposes. However, Fig. 40(a) indicates this median ratio may be reached when a structure is hit by an earthquake of  $8.5 M_w$ , and is founded on soil class E and on rupture distances ( $R_{rup}$ ) larger than 1000km. This implies that this ratio can be critical at larger rupture distances and at lower shear wave velocities. This is because the vertical to horizontal PGA ratio tend to increase at higher rupture distances. For instance, a critical scenario may be when the rupture distance is up to 100km and the structure is founded on soil class E. Then, at these conditions a predicted vertical to horizontal PGA ratio may be around 0.55 that is lower than 0.67. Therefore, the ratio that is suggested in the Peruvian seismic code (E030) overestimate the vertical PGA at rupture distances lower than 100km, which represents critical vertical to horizontal PGA ratios. Meanwhile, Fig 40(b) shows that lower magnitudes over higher rupture distances tend to reach the ratio adopted by the E030 considering soil class A. Moreover, Fig. 41 shows the vertical to horizontal ratios at spectral acceleration periods of 0.2, 0.3, 0.6, 1.0, 2.0, 3.0, 4.0, and 5.0s like it is presented in Fig. 40. Some important aspects can be concluded from those plots. First of all, spectral accelerations with 5% damping ratio for periods of 0.2, 3.0, 4.0 and 5.0s indicate that the vertical to horizontal spectral acceleration ( $S_a$ ) ratios may increase at lower  $V_{S30}$ . Meanwhile, spectral acceleration with 5% damping ratio for periods 0.3, 0.6, 1.0 and 2.0s show that the vertical to horizontal  $S_a$  ratios may increase at higher  $V_{S30}$ . Furthermore, all the spectral accelerations for the present study present a tendency of exceeding the vertical to horizontal spectral acceleration ratio of 0.67 for specific soil classes (as presented in Fig. 41). Finally, the increase tendency of the vertical to horizontal spectral acceleration ratio over distance tends to be flatten at higher spectral periods such as 4.0 and 5.0s. This may indicate that the vertical to horizontal  $S_a$  ratios may attenuate at higher rupture distances for spectral periods higher than 5.0s.

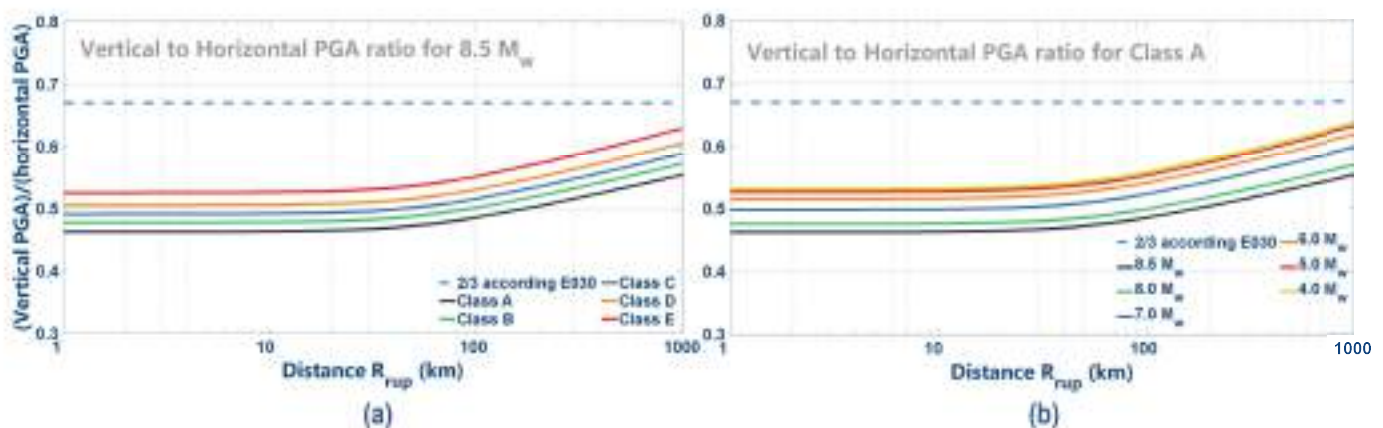


**Figure 40:** Comparison of the vertical to horizontal PGA ratio median prediction derived through: (a) different Shear wave velocities ( $V_{S30}$ ) of 1200, 700, 437, 270 and 140m/s that correspond soil classes A, B, C, D and E, respectively. These median ratios only resemble a 8.5  $M_w$  earthquake, and (b) different moment magnitude that correspond soil Class A with  $V_{S30}$  of 1200m/s.

**Table 10:** Comparison of the Site effect coefficients between the current seismic code from Peru (E030) and the present study for both horizontal and vertical GMs.

CURRENT PERUVIAN SEISMIC CODE E030				PRESENT STUDY - HORIZONTAL GMs			PRESENT STUDY - VERTICAL GMs		
SOIL CLASS	SHEAR VELOCITY $V_{s30}$ APLICABILITY RANGE	SITE EFFECT COEFFICIENTS	EQUIVALENT SITE EFFECT COEFFICIENTS FOR COMPARISON IN THIS STUDY	SOIL CLASS	SHEAR VELOCITY $V_{s30}$ APLICABILITY RANGE	SITE EFFECT COEFFICIENTS	SOIL CLASS	SHEAR VELOCITY $V_{s30}$ APLICABILITY RANGE	SITE EFFECT COEFFICIENTS
(1)	(2)	(3)	(4)	(5)	(6)	(7)	(8)	(9)	(10)
$S_0$	$1500 < V_{s30}$	0.80	1.00	A	$875 < V_{s30}$	1.00	A	$875 < V_{s30}$	1.00
$S_1$	$500 < V_{s30} \leq 1500$	1.00	1.25	B	$525 < V_{s30} \leq 875$	1.10	B	$525 < V_{s30} \leq 875$	1.10
$S_2$	$180 < V_{s30} \leq 500$	1.05	1.31	C	$350 < V_{s30} \leq 525$	1.20	C	$350 < V_{s30} \leq 525$	1.15
$S_2$	$180 \leq V_{s30} \leq 500$	1.05	1.31	D	$190 \leq V_{s30} \leq 350$	1.30	D	$190 \leq V_{s30} \leq 350$	1.25
$S_3$	$V_{s30} < 180$	1.10	1.38	E	$V_{s30} < 190$	1.45	E	$V_{s30} < 190$	1.35

**Table 11:** Comparison of site effect coefficients between the current seismic code from Peru (E030), the current seismic code from Chile (NCh 433), and the present study for both horizontal and vertical GMs.

CURRENT PERUVIAN SEISMIC CODE E030			CURRENT CHILEAN SEISMIC CODE NCh 433			PRESENT STUDY - HORIZONTAL GMs			PRESENT STUDY - VERTICAL GMs		
SOIL CLASS	SHEAR VELOCITY $V_{s30}$ APLICABILITY RANGE	SITE EFFECT COEFFICIENTS	SOIL CLASS	SHEAR VELOCITY $V_{s30}$ APLICABILITY RANGE	SITE EFFECT COEFFICIENTS	SOIL CLASS	SHEAR VELOCITY $V_{s30}$ APLICABILITY RANGE	SITE EFFECT COEFFICIENTS	SOIL CLASS	SHEAR VELOCITY $V_{s30}$ APLICABILITY RANGE	SITE EFFECT COEFFICIENTS
(1)	(2)	(3)	(4)	(5)	(6)	(7)	(8)	(9)	(10)	(11)	(12)
$S_0$	$1500 < V_{s30}$	0.80	A	$900 < V_{s30}$	0.90	A	$875 < V_{s30}$	0.90	A	$875 < V_{s30}$	0.90
$S_1$	$500 < V_{s30} \leq 1500$	1.00	B	$500 < V_{s30} \leq 900$	1.00	B	$525 < V_{s30} \leq 875$	1.00	B	$525 < V_{s30} \leq 875$	1.00
$S_2$	$180 < V_{s30} \leq 500$	1.05	C	$350 < V_{s30} \leq 500$	1.05	C	$350 < V_{s30} \leq 525$	1.10	C	$350 < V_{s30} \leq 525$	1.05
$S_2$	$180 \leq V_{s30} \leq 500$	1.05	D	$180 \leq V_{s30} \leq 350$	1.20	D	$190 \leq V_{s30} \leq 350$	1.20	D	$190 \leq V_{s30} \leq 350$	1.15
$S_3$	$V_{s30} < 180$	1.10	E	$V_{s30} < 180$	1.30	E	$V_{s30} < 190$	1.30	E	$V_{s30} < 190$	1.25

The average site effects coefficients presented in **Fig. 29** may suggest adequate values for the Peruvian Seismic code for strong earthquakes subjected to soil inelastic behavior. **Table 10** summarizes these values for soil classes A, B, C, D and E as presented in **Table 1** for both horizontal and vertical ground motions (as shown in column 7 and column 9, respectively). This soil classification was adopted for the present study like it was described in **Section 2.1** as previous studies suggested it [70], [71]. So, the site coefficients obtained are compared to the equivalent site coefficients of the Peruvian Seismic Code (E030) as presented in **Table 10** (Column 4). Herein, it can be observed the strong influence of the American seismic code ASCE-7-10 on the soil classification adopted in the E030. However, these shear velocity classifications may not capture properly the site amplification coefficients for soil classes  $S_1$  and  $S_2$  (see column 1 and 4 from **Table 10**) compared to the site coefficient for soil classes B, C, and D (column 4 and 7) obtained from the GMPE regression. The site coefficients for soil classes  $S_1$  and  $S_2$  may overestimate the PGA calculated from the rock reference ( $S_0$ ). However, this statement is contradicted when the Peruvian seismic code appoints that soil class  $S_1$  is the reference rock where the PGA values are given to be scaled according to the site coefficient values presented in Column 3 (**Table 10**). Then, **Table 11** adapted the site coefficients of the present study to be compatible not only with the Peruvian code, but also for the Chilean Seismic Code (NCh 433). Herein, this normativity aspect changes the assumption previous stated and it implies that the Peruvian code underestimate the PGA for classes  $S_2$  and  $S_3$  at around 12.5% and 15.4%, respectively. This is due to the lower site coefficient values adopted when it is compared to this study (see column 3 and 9 from **Table 11**). In addition, the site coefficient value for class  $S_0$  (which is 0.80) may underestimate the PGA at around 12% when it is



compared to the equivalent soil class A presented in this study. This situation may worsen PGA predictions for site classes  $S_0$ ,  $S_1$ ,  $S_2$  and  $S_3$  when the Peruvian code relies on PSHA that are based on foreign GMPEs that may underestimate this IM for PGA as previously stated. Finally, the site coefficients presented in this study are in well agreement with the site coefficient from the Chilean Seismic code (NCh 433), which are based on Leyton et al. (2018) [71] and almost presents the same  $V_{S30}$  classification performed in this study (See Columns 5, 6, 8 and 9 from **Table 11**). However, only the site coefficient of soil class C (from the Chilean Seismic code) is 5% lower than the site coefficient suggested in this study. It is worth mentioning that the soil classification adopted for the present study is almost compatible with the one proposed by Aguilar et al. (2019) [70]. Herein, this latest attempt suggests its implementation in the current Peruvian Seismic Code (E030) with higher site coefficients.

From **Fig. 36**, the predominant mean period ( $T_m$ ) values range between 0.10 and 0.65s considering a 8.5  $M_w$  earthquake up to a rupture distance of 300km for different site conditions for both horizontal and vertical GMs. Meanwhile, the  $T_m$  may vary between 0.20 and 0.90s considering the similar earthquake intensity for rupture distances larger than 300km. In addition, the  $T_m$  may vary between 0.10 and 0.70s from earthquakes between 6 and 8  $M_w$  and up to rupture distances of 300km over rock conditions (as shown in **Fig. 33**) for both horizontal and vertical GMs. In contrast, the  $T_m$  may vary between 0.04 and 0.35s from earthquakes between 4 and 5  $M_w$  and up to rupture distance values of 300km over rock conditions. These  $T_m$  values for critical PGA values are in synchrony with **Fig. 29**, where the critical zone for site amplification ranges between 0 and 1.0s for horizontal GMs and between 0 and 0.45s for vertical ground motions. Spectral values out of that range present a de-amplification respect to class A. This implies that structures with fundamental periods between 0.1 and 0.70s are more vulnerable to experience resonance with a 8.5  $M_w$  earthquake up to a rupture distance of 300km. This resonance can be worse if the soil presents similar fundamental periods between that range. This aforementioned critical conditions also applies for structures with vertical fundamental periods that cover that range. So, structures between this critical fundamental period range should be base isolated or equipped with linear or nonlinear dampers to avoid resonance.

Moreover, according to **Fig. 34** and **Fig. 37**, the median  $PGA/PGV$  ratio plus standard deviation for all the records from events up to  $M_w$  8.5 and up to  $R_{rup}$  values of 100km that comprises different soil classes for both horizontal and vertical GMs may be classified as high ranges. Meanwhile, the ground motion records from events equal or higher than  $M_w$  8.5 with  $R_{rup}$  values higher than 100km for all soil classes may classify as intermediate ranges. These classifications are based on Naumoski et al. (1988) [46] and Tso et al. (1992) [44]. Finally, **Fig. 35** indicates the  $PGA/(PGV f_m)$  ratio may vary between 0.77 and 0.38 for events with  $M_w$  between 6 and 8 and rupture distance values up to 1000km for both horizontal and vertical GMs on soil class A. Besides, **Fig. 38** shows the same variation range for the  $PGA/(PGV f_m)$  ratio considering a  $M_w$  8.5 earthquake up to rupture distance values of 1000km over different soil classes. It is worth mentioning that the median ratio of the aforementioned IM presents the lowest attenuation over distance and almost maintains a constant value up to rupture distance values of 300km.

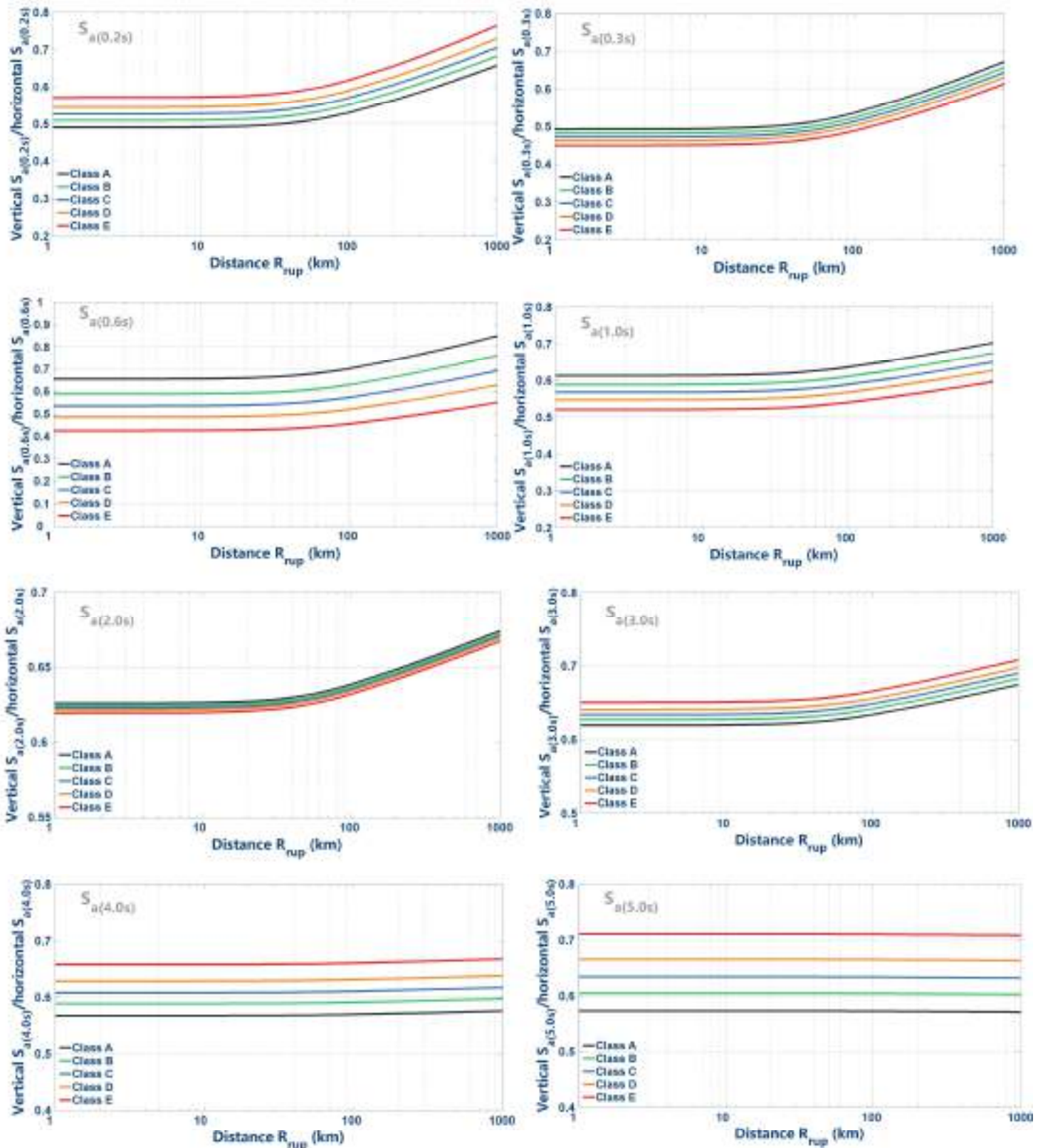


**Figure 41:** Comparison of the vertical to horizontal spectral acceleration ratios at 0.2, 0.3, 0.6, 1.0, 2.0, 3.0, 4.0, and 5.0s through different shear wave velocities ( $V_{S30}$ ) of 1200, 700, 437, 270 and 140m/s that correspond soil classes A, B, C, D, and E, respectively. These median ratios only resemble a 8.5  $M_w$  earthquake.

## CONCLUSIONS

- The proposed GMPE for interface events can predict both horizontal and vertical PGA and spectral accelerations at 0.2, 0.3, 0.6, 1.0, 2.0, 3.0, 4.0 and 5.0s for earthquakes in Peru, Chile and Ecuador and provides a better soil characterization compared to the Peruvian Seismic code (E030) that currently follows the American code ASCE-7-10.
- The GMPEs proposed by Abrahamson, Zhao, and Youngs for subduction events may underestimate the predicted PGA for earthquakes with  $M_w$  higher than 7.0 up to rupture distances values of 300km when it is compared to the proposed GMPE. Probabilistic hazard assessment for the Peruvian Territory utilized these foreign GMPEs to predict the PGA. This implies the current Peruvian seismic code (E030) may underestimate the predicted PGA considering that 45% of the earthquakes correspond to interface events as presented for the compiled dataset used in this study. So, interface events present a strong influence on the application of logic trees for PSHA applications. However, a stronger dataset should be collected from events higher than 7.0  $M_w$  to confirm the prediction capabilities of this new GMPE.
- The soil classification and site coefficient from the Peruvian Seismic code may underestimate the PGA for soil classes  $S_0$ ,  $S_2$  and  $S_3$  at around 12%, 12.5% and 15.4%, respectively. The site coefficient proposed in this study are consistent with the values suggested in the Chilean Seismic code (NCh 433) because its soil and  $V_{S30}$  classification are quite similar to this study.
- There is strong correlation between the  $T_m$  and the  $PGA/PGV$  ratio for both near- and far-source in two dimensional plots for the compiled data set used in this study that comprises both horizontal and vertical GMs. However, those parameters present the best correlation to earthquake magnitude, site-to-source distance, and site conditions by using the  $PGA/(PGV f_m)$  ratio as a predictor variable. This parameter is able to diminish the truncation effect of ground motion and other uncertainties that can be presented in the proxy variables.
- The regression models for the  $T_m$ , the  $PGA/PGV$  ratio, and the  $PGA/PGV f_m$  provide less uncertainty compared to PGA and spectral accelerations ( $S_a$ ). However, the  $PGA/PGV f_m$  ratio presents the lowest uncertainty compared to the other IMs. It may contribute to generate synthetic motions with different proxies such as  $M_w$  between 4 and 8,  $R_{rup}$  up to 1000km, and different site classification. So, proper synthetic motions may fill the gap where strong compiled data is not available such as the Peruvian subduction zone scenario.

- The vertical to horizontal PGA ratio of  $2/3$  suggested in the Peruvian Seismic code (E030) may overestimate the predicted PGA for vertical ground motions. However, this value may be reached if the structure undergoes a  $8.5 M_w$  earthquake located at rupture distances higher than 1000km and it is founded on soil class E. For critical scenarios this vertical to horizontal PGA ratio may be up to 0.55.
- The variability range of the  $PGA/PGV$  ratio encountered in this study indicates that any ground motion record from events up to  $M_w$  8.5 with  $R_{rup}$  values up to 100km subjected to any soil condition can be classified as high ranges for both horizontal and vertical GMs. Meanwhile, the ground motion records from events equal or higher than  $M_w$  8.5 with  $R_{rup}$  values higher than 100km for all soil classes may classify as intermediate ranges.
- Structures with fundamental periods between 0.1 and 0.70s are more vulnerable to experience resonance with earthquakes higher or equal than  $8.5 M_w$  over rupture distance up to 300km. This resonance can also be amplified if soil presents fundamental periods between that range. These critical conditions also apply for structures with vertical fundamental periods within that range. So, structures between this critical fundamental period range should be base isolated or equipped with linear or nonlinear dampers to avoid resonance.
- The  $PGA/(PGVf_m)$  ratio may vary between 0.77 and 0.38 considering earthquakes between 6 and 8  $M_w$  with rupture distances up to 1000km for both horizontal and vertical GMs on rock conditions. The same range variability applies to a  $M_w$  8.5 earthquake up to rupture distances of 1000km over different soil classes. Also, the  $PGA/(PGVf_m)$  ratio presents the lowest attenuation over distance and almost maintains a constant value up to rupture distances of 300km.

## RECOMMENDATIONS

- It is suggested improving the estimation of rupture distances through proper extended fault source characterization. This means obtaining the width ( $W$ ) and the length ( $L$ ) of the source, the fault dip ( $\delta$ ), and the site orientation. Also, the epicentral coordinates  $EV(Lat, Long)$  and the focal depth ( $D$ ) distribution should be well defined according to the indirect and direct approach.
- Further study to incorporate the truncation effect of ground motion at lower and higher rupture distances.
- Fully geophysical characterization of stations that lack this information so that the site-to site-residual against  $V_{S30}$  can be reduced.
- The Bayesian measurement error (BME) should be implemented on the development of GMPEs instead of the common maximum likelihood regression in order to reduce the  $\sigma$  value and get better predictor variables.
- It is better to unify one compiled dataset that comprises ground motion records from Peru, Chile, Ecuador, and Colombia. This will reduce the uncertainty in the predictor variables when developing a GMPE for interface, inslab and crustal events.



## REFERENCES

- [1] C. DeMets, R. G. Gordon, D. F. Argus, and S. Stein, “Current plate motions,” *Geophys. J. Int.*, vol. 101, no. 2, pp. 425–478, 1990, doi: <https://doi.org/10.1111/j.1365-246X.1990.tb06579.x>.
- [2] S. L. Bilek, “Seismicity along the South American subduction zone: Review of large earthquakes, tsunamis, and subduction zone complexity,” *Tectonophysics*, vol. 495, no. 1, pp. 2–14, 2010, doi: [10.1016/j.tecto.2009.02.037](https://doi.org/10.1016/j.tecto.2009.02.037).
- [3] K. Phillips and R. W. Clayton, “Structure of the subduction transition region from seismic array data in southern Peru,” *Geophys. J. Int.*, vol. 196, no. 3, pp. 1889–1905, 2014, doi: [10.1093/gji/ggt504](https://doi.org/10.1093/gji/ggt504).
- [4] C. M. Eakin, M. D. Long, L. S. Wagner, S. L. Beck, and H. Tavera, “Upper mantle anisotropy beneath Peru from SKS splitting: Constraints on flat slab dynamics and interaction with the Nazca Ridge,” *Earth Planet. Sci. Lett.*, vol. 412, no. 1, pp. 152–162, 2015, doi: [10.1016/j.epsl.2014.12.015](https://doi.org/10.1016/j.epsl.2014.12.015).
- [5] M. Chlieh *et al.*, “Interseismic coupling and seismic potential along the Central Andes subduction zone,” *J. Geophys. Res. Solid Earth*, vol. 116, no. 12, pp. 1–21, 2011, doi: [10.1029/2010JB008166](https://doi.org/10.1029/2010JB008166).
- [6] A. Lemoine, R. Madariaga, and J. Campos, “Slab-pull and slab-push earthquakes in the Mexican, Chilean and Peruvian subduction zones,” *Phys. Earth Planet. Inter.*, vol. 132, no. 1–3, pp. 157–175, 2002, doi: [10.1016/S0031-9201\(02\)00050-X](https://doi.org/10.1016/S0031-9201(02)00050-X).
- [7] S. Beck, S. Barrientos, E. Kausel, and M. Reyes, “Source characteristics of historic earthquakes along the central Chile subduction zone,” *J. South Am. Earth Sci.*, vol. 11, no. 2, pp. 115–129, 1998, doi: [10.1016/S0895-9811\(98\)00005-4](https://doi.org/10.1016/S0895-9811(98)00005-4).
- [8] S. Devlin, B. L. Isacks, M. E. Pritchard, W. D. Barnhart, and R. B. Lohman, “Depths and focal mechanisms of crustal earthquakes in the central Andes determined from teleseismic waveform analysis and InSAR,” *Tectonics*, vol. 31, no. 2, pp. 1–33, 2012, doi: [10.1029/2011TC002914](https://doi.org/10.1029/2011TC002914).
- [9] I. Santibáñez *et al.*, “Crustal faults in the Chilean Andes: Geological constraints and seismic potential,” *Andean Geol.*, vol. 46, no. 1, pp. 32–65, 2019, doi: [10.5027/andgeov46n1-3067](https://doi.org/10.5027/andgeov46n1-3067).
- [10] M. A. Rodríguez-Pascua *et al.*, “Did earthquakes strike Machu Picchu?,” *J. Seismol.*, vol. 24, no. 1, pp. 883–895, 2019, doi: [10.1007/s10950-019-09877-4](https://doi.org/10.1007/s10950-019-09877-4).
- [11] C. Benavente *et al.*, “Active transpressional tectonics in the Andean forearc of southern Peru quantified by <sup>10</sup>Be surface exposure dating of an active fault scarp,” *Adv. Earth Sp. Sci.*, vol. 36, no. 1, pp. 1662–1678, 2017, doi: [doi:10.1002/2017TC004523](https://doi.org/10.1002/2017TC004523).
- [12] E. A. Okal, J. C. Borrero, and C. E. Synolakis, “Evaluation of tsunami risk from regional earthquakes at Pisco, Peru,” *Bull. Seismol. Soc. Am.*, vol. 96, no. 5, pp. 1634–1648, 2006, doi: [10.1785/0120050158](https://doi.org/10.1785/0120050158).
- [13] H. Tavera and I. Bernal, “Distribucion espacial de areas de ruptura y lagunas sismicas en el borde oeste del Peru,” Lima, 2005. [Online]. Available: <https://repositorio.igp.gob.pe/handle/IGP/862>.



- [14] N. Pulido *et al.*, “Scenario source models and strong ground motion for future megaequakes: Application to Lima, central Peru,” *Bull. Seismol. Soc. Am.*, vol. 105, no. 1, pp. 368–386, 2015, doi: 10.1785/0120140098.
- [15] S. Das, I. D. Gupta, and V. K. Gupta, “A probabilistic seismic hazard analysis of Northeast India,” *Earthq. Spectra*, vol. 22, no. 1, pp. 1–27, 2006, doi: 10.1193/1.2163914.
- [16] K. Kayabali, “Modeling of seismic hazard for Turkey using the recent neotectonic data,” *Eng. Geol.*, vol. 63, no. 3–4, pp. 221–232, 2002, doi: 10.1016/S0013-7952(01)00082-5.
- [17] K. Kayabali and M. Akin, “Seismic hazard map of Turkey using the deterministic approach,” *Eng. Geol.*, vol. 69, no. 1–2, pp. 127–137, 2003, doi: 10.1016/S0013-7952(02)00272-7.
- [18] C. A. Cornell, “Engineering Seismic Risk Analysis,” vol. 58, no. 5, pp. 1583–1606, 1968.
- [19] G. F. Panza and J. Bela, “NDSHA: A new paradigm for reliable seismic hazard assessment,” *Eng. Geol.*, vol. 275, no. 1, pp. 1–14, 2020, doi: 10.1016/j.enggeo.2019.105403.
- [20] Z. Wang and M. Zhou, “Comment on ‘Why Do Modern Probabilistic Seismic-Hazard Analyses Often Lead to Increased Hazard Estimates?’ by Julian J. Bommer and Norman A. Abrahamson,” *Bull. Seismol. Soc. Am.*, vol. 97, no. 6, pp. 2212–2214, 2007, doi: 10.1785/0120070004.
- [21] R. K. McGuire, “Probabilistic seismic hazard analysis: Early history,” *Pacific Conf. Earthq. Eng.*, vol. 37, no. 1, pp. 329–338, 2008, doi: 10.1002/eqe.765.
- [22] M. D. Petersen *et al.*, “Seismic hazard, risk, and design for south america,” *Bull. Seismol. Soc. Am.*, vol. 108, no. 2, pp. 781–800, 2018, doi: 10.1785/0120170002.
- [23] R. Das *et al.*, “A probabilistic seismic hazard assessment of southern Peru and Northern Chile,” *Eng. Geol.*, vol. 271, no. 1, pp. 1–15, 2020, doi: 10.1016/j.enggeo.2020.105585.
- [24] Z. Aguilar, M. Roncal, and P. R., “Probabilistic seismic hazard assessment in the Peruvian Territory,” in *16th World Conference on Earthquake, Santiago de Chile, January 9th to 13th, 2017*, vol. Paper N° 3, no. S-A1464735658, pp. 1–10.
- [25] A. Petruccelli *et al.*, “Simultaneous Dependence of the Earthquake-Size Distribution on Faulting Style and Depth,” *Geophys. Res. Lett.*, vol. 46, no. 20, pp. 11044–11053, 2019, doi: 10.1029/2019GL083997.
- [26] O. Kulhanek, L. Persson, and P. Nuannin, “Variations of b-values preceding large earthquakes in the shallow subduction zones of Cocos and Nazca plates,” *J. South Am. Earth Sci.*, vol. 82, no. 1, pp. 207–214, 2018, doi: 10.1016/j.jsames.2018.01.005.
- [27] K. Tarbali and B. A. Bradley, “The effect of causal parameter bounds in PSHA-based ground motion selection,” *Earthq. Eng. Struct. Dyn.*, vol. 45, no. 1, pp. 1515–1535, 2016, doi: 10.1002/eqe.2721.
- [28] F. Scherbaum, E. Delavaud, and C. Riggelsen, “Model selection in seismic hazard analysis: An information-theoretic perspective,” *Bull. Seismol. Soc. Am.*, vol. 99, no. 6, pp. 3234–3247, 2009, doi: 10.1785/0120080347.

- [29] J. J. Bommer and F. Scherbaum, “The use and misuse of logic trees in probabilistic seismic hazard analysis,” *Earthq. Spectra*, vol. 24, no. 4, pp. 997–1009, 2008, doi: 10.1193/1.2977755.
- [30] J. Douglas, “Earthquake ground motion estimation using strong-motion records: A review of equations for the estimation of peak ground acceleration and response spectral ordinates,” *Earth-Science Rev.*, vol. 61, pp. 43–104, 2003, doi: 10.1016/S0012-8252(02)00112-5.
- [31] J. P. Stewart *et al.*, “Selection of ground motion prediction equations for the global earthquake model,” *Earthq. Spectra*, vol. 31, no. 1, pp. 19–45, 2015, doi: 10.1193/013013EQS017M.
- [32] C. Ji, A. Cabas, F. Cotton, M. Pilz, and D. Bindi, “Within-station variability in Kappa: Evidence of directionality effects,” *Bull. Seismol. Soc. Am.*, vol. 20, no. 20, pp. 1–13, 2020, doi: 10.1785/0120190253.
- [33] C. Cauzzi, E. Faccioli, M. Stupazzini, and M. Villani, “Including topographic amplification factors in GMPEs by means of 3D simulations of ground motions,” 2010, pp. 1–8.
- [34] S. Barani, M. Massa, S. Lovati, and D. Spallarossa, “Effects of surface topography on ground shaking prediction: Implications for seismic hazard analysis and recommendations for seismic design,” *Geophys. J. Int.*, vol. 197, pp. 1551–1565, 2014, doi: 10.1093/gji/ggu095.
- [35] R. Paolucci, “Amplification of earthquake ground motion by steep topographic irregularities,” *Earthq. Eng. Struct. Dyn.*, vol. 31, pp. 1831–1853, 2002, doi: 10.1002/eqe.192.
- [36] Y. Luo, X. Fan, R. Huang, Y. Wang, A. P. Yunus, and H. B. Havenith, “Topographic and near-surface stratigraphic amplification of the seismic response of a mountain slope revealed by field monitoring and numerical simulations,” *Eng. Geol.*, vol. 271, pp. 1–13, 2020, doi: 10.1016/j.enggeo.2020.105607.
- [37] J. N. Brune, “Tectonic Stress and the Spectra of Seismic Shear Waves from Earthquakes,” *J. Geophys. Res.*, vol. 75, no. 26, pp. 4997–5009, 1970.
- [38] F. Gallovič and Valentová, “Earthquake Stress Drops From Dynamic Rupture Simulations Constrained by Observed Ground Motions,” *Geophys. Res. Lett.*, vol. 47, pp. 1–10, 2020, doi: 10.1029/2019GL085880.
- [39] S. Akkar and O. Kale, “Developments in Ground Motion Predictive Models and Accelerometric Data Archiving in the Broader European Region,” *Geotech. Geol. Earthq. Eng.*, vol. 39, pp. 293–320, 2015, doi: 10.1007/978-3-319-16964-4\_1.
- [40] J. P. Stewart, D. M. Boore, E. Seyhan, and G. M. Atkinson, “NGA-West2 equations for predicting vertical-component PGA, PGV, and 5%-damped PSA from shallow crustal earthquakes,” *Earthq. Spectra*, vol. 32, no. 2, pp. 1005–1031, 2016, doi: 10.1193/072114EQS116M.

- [41] S. K. Kunnath, N. Abrahamson, Y. H. Chai, and Z. Yilmaz, “DEVELOPMENT OF GUIDELINES FOR INCORPORATION OF VERTICAL GROUND MOTION EFFECTS IN SEISMIC DESIGN OF HIGHWAY BRIDGES A Technical Report Submitted to the California Department of Transportation under Contract 59A0434 Department of Civil and Environmental Eng,” Sacramento, California, 2008.
- [42] B. Shrestha, “Vertical Ground Motions and Its Effect on Engineering Structures: a State-of-the-Art Review,” in *Proceeding of international seminar on hazard management for sustainable development: Kathmandu 29-30 November 2009*, 2009, pp. 190–202, doi: 10.13140/2.1.2863.6165.
- [43] Ministerio de vivienda y Construcción, “Norma Técnica E030 Diseño Sismorresistente.” pp. 1–80, 2019, [Online]. Available: [https://cdn.www.gob.pe/uploads/document/file/299950/d289856\\_opt.pdf](https://cdn.www.gob.pe/uploads/document/file/299950/d289856_opt.pdf) (in spanish).
- [44] W. K. Tso, T. J. Zhu, and A. C. Heidebrecht, “Engineering implication of ground motion A/V ratio,” *Soil Dyn. Earthq. Eng.*, vol. 11, no. 3, pp. 133–144, 1992, doi: 10.1016/0267-7261(92)90027-B.
- [45] T. J. Zhu, A. C. Heidebrecht, and W. K. Tso, “Effect of peak ground acceleration to velocity ratio on ductility demand of inelastic systems,” *Earthq. Eng. Struct. Dyn.*, vol. 16, pp. 63–79, 1988, doi: 10.1002/eqe.4290160106.
- [46] N. Naumoski, W. Tso, and A. Heidebrecht, “A selection of representative strong ground motion earthquake records having different A/V ratios. Report N° EERG 88/01,” Hamilton, Ontario, 1988.
- [47] R. Garg, J. P. Vernuri, and K. V. L. Subramaniam, “Correlating Peak Ground A/V Ratio with Ground Motion Frequency Content,” *Recent Adv. Struct. Eng.*, vol. 2, pp. 69–80, 2019, doi: [https://doi.org/10.1007/978-981-13-0365-4\\_6](https://doi.org/10.1007/978-981-13-0365-4_6).
- [48] E. A. Elhout, “The correlation between the ground motion intensity measure parameters of earthquakes,” *Asian J. Civ. Eng.*, vol. 21, pp. 829–840, 2020, doi: 10.1007/s42107-020-00243-1.
- [49] E. M. Rathje, F. Faraj, S. Russell, and J. D. Bray, “Empirical Relationships for Frequency Content Parameters of Earthquake Ground Motions,” *Earthq. Spectra*, vol. 20, no. 1, pp. 119–144, 2004, doi: 10.1193/1.1643356.
- [50] S. Yaghmaei-Sabegh, “Frequency-content parameters of the ground motions from the 2017 M w 7.3 Ezgeleh earthquake in Iran,” *Nat. Hazards*, vol. 101, pp. 349–365, 2020, doi: 10.1007/s11069-020-03876-2.
- [51] W. Du, “Empirical Correlations of Frequency-Content Parameters of Ground Motions with Other Intensity Measures,” *J. Earthq. Eng.*, vol. 23, no. 7, pp. 1073–1091, 2019, doi: 10.1080/13632469.2017.1342303.
- [52] M. C. Arango, F. O. Strasser, J. J. Bommer, R. Boroschek, D. Comte, and H. Tavera, “A strong-motion database from the Peru-Chile subduction zone,” *J. Seismol.*, vol. 15, pp. 19–41, 2011, doi: 10.1007/s10950-010-9203-x.
- [53] L. Casaverde and J. Vargas, “Zonificación Sísmica del Perú. II Seminario Latinoamericano de Ingeniería Sísmo-Resistente, Organización de Estados Americanos y Pontificia Universidad Católica del Perú. (in spanish).” 1980.

- [54] J. Chavez, “Leyes de atenuación para aceleraciones espectrales en el Perú, Undergraduate degree dissertation, Civil Engineering Department, National University of Engineering. Lima, Perú. (in spanish).” 2006.
- [55] F. Cotton, F. Scherbaum, J. J. Bommer, and H. Bungum, “Criteria for selecting and adjusting ground-motion models for specific target regions: Application to central Europe and rock sites,” *J. Seismol.*, vol. 10, pp. 137–156, 2006, doi: 10.1007/s10950-005-9006-7.
- [56] O. Charca, C. Gamarra, and D. Parra, “Selection of Subduction Ground Motion Prediction Equations for Seismic Hazard Assessment in Peru. Geotechnical Engineering in the XXI Century: Lessons learned and future challenges,” vol. 1, no. November. López - Acosta et al (Eds), pp. 1981–1990, 2019, doi: 10.3233/STAL190258.
- [57] F. Scherbaum, F. Cotton, and P. Smit, “On the use of response spectral-reference data for the selection and ranking of ground-motion models for seismic-hazard analysis in regions of moderate seismicity: The case of rock motion,” *Bull. Seismol. Soc. Am.*, vol. 94, no. 6, pp. 2164–2185, 2004, doi: 10.1785/0120030147.
- [58] N. Abrahamson, N. Gregor, and K. Addo, “BC hydro ground motion prediction equations for subduction earthquakes,” *Earthq. Spectra*, vol. 32, no. 1, pp. 23–44, 2016, doi: 10.1193/051712EQS188MR.
- [59] J. X. Zhao *et al.*, “Ground-motion prediction equations for subduction interface earthquakes in Japan using site class and simple geometric attenuation functions,” *Bull. Seismol. Soc. Am.*, vol. 106, no. 4, pp. 1518–1534, 2016, doi: 10.1785/0120150034.
- [60] J. X. Zhao *et al.*, “Ground-motion prediction equations for subduction slab earthquakes in Japan using site class and simple geometric attenuation functions,” *Bull. Seismol. Soc. Am.*, vol. 106, no. 4, pp. 1535–1551, 2016, doi: 10.1785/0120150056.
- [61] R. R. Youngs, S. J. Chiou, W. J. Silva, and J. R. Humphrey, “Strong ground motion attenuation relationships for subduction zone earthquakes,” *Seismol. Res. Lett.*, vol. 68, no. 1, pp. 58–73, 1997, doi: 10.1785/gssrl.68.1.58.
- [62] J. Douglas, D. Bertil, A. Roullé, P. Dominique, and P. Jousset, “A preliminary investigation of strong-motion data from the French Antilles,” *J. Seismol.*, vol. 10, no. 3, pp. 271–299, 2006, doi: 10.1007/s10950-006-9016-0.
- [63] S. Drouet, F. Scherbaum, F. Cotton, and A. Souriau, “Selection and ranking of ground motion models for seismic hazard analysis in the Pyrenees,” *J. Seismol.*, vol. 11, no. 1, pp. 87–100, 2007, doi: 10.1007/s10950-006-9039-6.
- [64] E. Hintersberger, F. Scherbaum, and S. Hainzl, “Update of likelihood-based ground-motion model selection for seismic hazard analysis in western central Europe,” *Bull. Earthq. Eng.*, vol. 5, no. 1, pp. 1–16, 2007, doi: 10.1007/s10518-006-9018-x.
- [65] P. J. Stafford, F. O. Strasser, and J. J. Bommer, “An evaluation of the applicability of the NGA models to ground-motion prediction in the Euro-Mediterranean region,” *Bull. Earthq. Eng.*, vol. 6, no. 2, pp. 149–177, 2008, doi: 10.1007/s10518-007-9053-2.
- [66] J. Douglas and R. Mohais, “Comparing predicted and observed ground motions from subduction earthquakes in the Lesser Antilles,” *J. Seismol.*, vol. 13, no. 4, pp. 577–587, 2009, doi: 10.1007/s10950-008-9150-y.

- [67] C. Beauval *et al.*, “On the testing of ground-motion prediction equations against small-magnitude data,” *Bull. Seismol. Soc. Am.*, vol. 102, no. 5, pp. 1994–2007, 2012, doi: 10.1785/0120110271.
- [68] N. M. Kuehn and N. A. Abrahamson, “The effect of uncertainty in predictor variables on the estimation of ground-motion prediction equations,” *Bull. Seismol. Soc. Am.*, vol. 108, no. 1, pp. 358–370, 2018, doi: 10.1785/0120170166.
- [69] J. E. Alva, “Foro: Importancia de las Rederred Acelerográficas para la definición de Parámetros de Diseño Sismorresistente,” 2019. <http://www.jorgealvahurtado.com/> (in spanish) (accessed Aug. 29, 2020).
- [70] Z. Aguilar, J. Tarazona, L. Vergaray, and J. Barrantes, “Site response analysis and its comparison with the peruvian seismic design spectrum,” *Tecnia*, vol. 29, no. 2, pp. 91–97, 2019.
- [71] F. Leyton *et al.*, “Geophysical characterization of the chilean seismological stations: First results,” *Seismol. Res. Lett.*, vol. 89, no. 2A, pp. 519–525, 2018, doi: 10.1785/0220170156.
- [72] S. Quispe, K. Chimoto, H. Yamanaka, H. Tavera, F. Lazares, and Z. Aguilar, “Estimation of s-wave velocity profiles at lima city, peru using microtremor arrays,” *J. Disaster Res.*, vol. 9, no. 6, pp. 931–938, 2014, doi: 10.20965/jdr.2014.p0931.
- [73] D. Calderon, T. Sekiguchi, Z. Aguilar, F. Lazares, and S. Nakai, “DYNAMIC CHARACTERISTICS OF THE SURFACE SOILS IN LIMA, PERU,” in *8th International Conference on Urban Earthquake Engineering March 7-8, 2011, Tokyo Institute of Technology, Tokyo, Japan*, 2011, pp. 537–542.
- [74] I. Bernal, H. Tavera, W. Sulla, L. Arredondo, and J. Oyola, “Geomorphology Characterization of Ica Basin and Its Influence on the Dynamic Response of Soils for Urban Seismic Hazards in Ica, Peru,” *Int. J. Geophys.*, vol. 2018, no. ID 9434251, pp. 1–12, 2018, doi: 10.1155/2018/9434251.
- [75] A. Cortez Flores, “Site Response of the 2001 Southern Peru Earthquake.,” 2004.
- [76] J. E. Alva, “Caracterización dinámica de los suelos en la ciudad de Tacna,” in *Congreso Nacional de Ingeniería Civil 2015, Huaraz, Peru*, 2015, pp. 1–8.
- [77] F. Leyton, C. Pastén, S. Ruiz, B. Idini, and F. Rojas, “Empirical site classification of CSN network using strong-motion records,” *Seismol. Res. Lett.*, vol. 89, no. 2A, pp. 512–518, 2018, doi: 10.1785/0220170167.
- [78] A. Becerra, L. Podestá, R. Monetta, E. Sáez, F. Leyton, and G. Yañez, “Seismic microzoning of Arica and Iquique, Chile,” *Nat. Hazards*, vol. 79, pp. 567–586, 2015, doi: 10.1007/s11069-015-1863-y.
- [79] C. Beauval *et al.*, “Comparison of observed ground-motion attenuation for the 16 April 2016 Mw 7.8 Ecuador Megathrust earthquake and its two largest aftershocks with existing ground-motion prediction equations,” *Seismol. Res. Lett.*, vol. 88, no. 2, pp. 287–299, 2017, doi: 10.1785/0220160150.



- [80] J. C. Singaicho, L. Aurore, C. Viracucha, M. Ruiz, and Area de Sismología - Instituto Geofísico, “Observaciones del sismo del 16 de Abril de 2016 de magnitud Mw 7.8, Intensidades y Aceleraciones. Sometido a la Revista Politécnica.” 2016. [Online]. Available: <https://www.igeppn.edu.ec/servicios/noticias/1324-informe-sismico-especial-n-18-2016> (in spanish).
- [81] Ministerio de Desarrollo Urbano y Vivienda and Cámara de la Industria de la Construcción, “NEC Norma Ecuatoriana de la Construcción,” *Norma Ecuatoriana de la Construcción*, pp. 1–42, 2015, [Online]. Available: <http://www.indeci.gob.pe/proyecto58530/objetos/archivos/20110606102841.pdf>.
- [82] G. M. Atkinson and D. M. Boore, “Empirical Ground-Motion Relations for Subduction Zone Earthquakes and Their Application to Cascadia and Other Regions,” *Bull. Seismol. Soc. Am.*, vol. 93, no. 4, pp. 1703–1729, 2003, doi: 10.1785/0120080108.
- [83] G. A. Montalva, N. Bastías, and A. Rodriguez-Marek, “Ground-motion prediction equation for the Chilean subduction zone,” *Bull. Seismol. Soc. Am.*, vol. 107, no. 2, pp. 901–911, 2017, doi: 10.1785/0120160221.
- [84] J. C. Thouret, J. Davila, and J. P. Eissen, “Largest explosive eruption in historical times in the Andes at Huaynaputina volcano, A.D. 1600, southern Peru,” *Geology*, vol. 27, pp. 435–438, 1999, doi: 10.1130/0091-7613(1999)027<0435:LEEIHT>2.3.CO;2.
- [85] M. R. Degg and D. K. Chester, “Seismic and volcanic hazards in Peru: Changing attitudes to disaster mitigation,” *Geogr. J.*, vol. 171, no. 2, pp. 125–145, 2005, doi: 10.1111/j.1475-4959.2005.00155.x.
- [86] Bulletin of Volcanology Editor-in-Chief, “New explosive eruption at Ubinas volcano (Peru),” *Bull. Volcanol.*, vol. 81, p. 49, 2019, doi: 10.1007/s00445-019-1315-8.
- [87] S. Barrientos and National Seismological Center (CNS) Team, “The Seismic Network of Chile,” *Seismol. Res. Lett.*, vol. 89, no. 2A, pp. 467–474, 2018, doi: 10.1785/0220160195.
- [88] I. G. from E. Ecuador and Escuela Politecnica Nacional, “Red Nacional de Simógrafos (RENSIG),” 2020. <https://www.igeppn.edu.ec/> (accessed Aug. 29, 2020).
- [89] E. Contreras-Reyes, P. Muñoz-Linford, V. Cortés-Rivas, J. P. Bello-González, J. A. Ruiz, and A. Krabbenhoft, “Structure of the Collision Zone Between the Nazca Ridge and the Peruvian Convergent Margin: Geodynamic and Seismotectonic Implications,” *Tectonics*, vol. 38, pp. 3416–3435, 2019, doi: 10.1029/2019TC005637.
- [90] A. Kumar *et al.*, “Seismicity and state of stress in the central and southern Peruvian flat slab,” *Earth Planet. Sci. Lett.*, vol. 441, pp. 71–80, 2016, doi: 10.1016/j.epsl.2016.02.023.
- [91] A. Margirier, L. Audin, X. Robert, A. Pêcher, and S. Schwartz, “Stress field evolution above the Peruvian flat-slab (Cordillera Blanca, northern Peru),” *J. South Am. Earth Sci.*, vol. 77, pp. 58–69, 2017, doi: 10.1016/j.jsames.2017.04.015.
- [92] W. Liu and H. Yao, “Rupture Process of the 26 May 2019 Mw 8.0 Northern Peru Intermediate-Depth Earthquake and Insights Into Its Mechanism,” *Geophys. Res. Lett.*, vol. 47, pp. 1–10, 2020, doi: 10.1029/2020GL087167.



- [93] V. C. Manea *et al.*, “A review of the geodynamic evolution of flat slab subduction in Mexico, Peru, and Chile,” *Tectonophysics*, vol. 695, pp. 27–52, 2017, doi: 10.1016/j.tecto.2016.11.037.
- [94] C. N. Garzzone *et al.*, “Tectonic Evolution of the Central Andean Plateau and Implications for the Growth of Plateaus,” *Annu. Rev. Earth Planet. Sci.*, vol. 45, pp. 529–559, 2017, doi: 10.1146/annurev-earth-063016-020612.
- [95] B. T. Bishop *et al.*, “Causes and consequences of flat-slab subduction in southern Peru,” *Geosphere*, vol. 13, no. 5, pp. 1392–1407, 2017, doi: 10.1130/GES01440.1.
- [96] L. S. Wagner and E. A. Okal, “The Pucallpa Nest and its constraints on the geometry of the Peruvian Flat Slab,” *Tectonophysics*, vol. 762, pp. 97–108, 2019, doi: 10.1016/j.tecto.2019.04.021.
- [97] H. Lim, Y. H. Kim, R. W. Clayton, and C. H. Thurber, “Seismicity and structure of Nazca Plate subduction zone in southern Peru,” *Earth Planet. Sci. Lett.*, vol. 498, pp. 334–347, 2018, doi: 10.1016/j.epsl.2018.07.014.
- [98] G. P. Hayes *et al.*, “Slab2, a comprehensive subduction zone geometry model,” *Science (80-. )*, vol. 362, pp. 58–61, 2018, doi: 10.1126/science.aat4723.
- [99] M. R. Falamarz-Sheikhabadi, A. Zerva, and M. Ghafory-Ashtiany, “Mean absolute input energy for in-plane vibrations of multiple-support structures subjected to non-stationary horizontal and rocking components,” *Probabilistic Eng. Mech.*, vol. 45, pp. 87–101, 2016, doi: 10.1016/j.probenmech.2016.03.001.
- [100] S. Akkar and J. J. Bommer, “Influence of long-period filter cut-off on elastic spectral displacements,” *Earthq. Eng. Struct. Dyn.*, vol. 35, pp. 1145–1165, 2006, doi: 10.1002/eqe.577.
- [101] A. Zerva, H. Morikawa, and S. Sawada, “Criteria for processing response-spectrum compatible seismic accelerations simulated via spectral representation,” *Earthquakes Struct.*, vol. 3, no. 3, pp. 341–363, 2012, doi: 10.12989/eas.2012.3.3.\_4.341.
- [102] D. M. Boore and J. J. Bommer, “Processing of strong-motion accelerograms: Needs, options and consequences,” *Soil Dyn. Earthq. Eng.*, vol. 25, pp. 93–115, 2005, doi: 10.1016/j.soildyn.2004.10.007.
- [103] V. Graizer, “Tilts in strong ground motion,” *Bull. Seismol. Soc. Am.*, vol. 96, no. 6, pp. 2090–2102, 2006, doi: 10.1785/0120060065.
- [104] M. Zaré and P. Y. Bard, “Strong motion dataset of Turkey: Data processing and site classification,” *Soil Dyn. Earthq. Eng.*, vol. 22, pp. 703–718, 2002, doi: 10.1016/S0267-7261(02)00028-3.
- [105] D. M. Boore, C. D. Stephens, and W. B. Joyner, “Comments on baseline correction of digital strong-motion data: Examples from the 1999 Hector Mine, California, earthquake,” *Bull. Seismol. Soc. Am.*, vol. 92, no. 4, pp. 1543–1560, 2002, doi: 10.1785/0120000926.
- [106] M. R. Falamarz-Sheikhabadi and A. Zerva, “Optimal Corner Frequency in High-Pass Filtering of Strong Ground Motions and Its Effect on Seismic Intensity,” *J. Earthq. Eng.*, vol. 1, pp. 1–31, 2019, doi: 10.1080/13632469.2019.1605947.

- [107] A. J. Kappos, “Sensitivity of Calculated Inelastic Seismic Response To Input Motion Characteristics,” in *4th U.S. National Conference on Earthquake Engineering, May 20 - 24, 1990, Palm Springs, California, 1990*, vol. 2, pp. 25–34.
- [108] J. Jones, E. Kalkan, and C. Stephens, “Processing and review interface for strong motion data (PRISM) software, version 1.0.0—Methodology and automated processing,” Reston, Virginia, 2017. doi: 10.3133/ofr20171008.
- [109] Siemens, “Window Types: Hanning, Flattop, Uniform, Tukey, and Exponential,” *online*, 2019. <https://community.sw.siemens.com/s/article/window-types-hanning-flattop-uniform-tukey-and-exponential> (accessed Aug. 20, 2020).
- [110] X. Jin, Q. Ma, and S. you Li, “Comparison of four numerical methods for calculating seismic response of SDOF system,” in *13th World Conference on Earthquake Engineering Vancouver, B.C., Canada August 1-6, 2004*, 2003, vol. Paper N° 2, no. 1, pp. 1–11.
- [111] N. M. Newmark, “A method of computation for structural dynamics,” *J. Eng. Mech.*, vol. 85, pp. 67–94, 1959.
- [112] N. C. Nigan and P. C. Jennings, “Calculation of response spectra from strong motion,” *Bull. Seismol. Soc. Am.*, vol. 59, no. 2, pp. 909–922, 1969.
- [113] V. W. Lee, “Efficient algorithm for computing displacement, velocity and acceleration responses of an oscillator to arbitrary ground motion,” *Soil Dyn. Earthq. Eng.*, vol. 9, no. 6, pp. 288–300, 1990, doi: 10.1016/S0267-7261(05)80015-6.
- [114] B. Wu, Q. Wang, H. Bao, and J. Ou, “Analysis and Preliminary Experimental Study on Central Difference Method for Real-time Substructure Testing,” *Report: Science and Technology of China*, 2005. <https://pdfs.semanticscholar.org/d383/9987a57ac0a8bceb2840e2d06e5c53493ab7.pdf> (accessed Aug. 20, 2020).
- [115] C. Liao, W. Ding, and F. Li, “An improved algorithm for numerical calculation of seismic response spectra,” *Geod. Geodyn.*, vol. 7, no. 2, pp. 148–155, 2016, doi: 10.1016/j.geog.2016.04.005.
- [116] E. M. Rathje, N. A. Abrahamson, and J. D. Bray, “Simplified Frequency Content Estimates of Earthquake Ground Motions,” *J. Geotech. GEOENVIRONMENTAL Eng.*, vol. 124, no. 2, pp. 150–159, 1998, doi: [https://doi.org/10.1061/\(ASCE\)1090-0241\(1998\)124:2\(150\)](https://doi.org/10.1061/(ASCE)1090-0241(1998)124:2(150)).
- [117] C. F. Richter, “An Instrumental Earthquake Magnitude Scale,” *Bull. Seismol. Soc. Am.*, vol. 25, no. 1–32, p. 348, 1935, doi: 10.2307/1779766.
- [118] L. K. Hutton and D. M. Boore, “The ML Scale in Southern California,” *Bull. Seismol. Soc. Am.*, vol. 77, no. 6, pp. 2074–2094, 1987.
- [119] H. Kanamori, “The Energy Release in Great Earthquakes,” *J. Geophys. Res.*, vol. 82, no. 20, pp. 2981–2987, 1977, doi: <https://doi.org/10.1029/JB082i020p02981>.
- [120] T. C. Hanks and H. Kanamori, “A Moment Magnitude Scale,” *J. Geophys. Res.*, vol. 84, pp. 2348–2350, 1979, doi: <https://doi.org/10.1029/JB084iB05p02348>.
- [121] G. M. Atkinson and T. C. Hanks, “A high-frequency magnitude scale A High-Frequency Magnitude Scale,” *Bull. Seismol. Soc. Am.*, vol. 85, no. 3, pp. 825–833, 1995.

- [122] D. Bindi, D. Spallarossa, M. Picozzi, D. Scafidi, and F. Cotton, “Impact of magnitude selection on aleatory variability associated with ground-motion prediction equations: Part I—local, energy, and moment magnitude calibration and stress-drop variability in central Italy,” *Bull. Seismol. Soc. Am.*, vol. 108, no. 3, pp. 1427–1442, 2018, doi: 10.1785/0120170356.
- [123] C. C. Tang, L. Zhu, and R. Huang, “Empirical Mw-ML, Mb, and Ms conversions in Western China,” *Bull. Seismol. Soc. Am.*, vol. 106, no. 6, pp. 2614–2623, 2016, doi: 10.1785/0120160148.
- [124] N. A. Abrahamson and K. M. Shedlock, “Overview,” *Seismol. Res. Lett.*, vol. 68, no. 1, pp. 9–23, 1997, doi: <https://doi.org/10.1785/gssrl.68.1.9>.
- [125] H. Kanamori, J. Mori, E. Hauksson, T. H. Heaton, K. Hutton, and L. M. Jones, “Determination of Earthquake Energy Release and ML using Terrascope,” *Bull. Seismol. Soc. Am.*, vol. 83, no. 2, pp. 330–346, 1993, [Online]. Available: <https://resolver.caltech.edu/CaltechAUTHORS:20121121-113646769>.
- [126] G. M. Atkinson and D. M. Boore, “Some comparisons between recent ground-motion relations,” *Seismol. Res. Lett.*, vol. 68, no. 1, pp. 24–38, 1997, doi: 10.1785/gssrl.68.1.24.
- [127] B. Tavakoli, F. Sedaghati, and S. Pezeshk, “An analytical effective point-source-based distance-conversion approach to mimic the effects of extended faults on seismic hazard assessment,” *Bull. Seismol. Soc. Am.*, vol. 108, no. 2, pp. 742–760, 2018, doi: 10.1785/0120170171.
- [128] F. Scherbaum, J. Schmedes, and F. Cotton, “On the conversion of source-to-site distance measures for extended earthquake source models,” *Bull. Seismol. Soc. Am.*, vol. 94, no. 3, pp. 1053–1069, 2004, doi: 10.1785/0120030055.
- [129] S. Das and C. H. Scholz, “Why large earthquakes do not nucleate at shallow depths,” *Nature*, vol. 305, pp. 621–623, 1983, doi: 10.1038/305621a0.
- [130] J. Mori and R. E. Abercrombie, “Depth dependence of earthquake frequency-magnitude distributions in California: Implications for rupture initiation,” *J. Geophys. Res. Solid Earth*, vol. 102, no. B7, pp. 15081–15090, 1997, doi: 10.1029/97jb01356.
- [131] F. O. Strasser, A. M. C., and J. J. Bommer, “Scaling of the Source Dimensions of Interface and Intraslab Subduction-zone Earthquakes with Moment Magnitude,” *Seismol. Res. Lett.*, vol. 81, no. 6, pp. 941–950, 2010, doi: 10.1785/gssrl.81.6.941.
- [132] H. Jang, Y. H. Kim, H. Lim, and R. W. Clayton, “Seismic attenuation structure of southern Peruvian subduction system,” *Tectonophysics*, vol. 771, pp. 1–12, 2019, doi: 10.1016/j.tecto.2019.228203.
- [133] H. Tavera and E. Buforn, “Source mechanism of earthquakes in Peru,” *J. Seismol.*, vol. 5, no. 4, pp. 519–539, 2001, doi: 10.1023/A:1012027430555.
- [134] D. M. Boore, “Comparing stochastic point-source and finite-source ground-motion simulations: SMSIM and EXSIM,” *Bull. Seismol. Soc. Am.*, vol. 99, no. 6, pp. 3202–3216, 2009, doi: 10.1785/0120090056.
- [135] D. M. Boore, C. Di Alessandro, and N. A. Abrahamson, “A generalization of the double-corner-frequency source spectral model and its use in the SCEC BBP validation exercise,” *Bull. Seismol. Soc. Am.*, vol. 104, no. 5, pp. 2387–2398, 2014, doi: 10.1785/0120140138.

- [136] E. Yenier and G. M. Atkinson, “Equivalent point-source modeling of moderate-to-large magnitude earthquakes and associated ground-motion saturation effects,” *Bull. Seismol. Soc. Am.*, vol. 104, no. 3, pp. 1458–1478, 2014, doi: 10.1785/0120130147.
- [137] G. M. Atkinson and W. Silva, “Stochastic modeling of California ground motions,” *Bull. Seismol. Soc. Am.*, vol. 90, no. 2, pp. 255–274, 2000, doi: 10.1785/0119990064.
- [138] B. Halldorsson and A. S. Papageorgiou, “Calibration of the specific barrier model to earthquakes of different tectonic regions,” *Bull. Seismol. Soc. Am.*, vol. 95, no. 4, pp. 1276–1300, 2005, doi: 10.1785/0120040157.
- [139] A. A. Skarlatoudis, C. B. Papazachos, B. N. Margaris, C. Ventouzi, and I. Kalogeras, “Ground-motion prediction equations of intermediate-depth earthquakes in the Hellenic arc, southern Aegean subduction area,” *Bull. Seismol. Soc. Am.*, vol. 103, no. 3, pp. 1952–1968, 2013, doi: 10.1785/0120120265.
- [140] J. Douglas, “Ground-motion prediction equations 1964-2010, NCREE Report N° NCREE-17-009,” Berkeley, CA., 2011. [Online]. Available: [https://peer.berkeley.edu/sites/default/files/webpeer-2011-102-john\\_douglas\\_-\\_published\\_jointly\\_by\\_brgm.pdf](https://peer.berkeley.edu/sites/default/files/webpeer-2011-102-john_douglas_-_published_jointly_by_brgm.pdf).
- [141] S. Sabermahani and P. Ashjanas, “Sensitivity analysis of ground motion prediction equation using next generation attenuation dataset,” *Geod. Geodyn.*, vol. 11, no. 1, pp. 40–45, 2020, doi: 10.1016/j.geog.2019.09.004.
- [142] A. H. Alavi and A. H. Gandomi, “Prediction of principal ground-motion parameters using a hybrid method coupling artificial neural networks and simulated annealing,” *Comput. Struct.*, vol. 89, no. 23–24, pp. 2176–2194, 2011, doi: 10.1016/j.compstruc.2011.08.019.
- [143] M. Segou and N. Voulgaris, “The use of stochastic optimization in ground motion prediction,” *Earthq. Spectra*, vol. 29, no. 1, pp. 283–308, 2013, doi: 10.1193/1.4000098.
- [144] N. A. Abrahamson and R. R. Youngs, “A stable algorithm for regression analyses using the random effects model,” *Bull. Seismol. Soc. Am.*, vol. 82, no. 1, pp. 505–510, 1992.
- [145] Z. Wang, I. Zentner, and E. Zio, “Accounting for uncertainties of magnitude-and site-related parameters on neural network-computed ground-motion prediction equations,” *Bull. Seismol. Soc. Am.*, vol. 110, no. 2, pp. 629–646, 2020, doi: 10.1785/0120180309.
- [146] F. Khosravikia, P. Clayton, and Z. Nagy, “Artificial neural network-based framework for developing ground-motion models for natural and induced earthquakes in Oklahoma, Kansas, and Texas,” *Seismol. Res. Lett.*, vol. 20, no. 20, pp. 1–10, 2019, doi: 10.1785/0220180218.
- [147] J. Dhanya and S. T. G. Raghukanth, “Ground Motion Prediction Model Using Artificial Neural Network,” *Pure Appl. Geophys.*, vol. 175, pp. 1035–1064, 2018, doi: 10.1007/s00024-017-1751-3.
- [148] Y. Fukushima and T. Tanaka, “A new attenuation relation for peak horizontal acceleration of strong earthquake ground motion in Japan,” *Bull. Seismol. Soc. Am.*, vol. 80, no. 4, pp. 757–783, 1990.
- [149] W. B. Joyner and D. M. Boore, “Methods for regression analysis of strong-motion data,” *Bull. - Seismol. Soc. Am.*, vol. 83, no. 2, pp. 469–487, 1993.

- [150] S. H. Chao and Y. H. Chen, “A novel regression analysis method for randomly truncated strong-motion data,” *Earthq. Spectra*, vol. 35, no. 2, pp. 977–1001, 2019, doi: 10.1193/022218EQS044M.
- [151] N. A. Abrahamson, W. J. Silva, and R. Kamai, “Summary of the ASK14 ground motion relation for active crustal regions,” *Earthq. Spectra*, vol. 30, no. 3, pp. 1025–1055, 2014, doi: 10.1193/070913EQS198M.
- [152] P. L. Bragato, “Regression analysis with truncated samples and its application to ground-motion attenuation studies,” *Bull. Seismol. Soc. Am.*, vol. 94, no. 4, pp. 1369–1378, 2004, doi: 10.1785/012003083.
- [153] B. S. J. Chiou and R. R. Youngs, “Update of the Chiou and Youngs NGA model for the average horizontal component of peak ground motion and response spectra,” *Earthq. Spectra*, vol. 30, no. 3, pp. 1117–1153, 2014, doi: 10.1193/072813EQS219M.
- [154] W. B. Joyner and D. M. Boore, “Peak horizontal acceleration and velocity from strong-motion records including records from the 1979 imperial valley, California, earthquake,” *Bull. Seismol. Soc. Am.*, vol. 71, no. 6, pp. 2011–2038, 1981, [Online]. Available: file://c:/Documents and Settings/Jack/My Documents/1 Research/EndNote/References.Data/PDF/2011-0278624768/2011.pdf%5Cnhttp://www.bssaonline.org/cgi/content/abstract/71/6/2011.
- [155] K. L. McLaughlin, “Maximum Likelihood Estimation of Strong-Motion Attenuation Relationships,” *Earthq. Spectra*, vol. 83, pp. 469–487, 1991, doi: https://doi.org/10.1193/1.1585628.
- [156] N. A. Abrahamson and J. J. Litehiser, “Attenuation of Vertical Peak Acceleration,” *Bull. Seismol. Soc. Am.*, vol. 79, no. 3, pp. 549–580, 1989.
- [157] P. Anbazhagan, A. Kumar, and T. G. Sitharam, “Ground motion prediction equation considering combined dataset of recorded and simulated ground motions,” *Soil Dyn. Earthq. Eng.*, vol. 53, pp. 92–108, 2013, doi: 10.1016/j.soildyn.2013.06.003.
- [158] K. W. Campbell, “Near-source attenuation of peak horizontal acceleration,” *Bull. Seismol. Soc. Am.*, vol. 71, no. 6, pp. 2039–2070, 1981.
- [159] R. N. Iyengar and S. T. G. Raghu Kanth, “Attenuation of Strong Ground Motion in Peninsular India,” *Seismol. Res. Lett.*, vol. 75, no. 4, pp. 530–540, 2004.
- [160] W. Joyner and D. M. Boore, “Measurement, characterization, and prediction of strong ground motion,” in *Earthquake Engineering & Soil Dynamics II GT Div/ASCE, Park City, Utah, June 27-30, 1988*, 1988, pp. 43–102.
- [161] A. Kumar, H. Mittal, R. Kumar, and R. S. Ahluwalia, “Empirical Attenuation relationship for Peak Ground Horizontal Acceleration for North-East Himalaya,” *Vietnam J. Earth Sci.*, vol. 39, no. 1, pp. 47–57, 2017, doi: 10.15625/0866-7187/39/1/9183.
- [162] M. L. Sharma, “Attenuation relationship for estimation of peak ground horizontal acceleration using data from strong-motion arrays in India,” *Bull. Seismol. Soc. Am.*, vol. 88, no. 4, pp. 1063–1069, 1998.
- [163] A. C. Rencher and G. B. Schaalje, *Linear models in statistics*, Second Edi., vol. 38, no. 07. Hoboken, New Jersey, 2008.

- [164] M. Mousavi, A. Azarbakht, S. Rahpeyma, and A. Farhadi, “On the Application of Genetic Programming for New Generation of Ground Motion Prediction Equations,” in *Handbook of Genetic Programming Applications*, R. C. (eds) Gandomi A., Alavi A., Ed. Springer, 2015, pp. 1–593.
- [165] S. L. Kramer, *Geotechnical Earthquake Engineering*. Englewood Cliffs, NJ.: Prentice Hall Inc., 1996.
- [166] A. K. Chopra, *Dynamics of Structures: Theory and Application to Earthquake Engineering*. Englewood Cliffs, NJ.: Prentice Hall Inc., 2001.



**A.1. LIST OF STATIONS**

Six networks were considered in this study that comprise five-hundred and twenty-three (523) stations. Nine-teen (19) stations belong to the National Accelerometer Network of the Department of Civil Engineering (RENADIC) from Chile, one-hundred and seventy-seven (177) are monitored by the Chilean National Seismological Centre (CSN), seventy-two (72) stations belong to the Japan- Peru Centre for Seismic Research and Disaster Mitigation (CISMID) from Peru, one-hundred and sixty (160) stations are monitored by the Geophysical Institute of Peru (IGP), seventy-four (74) stations belong to the Graduate Faculty of Civil Engineering of the National University of Engineering (FIC-UNI), and twenty-one (21) stations belong to the National Accelerometer Network (RENAC) from Ecuador. The following table summarizes the information from all the stations. The network name, the station name, the latitude, and longitude are given in column 1, 2, 3 and 4, respectively. Meanwhile, column 5 indicates the  $V_{S30}$  data provided by the United States Geological Survey (USGS). Besides, column 6 provides the  $V_{S3}$  obtained from different investigations that performed geophysical characterization of some stations as described in the Introduction Section. Column 7 indicates the final  $V_{S30}$  used in each station. To do so, where no  $V_{S30}$  data was provided from previous investigations (Column 6), the approximate  $V_{S30}$  value from the USGS prevails (column 4). Column 8 indicates the soil classification used in this study (as presented in **Table 1**) according to the  $V_{S30}$  values of column 7. Column 9 indicates the average soil classification used for each station for the GMPE regression analysis whose  $V_{S30}$  values are presented in Column 10.

NETWORK NAME	STATION NAME	LATITUDE	LONGITUDE	Vs30 FROM USGS (m/s)	Vs30 FROM RESEARCH PAPERS (m/s)	Vs30 (m/s)	SITE CLASSIFICATION	SITE CLASSIFICATION FOR THE GMPE REGRESSION	REPRESENTATIVE Vs30 FOR THE GMPE REGRESSION (m/s)
(1)	(2)	(3)	(4)	(5)	(6)	(7)	(8)	(9)	(10)
CISMID	PIU001 (SCPIU)	-5.194	-80.641	209.0	0.0	209.0	D	DE	190.0
CISMID	ACAPU	-12.022	-77.137	262.0	0.0	262.0	D	D	270.0
CISMID	AMORE	-11.893	-77.110	637.0	0.0	637.0	B	B	700.0
CISMID	ANCON	-11.775	-77.168	437.0	547.4	547.4	B	BC	525.0
CISMID	ANRA (SCO)	-12.130	-76.980	394.0	0.0	394.0	C	CD	350.0
CISMID	AQP001	-16.404	-71.524	461.0	0.0	461.0	C	C	437.5
CISMID	AQP002	-16.465	-71.493	395.0	0.0	395.0	C	CD	350.0
CISMID	BONDY	-12.042	-77.087	338.0	0.0	338.0	D	CD	350.0
CISMID	BORJA	-12.086	-77.006	354.0	0.0	354.0	C	CD	350.0
CISMID	CAL001	-12.066	-77.156	600.0	528.0	528.0	B	BC	525.0
CISMID	CAL002	-12.061	-77.124	292.0	0.0	292.0	D	D	270.0
CISMID	CAL002 (NISTA)	-12.061	-77.124	292.0	0.0	292.0	D	D	270.0
CISMID	CARAB	-11.901	-77.034	520.0	0.0	520.0	C	BC	525.0
CISMID	CENEP	-12.092	-77.016	347.0	0.0	347.0	D	CD	350.0
CISMID	CEPRE	-12.013	-77.051	461.0	0.0	461.0	C	C	437.5
CISMID	CIPCN	-12.115	-77.029	319.0	0.0	319.0	D	CD	350.0
CISMID	COMAS	-11.949	-77.060	356.0	0.0	356.0	C	CD	350.0
CISMID	DHNPE	-12.066	-77.156	600.0	528.0	528.0	B	BC	525.0
CISMID	DSMI	-12.061	-77.145	261.0	0.0	261.0	D	D	270.0
CISMID	ESTAL	-12.012	-77.104	295.0	0.0	295.0	D	D	270.0
CISMID	FICPE	-12.022	-77.049	318.0	0.0	318.0	D	CD	350.0
CISMID	ICA002	-14.088	-75.732	237.0	0.0	237.0	D	DE	190.0
CISMID	IMCA	-12.070	-76.955	355.0	0.0	355.0	C	CD	350.0
CISMID	INDEP	-11.997	-77.054	397.0	0.0	397.0	C	CD	350.0
CISMID	INICT	-12.084	-76.997	351.0	0.0	351.0	C	CD	350.0
CISMID	JALVA	-12.013	-77.050	461.0	0.0	461.0	C	C	437.5
CISMID	JOSEO	-11.967	-77.038	827.0	0.0	827.0	B	AB	875.0
CISMID	LIM001	-12.014	-77.051	461.0	746.6	746.6	B	B	700.0
CISMID	LIM001 (RIMA) / CMD	-12.014	-77.051	461.0	746.6	746.6	B	B	700.0
CISMID	LIM001-2	-12.013	-77.050	461.0	0.0	461.0	C	C	437.5

NETWORK NAME	STATION NAME	LATITUDE	LONGITUDE	Vs30 FROM USGS (m/s)	Vs30 FROM RESEARCH PAPERS (m/s)	Vs30 (m/s)	SITE CLASSIFICATION	SITE CLASSIFICATION FOR THE GMPE REGRESSION	REPRESENTATIVE Vs30 FOR THE GMPE REGRESSION (m/s)
(1)	(2)	(3)	(4)	(5)	(6)	(7)	(8)	(9)	(10)
CISMID	LIM002	-12.022	-77.049	318.0	0.0	318.0	D	CD	350.0
CISMID	LIM002 (FICPE)	-12.022	-77.049	318.0	0.0	318.0	D	CD	350.0
CISMID	LIM004	-12.089	-76.896	742.0	0.0	742.0	B	B	700.0
CISMID	LIM005	-12.073	-77.031	336.0	0.0	336.0	D	CD	350.0
CISMID	LIM006	-11.852	-77.074	285.0	628.6	628.6	B	B	700.0
CISMID	LIM007	-12.213	-76.939	480.0	0.0	480.0	C	BC	525.0
CISMID	LIM008	-12.018	-77.056	377.0	0.0	377.0	C	CD	350.0
CISMID	LIM009	-12.086	-77.006	354.0	0.0	354.0	C	CD	350.0
CISMID	LIM009 (BORJA)	-12.086	-77.006	354.0	0.0	354.0	C	CD	350.0
CISMID	LIM-SLP	-12.015	-77.047	461.0	0.0	461.0	C	C	437.5
CISMID	LIM-UNI1	-12.020	-77.049	461.0	0.0	461.0	C	C	437.5
CISMID	LIM-UNI2	-12.019	-77.047	461.0	0.0	461.0	C	C	437.5
CISMID	LIM-UNI4	-12.020	-77.050	461.0	0.0	461.0	C	C	437.5
CISMID	LLB001	-8.090	-79.008	339.0	0.0	339.0	D	CD	350.0
CISMID	LMO (MOL)	-12.085	-76.948	284.0	1,000.0	1,000.0	A	A	1,150.0
CISMID	MDPP	-11.867	-77.077	288.0	280.0	280.0	D	D	270.0
CISMID	MOQ001	-17.186	-70.928	437.0	421.0	421.0	C	C	437.5
CISMID	MOQ002	-17.195	-70.921	515.0	542.0	542.0	B	BC	525.0
CISMID	MOQ005	-17.190	-70.942	467.0	950.0	950.0	A	C	437.5
CISMID	MOQA (MOQ001)	-17.186	-70.928	437.0	421.0	421.0	C	C	437.5
CISMID	MOY001	-6.034	-76.970	411.0	0.0	411.0	C	C	437.5
CISMID	NISTA	-12.060	-77.123	292.0	960.0	960.0	A	A	1,150.0
CISMID	OLIVO	-11.992	-77.071	297.0	0.0	297.0	D	D	270.0
CISMID	PQR	-12.071	-77.033	336.0	500.0	500.0	C	BC	525.0
CISMID	PRADO	-12.074	-77.119	372.0	0.0	372.0	C	CD	350.0
CISMID	RAMON	-12.042	-77.124	292.0	0.0	292.0	D	D	270.0
CISMID	SCARQ	-16.394	-71.537	459.0	0.0	459.0	C	C	437.5
CISMID	SCARQ (AQP003)	-16.394	-71.537	459.0	0.0	459.0	C	C	437.5
CISMID	SCAYA	-13.174	-74.204	511.0	0.0	511.0	C	BC	525.0
CISMID	SCCUS	-13.525	-71.962	544.0	0.0	544.0	B	BC	525.0
CISMID	SCHYO	-12.062	-75.213	373.0	0.0	373.0	C	CD	350.0
CISMID	SCICA	-14.060	-75.738	608.0	400.0	400.0	C	B	700.0
CISMID	SCIQU	-3.741	-73.245	202.0	0.0	202.0	D	DE	190.0
CISMID	SCPIU	-5.194	-80.641	209.0	0.0	209.0	D	DE	190.0
CISMID	SCTAC	-18.012	-70.250	401.0	0.0	401.0	C	C	437.5
CISMID	SCTAC (TAC004)	-18.012	-70.250	401.0	400.0	400.0	C	CD	350.0
CISMID	SCTRU	-8.090	-79.008	339.0	0.0	339.0	D	CD	350.0
CISMID	SROSA	-11.787	-77.157	447.0	0.0	447.0	C	C	437.5
CISMID	TAC001	-18.024	-70.249	398.0	571.0	571.0	B	BC	525.0
CISMID	TAC002	-18.005	-70.226	395.0	545.0	545.0	B	BC	525.0
CISMID	UNFV	-12.094	-77.077	465.0	0.0	465.0	C	C	437.5
CISMID	UPCSM	-12.085	-77.095	431.0	0.0	431.0	C	C	437.5
CISMID	UPCVI	-12.198	-77.007	258.0	0.0	258.0	D	D	270.0
CISMID	URPPE	-12.132	-76.979	488.0	0.0	488.0	C	BC	525.0
CISMID	USILM	-12.073	-76.952	325.0	1,000.0	1,000.0	A	A	1,150.0
CISMID	USILP	-12.236	-76.868	344.0	1,000.0	1,000.0	A	A	1,150.0
CISMID	USMP	-12.072	-76.941	389.0	0.0	389.0	C	CD	350.0
CISMID	VHAYA	-11.938	-77.136	376.0	0.0	376.0	C	CD	350.0
CISMID	VSAL (LIM007)	-12.213	-76.939	480.0	0.0	480.0	C	BC	525.0
CNS	A01F	-23.640	-70.396	361.0	0.0	361.0	C	CD	350.0
CNS	A01P	-18.219	-69.321	438.0	0.0	438.0	C	C	437.5
CNS	A01Y	-44.728	-72.683	591.0	248.0	248.0	D	D	270.0
CNS	A02F	-23.101	-70.445	371.0	0.0	371.0	C	CD	350.0
CNS	A02P	-17.595	-69.477	317.0	0.0	317.0	D	CD	350.0
CNS	A02Y	-45.396	-72.681	219.0	0.0	219.0	D	DE	190.0
CNS	A03F	-23.453	-70.441	314.0	0.0	314.0	D	CD	350.0
CNS	A03P	-18.497	-69.154	399.0	0.0	399.0	C	CD	350.0
CNS	A04C	-27.300	-70.413	273.0	534.0	534.0	B	BC	525.0
CNS	A04F	-23.667	-70.401	594.0	0.0	594.0	B	B	700.0
CNS	A04P	-18.834	-69.744	457.0	483.0	483.0	C	BC	525.0
CNS	A05C	-27.361	-70.340	453.0	632.0	632.0	B	B	700.0
CNS	A05F	-22.891	-69.321	334.0	0.0	334.0	D	CD	350.0
CNS	A05P	-18.486	-70.301	335.0	446.0	446.0	C	C	437.5
CNS	A06F	-22.344	-69.658	215.0	0.0	215.0	D	DE	190.0
CNS	A06P	-18.470	-70.293	351.0	500.0	500.0	C	BC	525.0
CNS	A06Y	-47.253	-72.572	502.0	261.0	261.0	D	D	270.0
CNS	A07C	-27.374	-70.318	329.0	441.0	441.0	C	C	437.5
CNS	A07F	-21.628	-69.551	523.0	0.0	523.0	C	BC	525.0
CNS	A07P	-18.446	-70.293	407.0	560.0	560.0	B	BC	525.0
CNS	A07Y	-43.773	-72.955	600.0	226.0	226.0	D	DE	190.0
CNS	A08P	-18.480	-70.331	600.0	997.0	997.0	A	A	1,150.0
CNS	A08Y	-43.896	-73.741	307.0	0.0	307.0	D	CD	350.0

NETWORK NAME	STATION NAME	LATITUDE	LONGITUDE	Vs30 FROM USGS (m/s)	Vs30 FROM RESEARCH PAPERS (m/s)	Vs30 (m/s)	SITE CLASSIFICATION	SITE CLASSIFICATION FOR THE GMPE REGRESSION	REPRESENTATIVE Vs30 FOR THE GMPE REGRESSION (m/s)
(1)	(2)	(3)	(4)	(5)	(6)	(7)	(8)	(9)	(10)
CNS	A09P	-18.480	-70.325	518.0	1,054.0	1,054.0	A	A	1,150.0
CNS	A09Y	-44.747	-72.214	650.0	0.0	650.0	B	B	700.0
CNS	A10F	-25.411	-70.484	622.0	0.0	622.0	B	B	700.0
CNS	A10Y	-45.164	-73.523	600.0	0.0	600.0	B	B	700.0
CNS	A11F	-21.425	-70.057	326.0	0.0	326.0	D	CD	350.0
CNS	A11P	-18.479	-70.271	670.0	804.0	804.0	B	B	700.0
CNS	A12P	-18.453	-70.067	489.0	560.0	560.0	B	BC	525.0
CNS	A13P	-18.519	-70.179	900.0	531.0	531.0	B	BC	525.0
CNS	A14C	-26.342	-70.612	627.0	0.0	627.0	B	B	700.0
CNS	A14F	-22.093	-70.200	727.0	0.0	727.0	B	B	700.0
CNS	A14P	-18.351	-70.336	325.0	474.0	474.0	C	C	437.5
CNS	A15C	-26.393	-70.048	399.0	0.0	399.0	C	CD	350.0
CNS	A15F	-23.704	-70.421	456.0	0.0	456.0	C	C	437.5
CNS	A15P	-18.472	-70.313	464.0	390.0	390.0	C	CD	350.0
CNS	A16C	-26.250	-69.626	528.0	0.0	528.0	B	BC	525.0
CNS	A16F	-22.108	-70.210	900.0	0.0	900.0	A	AB	875.0
CNS	A16P	-19.160	-70.180	392.0	0.0	392.0	C	CD	350.0
CNS	A17C	-26.753	-69.906	432.0	0.0	432.0	C	C	437.5
CNS	A17F	-22.460	-68.919	334.0	0.0	334.0	D	CD	350.0
CNS	A17P	-18.853	-69.143	715.0	0.0	715.0	B	B	700.0
CNS	A18F	-22.457	-68.929	341.0	0.0	341.0	D	CD	350.0
CNS	A18P	-18.200	-69.562	611.0	0.0	611.0	B	B	700.0
CNS	A19C	-27.830	-70.108	312.0	507.0	507.0	C	BC	525.0
CNS	A19F	-23.489	-70.412	466.0	0.0	466.0	C	C	437.5
CNS	A19P	-18.494	-70.299	441.0	727.0	727.0	B	B	700.0
CNS	A20F	-22.454	-68.910	357.0	0.0	357.0	C	CD	350.0
CNS	A20P	-18.448	-69.881	570.0	0.0	570.0	B	BC	525.0
CNS	A21F	-21.226	-68.256	250.0	0.0	250.0	D	D	270.0
CNS	A22F	-22.909	-68.201	342.0	0.0	342.0	D	CD	350.0
CNS	A23F	-22.337	-68.651	401.0	0.0	401.0	C	C	437.5
CNS	A24F	-23.610	-70.262	345.0	0.0	345.0	D	CD	350.0
CNS	A26F	-25.109	-70.496	600.0	0.0	600.0	B	B	700.0
CNS	A27C	-27.367	-70.331	396.0	473.0	473.0	C	C	437.5
CNS	A27F	-24.256	-69.133	478.0	0.0	478.0	C	BC	525.0
CNS	A28C	-27.466	-70.265	339.0	522.0	522.0	C	BC	525.0
CNS	A28F	-25.107	-69.521	470.0	0.0	470.0	C	C	437.5
CNS	A29F	-22.164	-70.087	457.0	0.0	457.0	C	C	437.5
CNS	AC04	-28.205	-71.074	381.0	0.0	381.0	C	CD	350.0
CNS	AF01	-22.952	-68.179	258.0	0.0	258.0	D	D	270.0
CNS	AP01	-18.371	-70.342	388.0	355.0	355.0	C	CD	350.0
CNS	AY01	-44.421	-72.648	600.0	0.0	600.0	B	B	700.0
CNS	B07I	-36.816	-73.026	426.0	0.0	426.0	C	C	437.5
CNS	B11I	-38.345	-73.493	336.0	0.0	336.0	D	CD	350.0
CNS	B14I	-37.605	-73.654	452.0	0.0	452.0	C	C	437.5
CNS	C01O	-29.877	-71.238	463.0	447.0	447.0	C	C	437.5
CNS	C09O	-29.511	-71.200	560.0	754.0	754.0	B	B	700.0
CNS	C10O	-30.234	-71.082	311.0	0.0	311.0	D	CD	350.0
CNS	C11O	-30.697	-70.959	313.0	626.0	626.0	B	B	700.0
CNS	C14O	-30.123	-70.491	518.0	0.0	518.0	C	BC	525.0
CNS	C18O	-30.278	-70.669	612.0	0.0	612.0	B	B	700.0
CNS	C19O	-30.094	-71.369	328.0	1,106.0	1,106.0	A	A	1,150.0
CNS	C20O	-29.968	-71.337	376.0	737.0	737.0	B	B	700.0
CNS	C22O	-29.966	-71.351	446.0	1,228.0	1,228.0	A	A	1,150.0
CNS	C23O	-31.784	-70.970	332.0	751.0	751.0	B	B	700.0
CNS	C26O	-30.259	-71.491	254.0	364.0	364.0	C	CD	350.0
CNS	C27O	-29.384	-70.745	574.0	0.0	574.0	B	BC	525.0
CNS	C28O	-29.291	-71.308	322.0	0.0	322.0	D	CD	350.0
CNS	C32O	-30.855	-70.707	769.0	578.0	578.0	B	B	700.0
CNS	C33O	-29.911	-71.251	425.0	587.0	587.0	B	B	700.0
CNS	C003	-30.839	-70.689	468.0	0.0	468.0	C	C	437.5
CNS	C006	-30.674	-71.635	501.0	0.0	501.0	C	BC	525.0
CNS	G001	-19.669	-69.194	712.0	0.0	712.0	B	B	700.0
CNS	G002	-25.163	-69.590	431.0	0.0	431.0	C	C	437.5
CNS	G004	-30.173	-70.799	716.0	0.0	716.0	B	B	700.0
CNS	G007	-43.114	-73.664	368.0	354.0	354.0	C	CD	350.0
CNS	HMBCX	-20.278	-69.888	323.0	742.7	742.7	B	B	700.0
CNS	L01C	-38.773	-72.597	299.0	0.0	299.0	D	D	270.0
CNS	L05L	-41.154	-73.418	235.0	255.0	255.0	D	D	270.0
CNS	L06R	-40.293	-73.084	400.0	448.0	448.0	C	C	437.5
CNS	L07R	-40.128	-72.394	489.0	229.0	229.0	D	DE	190.0
CNS	L09L	-41.865	-73.826	437.0	182.0	182.0	E	DE	190.0
CNS	L10R	-40.070	-72.873	268.0	384.0	384.0	C	CD	350.0

NETWORK NAME	STATION NAME	LATITUDE	LONGITUDE	Vs30 FROM USGS (m/s)	Vs30 FROM RESEARCH PAPERS (m/s)	Vs30 (m/s)	SITE CLASSIFICATION	SITE CLASSIFICATION FOR THE GMPE REGRESSION	REPRESENTATIVE Vs30 FOR THE GMPE REGRESSION (m/s)
(1)	(2)	(3)	(4)	(5)	(6)	(7)	(8)	(9)	(10)
CNS	LL01	-42.379	-72.412	900.0	0.0	900.0	A	AB	875.0
CNS	LL03	-41.138	-72.403	900.0	233.0	233.0	D	DE	190.0
CNS	LL04	-40.910	-72.408	788.0	0.0	788.0	B	B	700.0
CNS	LL06	-42.215	-73.628	299.0	0.0	299.0	D	D	270.0
CNS	LL07	-42.832	-73.478	600.0	435.0	435.0	C	C	437.5
CNS	LMEL	-33.848	-70.207	900.0	0.0	900.0	A	AB	875.0
CNS	LRO2	-39.806	-73.251	301.0	217.0	217.0	D	DE	190.0
CNS	M02L	-35.000	-70.812	603.0	0.0	603.0	B	B	700.0
CNS	M03L	-34.976	-71.232	299.0	715.0	715.0	B	B	700.0
CNS	M09L	-35.591	-72.281	363.0	400.0	400.0	C	CD	350.0
CNS	M11L	-35.440	-71.632	301.0	482.0	482.0	C	BC	525.0
CNS	M13L	-36.141	-71.824	271.0	309.0	309.0	D	CD	350.0
CNS	MNMCX	-19.131	-69.596	409.0	0.0	409.0	C	C	437.5
CNS	MT01	-33.864	-71.251	614.0	0.0	614.0	B	B	700.0
CNS	MT05	-33.392	-70.738	495.0	0.0	495.0	C	BC	525.0
CNS	MT09	-33.776	-70.989	900.0	0.0	900.0	A	AB	875.0
CNS	PATCX	-20.821	-70.153	900.0	0.0	900.0	A	AB	875.0
CNS	PB01	-21.043	-69.487	438.0	0.0	438.0	C	C	437.5
CNS	PB02	-21.320	-69.896	568.0	0.0	568.0	B	BC	525.0
CNS	PB03	-22.048	-69.753	616.0	0.0	616.0	B	B	700.0
CNS	PB04	-22.334	-70.149	389.0	0.0	389.0	C	CD	350.0
CNS	PB06	-22.706	-69.572	287.0	0.0	287.0	D	D	270.0
CNS	PB07	-21.727	-69.886	327.0	0.0	327.0	D	CD	350.0
CNS	PB08	-20.141	-69.153	722.0	0.0	722.0	B	B	700.0
CNS	PB09	-21.796	-69.242	535.0	0.0	535.0	B	BC	525.0
CNS	PB11	-19.761	-69.656	359.0	1,048.5	1,048.5	A	A	1,150.0
CNS	PB12	-18.614	-70.328	900.0	0.0	900.0	A	AB	875.0
CNS	PB15	-23.208	-69.471	612.0	0.0	612.0	B	B	700.0
CNS	PB16	-18.335	-69.508	900.0	0.0	900.0	A	AB	875.0
CNS	PB19	-23.905	-69.291	614.0	0.0	614.0	B	B	700.0
CNS	PSGCX	-19.597	-70.123	668.0	1,641.3	1,641.3	A	A	1,150.0
CNS	PX03	-20.403	-69.631	222.0	0.0	222.0	D	DE	190.0
CNS	R02M	-33.473	-70.660	277.0	724.0	724.0	B	B	700.0
CNS	R05M	-33.443	-70.535	503.0	635.0	635.0	B	B	700.0
CNS	R12M	-33.389	-70.622	235.0	267.0	267.0	D	D	270.0
CNS	R13M	-33.216	-70.767	318.0	281.0	281.0	D	D	270.0
CNS	R14M	-33.397	-70.546	411.0	574.0	574.0	B	BC	525.0
CNS	R16M	-33.400	-70.659	299.0	0.0	299.0	D	D	270.0
CNS	R18M	-33.508	-70.749	269.0	370.0	370.0	C	CD	350.0
CNS	R19M	-33.699	-71.217	543.0	471.0	471.0	C	C	437.5
CNS	R20M	-33.665	-70.929	324.0	577.0	577.0	B	B	700.0
CNS	R21M	-33.381	-70.796	223.0	347.0	347.0	D	CD	350.0
CNS	R22M	-33.453	-70.592	331.0	647.0	647.0	B	B	700.0
CNS	R23M	-33.585	-70.701	312.0	0.0	312.0	D	CD	350.0
CNS	ROC1	-32.976	-71.016	900.0	0.0	900.0	A	AB	875.0
CNS	T01A	-20.273	-70.122	768.0	339.0	339.0	D	CD	350.0
CNS	T02A	-20.252	-70.118	900.0	269.3	269.3	D	D	270.0
CNS	T03A	-20.230	-70.146	600.0	613.1	613.1	B	B	700.0
CNS	T04A	-20.239	-70.133	616.0	1,305.0	1,305.0	A	A	1,150.0
CNS	T05A	-20.210	-70.150	319.0	1,024.9	1,024.9	A	A	1,150.0
CNS	T06A	-20.214	-70.138	392.0	1,257.6	1,257.6	A	A	1,150.0
CNS	T07A	-20.256	-69.786	257.0	326.2	326.2	D	CD	350.0
CNS	T08A	-20.270	-70.094	295.0	985.9	985.9	A	A	1,150.0
CNS	T09A	-19.596	-70.211	900.0	1,585.8	1,585.8	A	A	1,150.0
CNS	T10A	-19.995	-69.767	248.0	335.6	335.6	D	CD	350.0
CNS	T11A	-19.312	-69.427	900.0	0.0	900.0	A	AB	875.0
CNS	T12A	-20.071	-69.217	533.0	0.0	533.0	B	BC	525.0
CNS	T13A	-20.496	-69.337	396.0	377.9	377.9	C	CD	350.0
CNS	T14A	-20.295	-70.128	790.0	1,205.0	1,205.0	A	A	1,150.0
CNS	T15A	-20.239	-70.054	618.0	1,003.0	1,003.0	A	A	1,150.0
CNS	T16A	-20.540	-70.177	579.0	1,545.0	1,545.0	A	A	1,150.0
CNS	T18A	-20.708	-68.695	360.0	0.0	360.0	C	CD	350.0
CNS	T19A	-20.287	-70.105	900.0	822.0	822.0	B	B	700.0
CNS	T20A	-19.924	-69.512	506.0	517.0	517.0	C	BC	525.0
CNS	T21A	-20.945	-69.529	259.0	0.0	259.0	D	D	270.0
CNS	T23A	-20.885	-70.039	294.0	0.0	294.0	D	D	270.0
CNS	TA01	-20.566	-70.181	419.0	1,339.0	1,339.0	A	A	1,150.0
CNS	TA02	-20.270	-70.131	600.0	489.0	489.0	C	BC	525.0
CNS	V01A	-33.053	-71.622	765.0	607.0	607.0	B	B	700.0
CNS	V02A	-33.023	-71.518	596.0	596.0	596.0	B	B	700.0
CNS	V07A	-33.365	-71.669	451.0	549.0	549.0	B	BC	525.0
CNS	V09A	-33.048	-71.605	561.0	212.0	212.0	D	DE	190.0

NETWORK NAME	STATION NAME	LATITUDE	LONGITUDE	Vs30 FROM USGS (m/s)	Vs30 FROM RESEARCH PAPERS (m/s)	Vs30 (m/s)	SITE CLASSIFICATION	SITE CLASSIFICATION FOR THE GMPE REGRESSION	REPRESENTATIVE Vs30 FOR THE GMPE REGRESSION (m/s)
(1)	(2)	(3)	(4)	(5)	(6)	(7)	(8)	(9)	(10)
CNS	V13A	-32.506	-71.442	600.0	0.0	600.0	B	B	700.0
CNS	V15A	-32.915	-71.233	476.0	323.0	323.0	D	CD	350.0
CNS	V16A	-33.591	-71.605	504.0	477.0	477.0	C	BC	525.0
CNS	V17A	-33.606	-71.614	374.0	281.0	281.0	D	D	270.0
CNS	V22A	-33.020	-71.636	600.0	854.0	854.0	B	AB	875.0
CNS	V24A	-33.622	-71.613	314.0	0.0	314.0	D	CD	350.0
CNS	VA01	-33.023	-71.637	600.0	882.0	882.0	A	AB	875.0
CNS	VA03	-32.764	-70.551	604.0	937.0	937.0	A	A	1,150.0
CNS	VA05	-33.657	-71.614	316.0	485.0	485.0	C	BC	525.0
CNS	VA06	-32.561	-71.298	307.0	0.0	307.0	D	CD	350.0
IGP	ABAN	-13.600	-72.900	900.0	0.0	900.0	A	AB	875.0
IGP	ACOM	-13.900	-71.700	900.0	0.0	900.0	A	AB	875.0
IGP	AGUA	-9.000	-75.500	259.0	0.0	259.0	D	D	270.0
IGP	ANCA	-11.777	-77.151	356.0	547.4	547.4	B	BC	525.0
IGP	ANDA	-13.700	-73.400	773.0	0.0	773.0	B	B	700.0
IGP	ANRA	-12.130	-76.980	394.0	0.0	394.0	C	CD	350.0
IGP	APLA	-16.100	-72.500	900.0	0.0	900.0	A	AB	875.0
IGP	AREQ	-16.400	-71.500	564.0	0.0	564.0	B	BC	525.0
IGP	ATIC	-16.200	-73.600	875.0	0.0	875.0	B	AB	875.0
IGP	AYAA	-13.200	-74.200	500.0	0.0	500.0	C	BC	525.0
IGP	AYAB	-4.600	-79.700	571.0	0.0	571.0	B	BC	525.0
IGP	AZPV	-14.900	-70.200	298.0	0.0	298.0	D	D	270.0
IGP	BAGU	-5.600	-78.500	512.0	0.0	512.0	C	BC	525.0
IGP	BCAA	-10.800	-77.800	600.0	0.0	600.0	B	B	700.0
IGP	CAFZ	-17.300	-70.200	567.0	0.0	567.0	B	BC	525.0
IGP	CAMA	-12.100	-77.000	352.0	857.0	857.0	B	AB	875.0
IGP	CANT	-11.500	-76.600	900.0	0.0	900.0	A	AB	875.0
IGP	CARA	-11.901	-77.034	520.0	0.0	520.0	C	BC	525.0
IGP	CARV	-15.800	-73.400	572.0	0.0	572.0	B	BC	525.0
IGP	CASM	-9.500	-78.300	424.0	0.0	424.0	C	C	437.5
IGP	CBT1	-9.100	-78.600	600.0	0.0	600.0	B	B	700.0
IGP	CBTA	-9.100	-78.500	443.0	0.0	443.0	C	C	437.5
IGP	CBTB	-9.100	-78.600	600.0	0.0	600.0	B	B	700.0
IGP	CCTA	-17.500	-70.000	823.0	0.0	823.0	B	B	700.0
IGP	CELE	-6.900	-78.100	900.0	0.0	900.0	A	AB	875.0
IGP	CERA	-12.104	-76.999	352.0	360.8	360.8	C	CD	350.0
IGP	CHAL	-15.850	-74.250	521.0	0.0	521.0	C	BC	525.0
IGP	CHCA	-6.200	-77.900	759.0	0.0	759.0	B	B	700.0
IGP	CHEP	-7.200	-79.400	359.0	0.0	359.0	C	CD	350.0
IGP	CHIA	-13.400	-76.100	401.0	0.0	401.0	C	C	437.5
IGP	CHIV	-15.600	-71.600	662.0	0.0	662.0	B	B	700.0
IGP	CHNG	-6.600	-79.400	320.0	0.0	320.0	D	CD	350.0
IGP	CHOR	-12.200	-77.000	370.0	0.0	370.0	C	CD	350.0
IGP	CHSC	-11.900	-76.700	900.0	0.0	900.0	A	AB	875.0
IGP	CHUL	-5.100	-80.200	186.0	0.0	186.0	E	DE	190.0
IGP	CHUQ	-15.800	-72.700	447.0	0.0	447.0	C	C	437.5
IGP	CHYA	-6.800	-79.900	212.0	0.0	212.0	D	DE	190.0
IGP	CIJS	-12.100	-76.800	596.0	0.0	596.0	B	B	700.0
IGP	CITY	-12.300	-76.800	406.0	0.0	406.0	C	C	437.5
IGP	CMNA	-16.600	-72.700	554.0	0.0	554.0	B	BC	525.0
IGP	CNMC	-18.000	-70.200	427.0	427.0	427.0	C	C	437.5
IGP	COIR	-12.000	-77.100	299.0	0.0	299.0	D	D	270.0
IGP	CONC	-11.900	-75.300	433.0	0.0	433.0	C	C	437.5
IGP	CONV	-12.900	-72.700	900.0	0.0	900.0	A	AB	875.0
IGP	COTA	-15.200	-72.900	509.0	0.0	509.0	C	BC	525.0
IGP	CRQN	-11.100	-77.600	309.0	0.0	309.0	D	CD	350.0
IGP	CUSC	-13.500	-72.000	464.0	0.0	464.0	C	C	437.5
IGP	ENPE	-12.100	-77.200	372.0	0.0	372.0	C	CD	350.0
IGP	ESPI	-14.800	-71.400	283.0	0.0	283.0	D	D	270.0
IGP	HCSC	-13.900	-74.300	443.0	0.0	443.0	C	C	437.5
IGP	HJUN	-12.100	-77.000	352.0	0.0	352.0	C	CD	350.0
IGP	HMY1	-10.100	-78.200	600.0	0.0	600.0	B	B	700.0
IGP	HMY2	-10.100	-78.100	597.0	0.0	597.0	B	B	700.0
IGP	HUAA	-11.100	-77.600	309.0	0.0	309.0	D	CD	350.0
IGP	HUAL	-11.500	-77.200	341.0	0.0	341.0	D	CD	350.0
IGP	HUAR	-9.400	-77.200	900.0	0.0	900.0	A	AB	875.0
IGP	HVCA	-12.800	-75.000	900.0	0.0	900.0	A	AB	875.0
IGP	HYOJ	-12.100	-75.200	242.0	0.0	242.0	D	D	270.0
IGP	ILOM	-17.600	-71.300	794.0	0.0	794.0	B	B	700.0
IGP	INDE	-12.000	-77.100	299.0	0.0	299.0	D	D	270.0
IGP	IQUI	-3.800	-73.300	206.0	0.0	206.0	D	DE	190.0
IGP	ITEJ	-17.900	-71.000	600.0	0.0	600.0	B	B	700.0



NETWORK NAME	STATION NAME	LATITUDE	LONGITUDE	Vs30 FROM USGS (m/s)	Vs30 FROM RESEARCH PAPERS (m/s)	Vs30 (m/s)	SITE CLASSIFICATION	SITE CLASSIFICATION FOR THE GMPE REGRESSION	REPRESENTATIVE Vs30 FOR THE GMPE REGRESSION (m/s)
(1)	(2)	(3)	(4)	(5)	(6)	(7)	(8)	(9)	(10)
IGP	IYAM	-17.400	-70.500	449.0	0.0	449.0	C	C	437.5
IGP	JAEN	-5.700	-78.800	417.0	0.0	417.0	C	C	437.5
IGP	JEMA	-12.100	-77.000	352.0	0.0	352.0	C	CD	350.0
IGP	JUAJ	-7.200	-76.700	264.0	0.0	264.0	D	D	270.0
IGP	JUNI	-11.200	-76.000	390.0	0.0	390.0	C	CD	350.0
IGP	LAGU	-7.000	-79.650	226.0	0.0	226.0	D	DE	190.0
IGP	LANC	-4.600	-80.500	256.0	0.0	256.0	D	D	270.0
IGP	LIMA	-13.500	-72.500	515.0	0.0	515.0	C	BC	525.0
IGP	LOLI	-12.000	-77.100	299.0	0.0	299.0	D	D	270.0
IGP	LOMA	-4.700	-80.200	394.0	0.0	394.0	C	CD	350.0
IGP	LURN	-12.300	-76.900	600.0	0.0	600.0	B	B	700.0
IGP	LYAA	-18.200	-70.600	321.0	0.0	321.0	D	CD	350.0
IGP	MAGD	-12.100	-77.100	600.0	0.0	600.0	B	B	700.0
IGP	MALA	-12.700	-76.600	594.0	0.0	594.0	B	B	700.0
IGP	MARQ	-11.900	-77.100	591.0	0.0	591.0	B	B	700.0
IGP	MATU	-11.800	-76.400	900.0	0.0	900.0	A	AB	875.0
IGP	MAYA	-12.055	-76.944	477.0	529.6	529.6	B	BC	525.0
IGP	MIRA	-12.100	-77.000	352.0	0.0	352.0	C	CD	350.0
IGP	MOLL	-17.000	-72.000	546.0	0.0	546.0	B	BC	525.0
IGP	MOQA	-17.186	-70.928	437.0	428.0	428.0	C	C	437.5
IGP	MORR	-5.200	-80.000	487.0	0.0	487.0	C	BC	525.0
IGP	MOTU	-6.200	-79.700	233.0	0.0	233.0	D	DE	190.0
IGP	NASC	-14.800	-74.900	900.0	0.0	900.0	A	AB	875.0
IGP	NNAA	-11.987	-76.839	884.0	0.0	884.0	A	AB	875.0
IGP	NSLO	-17.800	-70.900	637.0	0.0	637.0	B	B	700.0
IGP	OCCO	-13.300	-74.500	575.0	0.0	575.0	B	BC	525.0
IGP	OCUC	-14.400	-75.700	574.0	0.0	574.0	B	BC	525.0
IGP	OLMO	-6.000	-79.750	289.0	0.0	289.0	D	D	270.0
IGP	OMAM	-16.700	-71.000	837.0	0.0	837.0	B	AB	875.0
IGP	ORCO	-15.300	-72.300	835.0	0.0	835.0	B	AB	875.0
IGP	ORGA	-4.200	-81.100	342.0	0.0	342.0	D	CD	350.0
IGP	OTUZ	-7.900	-78.600	500.0	0.0	500.0	C	BC	525.0
IGP	OYOA	-10.700	-76.800	900.0	0.0	900.0	A	AB	875.0
IGP	PAIT	-5.100	-81.100	243.0	0.0	243.0	D	D	270.0
IGP	PALC	-17.800	-70.000	868.0	0.0	868.0	B	AB	875.0
IGP	PALP	-14.500	-75.200	388.0	0.0	388.0	C	CD	350.0
IGP	PARA	-13.850	-76.200	300.0	0.0	300.0	D	D	270.0
IGP	PARC	-14.042	-75.699	379.0	0.0	379.0	C	CD	350.0
IGP	PASC	-10.700	-76.200	786.0	0.0	786.0	B	B	700.0
IGP	PAUC	-13.300	-71.600	504.0	0.0	504.0	C	BC	525.0
IGP	PAVE	-11.800	-77.200	600.0	0.0	600.0	B	B	700.0
IGP	PERL	-12.100	-77.100	600.0	0.0	600.0	B	B	700.0
IGP	PHER	-12.300	-76.800	406.0	0.0	406.0	C	C	437.5
IGP	PICO	-6.900	-76.300	646.0	0.0	646.0	B	B	700.0
IGP	PIDR	-11.852	-77.074	285.0	594.0	594.0	B	B	700.0
IGP	PISC	-13.700	-76.200	275.0	276.0	276.0	D	D	270.0
IGP	PMYO	-7.100	-80.420	298.0	0.0	298.0	D	B	700.0
IGP	PNEG	-12.400	-76.800	600.0	0.0	600.0	B	B	700.0
IGP	PQIO	-14.700	-74.100	829.0	0.0	829.0	B	AB	875.0
IGP	PRS2	-13.600	-75.500	900.0	0.0	900.0	A	AB	875.0
IGP	PUCA	-8.400	-74.700	233.0	0.0	233.0	D	DE	190.0
IGP	PUCU	-12.500	-76.800	457.0	0.0	457.0	C	C	437.5
IGP	QUEQ	-16.600	-71.500	684.0	0.0	684.0	B	B	700.0
IGP	RIMA	-12.000	-77.000	508.0	717.2	717.2	B	B	700.0
IGP	RINC	-12.084	-76.921	463.0	0.0	463.0	C	C	437.5
IGP	RIOJ	-6.100	-77.200	465.0	0.0	465.0	C	C	437.5
IGP	SACH	-8.100	-78.200	900.0	0.0	900.0	A	AB	875.0
IGP	SAND	-11.200	-76.600	900.0	0.0	900.0	A	AB	875.0
IGP	SANI	-12.000	-77.000	508.0	0.0	508.0	C	BC	525.0
IGP	SAYA	-17.900	-70.600	314.0	0.0	314.0	D	CD	350.0
IGP	SAYH	-11.100	-77.200	810.0	0.0	810.0	B	B	700.0
IGP	SBRT	-12.400	-76.800	600.0	0.0	600.0	B	B	700.0
IGP	SCVM	-12.100	-76.900	900.0	0.0	900.0	A	AB	875.0
IGP	SDOL	-12.200	-76.500	691.0	0.0	691.0	B	B	700.0
IGP	SECH	-5.600	-80.800	180.0	0.0	180.0	E	DE	190.0
IGP	SICU	-14.300	-71.200	900.0	0.0	900.0	A	AB	875.0
IGP	SJLJ	-12.000	-77.000	508.0	0.0	508.0	C	BC	525.0
IGP	SJMI	-12.200	-77.000	370.0	0.0	370.0	C	CD	350.0
IGP	SLN1	-12.064	-77.155	600.0	0.0	600.0	B	B	700.0
IGP	SLUI	-12.100	-77.000	352.0	0.0	352.0	C	CD	350.0
IGP	SMDP	-12.000	-77.100	299.0	0.0	299.0	D	D	270.0
IGP	SMIL	-12.100	-77.100	600.0	0.0	600.0	B	B	700.0

NETWORK NAME	STATION NAME	LATITUDE	LONGITUDE	Vs30 FROM USGS (m/s)	Vs30 FROM RESEARCH PAPERS (m/s)	Vs30 (m/s)	SITE CLASSIFICATION	SITE CLASSIFICATION FOR THE GMPE REGRESSION	REPRESENTATIVE Vs30 FOR THE GMPE REGRESSION (m/s)
(1)	(2)	(3)	(4)	(5)	(6)	(7)	(8)	(9)	(10)
IGP	SNIS	-12.100	-77.000	352.0	0.0	352.0	C	CD	350.0
IGP	STRS	-11.500	-75.900	897.0	0.0	897.0	A	AB	875.0
IGP	SULL	-4.900	-80.700	285.0	0.0	285.0	D	D	270.0
IGP	SVIC	-13.100	-76.400	273.0	0.0	273.0	D	D	270.0
IGP	TALA	-4.600	-81.300	284.0	0.0	284.0	D	D	270.0
IGP	TAYA	-8.300	-77.300	900.0	0.0	900.0	A	AB	875.0
IGP	TIBI	-14.100	-75.200	900.0	0.0	900.0	A	AB	875.0
IGP	TIMA	-9.300	-76.000	324.0	0.0	324.0	D	CD	350.0
IGP	TOCA	-8.200	-76.500	476.0	0.0	476.0	C	BC	525.0
IGP	TOQA	-17.300	-70.600	585.0	0.0	585.0	B	B	700.0
IGP	TRUJ	-8.100	-79.000	341.0	0.0	341.0	D	CD	350.0
IGP	UBIS	-16.400	-70.900	900.0	0.0	900.0	A	AB	875.0
IGP	UCYL	-8.400	-74.600	197.0	0.0	197.0	D	DE	190.0
IGP	UDEP	-5.200	-80.600	236.0	0.0	236.0	D	DE	190.0
IGP	UICA	-14.088	-75.732	237.0	0.0	237.0	D	DE	190.0
IGP	UNAL	-12.100	-76.900	900.0	0.0	900.0	A	AB	875.0
IGP	URCO	-13.700	-71.600	294.0	0.0	294.0	D	D	270.0
IGP	URUB	-13.300	-72.100	900.0	0.0	900.0	A	AB	875.0
IGP	VENB	-11.900	-77.100	591.0	0.0	591.0	B	B	700.0
IGP	VICT	-12.100	-77.000	352.0	0.0	352.0	C	CD	350.0
IGP	VIRA	-8.400	-78.800	315.0	0.0	315.0	D	CD	350.0
IGP	VITO	-16.500	-71.900	361.0	0.0	361.0	C	CD	350.0
IGP	VSAL	-12.213	-76.939	480.0	590.0	590.0	B	B	700.0
IGP	ZARM	-3.500	-80.300	130.0	717.2	717.2	B	B	700.0
IGP	ZORR	-3.700	-80.700	328.0	0.0	328.0	D	CD	350.0
IGP	ZUNI	-12.900	-76.000	900.0	0.0	900.0	A	AB	875.0
RENADIC	ALTO HOSPICIO	-20.265	-70.101	413.0	0.0	413.0	C	C	437.5
RENADIC	ANTOFAGASTA UCN	-23.681	-70.411	758.0	0.0	758.0	B	B	700.0
RENADIC	ARICA	-18.482	-70.313	525.0	0.0	525.0	C	BC	525.0
RENADIC	ARICA CEMENTERIO	-18.479	-70.308	385.0	406.0	406.0	C	CD	350.0
RENADIC	ARICA COSTANERA	-18.471	-70.313	600.0	389.0	389.0	C	B	700.0
RENADIC	COPIAPO	-27.374	-70.322	296.0	0.0	296.0	D	D	270.0
RENADIC	CUYA	-19.160	-70.180	392.0	467.7	467.7	C	C	437.5
RENADIC	EL LOA (SMA-1)	-21.425	-70.057	326.0	0.0	326.0	D	CD	350.0
RENADIC	FUERTE BAQUEDANO	-20.135	-69.755	321.0	0.0	321.0	D	CD	350.0
RENADIC	IQUIQUE	-20.214	-70.138	392.0	0.0	392.0	C	CD	350.0
RENADIC	IQUIQUE ESCUELA CHIPANA	-20.252	-70.126	900.0	0.0	900.0	A	AB	875.0
RENADIC	MICHILLA	-22.758	-70.281	573.0	0.0	573.0	B	BC	525.0
RENADIC	PICA	-20.492	-69.330	388.0	0.0	388.0	C	CD	350.0
RENADIC	PISAGUA	-19.595	-70.211	900.0	0.0	900.0	A	AB	875.0
RENADIC	PISAGUA ETNA	-19.595	-70.211	900.0	0.0	900.0	A	AB	875.0
RENADIC	POCON CHILE	-18.453	-70.067	489.0	511.0	511.0	C	BC	525.0
RENADIC	POCONCHILE ETNA	-18.453	-70.067	489.0	0.0	489.0	C	BC	525.0
RENADIC	PUERTO PATACHE	-20.810	-70.200	379.0	0.0	379.0	C	CD	350.0
RENADIC	PUTRE	-18.195	-69.559	770.0	0.0	770.0	B	B	700.0
RENADIC	PUTRE(SMA-1)	-18.195	-69.559	770.0	0.0	770.0	B	B	700.0
RENADIC	SAN DE PEDRO ATACAMA	-22.911	-68.200	342.0	536.3	536.3	B	BC	525.0
RENADIC	TOCOPILLA (SMA-1)	-22.090	-70.201	727.0	0.0	727.0	B	B	700.0
FIC -UNI	9E7E	-12.092	-77.049	329.0	0.0	329.0	D	CD	350.0
FIC -UNI	B863	-12.674	-76.654	235.0	0.0	235.0	D	DE	190.0
FIC -UNI	BA28	-8.128	-79.033	276.0	0.0	276.0	D	D	270.0
FIC -UNI	BC54	-14.074	-75.730	238.0	0.0	238.0	D	DE	190.0
FIC -UNI	BDBF	-10.726	-77.773	396.0	0.0	396.0	C	CD	350.0
FIC -UNI	BDC9	-9.053	-78.591	520.0	0.0	520.0	C	BC	525.0
FIC -UNI	BDD5	-6.033	-76.974	408.0	0.0	408.0	C	C	437.5
FIC -UNI	BDE6	-9.517	-77.525	613.0	0.0	613.0	B	B	700.0
FIC -UNI	BDFD	-7.399	-79.564	298.0	0.0	298.0	D	D	270.0
FIC -UNI	BDFE	-13.537	-71.906	494.0	0.0	494.0	C	BC	525.0
FIC -UNI	BE0A	-13.147	-74.222	594.0	0.0	594.0	B	B	700.0
FIC -UNI	BE0F	-6.235	-77.855	575.0	0.0	575.0	B	BC	525.0
FIC -UNI	BE28	-12.115	-77.029	319.0	0.0	319.0	D	CD	350.0
FIC -UNI	C120	-6.818	-79.913	222.0	0.0	222.0	D	DE	190.0
FIC -UNI	C12A	-6.229	-77.876	519.0	0.0	519.0	C	BC	525.0
FIC -UNI	C131	-7.175	-78.509	606.0	0.0	606.0	B	B	700.0
FIC -UNI	C163	-9.117	-78.516	361.0	0.0	361.0	C	CD	350.0
FIC -UNI	C164	-5.174	-80.629	236.0	0.0	236.0	D	DE	190.0
FIC -UNI	C165	-4.552	-81.179	245.0	0.0	245.0	D	D	270.0
FIC -UNI	C166	-16.447	-71.502	425.0	0.0	425.0	C	C	437.5
FIC -UNI	C167	-17.190	-70.932	495.0	542.0	542.0	B	BC	525.0
FIC -UNI	C168	-8.123	-79.035	276.0	0.0	276.0	D	B	700.0
FIC -UNI	C16B	-17.954	-70.184	422.0	0.0	422.0	C	C	437.5
FIC -UNI	C177	-13.080	-76.387	305.0	0.0	305.0	D	CD	350.0

NETWORK NAME	STATION NAME	LATITUDE	LONGITUDE	Vs30 FROM USGS (m/s)	Vs30 FROM RESEARCH PAPERS (m/s)	Vs30 (m/s)	SITE CLASSIFICATION	SITE CLASSIFICATION FOR THE GMPE REGRESSION	REPRESENTATIVE Vs30 FOR THE GMPE REGRESSION (m/s)
(1)	(2)	(3)	(4)	(5)	(6)	(7)	(8)	(9)	(10)
FIC -UNI	C17A	-9.936	-76.243	414.0	0.0	414.0	C	C	437.5
FIC -UNI	C17B	-12.115	-77.029	319.0	0.0	319.0	D	CD	350.0
FIC -UNI	C17C	-3.555	-80.429	212.0	0.0	212.0	D	DE	190.0
FIC -UNI	C17E	-10.887	-77.529	332.0	0.0	332.0	D	CD	350.0
FIC -UNI	C189	-17.994	-70.256	704.0	0.0	704.0	B	B	700.0
FIC -UNI	C1EA	-18.032	-70.272	396.0	0.0	396.0	C	CD	350.0
FIC -UNI	C1F1	-5.708	-78.805	472.0	0.0	472.0	C	C	437.5
FIC -UNI	C23A	-12.597	-69.188	420.0	0.0	420.0	C	C	437.5
FIC -UNI	C23E	-9.129	-78.521	311.0	0.0	311.0	D	CD	350.0
FIC -UNI	C247	-12.784	-74.975	596.0	0.0	596.0	B	B	700.0
FIC -UNI	D2FB	-12.115	-77.029	319.0	0.0	319.0	D	CD	350.0
FIC -UNI	D84D	-14.850	-74.939	503.0	0.0	503.0	C	BC	525.0
FIC -UNI	D84F	-14.533	-75.186	394.0	594.0	594.0	B	B	700.0
FIC -UNI	D851	-6.461	-76.428	653.0	0.0	653.0	B	B	700.0
FIC -UNI	D853	-6.760	-79.862	228.0	0.0	228.0	D	DE	190.0
FIC -UNI	D855	-12.071	-77.164	600.0	0.0	600.0	B	B	700.0
FIC -UNI	D859	-14.533	-75.186	394.0	0.0	394.0	C	CD	350.0
FIC -UNI	D85C	-16.399	-72.182	382.0	0.0	382.0	C	CD	350.0
FIC -UNI	D85D	-13.638	-72.877	900.0	0.0	900.0	A	AB	875.0
FIC -UNI	D863	-12.670	-76.650	291.0	0.0	291.0	D	D	270.0
FIC -UNI	D875	-8.384	-74.531	257.0	0.0	257.0	D	D	270.0
FIC -UNI	D876	-3.743	-73.252	144.0	0.0	144.0	E	DE	190.0
FIC -UNI	D877	-17.190	-70.932	495.0	542.0	542.0	B	BC	525.0
FIC -UNI	D87C	-12.062	-75.204	398.0	0.0	398.0	C	CD	350.0
FIC -UNI	D87D	-10.662	-76.252	515.0	0.0	515.0	C	BC	525.0
FIC -UNI	D87E	-15.015	-73.785	556.0	0.0	556.0	B	BC	525.0
FIC -UNI	D87F	-15.489	-70.152	278.0	0.0	278.0	D	D	270.0
FIC -UNI	D88C	-9.150	-77.743	500.0	0.0	500.0	C	BC	525.0
FIC -UNI	D88E	-7.225	-79.436	453.0	0.0	453.0	C	C	437.5
FIC -UNI	D893	-8.347	-74.588	236.0	0.0	236.0	D	DE	190.0
FIC -UNI	D89B	-12.035	-75.239	455.0	0.0	455.0	C	C	437.5
FIC -UNI	D89C	-15.820	-70.020	621.0	0.0	621.0	B	B	700.0
FIC -UNI	D89D	-8.115	-79.040	281.0	0.0	281.0	D	D	270.0
FIC -UNI	D89F	-13.529	-71.971	478.0	0.0	478.0	C	BC	525.0
FIC -UNI	D8A0	-9.311	-76.000	367.0	0.0	367.0	C	CD	350.0
FIC -UNI	D8A5	-17.601	-71.341	517.0	950.0	950.0	A	A	1,150.0
FIC -UNI	D8A6	-15.532	-70.117	208.0	0.0	208.0	D	DE	190.0
FIC -UNI	D8CE	-13.718	-76.208	289.0	0.0	289.0	D	D	270.0
FIC -UNI	D8CF	-16.401	-71.539	403.0	0.0	403.0	C	C	437.5
FIC -UNI	D8D2	-9.529	-77.528	479.0	0.0	479.0	C	BC	525.0
FIC -UNI	D8DC	-9.300	-75.998	324.0	0.0	324.0	D	CD	350.0
FIC -UNI	D90A	-5.897	-76.129	307.0	0.0	307.0	D	CD	350.0
FIC -UNI	D90B	-17.016	-72.034	535.0	950.0	950.0	A	A	1,150.0
FIC -UNI	D917	-12.890	-76.510	567.0	0.0	567.0	B	BC	525.0
FIC -UNI	D919	-5.170	-80.630	228.0	0.0	228.0	D	DE	190.0
FIC -UNI	D921	-7.167	-78.495	339.0	0.0	339.0	D	CD	350.0
FIC -UNI	D925	-12.033	-76.975	341.0	950.0	950.0	A	A	1,150.0
FIC -UNI	D928	-12.213	-76.932	497.0	0.0	497.0	C	BC	525.0
FIC -UNI	KMI	-13.537	-71.903	407.0	0.0	407.0	C	C	437.5
FIC -UNI	SCIQ	-3.741	-73.245	202.0	0.0	202.0	D	DE	190.0
RENAC	AAM2	-1.269	-78.611	311.0	0.0	311.0	D	D	270.0
RENAC	ACH1	-3.287	-79.910	133.0	0.0	133.0	E	E	180.0
RENAC	ACHN	-0.698	-80.084	133.0	200.0	200.0	D	D	270.0
RENAC	ACUE	-2.910	-78.959	340.0	0.0	340.0	D	D	270.0
RENAC	AES2	0.991	-79.646	182.0	0.0	182.0	E	E	180.0
RENAC	AGYE	-2.054	-79.952	306.0	1,800.0	1,800.0	A	A	1,150.0
RENAC	AIB1	0.347	-78.125	163.0	0.0	163.0	E	E	180.0
RENAC	AIB2	0.349	-78.106	447.0	0.0	447.0	C	C	437.5
RENAC	ALAT	-0.926	-78.618	275.0	0.0	275.0	D	D	270.0
RENAC	ALIB	-2.243	-80.846	165.0	429.0	429.0	C	C	437.5
RENAC	ALJ1	-3.987	-79.197	334.0	0.0	334.0	D	D	270.0
RENAC	ALOR	1.293	-78.847	136.0	0.0	136.0	E	E	180.0
RENAC	AMIL	-2.181	-79.529	116.0	0.0	116.0	E	E	180.0
RENAC	AMNT	-0.941	-80.735	288.0	496.0	496.0	C	C	437.5
RENAC	AOTA	0.240	-78.256	298.0	0.0	298.0	D	D	270.0
RENAC	APED	0.068	-80.057	215.0	342.0	342.0	D	D	270.0
RENAC	APO1	-1.038	-80.460	299.0	224.0	224.0	D	D	270.0
RENAC	ASDO	-0.263	-79.124	290.0	0.0	290.0	D	D	270.0
RENAC	ATUL	0.772	-77.723	324.0	0.0	324.0	D	D	270.0
RENAC	EPNL	-0.212	-78.492	287.0	0.0	287.0	D	D	270.0
RENAC	PRAM	-0.145	-78.495	306.0	0.0	306.0	D	D	270.0

## A.2. LIST OF EVENTS

Four-hundred and fifty-four (454) events mainly from Peru, Chile, Ecuador are described in the following table. These events comprise three-thousands seven-hundred and fifty (3750) records. Each record has two horizontal and one vertical components. All this information presented was used for the regression analysis to develop the GMPE for each IM.

EVENT ID	DEPTH (km)	DATE	UTC TIME	LOCATION	LATITUDE	LONGITUDE	MOMENT MAGNITUDE Mw	NUMBER OF STATIONS
(1)	(2)	(3)	(4)	(5)	(6)	(7)	(8)	(9)
1	50.00	31/01/1951	16:39:00	Lima, Peru	-12.210	-76.930	5.7	1
2	24.00	17/10/1966	21:41:00	Barranca, Lima, Peru	-10.700	-78.700	8.1	1
3	64.00	31/05/1970	20:23:00	Chimbote, Peru	-9.360	-78.870	7.1	1
4	53.90	29/11/1971	20:14:13	Huacho, Lima Peru	-11.340	-77.790	5.6	1
5	13.00	03/10/1974	14:21:00	Lima, Peru	-12.500	-77.980	7.1	2
6	12.80	09/11/1974	12:59:54	Lima, Peru	-12.520	-77.590	6.4	2
7	113.80	01/04/1997	18:33:32	Putre, Chile	-18.298	-69.526	6.2	2
8	58.40	11/08/2000	17:31:13	Tacna, Peru	-18.184	-70.471	5.2	1
9	33.00	23/06/2001	20:33:07	Atico, Arequipa, Peru	-16.173	-73.706	8.4	8
10	33.00	07/07/2001	11:55:59	Ilo, Moquegua, Peru	-17.490	-72.000	4.8	1
11	33.00	07/07/2001	21:27:33	Ilo, Moquegua, Peru	-17.590	-71.710	5.0	1
12	33.00	02/01/2003	00:20:00	Mollendo, Arequipa, Peru	-17.700	-72.240	5.1	1
13	33.00	20/02/2003	20:07:00	Tacna, Peru	-18.490	-71.400	5.1	3
14	33.00	06/04/2003	03:16:00	Lima, Peru	-12.050	-77.660	4.7	1
15	44.00	15/04/2003	19:14:00	Lima, Peru	-12.130	-77.380	4.1	1
16	33.00	26/04/2003	12:52:00	Punta Negra, Lima, Peru	-12.510	-77.180	4.2	1
17	51.00	28/05/2003	21:26:00	Punta Negra, Lima, Peru	-12.510	-77.190	5.4	1
18	33.00	29/05/2003	04:48:00	Punta Negra, Lima, Peru	-12.520	-77.230	4.4	1
19	34.00	29/05/2003	10:42:00	Punta Negra, Lima, Peru	-12.520	-77.290	4.3	1
20	33.00	01/06/2003	06:26:00	Punta Negra, Lima, Peru	-12.560	-77.270	4.0	1
21	33.00	13/06/2003	04:42:00	Punta Negra, Lima, Peru	-12.520	-77.190	4.1	1
22	66.00	02/07/2003	20:30:00	Lima, Peru	-12.110	-76.670	4.7	1
23	345.00	27/07/2003	11:41:28	Sucre, Bolivia	-20.050	-65.070	5.7	3
24	55.00	19/09/2003	11:33:00	San Lorenzo, Lima, Peru	-12.110	-77.190	4.4	1
25	44.00	16/10/2003	00:21:00	Huaral, Lima, Peru	-11.690	-77.790	4.4	1
26	33.00	08/12/2003	22:27:00	Lima, Peru	-12.440	-77.860	4.8	1
27	55.00	30/12/2003	23:41:00	Pucusana, Lima, Peru	-12.690	-76.940	4.5	1
28	121.00	03/01/2004	21:08:00	Arequipa, Peru	-16.280	-71.430	4.7	1
29	86.00	25/01/2004	23:36:00	Las Yaras, Tacna, Peru	-17.840	-70.560	4.3	2
30	54.00	23/02/2004	04:43:00	Lima, Peru	-12.160	-76.660	4.0	1
31	50.00	24/02/2004	14:46:31	Pucusana, Lima, Peru	-12.520	-76.930	4.2	1
32	37.00	02/04/2004	16:54:39	Asia, Lima, Peru	-12.980	-77.130	4.7	1
33	74.00	19/04/2004	00:51:51	Huachochiri, Lima, Peru	-12.230	-76.400	4.3	1
34	42.00	19/05/2004	20:54:46	Lima, Peru	-12.250	-77.460	4.5	1
35	100.00	30/05/2004	16:44:07	Arequipa, Peru	-16.610	-71.230	4.6	1
36	34.00	15/07/2004	14:30:43	Lima, Peru	-12.410	-77.280	4.1	1
37	99.00	21/07/2004	07:35:00	Moquegua, Peru	-17.320	-70.910	4.5	2
38	52.00	23/07/2004	12:13:00	Arica, Chile	-18.650	-70.920	4.7	2
39	95.00	30/07/2004	10:33:00	San Mateo, Lima, Peru	-11.900	-76.020	4.5	1
40	93.00	25/08/2004	05:12:50	Tarapaca, Chile	-20.353	-68.930	5.1	1
41	45.00	05/09/2004	11:45:34	Lima, Peru	-12.100	-77.490	4.4	1
42	45.00	16/09/2004	02:09:00	Pucusana, Lima, Peru	-12.530	-76.960	4.2	1
43	46.00	27/09/2004	07:34:00	Lurín, Lima, Peru	-12.360	-77.000	4.2	1
44	59.00	02/10/2004	02:25:00	Lima, Peru	-12.000	-77.070	4.2	1
45	56.00	23/10/2004	10:49:00	Mala, Lima, Peru	-12.500	-76.510	4.2	1
46	68.00	26/10/2004	15:28:30	Punta Negra, Lima, Peru	-12.370	-76.850	4.3	1
47	41.00	10/11/2004	02:21:00	Pucusana, Lima, Peru	-12.720	-77.030	4.5	1
48	52.00	24/12/2004	16:52:00	Pucusana, Lima, Peru	-12.450	-76.850	4.3	1
49	109.20	19/03/2005	01:35:59	Chile - Bolivia-Border	-20.415	-68.626	5.4	1
50	96.10	25/03/2005	03:54:27	Lirima, Chile	-20.290	-68.937	5.1	1
51	71.00	03/05/2005	19:13:00	Marcona, Peru	-15.010	-74.810	5.5	2
52	118.00	03/06/2005	19:24:00	Coalaque, Peru	-16.660	-71.060	4.7	6
53	90.00	08/06/2005	12:50:00	Arica y Parinacota, Chile	-18.880	-69.260	5.0	5
54	77.00	13/07/2005	12:06:08	Tacna, Peru	-17.940	-70.050	4.9	2
55	72.00	13/07/2005	22:41:00	Tacna, Peru	-17.950	-70.320	4.9	1
56	49.00	19/07/2005	08:45:19	Lima, Peru	-12.850	-76.840	4.4	1
57	115.00	26/09/2005	01:55:41	Yurimaguas, Peru	-5.800	-76.200	6.5	3
58	34.60	09/04/2006	20:50:46	Iquique, Chile	-20.450	-70.244	5.7	2
59	88.80	06/06/2006	13:57:49	Tarapacá, Chile	-20.789	-69.122	5.0	1
60	80.90	15/08/2007	12:00:50	Tarapacá, Chile	-20.744	-69.131	4.4	1
61	40.00	15/08/2007	23:40:58	Pisco, Peru	-13.670	-76.760	7.9	5
62	100.00	25/10/2007	08:35:18	Tarapacá, Chile	-20.602	-68.754	5.6	1
63	40.00	14/11/2007	15:40:51	Tocopilla, Chile	-22.247	-69.890	7.7	12
64	97.20	18/11/2007	07:02:42	Arica y Parinacota, Chile	-18.625	-69.580	5.3	1
65	60.00	02/01/2008	00:33:55	San Vicente de Cañete, Peru	-13.190	-76.330	4.4	1

EVENT ID	DEPTH (km)	DATE	UTC TIME	LOCATION	LATITUDE	LONGITUDE	MOMENT MAGNITUDE Mw	NUMBER OF STATIONS
(1)	(2)	(3)	(4)	(5)	(6)	(7)	(8)	(9)
66	45.20	22/01/2008	09:09:28	Tarapacá, Chile	-19.842	-69.951	5.4	4
67	35.00	04/02/2008	17:01:30	Iquique, Chile	-20.166	-70.037	6.3	4
68	26.00	03/03/2008	15:52:47	Pisco, Peru	-13.810	-77.450	4.6	1
69	48.00	08/03/2008	23:51:39	San Vicente de Cañete, Peru	-13.290	-76.690	4.8	1
70	51.00	29/03/2008	12:51:18	Callao, Peru	-12.250	-77.250	5.2	2
71	25.00	15/07/2008	19:17:43	Cobija, Chile	-22.540	-70.226	5.1	1
72	109.00	11/02/2009	20:45:33	Pica, Chile	-20.249	-68.794	5.6	1
73	25.00	17/04/2009	02:08:09	Pisagua, Chile	-19.584	-70.483	6.1	1
74	66.50	29/10/2009	01:25:13	Iquique, Chile	-20.764	-69.620	4.9	1
75	83.20	13/01/2010	03:52:24	Pica, Chile	-20.298	-68.931	5.1	1
76	36.00	06/05/2010	02:42:00	Tacna, Peru	-18.340	-71.170	6.1	2
77	83.00	12/07/2010	12:44:00	Tacna, Peru	-17.530	-70.670	4.7	2
78	132.20	27/03/2011	13:26:36	Huanuco, Peru	-8.700	-74.620	4.9	1
79	83.00	02/04/2011	10:59:41	Tarapacá, Chile	-19.560	-69.070	5.7	1
80	49.00	26/06/2011	11:45:50	Coast of Lima, Peru	-12.540	-76.870	4.3	2
81	54.00	11/07/2011	15:20:17	Coast of Lima, Peru	-12.520	-77.090	4.2	3
82	54.00	13/07/2011	10:07:51	Coast of Lima, Peru	-12.430	-76.960	5.2	3
83	31.00	30/07/2011	14:02:20	Coast of Lima, Peru	-12.770	-77.390	4.4	4
84	63.00	01/08/2011	14:30:09	Coast of Lima, Peru	-11.770	-77.450	4.3	4
85	24.00	28/10/2011	18:54:34	Ica, Peru	-14.440	-75.970	6.9	5
86	35.00	28/10/2011	23:46:00	Coast of Ica, Peru	-14.540	-76.050	5.6	3
87	56.00	20/11/2011	03:00:28	Coast of Lima, Peru	-11.870	-77.490	4.2	3
88	53.20	19/12/2011	05:37:58	Coast of Lima, Peru	-12.200	-77.090	4.8	6
89	52.00	26/12/2011	20:29:41	Coast of Lima, Peru	-12.810	-76.660	4.3	7
90	52.00	29/12/2011	13:45:40	Coast of Lima, Peru	-12.550	-76.780	4.7	8
91	49.20	30/12/2011	09:22:16	Ica, Peru	-14.420	-75.480	5.0	7
92	48.00	19/01/2012	20:58:34	Coast of Lima, Peru	-12.610	-77.200	4.2	6
93	37.00	23/01/2012	02:31:13	Coast of Lima, Peru	-12.040	-77.710	4.6	4
94	42.00	14/02/2012	04:42:20	Coast of Lima, Peru	-12.410	-76.940	4.9	10
95	47.00	19/02/2012	02:19:23	Coast of Lima, Peru	-11.990	-77.230	4.3	9
96	40.00	29/02/2012	08:50:15	Coast of Lima, Peru	-12.690	-76.750	4.5	4
97	47.10	04/03/2012	16:27:20	Antofagasta, Chile	-21.602	-70.061	5.2	2
98	49.00	07/03/2012	03:52:03	Coast of Lima, Peru	-12.310	-77.110	4.1	5
99	52.00	11/03/2012	08:20:36	Coast of Lima, Peru	-12.540	-77.130	4.2	3
100	45.00	19/03/2012	23:21:45	Coast of Lima, Peru	-11.930	-77.440	4.3	4
101	64.00	20/03/2012	02:36:25	Lima, Peru	-12.880	-76.230	4.6	1
102	61.00	14/04/2012	07:11:10	Coast of Ancash, Peru	-10.480	-78.070	4.7	1
103	60.00	15/05/2012	00:45:49	Coast of Lima, Peru	-13.240	-76.440	4.3	6
104	44.00	27/05/2012	05:21:30	Coast of Ica, Peru	-13.730	-76.340	4.7	3
105	40.00	08/06/2012	12:54:17	Coast of Lima, Peru	-12.700	-77.390	4.5	4
106	48.00	19/06/2012	20:58:34	Coast of Lima, Peru	-12.610	-77.200	4.2	2
107	44.00	28/06/2012	11:18:59	Coast of Lima, Peru	-12.170	-77.650	4.5	6
108	33.00	02/07/2012	23:31:30	Coast of Ica, Peru	-15.010	-76.290	5.5	1
109	50.00	04/07/2012	16:01:37	Coast of Lima, Peru	-12.120	-77.050	4.6	1
110	40.00	16/07/2012	17:21:06	Coast of Lima, Peru	-12.350	-76.860	4.2	3
111	38.00	29/07/2012	02:07:38	Coast of Lima, Peru	-12.420	-77.420	4.1	7
112	58.00	29/07/2012	17:35:49	Coast of Lima, Peru	-12.020	-77.200	4.7	9
113	46.00	01/08/2012	13:02:15	Coast of Lima, Peru	-12.320	-77.340	4.1	8
114	150.00	02/08/2012	09:38:14	Ucayali, Peru	-8.640	-74.190	6.0	7
115	56.00	03/08/2012	13:46:49	Lima, Peru	-12.530	-76.650	4.2	3
116	32.00	08/08/2012	02:53:02	Coast of Lima, Peru	-12.790	-77.250	4.2	5
117	68.00	24/08/2012	07:22:12	Coast of Lima, Peru	-11.760	-77.320	4.2	3
118	40.00	25/08/2012	16:06:37	Coast of Lima, Peru	-12.330	-77.300	4.2	5
119	50.00	10/09/2012	01:35:55	Coast of Lima, Peru	-12.560	-76.830	4.2	4
120	47.00	15/09/2012	11:27:50	Coast of Lima, Peru	-12.520	-77.330	4.3	6
121	42.00	25/09/2012	06:50:45	Coast of Lima, Peru	-12.220	-77.320	4.2	5
122	30.00	03/10/2012	22:48:54	Coast of Ica, Peru	-14.390	-76.310	4.9	3
123	39.00	09/10/2012	02:32:26	Coast of Ica, Peru	-14.060	-76.320	4.7	2
124	30.00	14/10/2012	16:50:29	Coast of Lima, Peru	-11.980	-77.600	4.1	5
125	48.00	22/10/2012	02:26:58	Lima, Peru	-12.090	-76.930	4.2	4
126	52.00	30/10/2012	07:48:53	Coast of Lima, Peru	-12.540	-76.850	4.2	6
127	56.00	30/10/2012	13:35:46	Coast of Lima, Peru	-12.580	-76.920	4.2	4
128	55.00	30/10/2012	19:44:54	Coast of Lima, Peru	-12.520	-76.830	4.5	6
129	50.00	05/11/2012	08:08:11	Coast of Lima, Peru	-12.510	-76.810	4.2	1
130	45.00	10/11/2012	06:57:44	Lima, Peru	-12.450	-76.710	4.2	2
131	38.00	13/11/2012	03:03:47	Coast of Lima, Peru	-12.560	-76.810	4.2	1
132	93.00	13/11/2012	03:11:25	Tarapacá, Chile	-20.540	-69.030	5.1	1
133	50.00	13/11/2012	05:48:58	Coast of Lima, Peru	-12.610	-76.770	4.3	1



EVENT ID	DEPTH (km)	DATE	UTC TIME	LOCATION	LATITUDE	LONGITUDE	MOMENT MAGNITUDE Mw	NUMBER OF STATIONS
(1)	(2)	(3)	(4)	(5)	(6)	(7)	(8)	(9)
134	61.70	16/11/2012	00:38:05	Tarapacá, Chile	-21.506	-69.488	5.0	5
135	50.00	20/11/2012	05:11:14	Coast of Lima, Peru	-12.260	-77.400	4.2	4
136	49.00	27/11/2012	01:50:56	Lima, Peru	-12.500	-76.740	4.2	1
137	51.00	27/11/2012	09:19:59	Coast of Lima, Peru	-10.840	-77.720	4.6	8
138	46.00	05/12/2012	01:33:00	Lima, Peru	-12.010	-77.000	4.0	5
139	51.00	10/12/2012	11:25:24	Coast of Lima, Peru	-11.860	-77.230	4.5	10
140	51.00	22/12/2012	06:43:39	Coast of Lima, Peru	-12.560	-76.820	4.5	10
141	81.50	30/12/2012	13:32:49	Lima - Pasco Border, Peru	-10.750	-76.670	4.5	5
142	58.60	01/01/2013	03:51:12	Tarapacá, Chile	-20.810	-69.670	5.1	2
143	40.00	10/01/2013	05:14:22	Coast of Lima, Peru	-11.670	-77.890	4.5	5
144	91.65	13/01/2013	21:23:27	Tarapacá, Chile	-20.125	-69.324	5.3	3
145	48.00	15/01/2013	19:01:17	Coast of Lima, Peru	-12.370	-77.070	4.9	7
146	40.00	18/01/2013	18:40:00	Coast of Lima, Peru	-12.040	-77.660	5.1	1
147	42.00	02/03/2013	02:51:25	Coast of Lima, Peru	-12.710	-76.930	4.4	6
148	35.00	05/03/2013	04:24:03	Coast of Lima, Peru	-12.630	-76.850	4.2	6
149	45.00	11/03/2013	14:33:09	Coast of Lima, Peru	-12.880	-77.170	4.5	7
150	66.45	19/03/2013	23:06:29	Lima - Ica Border, Peru	-13.004	-76.087	4.9	6
151	26.00	30/03/2013	17:30:46	Coast of Ancash - La Libertad Border, Peru	-9.531	-79.237	5.2	4
152	67.30	06/04/2013	08:49:27	Coast of Ancash - La Libertad Border, Peru	-8.871	-78.913	4.5	3
153	45.75	07/04/2013	20:40:49	Coast of Lima - Ica Border, Peru	-13.588	-76.364	4.7	5
154	58.00	12/04/2013	13:53:24	Coast of Lima, Peru	-11.740	-77.200	4.2	4
155	75.75	21/04/2013	09:40:00	Ica, Peru	-13.695	-75.672	4.5	1
156	34.65	04/05/2013	04:06:19	Coast of Lima, Peru	-12.513	-78.157	4.6	1
157	48.00	15/06/2013	19:01:17	Coast of Lima, Peru	-12.370	-77.070	4.9	2
158	52.40	18/06/2013	18:40:01	Coast of Lima, Peru	-11.857	-77.469	5.1	7
159	42.20	12/07/2013	19:27:35	Coast of Lima, Peru	-12.580	-77.018	4.3	4
160	20.00	19/08/2013	15:21:43	Coast of Moquegua - Ica Border, Peru	-18.290	-71.640	4.9	2
161	100.10	07/09/2013	19:13:31	Tarapacá, Chile	-19.617	-69.299	5.2	1
162	59.00	24/09/2013	00:18:40	Coast of Lima, Peru	-12.460	-76.850	4.3	5
163	56.00	11/10/2013	16:49:43	Coast of Lima - Peru	-11.900	-77.140	4.2	6
164	45.00	17/10/2013	10:51:01	Coast of Lima - Peru	-12.310	-77.230	4.2	7
165	27.00	18/10/2013	07:32:30	Coast of Lima - Peru	-12.540	-77.100	4.5	6
166	60.00	18/10/2013	09:47:54	Coast of Lima - Peru	-12.340	-76.800	4.2	6
167	55.00	20/10/2013	01:16:17	Lima - Peru	-11.320	-77.140	4.2	5
168	67.79	25/11/2013	20:06:28	Lima - Peru	-12.685	-76.341	5.6	4
169	70.80	04/12/2013	05:39:33	Antofagasta, Chile	-24.574	-69.298	5.3	2
170	38.49	02/01/2014	22:27:46	Coast of Lima - Ancash Border, Peru	-11.163	-78.246	4.4	3
171	99.35	12/02/2014	11:43:10	Antofagasta, Chile	-22.348	-68.767	5.5	2
172	54.00	13/02/2014	03:45:33	Coast of Lima	-11.470	-77.870	4.4	3
173	50.52	18/02/2014	23:35:55	Ica, Peru	-14.362	-75.865	5.9	5
174	38.00	20/02/2014	20:15:35	Coast of Lima	-12.830	-76.990	4.4	5
175	40.00	22/02/2014	16:26:40	Coast of Lima	-11.900	-77.210	4.3	6
176	72.00	25/02/2014	03:05:28	Lima, Peru	-11.190	-77.110	4.6	4
177	50.48	01/03/2014	10:52:31	Coast of Lima - Ica Border, Peru	-13.612	-76.432	4.7	1
178	38.00	13/03/2014	05:06:05	Coast of Lima, Peru	-12.610	-76.960	4.2	3
179	92.60	14/03/2014	15:31:18	Tarapacá, Chile	-19.459	-69.453	5.0	1
180	18.00	15/03/2014	08:59:19	Coast of Ica, Peru	-14.212	-76.446	6.1	6
181	20.60	16/03/2014	21:16:29	Coast of Tarapaca, Chile	-19.965	-70.814	6.7	12
182	22.70	17/03/2014	00:12:11	Coast of Tarapaca, Chile	-19.987	-70.747	4.7	1
183	28.30	17/03/2014	05:11:34	Coast of Tarapaca, Chile	-19.962	-70.944	6.3	9
184	36.20	17/03/2014	05:19:35	Coast of Tarapaca, Chile	-19.994	-70.885	5.1	1
185	9.60	17/03/2014	05:44:33	Coast of Tarapaca, Chile	-20.012	-70.834	4.7	1
186	32.90	17/03/2014	11:12:17	Coast of Tarapaca, Chile	-19.912	-70.908	5.1	1
187	45.00	18/03/2014	12:51:26	Coast of Lima, Peru	-12.790	-77.040	4.2	2
188	19.80	18/03/2014	21:33:08	Coast of Tarapaca, Chile	-20.025	-70.844	5.0	1
189	83.00	20/03/2014	12:05:10	Lima - Junin Border, Peru	-11.890	-76.130	4.6	5
190	99.55	22/03/2014	05:56:04	Arica y Parinacota, Chile	-18.428	-69.818	4.6	2
191	31.80	22/03/2014	12:59:54	Coast of Tarapaca - Arica y Parinacota border, Chile	-19.836	-71.384	5.6	6
192	20.10	22/03/2014	13:14:56	Coast of Tarapaca - Arica y Parinacota border, Chile	-19.821	-70.881	5.2	2
193	33.33	23/03/2014	18:20:02	Coast of Tarapaca - Arica y Parinacota border, Chile	-19.737	-70.931	6.3	12
194	43.00	24/03/2014	15:45:32	Coast of Tarapaca - Arica y Parinacota border, Chile	-19.594	-70.791	5.4	2
195	94.25	31/03/2014	12:53:06	Tarapacá, Chile	-19.457	-69.068	5.6	8
196	34.30	01/04/2014	23:46:46	Coast of Tarapaca - Arica y Parinacota border, Chile	-19.583	-70.863	8.2	29
197	22.50	02/04/2014	00:03:13	Coast of Tarapaca - Arica y Parinacota border, Chile	-19.839	-70.934	6.1	5
198	36.20	02/04/2014	00:04:54	Coast of Tarapaca - Arica y Parinacota border, Chile	-19.624	-70.628	5.1	1
199	23.30	02/04/2014	00:33:47	Tarapacá, Chile	-20.191	-70.821	5.5	2
200	34.00	02/04/2014	00:37:51	Coast of Tarapaca, Chile	-20.032	-70.521	5.1	7
201	33.00	02/04/2014	00:57:52	Coast of Tarapaca, Chile	-19.805	-70.485	4.7	1

EVENT ID	DEPTH (km)	DATE	UTC TIME	LOCATION	LATITUDE	LONGITUDE	MOMENT MAGNITUDE Mw	NUMBER OF STATIONS
(1)	(2)	(3)	(4)	(5)	(6)	(7)	(8)	(9)
202	42.10	02/04/2014	03:04:41	Tarapacá, Chile	-19.750	-69.973	4.7	7
203	30.50	02/04/2014	03:20:48	Tarapacá, Chile	-20.119	-70.394	4.7	1
204	33.30	02/04/2014	03:40:15	Coast of Tarapaca, Chile	-19.966	-71.116	5.0	1
205	33.70	02/04/2014	04:13:10	Coast of Tarapaca - Arica y Parinacota border, Chile	-19.573	-70.530	4.9	4
206	28.80	02/04/2014	04:16:11	Coast of Tarapaca, Chile	-19.955	-70.879	5.0	1
207	38.60	02/04/2014	04:46:20	Coast of Tarapaca, Chile	-20.134	-70.792	5.5	3
208	26.30	02/04/2014	05:09:21	Coast of Tarapaca, Chile	-20.382	-70.585	4.8	1
209	45.70	02/04/2014	07:03:44	Coast of Tarapaca, Chile	-20.148	-70.103	4.7	6
210	32.20	02/04/2014	11:07:32	Coast of Tarapaca, Chile	-19.992	-71.053	5.5	1
211	28.10	02/04/2014	19:50:23	Coast of Tarapaca, Chile	-20.058	-70.520	4.7	1
212	35.00	03/04/2014	01:58:31	Coast of Tarapaca, Chile	-20.300	-70.635	6.6	11
213	24.00	03/04/2014	02:43:16	Coast of Tarapaca, Chile	-20.510	-70.420	7.4	27
214	12.90	03/04/2014	02:56:08	Coast of Tarapaca, Chile	-20.737	-70.540	5.2	3
215	28.50	03/04/2014	02:59:54	Coast of Tarapaca, Chile	-20.568	-70.426	4.7	1
216	36.10	03/04/2014	03:11:19	Coast of Tarapaca, Chile	-20.615	-70.556	5.1	3
217	20.40	03/04/2014	03:45:55	Coast of Tarapaca, Chile	-19.965	-70.913	5.0	1
218	26.10	03/04/2014	04:04:47	Coast of Tarapaca, Chile	-20.348	-70.544	4.7	5
219	12.10	03/04/2014	04:17:59	Coast of Tarapaca, Chile	-20.593	-70.675	5.0	1
220	29.80	03/04/2014	05:26:15	Coast of Tarapaca, Chile	-20.799	-70.675	6.3	9
221	19.60	03/04/2014	05:34:33	Coast of Tarapaca, Chile	-20.466	-70.573	4.7	1
222	31.00	03/04/2014	05:51:45	Coast of Tarapaca, Chile	-20.769	-70.437	5.4	4
223	30.10	03/04/2014	06:54:32	Coast of Tarapaca, Chile	-20.625	-70.635	4.8	1
224	37.10	03/04/2014	09:08:57	Coast of Tarapaca, Chile	-20.284	-70.468	4.9	5
225	16.10	03/04/2014	09:23:23	Coast of Tarapaca, Chile	-20.595	-70.767	5.2	3
226	32.40	03/04/2014	11:50:48	Coast of Tarapaca, Chile	-20.657	-70.338	4.8	1
227	27.50	03/04/2014	13:49:23	Coast of Tarapaca, Chile	-20.475	-70.486	4.7	1
228	41.10	03/04/2014	23:37:51	Coast of Tarapaca, Chile	-20.178	-70.627	5.1	4
229	32.60	04/04/2014	01:37:52	Coast of Tarapaca, Chile	-20.622	-70.605	6.1	8
230	20.30	04/04/2014	09:53:25	Coast of Tarapaca, Chile	-20.625	-70.702	4.7	1
231	40.20	05/04/2014	00:33:58	Coast of Tarapaca, Chile	-20.173	-70.513	4.9	2
232	30.10	05/04/2014	04:05:03	Coast of Tarapaca, Chile	-20.707	-70.688	4.8	2
233	21.20	05/04/2014	05:28:58	Coast of Tarapaca, Chile	-20.604	-70.674	4.7	1
234	43.20	05/04/2014	05:44:56	Coast of Tarapaca, Chile	-20.161	-70.538	5.4	5
235	45.20	05/04/2014	20:20:28	Coast of Tarapaca, Chile	-19.872	-70.225	4.7	6
236	40.70	06/04/2014	20:55:56	Coast of Tarapaca, Chile	-19.776	-70.495	4.7	3
237	35.60	07/04/2014	13:43:20	Coast of Tarapaca, Chile	-20.131	-70.905	6.1	8
238	20.30	07/04/2014	13:47:34	Coast of Tarapaca, Chile	-20.135	-70.921	5.0	4
239	29.40	07/04/2014	17:46:33	Coast of Tarapaca, Chile	-20.135	-70.374	4.8	7
240	39.10	08/04/2014	01:03:02	Coast of Tarapaca, Chile	-19.768	-70.481	5.0	11
241	30.00	08/04/2014	05:40:48	Coast of Tarapaca, Chile	-20.512	-70.654	4.7	4
242	26.00	08/04/2014	05:43:55	Coast of Tarapaca, Chile	-20.541	-70.699	4.9	2
243	33.30	09/04/2014	07:49:23	Coast of Tarapaca, Chile	-19.869	-70.937	4.7	1
244	32.80	09/04/2014	07:52:57	Coast of Tarapaca, Chile	-19.874	-70.883	4.7	1
245	15.20	09/04/2014	11:06:14	Coast of Tarapaca, Chile	-20.784	-70.806	5.0	1
246	22.90	09/04/2014	11:14:44	Coast of Tarapaca, Chile	-20.616	-70.923	5.5	3
247	15.80	10/04/2014	00:10:34	Coast of Tarapaca, Chile	-20.336	-70.871	4.8	2
248	38.20	11/04/2014	00:01:44	Coast of Tarapaca, Chile	-20.715	-70.653	6.2	17
249	40.00	11/04/2014	12:00:52	Coast of Tarapaca, Chile	-20.080	-70.510	5.2	14
250	22.10	11/04/2014	23:56:39	Coast of Tarapaca, Chile	-20.706	-70.720	4.7	2
251	22.10	13/04/2014	12:11:31	Coast of Tarapaca, Chile	-20.584	-70.718	5.2	9
252	25.60	14/04/2014	05:56:18	Coast of Tarapaca, Chile	-20.732	-70.789	5.0	5
253	43.50	14/04/2014	22:20:36	Peru - Chile Border	-18.558	-70.898	4.7	1
254	27.90	15/04/2014	16:21:17	Coast of Tarapaca, Chile	-20.189	-70.827	5.2	7
255	67.00	21/04/2014	01:05:34	Southern Lima, Peru	-13.010	-76.190	4.5	3
256	35.00	27/04/2014	16:28:23	Coast of Lima, Peru	-13.180	-76.840	4.5	1
257	43.70	28/04/2014	04:59:36	Coast of Tarapaca, Chile	-19.562	-70.374	5.0	12
258	26.70	01/05/2014	16:45:23	Coast of Tarapaca - Arica y Parinacota border, Chile	-19.953	-71.283	4.9	1
259	31.80	04/05/2014	04:46:48	Coast of Tarapaca - Arica y Parinacota border, Chile	-20.011	-71.055	5.0	3
260	42.50	05/05/2014	02:01:39	Coast of Tarapaca, Chile	-20.176	-70.351	4.7	11
261	37.90	05/05/2014	09:02:56	Coast of Tarapaca - Arica y Parinacota border, Chile	-19.279	-71.027	4.8	2
262	33.60	07/05/2014	13:27:08	Coast of Tarapaca - Arica y Parinacota border, Chile	-19.961	-70.979	4.9	3
263	95.30	10/05/2014	03:12:03	Tarapacá, Chile	-20.171	-69.230	4.7	9
264	44.00	10/05/2014	17:57:11	Coast of Lima, Peru	-12.630	-77.060	4.7	1
265	33.40	17/05/2014	10:18:00	Coast of Tarapaca, Chile	-19.960	-70.977	4.7	3
266	39.00	24/05/2014	18:58:24	Coast of Lima, Peru	-11.840	-77.460	4.2	1
267	30.10	27/05/2014	03:34:41	Coast of Tarapaca, Chile	-20.859	-70.470	4.8	3
268	33.60	28/05/2014	18:14:04	Coast of Tarapaca, Chile	-20.250	-70.722	4.6	1
269	59.60	30/05/2014	15:32:27	Southern Coast of Tarapaca, Chile	-21.302	-69.999	5.5	6

EVENT ID	DEPTH (km)	DATE	UTC TIME	LOCATION	LATITUDE	LONGITUDE	MOMENT MAGNITUDE Mw	NUMBER OF STATIONS
(1)	(2)	(3)	(4)	(5)	(6)	(7)	(8)	(9)
270	37.17	03/06/2014	21:34:11	Coast of Lima, Peru	-12.552	-77.148	5.3	5
271	23.80	04/06/2014	17:04:29	Coast of Tarapaca, Chile	-20.645	-70.790	5.0	5
272	37.40	05/06/2014	20:19:31	Coast of Tarapaca, Chile	-20.356	-70.220	5.0	9
273	56.27	10/06/2014	04:03:26	Coast of Arequipa, Peru	-16.610	-73.036	5.3	1
274	19.20	18/06/2014	04:02:26	Coast of Tarapaca, Chile	-20.210	-70.885	4.7	1
275	21.20	19/06/2014	09:38:37	Coast of Tarapaca, Chile	-19.939	-70.948	5.3	11
276	33.20	20/06/2014	20:22:29	Coast of Tarapaca - Arica y Parinacota border, Chile	-19.761	-71.037	5.8	6
277	34.35	08/07/2014	16:04:21	Coast of Tarapaca, Chile	-20.784	-70.528	4.7	3
278	38.55	13/07/2014	20:54:15	Coast of Tarapaca, Chile	-20.235	-70.312	5.6	19
279	12.00	14/07/2014	16:24:34	Coast of Arequipa, Peru	-17.899	-73.530	5.2	2
280	36.00	15/07/2014	09:01:42	Coast of Lima, Peru	-12.170	-77.450	4.4	1
281	35.85	18/07/2014	05:24:09	Coast of Arequipa, Peru	-20.158	-71.011	4.7	1
282	38.85	21/07/2014	00:21:29	Coast of Tarapaca, Chile	-20.160	-70.555	4.8	5
283	34.83	23/07/2014	09:57:46	Coast of Piura, Peru	-5.686	-80.985	5.0	1
284	27.40	29/07/2014	00:47:18	Coast of Tarapaca, Chile	-20.130	-70.497	4.7	8
285	43.00	12/08/2014	05:12:55	Coast of Lima, Peru	-11.810	-77.670	4.5	4
286	50.90	14/08/2014	00:02:55	Tarapacá, Chile	-20.158	-70.023	5.5	16
287	90.45	16/08/2014	09:42:58	Northern Antofagasta, Chile	-21.751	-69.113	4.9	4
288	100.20	23/08/2014	04:45:33	Tarapacá, Chile	-20.187	-69.081	5.5	18
289	59.00	25/08/2014	14:31:37	Arequipa, Peru	-16.258	-73.262	5.5	2
290	36.15	04/09/2014	09:26:53	Tarapacá, Chile	-20.713	-70.348	5.0	7
291	42.90	26/10/2014	02:52:53	Tarapacá, Chile	-20.575	-70.568	4.7	6
292	39.96	15/11/2014	00:18:38	Coast of Lima, Peru	-12.795	-77.032	5.4	6
293	16.55	22/11/2014	06:50:55	Coast of Tarapaca, Chile	-20.035	-71.120	5.0	2
294	29.60	29/11/2014	14:18:10	Coast of Tarapaca - Arica and Parinacota border, Chile	-19.948	-71.133	5.1	3
295	34.50	02/12/2014	03:56:47	Coast of Tarapaca, Chile	-20.281	-71.053	4.7	1
296	33.55	12/12/2014	12:35:32	Coast of Tarapaca - Arica and Parinacota border, Chile	-19.855	-70.912	5.3	5
297	99.50	16/12/2014	04:43:48	Tarapacá, Chile	-20.469	-68.969	4.8	5
298	103.30	18/12/2014	06:24:38	Tarapacá, Chile	-20.381	-68.867	5.2	6
299	41.00	11/01/2015	21:39:37	Coast of Arequipa, Peru	-16.030	-74.150	5.1	6
300	48.20	22/01/2015	16:15:37	Antofagasta, Chile	-22.990	-70.222	4.7	2
301	118.95	23/01/2015	14:12:29	Arica y Parinacota, Chile	-18.130	-69.479	5.0	1
302	27.00	12/02/2015	01:59:37	Coast of Ancash - La Libertad Border, Peru	-9.260	-79.360	5.0	3
303	48.61	01/03/2015	15:08:29	Coast of Arequipa, Peru	-17.211	-71.839	4.9	12
304	44.50	18/03/2015	05:39:18	Coast of Tacna, Peru	-18.438	-71.260	4.8	15
305	45.00	18/03/2015	19:56:12	Coast of Arequipa, Peru	-16.760	-72.895	4.9	12
306	48.52	19/03/2015	11:51:59	Coast of Tumbes, Peru	-3.386	-80.713	5.0	2
307	26.53	19/03/2015	13:11:49	Coast of Tacna, Peru	-18.512	-71.514	4.7	3
308	45.50	21/03/2015	16:58:14	Coast of Ancash, Peru	-9.372	-78.909	5.0	3
309	15.50	24/03/2015	22:46:52	Coast of Tarapaca, Chile	-20.680	-70.785	4.9	6
310	46.12	28/03/2015	22:19:33	Coast of Ancash, Peru	-9.915	-78.659	4.7	6
311	40.33	01/04/2015	16:45:19	Coast of Ancash - Lima Border, Peru	-10.674	-78.330	5.3	22
312	26.11	13/04/2015	14:32:29	Coast of La Libertad, Peru	-8.406	-80.216	5.0	3
313	15.50	15/04/2015	06:59:15	Coast of Ica, Peru	-14.596	-76.396	5.2	13
314	27.00	26/04/2015	23:35:27	Coast of Ica, Peru	-8.381	-80.067	5.6	3
315	48.89	14/05/2015	18:33:32	Ica, Peru	-14.280	-75.727	5.3	4
316	86.29	17/05/2015	10:50:09	Ayacucho - Huancavelica Border, Peru	-13.351	-74.844	4.7	2
317	27.40	23/05/2015	13:09:46	Coast of Tarapaca, Chile	-20.190	-70.807	4.7	1
318	32.00	31/05/2015	16:08:30	Coast of Tarapaca, Chile	-19.910	-70.911	5.0	2
319	32.84	01/06/2015	11:57:19	Coast of Tacna, Peru	-18.284	-71.189	4.7	4
320	24.38	04/06/2015	21:34:57	Coast of Lima, Peru	-12.465	-77.633	4.8	8
321	17.13	07/06/2015	06:39:27	Coast of Piura - Lambayeque border, Peru	-6.645	-81.211	5.0	2
322	31.30	09/06/2015	12:38:51	Coast of Tarapaca, Chile	-20.207	-70.945	4.7	2
323	31.13	28/06/2015	10:16:55	Coast of Arequipa, Peru	-15.893	-74.587	5.0	10
324	25.50	29/06/2015	09:09:14	Coast of Arequipa, Peru	-16.143	-74.338	5.8	16
325	76.72	23/07/2015	15:39:47	Arequipa, Peru	-16.006	-73.253	4.7	2
326	38.50	24/07/2015	23:14:40	Coast of Tarapaca, Chile	-20.289	-70.176	5.3	11
327	89.80	28/08/2015	18:39:13	Lima, Peru	-12.284	-76.171	5.1	35
328	97.20	01/09/2015	15:28:51	Tarapacá, Chile	-19.785	-69.245	5.5	14
329	16.54	04/09/2015	03:51:20	Coast of Ica, Peru	-14.320	-76.698	5.0	15
330	30.70	10/09/2015	14:40:16	Coast of Tarapaca, Chile	-19.979	-70.970	4.7	1
331	35.70	15/09/2015	22:03:34	Coast of Tarapaca, Chile	-19.997	-70.961	5.2	3
332	34.80	16/09/2015	18:24:22	Coast of Tarapaca, Chile	-19.936	-70.959	5.2	4
333	17.15	16/09/2015	22:54:28	Coast of Coquimbo, Chile	-31.594	-71.801	8.4	54
334	26.10	16/09/2015	22:59:15	Coast of Coquimbo, Chile	-31.626	-71.762	7.1	17
335	25.50	16/09/2015	23:18:37	Coast of Coquimbo, Chile	-31.596	-71.718	7.4	49
336	90.70	25/09/2015	03:21:57	Tarapacá, Chile	-20.910	-69.221	5.2	8
337	88.00	04/10/2015	14:50:34	Arequipa, Peru	-16.344	-72.238	5.3	18

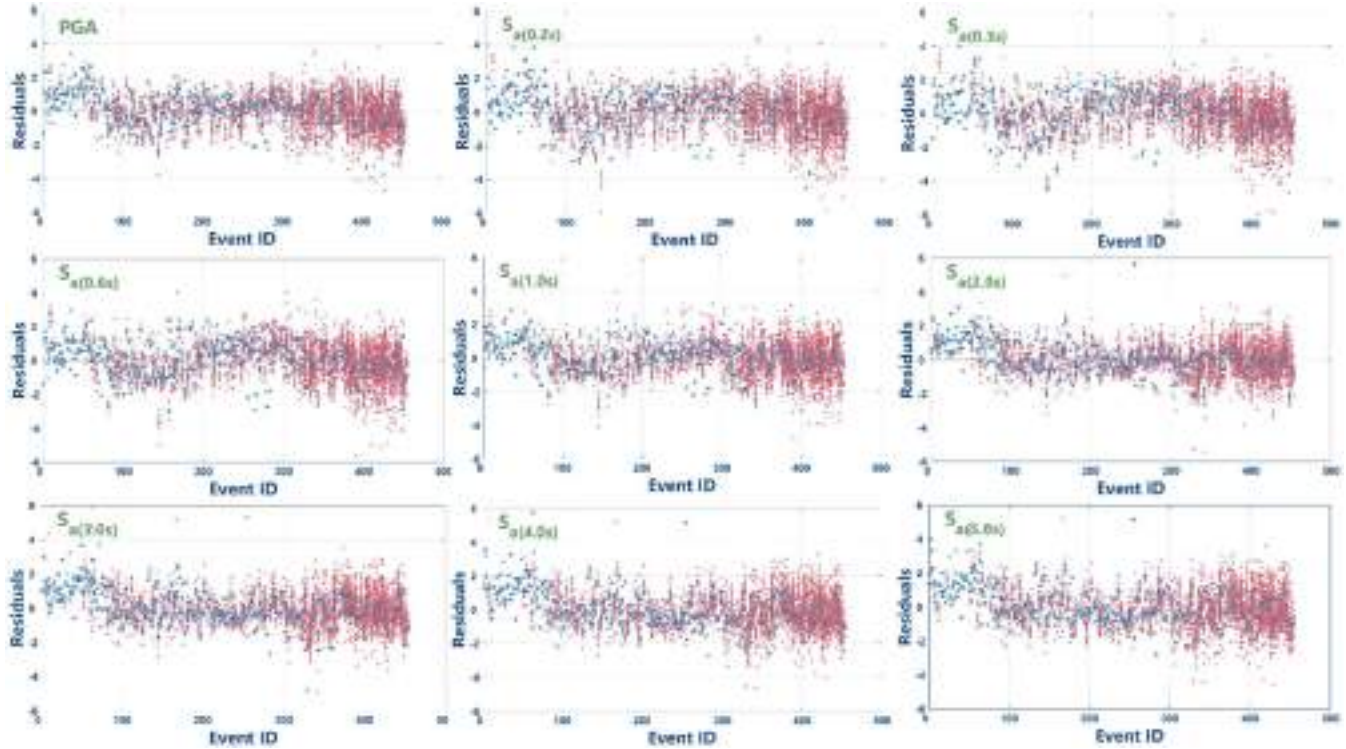
EVENT ID	DEPTH (km)	DATE	UTC TIME	LOCATION	LATITUDE	LONGITUDE	MOMENT MAGNITUDE Mw	NUMBER OF STATIONS
(1)	(2)	(3)	(4)	(5)	(6)	(7)	(8)	(9)
338	95.16	12/11/2015	19:49:21	Arequipa, Peru	-16.092	-72.131	5.1	7
339	37.20	27/11/2015	21:00:21	Coast of Antofagasta, Chile	-24.779	-70.546	6.2	24
340	38.90	27/11/2015	21:45:13	Coast of Antofagasta, Chile	-24.740	-70.547	5.0	1
341	124.10	01/12/2015	13:39:56	Arequipa - Moquegua Border , Peru	-16.500	-71.231	5.0	15
342	55.35	23/12/2015	04:14:43	Ica - Arequipa Border, Peru	-15.181	-74.922	5.0	20
343	50.26	04/01/2016	19:01:53	Coast of Ancash, Peru	-9.721	-78.413	5.1	3
344	53.10	13/01/2016	12:20:40	Northern Tarapaca, Chile	-19.278	-70.131	5.0	4
345	90.80	17/01/2016	15:28:40	Antofagasta - Tarapaca border, Chile	-21.339	-68.885	5.0	3
346	108.02	19/01/2016	02:04:31	Apurimac, Peru	-14.061	-72.978	5.2	5
347	55.03	20/01/2016	12:01:19	Arequipa, Peru	-15.927	-74.099	5.1	7
348	86.97	09/02/2016	08:18:56	Arequipa, Peru	-15.562	-73.363	5.0	17
349	29.50	16/02/2016	10:46:27	Coast of Arequipa, Peru	-16.632	-73.742	5.7	17
350	40.15	02/03/2016	09:49:55	Peru - Chile Border	-18.660	-70.707	5.2	12
351	20.67	16/04/2016	23:58:35	Manabís - Esmeralda border, Ecuador	0.371	-79.970	7.5	21
352	15.00	12/05/2016	23:09:27	Ica - Arequipa Border, Peru	-15.833	-75.051	5.1	6
353	30.67	05/06/2016	04:07:05	Coast of Arequipa, Peru	-15.994	-74.162	5.1	10
354	31.95	05/07/2016	02:29:03	Coast of Tarapaca, Chile	-20.157	-70.979	5.0	2
355	25.00	08/08/2016	19:03:23	Coast of Ica, Peru	-14.519	-76.343	5.2	8
356	49.46	19/08/2016	09:49:11	Coast of Arequipa, Peru	-17.052	-72.360	5.3	17
357	77.79	01/09/2016	08:04:11	Arequipa, Peru	-16.520	-72.263	5.0	17
358	30.48	25/09/2016	18:23:59	Coast of Peru - Ecuador Border	-3.332	-80.850	5.0	1
359	33.37	16/10/2016	13:04:25	Coast of Lambayeque, Peru	-7.055	-80.273	5.3	5
360	52.42	17/10/2016	17:16:00	Ica, Peru	-14.295	-75.555	5.0	6
361	50.56	19/10/2016	19:31:14	Coast of Ica, Peru	-13.608	-76.400	5.0	15
362	59.69	28/10/2016	03:47:30	Coast of Lima, Peru	-11.941	-77.405	5.0	31
363	30.00	25/12/2016	14:22:23	Coast De Los Lagos - Aysen border, Chile	-43.517	-74.391	7.6	24
364	31.50	03/01/2017	13:41:52	Coast of Tarapaca, Chile	-19.785	-70.680	5.2	18
365	36.96	06/01/2017	22:55:30	Coast of Lima - Ancash border, Peru	-11.405	-78.387	5.0	5
366	88.85	07/01/2017	16:04:52	Southern Loreto, Peru	-7.797	-75.529	5.0	5
367	36.33	27/01/2017	21:27:57	Ica, Peru	-14.006	-76.188	5.2	6
368	40.08	28/01/2017	06:42:30	Coast of Ancash - La Libertad Border, Peru	-9.351	-79.151	5.3	7
369	30.00	28/01/2017	11:42:28	Coast of Ancash - La Libertad Border, Peru	-9.350	-79.300	5.4	6
370	16.86	06/04/2017	17:15:18	Coast of Arequipa - Moquegua, Peru	-17.784	-72.690	5.1	2
371	35.90	30/04/2017	09:36:03	Coast of Tarapaca, Chile	-19.990	-70.969	5.1	1
372	48.76	03/05/2017	12:42:49	Coast of Arequipa, Peru	-16.275	-73.417	5.1	7
373	33.50	05/06/2017	11:34:10	Tumbes, Peru	-4.121	-80.509	5.6	22
374	98.10	06/06/2017	17:35:10	Antofagasta, Chile	-22.927	-68.755	5.4	9
375	92.50	04/07/2017	02:25:26	Tarapacá, Chile	-19.403	-69.582	5.0	21
376	37.92	18/07/2017	02:05:20	Coast Arequipa, Peru	-16.577	-73.652	6.4	28
377	77.10	26/07/2017	10:11:02	Antofagasta, Chile	-23.990	-69.515	5.0	1
378	39.67	11/08/2017	21:45:09	Coast of Arequipa, Peru	-16.457	-73.611	5.6	20
379	31.10	12/08/2017	15:59:31	Coast of Tarapaca, Chile	-19.992	-70.989	5.2	3
380	65.17	04/09/2017	21:55:19	Tarapacá, Chile	-19.356	-70.117	5.2	48
381	122.39	20/09/2017	05:26:10	Arequipa, Peru	-16.378	-71.394	5.3	17
382	95.00	10/10/2017	06:32:20	Arica y Parinacota, Chile	-18.657	-69.784	6.3	71
383	76.53	17/11/2017	13:40:41	Guayas, Ecuador	-2.436	-79.915	5.4	5
384	15.97	29/11/2017	06:29:05	Coast of Ica, Peru	-14.488	-76.286	5.7	43
385	33.50	11/12/2017	19:00:57	Coast of Tarapaca - Arica y Parinacota border, Chile	-19.656	-71.155	5.4	4
386	53.40	28/12/2017	03:54:52	Antofagasta, Chile	-24.910	-70.172	5.4	11
387	97.33	30/12/2017	08:20:50	Tarapacá, Chile	-19.322	-69.400	5.2	29
388	33.00	14/01/2018	09:18:46	Coast of Arequipa, Peru	-15.827	-74.742	7.0	66
389	80.61	19/01/2018	01:11:38	Huancavelica - Ayacucho border, Peru	-13.255	-74.622	5.2	39
390	30.67	19/01/2018	17:44:26	Coast of Arequipa, Peru	-15.975	-74.796	5.1	9
391	28.69	21/01/2018	06:40:55	Coast of Arequipa, Peru	-15.816	-74.774	5.0	13
392	26.68	26/01/2018	22:27:07	Coast of Arequipa, Peru	-15.919	-74.806	5.0	7
393	25.00	05/02/2018	22:31:00	Coast of Arequipa, Peru	-15.999	-74.780	5.0	6
394	13.33	11/02/2018	04:11:10	Coast of Arequipa, Peru	-16.663	-74.153	5.4	13
395	29.27	16/02/2018	08:01:25	Coast of Piura, Peru	-5.889	-81.154	5.2	13
396	39.00	05/04/2018	11:12:11	Coast of Tarapaca, Chile	-20.338	-70.598	5.6	32
397	46.00	05/04/2018	16:12:12	Coast of Tarapaca, Chile	-20.287	-70.526	5.6	2
398	21.05	06/04/2018	00:40:17	Coast of Ica, Peru	-15.243	-75.593	5.0	15
399	24.32	06/04/2018	04:16:56	Coast of Ica, Peru	-15.386	-75.740	5.0	9
400	44.45	07/04/2018	20:15:07	Coast of Lima - Ancash border, Peru	-10.935	-78.472	5.0	18
401	37.33	09/04/2018	19:08:46	Coast of Arequipa, Peru	-15.966	-74.477	5.2	12
402	55.37	17/05/2018	11:07:14	Coast of Lima, Peru	-12.701	-76.666	5.4	47
403	22.00	22/05/2018	22:12:20	Coast of La Libertad, Peru	-8.986	-80.455	5.0	12
404	72.87	04/08/2018	01:02:24	Tarapacá, Chile	-19.666	-69.567	5.2	32
405	94.50	07/09/2018	02:12:04	Chimborazo, Ecuador	-2.256	-78.835	6.2	29

EVENT ID	DEPTH (km)	DATE	UTC TIME	LOCATION	LATITUDE	LONGITUDE	MOMENT MAGNITUDE Mw	NUMBER OF STATIONS
(1)	(2)	(3)	(4)	(5)	(6)	(7)	(8)	(9)
406	20.00	08/09/2018	14:39:58	Coast of Piura, Peru	-4.370	-81.462	5.2	3
407	56.10	19/09/2018	18:42:22	Coast of Tarapaca, Chile	-19.537	-70.375	5.0	19
408	26.85	20/09/2018	08:45:16	Coast of Ica, Peru	-14.941	-75.871	5.0	9
409	45.39	25/09/2018	22:56:47	Arequipa - Ica border, Peru	-15.345	-74.990	5.2	20
410	132.33	26/10/2018	09:11:51	Pastaza, Ecuador	-1.451	-77.910	5.0	8
411	48.61	20/11/2018	06:38:05	Coast of Ancash, Peru	-9.877	-78.712	5.4	57
412	15.67	06/12/2018	04:17:25	Coast of Ica, Peru	-14.953	-75.945	5.0	12
413	44.20	15/01/2019	20:24:08	Coast of La Libertad - Ancash border, Peru	-9.000	-79.171	5.2	21
414	105.67	18/01/2019	21:27:00	Loreto, Peru	-3.247	-76.866	5.6	23
415	55.25	25/01/2019	04:45:20	Ica, Peru	-14.662	-75.551	5.7	49
416	68.67	04/02/2019	17:45:47	Guayas, Ecuador	-2.438	-79.919	5.8	19
417	50.22	19/02/2019	08:32:18	Ica, Peru	-14.661	-75.721	5.2	26
418	82.06	21/02/2019	22:17:33	Arequipa, Peru	-15.349	-73.080	5.2	20
419	137.25	22/02/2019	10:17:22	Pastaza, Ecuador	-2.184	-77.047	7.6	69
420	61.30	28/03/2019	15:05:32	Antofagasta, Chile	-24.603	-70.124	5.4	14
421	14.33	31/03/2019	07:04:04	Coast of Santa Elena, Ecuador	-1.974	-80.896	6.2	13
422	33.00	31/03/2019	15:27:57	Coast of Ancash, Peru	-10.023	-79.546	5.5	43
423	14.11	08/05/2019	13:47:19	Coast of Arequipa - Ica, Peru	-15.877	-75.167	5.8	29
424	89.36	13/05/2019	07:10:30	Huancavelica, Peru	-12.195	-74.991	5.2	35
425	84.71	13/05/2019	12:41:53	Ayacucho, Peru	-14.086	-74.458	5.2	21
426	137.72	16/05/2019	04:04:50	Pastaza, Ecuador	-2.205	-77.037	5.6	13
427	127.12	26/05/2019	07:41:14	Loreto, Peru	-5.783	-75.373	8.0	187
428	27.00	28/05/2019	03:28:16	Coast of Arequipa - Ica, Peru	-15.820	-75.062	5.0	15
429	16.67	30/05/2019	09:20:36	Coast of Ica, Peru	-15.189	-75.794	5.0	18
430	54.87	04/07/2019	18:20:59	Piura, Peru	-4.290	-80.463	5.0	16
431	32.40	28/08/2019	15:53:03	Coast of Tarapaca, Chile	-20.561	-70.363	5.0	6
432	34.00	01/09/2019	21:32:15	Coast of Peru - Chile border	-18.605	-71.054	5.1	12
433	86.00	02/09/2019	16:35:28	Apurimac, Peru	-14.092	-72.647	5.0	16
434	91.94	11/09/2019	14:52:30	Tacna, Peru	-18.058	-70.068	5.3	10
435	152.97	27/09/2019	03:17:58	Ucayali, Peru	-8.222	-74.275	5.2	34
436	42.00	04/11/2019	13:03:40	Coast of Antofagasta - Tarapaca border, Chile	-21.391	-70.435	5.1	6
437	130.90	14/11/2019	20:52:26	Huanuco - Ucayali border, Peru	-8.561	-74.633	5.2	19
438	22.70	03/12/2019	07:29:31	Coast of Tarapaca, Chile	-20.875	-70.841	5.3	2
439	38.55	03/12/2019	08:46:35	Coast of Peru - Chile border	-18.481	-70.727	6.0	35
440	54.50	03/01/2020	14:16:40	Coast of Peru - Ecuador Border	-3.304	-80.259	5.0	12
441	39.68	15/01/2020	09:45:18	Coast of Ancash, Peru	-10.347	-78.639	5.4	48
442	79.08	24/01/2020	05:13:50	Moquegua, Peru	-17.436	-71.044	5.4	22
443	47.69	05/02/2020	01:51:44	Piura, Peru	-5.851	-80.783	5.2	19
444	109.50	08/02/2020	06:17:58	Tarapacá, Chile	-20.838	-68.701	5.3	8
445	37.33	13/02/2020	04:31:51	Coast of Arequipa, Peru	-15.969	-74.661	5.1	24
446	26.74	25/02/2020	04:15:00	Coast of La Libertad, Peru	-8.090	-80.078	5.3	34
447	73.60	13/04/2020	13:18:27	Apurimac, Peru	-14.288	-73.273	5.2	28
448	76.08	19/05/2020	00:24:53	Apurimac, Peru	-14.510	-72.965	5.3	9
449	90.30	22/05/2020	14:59:33	Antofagasta, Chile	-22.933	-69.046	5.1	3
450	107.67	07/06/2020	10:31:18	Loreto, Peru	-4.141	-77.091	5.7	25
451	17.33	22/06/2020	13:08:58	Coast of Piura, Peru	-6.089	-81.535	5.1	13
452	30.68	25/06/2020	07:52:46	Coast of Tarapaca, Chile	-20.204	-70.703	5.0	5
453	30.68	27/06/2020	07:52:45	Coast of Tarapaca, Chile	-20.204	-70.703	5.0	5
454	27.13	15/07/2020	22:25:23	Coast of Arequipa, Peru	-16.385	-74.046	5.0	7

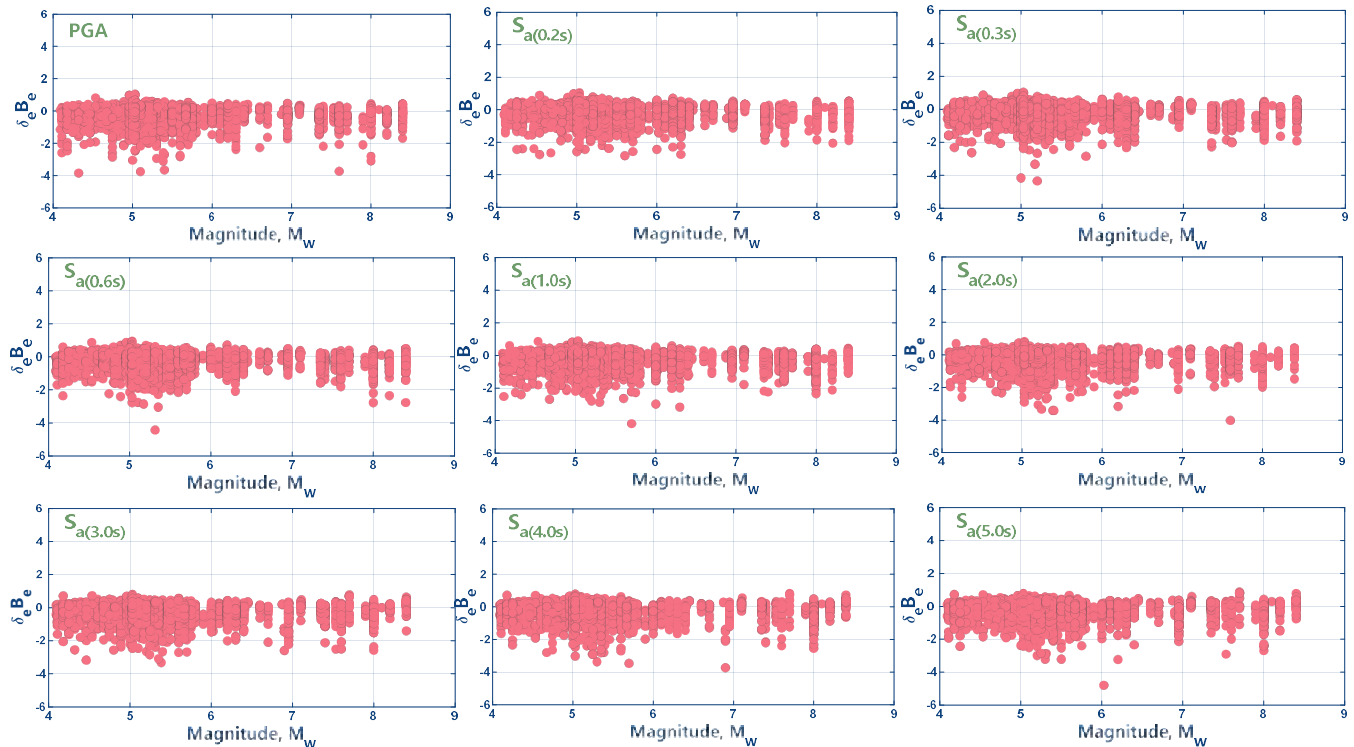


### A.3. RESIDUAL PLOTS FOR THE HORIZONTAL GMs

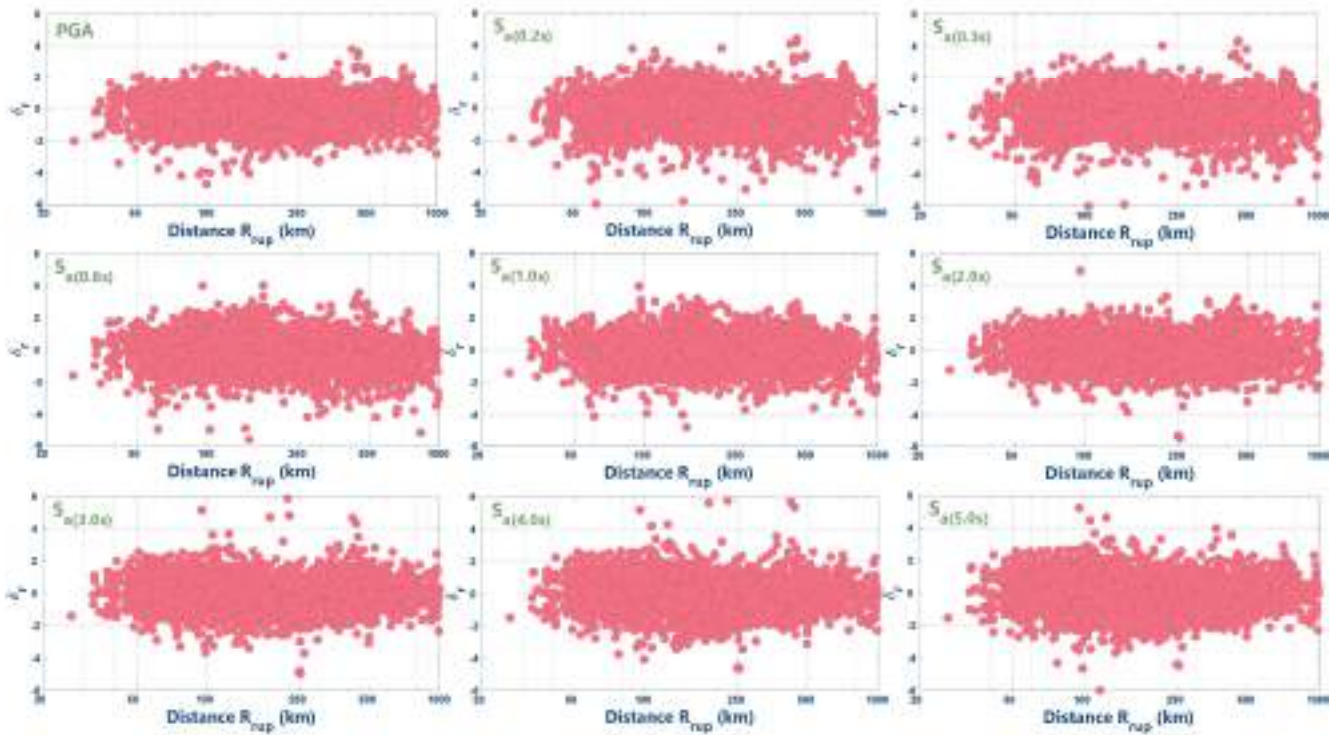
The residual plots for each IM for the 454 events considering the geometric mean of the horizontal GMs are presented. Herein the blue points are the residuals for each event respect to the median (0.0 residual value), and the red points are the number of observed IMs for each event. These plots are shown as follows:



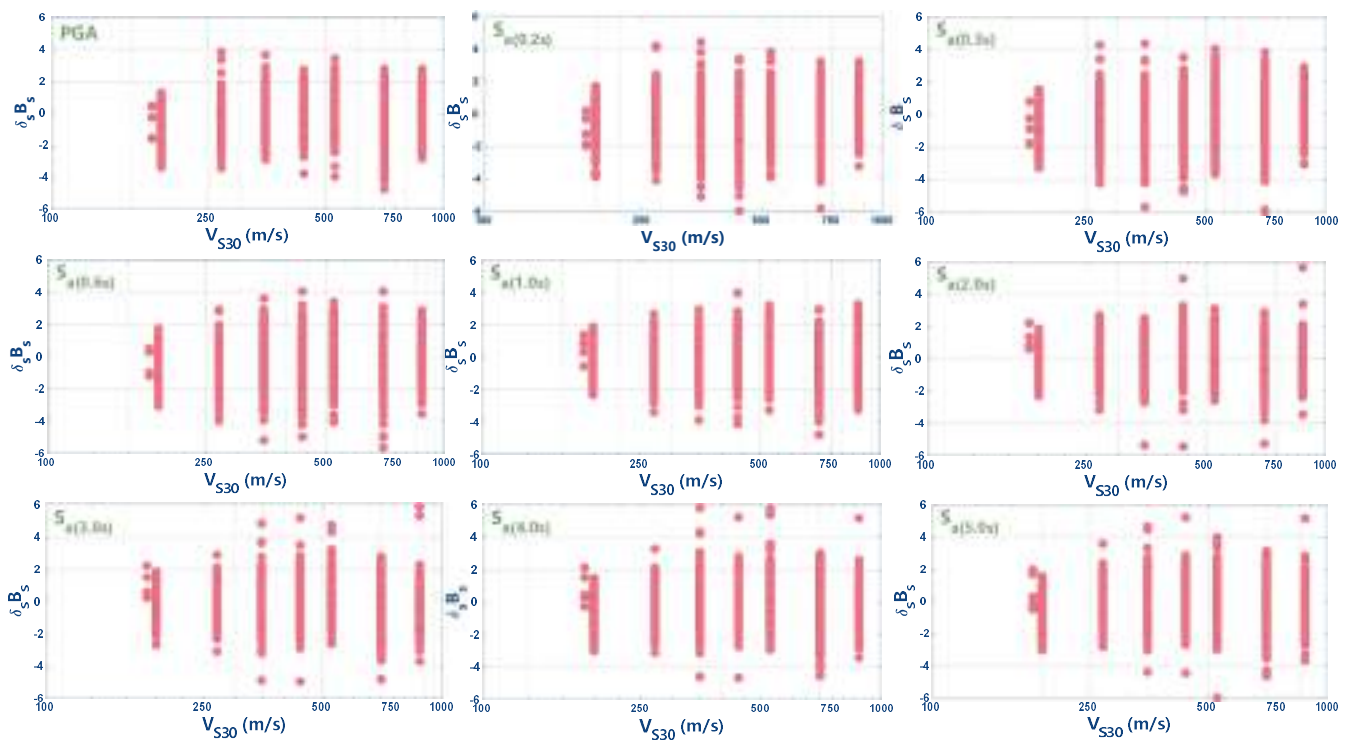
Now, the between-event ( $\delta_e B_e$ ) residual plots versus Moment Magnitude ( $M_w$ ) for each IM for the horizontal GMs are presented as follows:



Also, the within-event ( $\delta_r$ ) residual plots versus Rupture Distance ( $R_{rup}$ ) for each IM for the horizontal GMs are presented as follows:

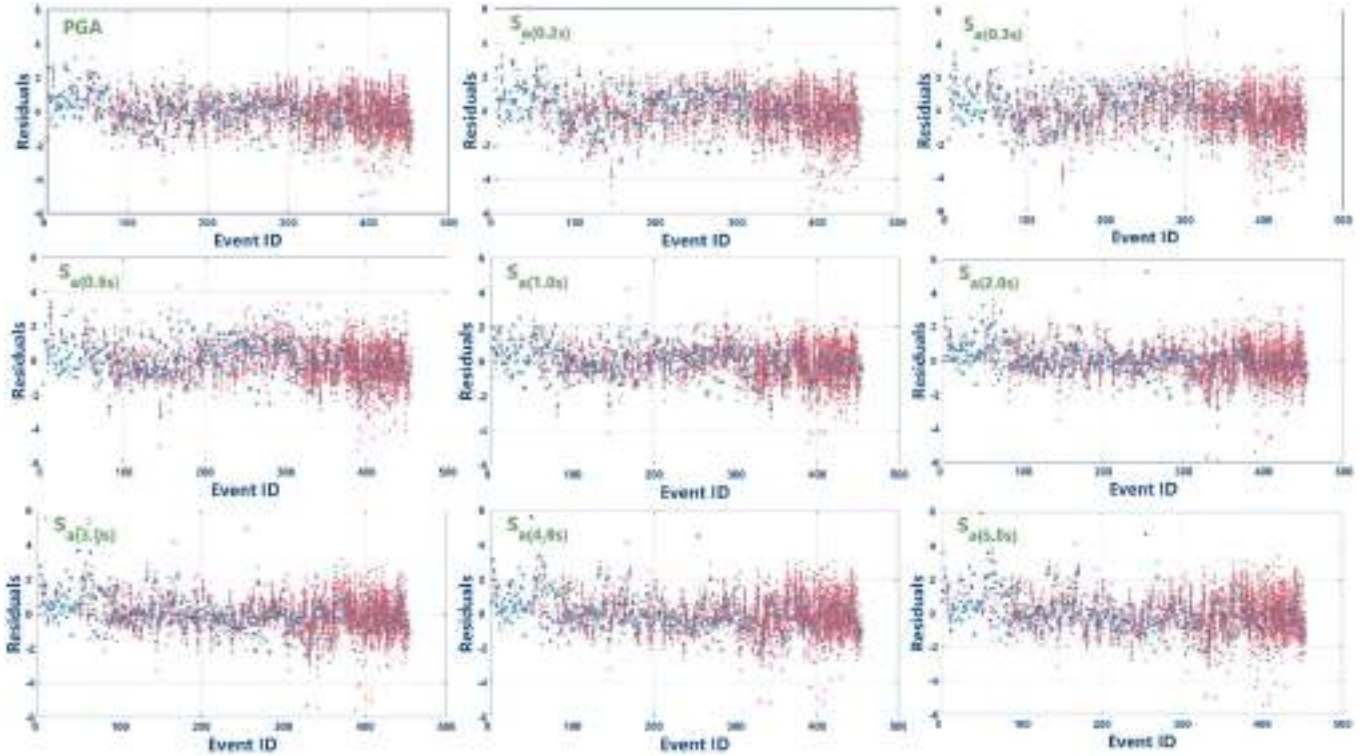


Finally, the within-event ( $\delta_{S_{30}}$ ) residual plots versus Shear Wave Velocity of the upper 30m ( $V_{S30}$ ) for each station and each IM for the horizontal GMs are presented as follows:

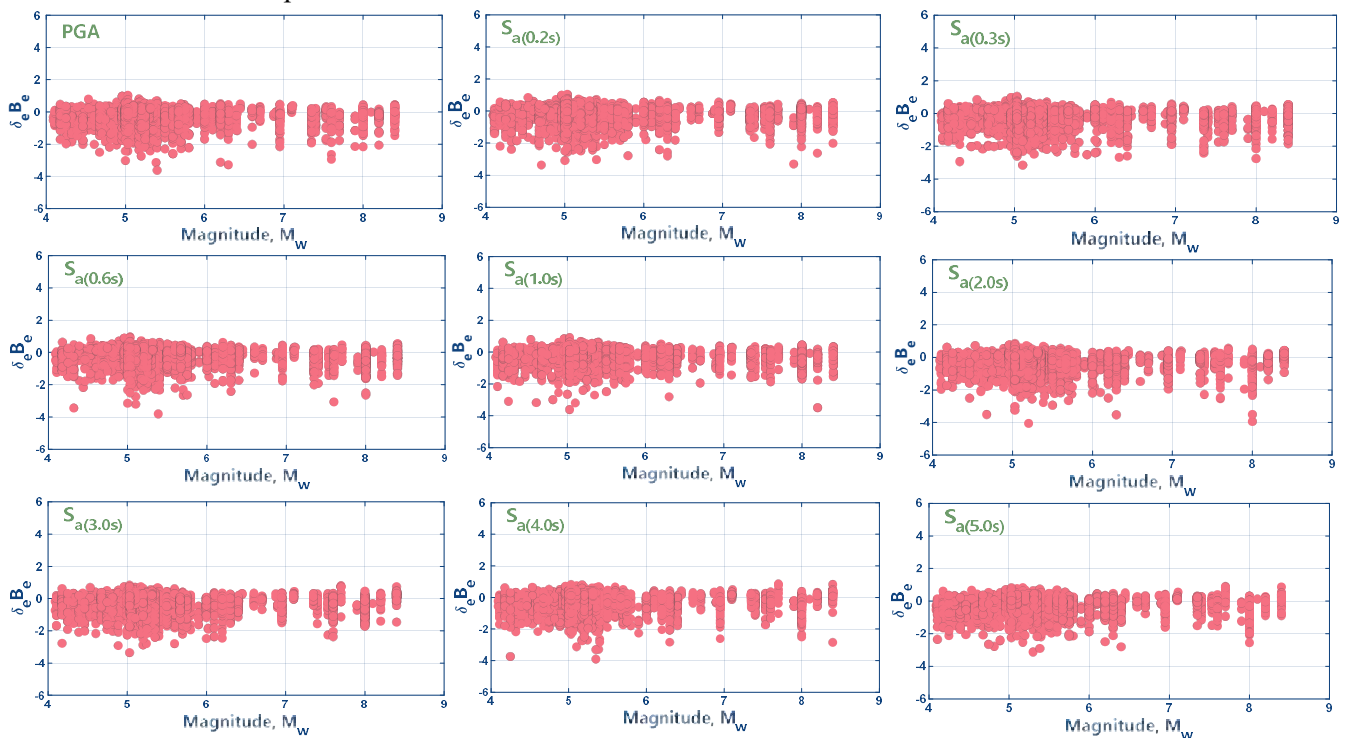


#### A.4. RESIDUAL PLOTS FOR THE VERTICAL GMs:

The residual plots for each IM for the 454 events considering the vertical GMs are presented. Herein the blue points are the residuals for each event respect to the median (0.0 residual value), and the red points are the number of observed IMs for each event. These plots are shown as follows:

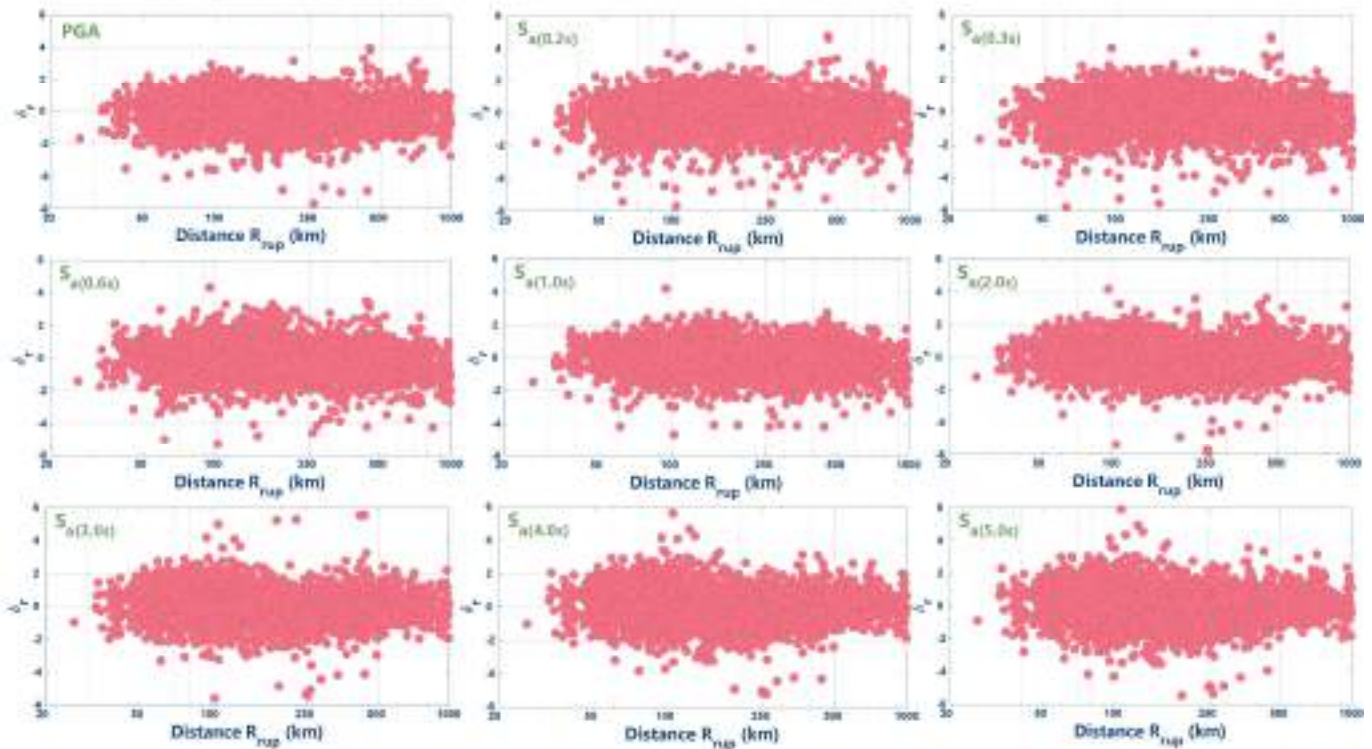


Now, the between-event ( $\delta_e B_e$ ) residual plots versus Moment Magnitude ( $M_w$ ) for each IM for the vertical GMs are presented as follows:

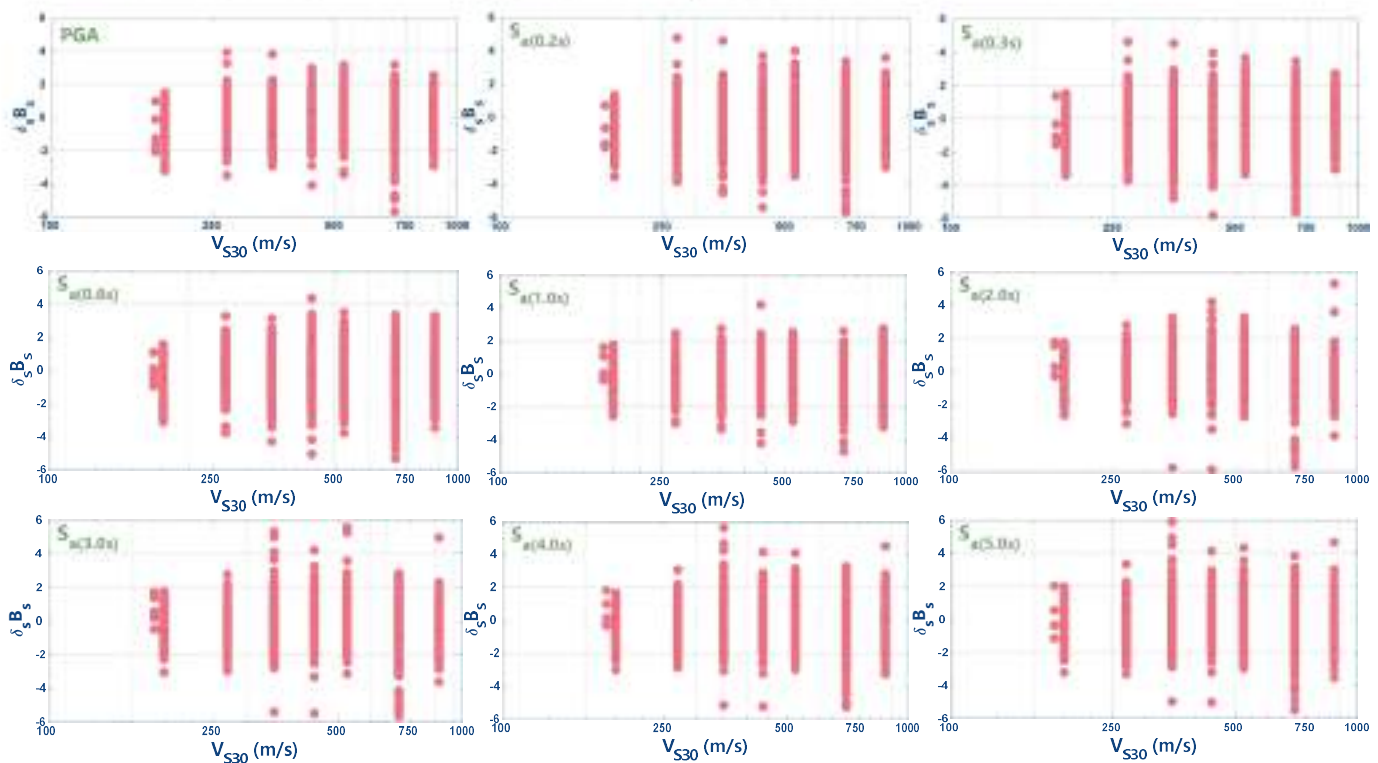




Also, the within-event ( $\delta_r$ ) residual plots versus Rupture Distance ( $R_{rup}$ ) for each IM for the vertical GMs are presented as follows:



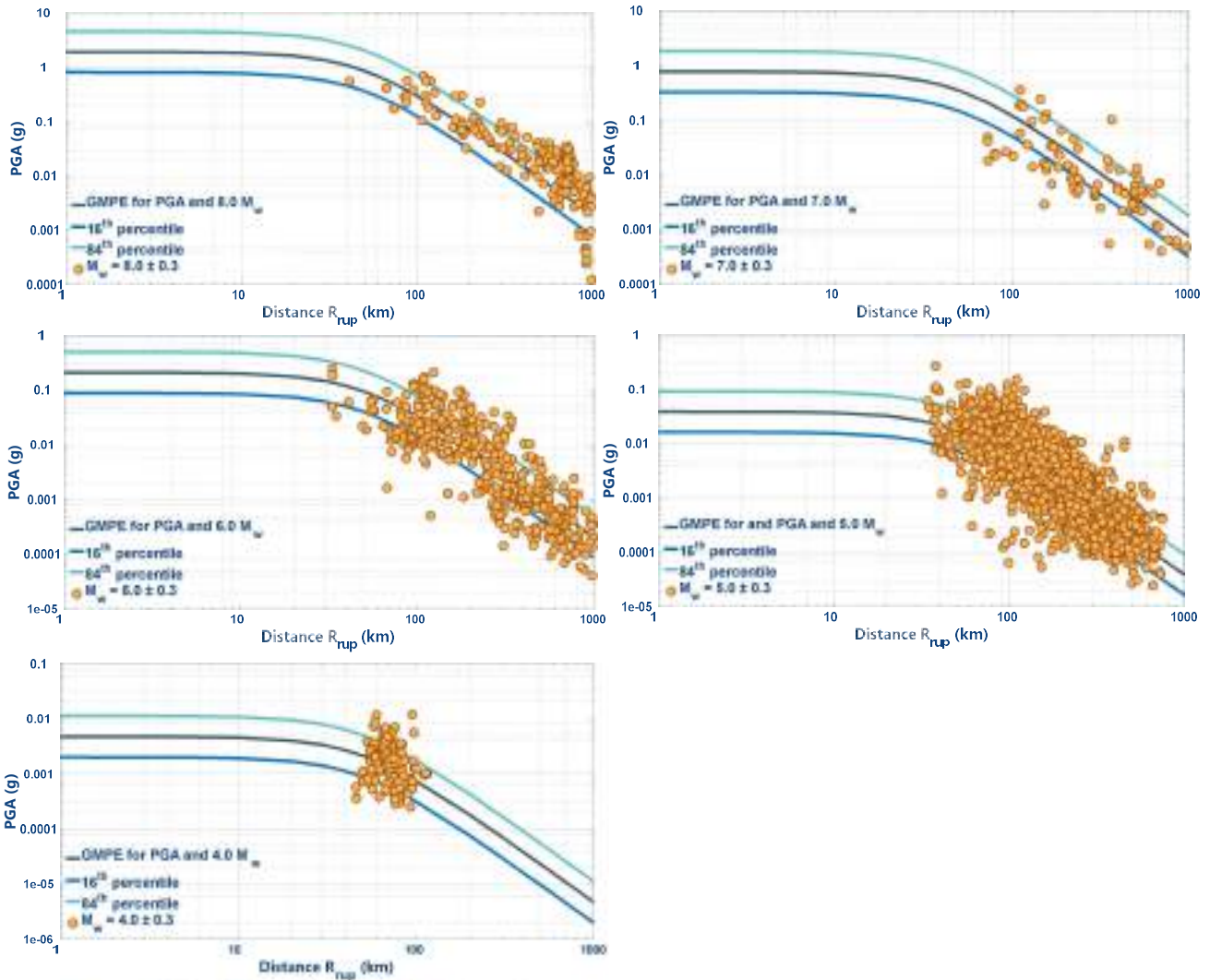
Finally, the within-event ( $\delta_s B_s$ ) residual plots versus Shear Wave Velocity of the upper 30m ( $V_{S30}$ ) for each station and each IM for the vertical GMs are presented as follows:



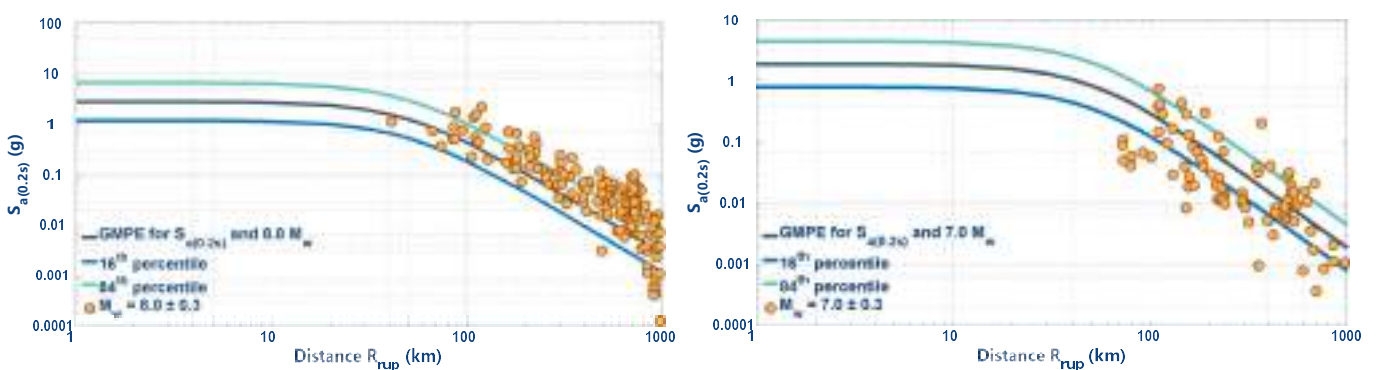
## A.5. COMPARISON BETWEEN MODEL FITTED WITH ALL DATA CONSIDERING DIFFERENT MOMENT MAGNITUDES AND DIFFERENT IMs FOR HORIZONTAL GMs:

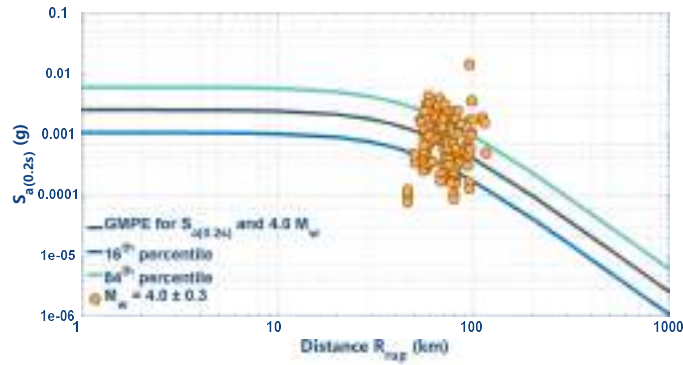
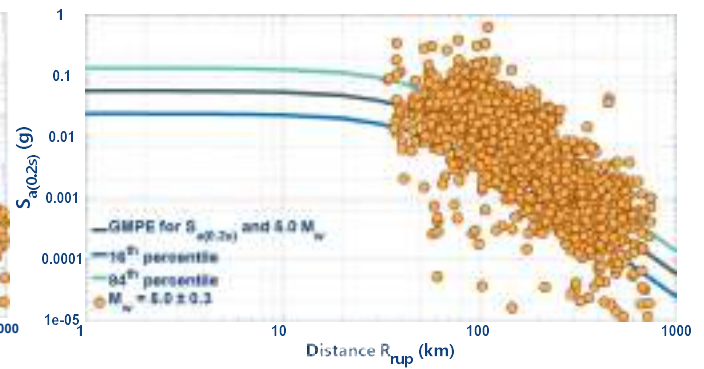
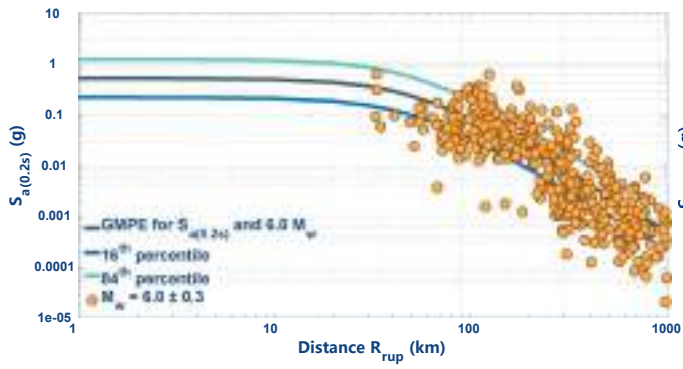
The main model mean of the GMPEs for a reference rock site ( $V_{s30} = 1200m/s$ ) and their standard deviations for each IM are plotted considering the compiled dataset for different magnitudes used for their regression.

### Peak Ground Acceleration (PGA)

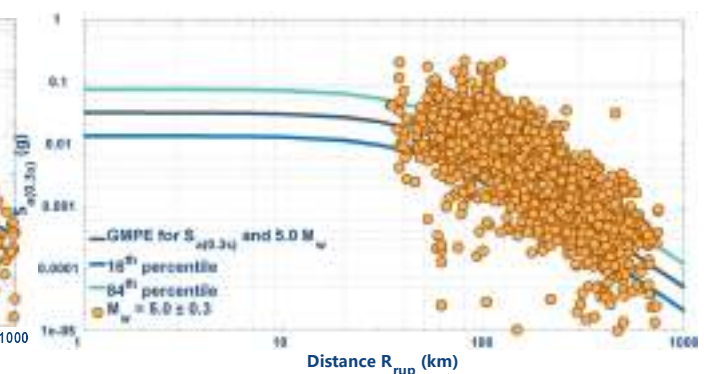
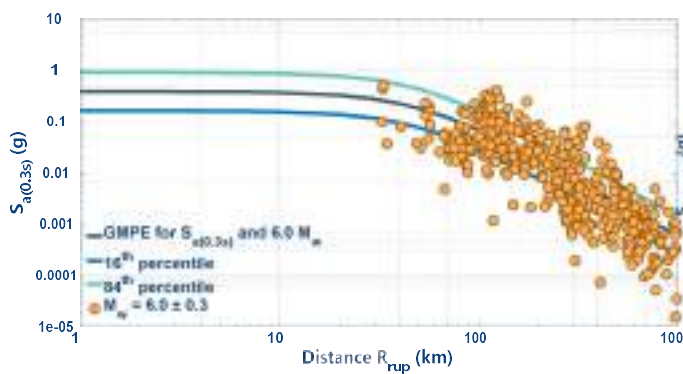
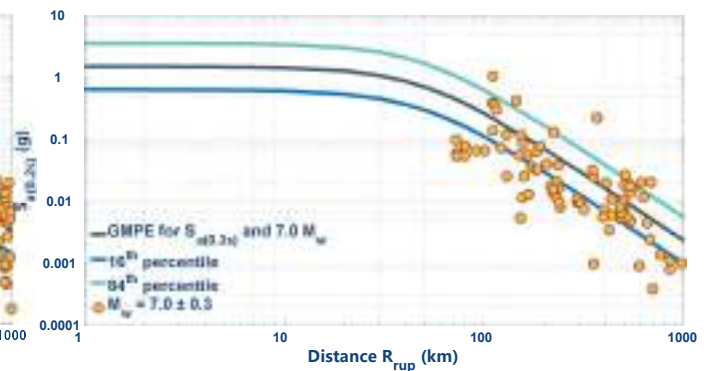
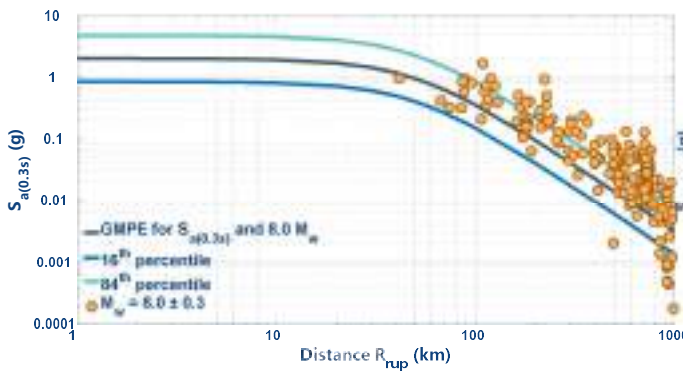


### Spectral Acceleration at 0.2s ( $S_{a(0.2s)}$ )

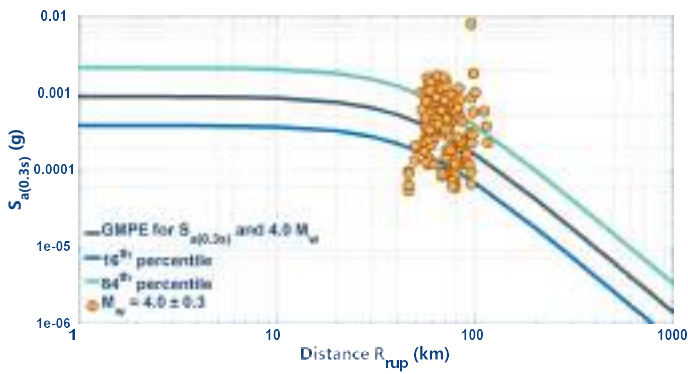




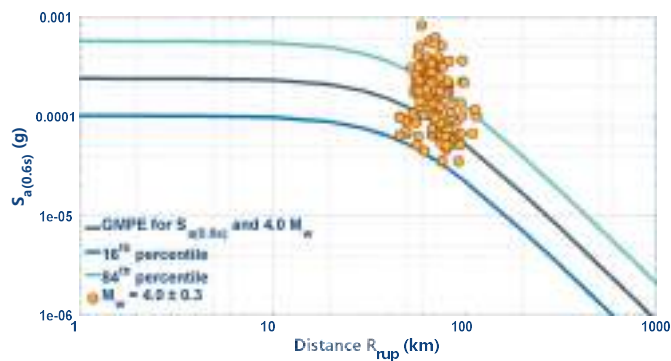
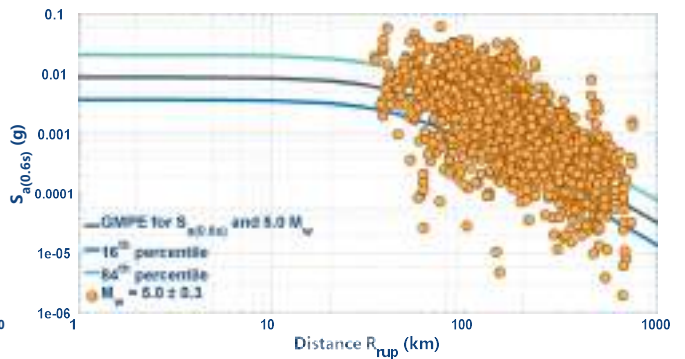
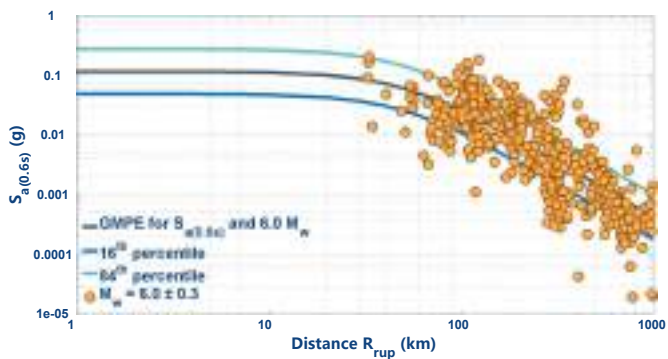
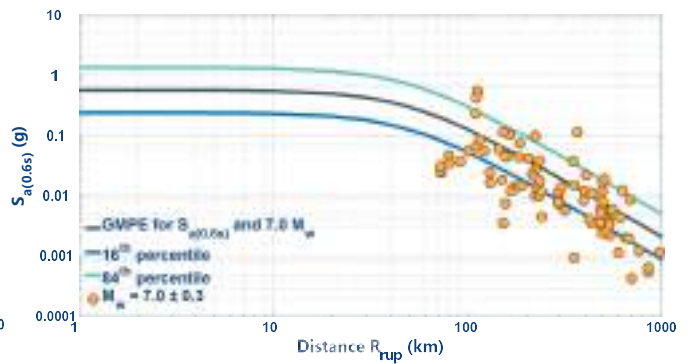
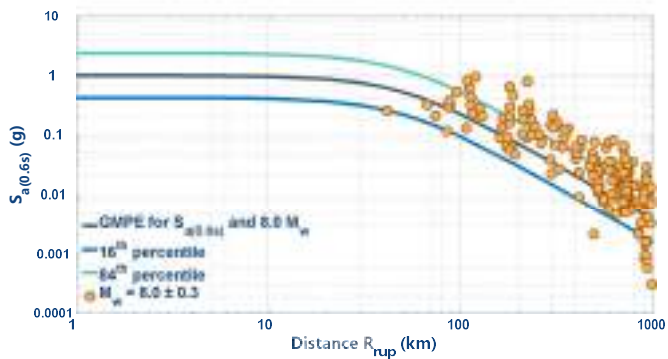
### Spectral Acceleration at 0.3s ( $S_{a(0.3s)}$ )



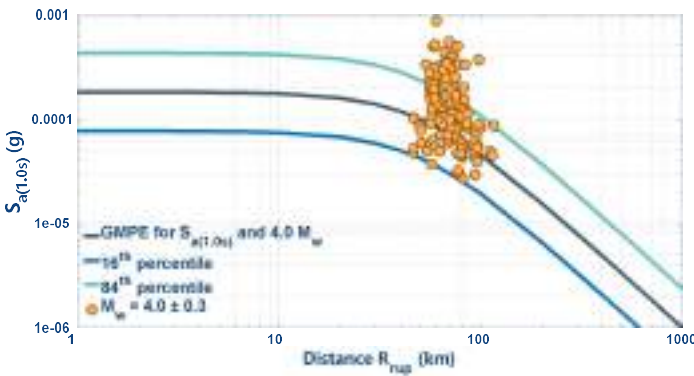
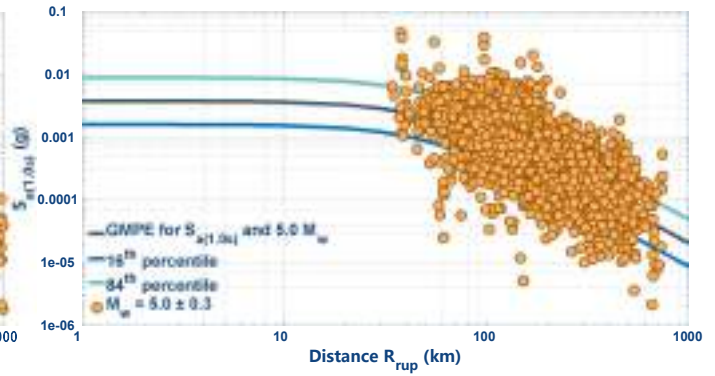
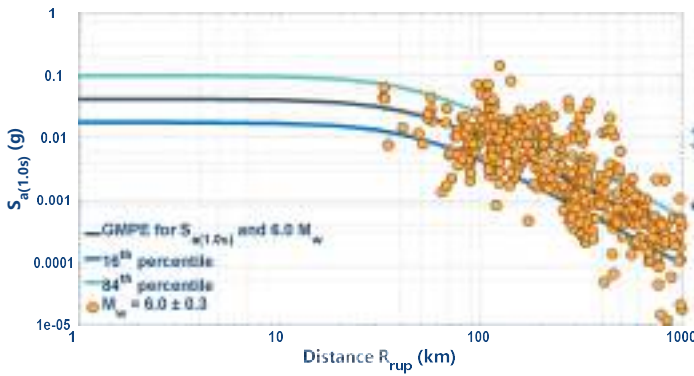
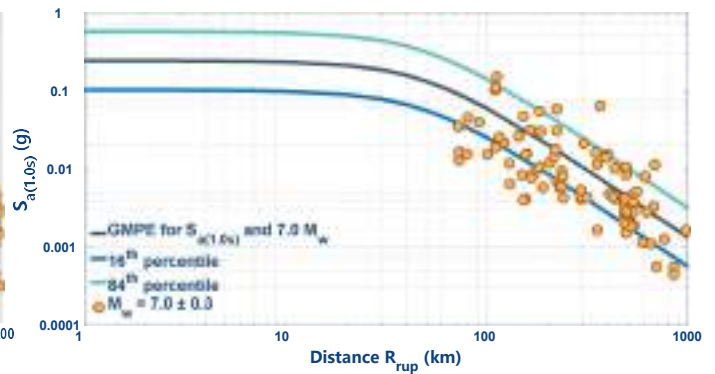
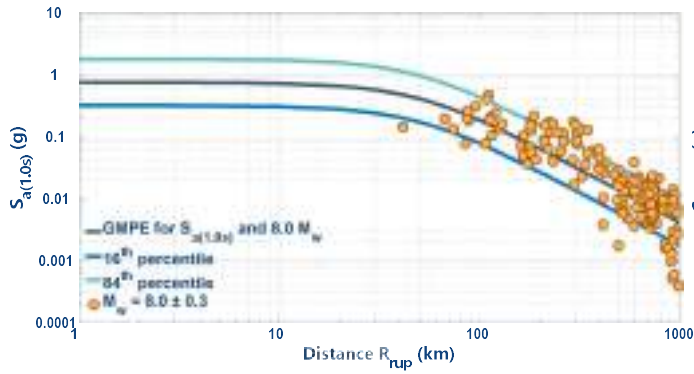




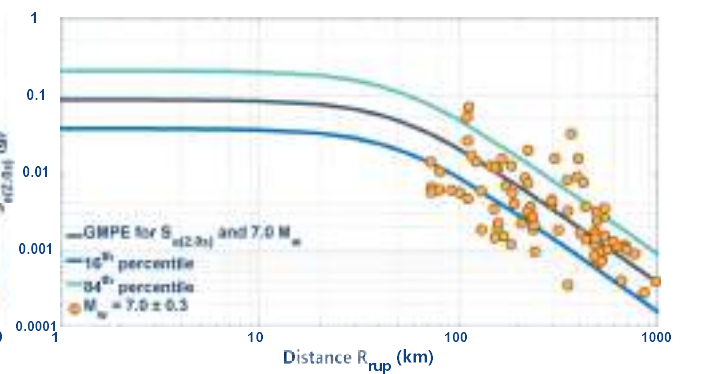
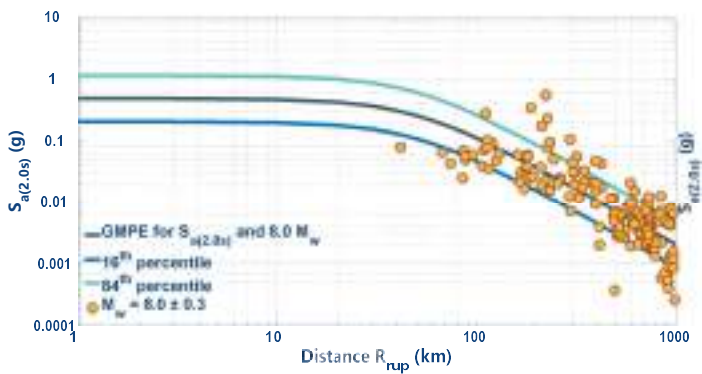
### Spectral Acceleration at 0.6s ( $S_{a(0.6s)}$ )

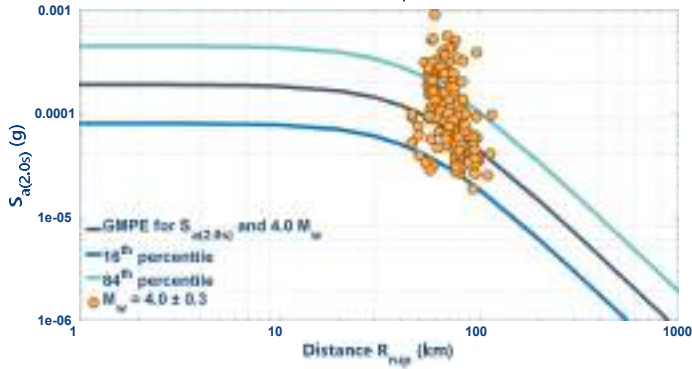
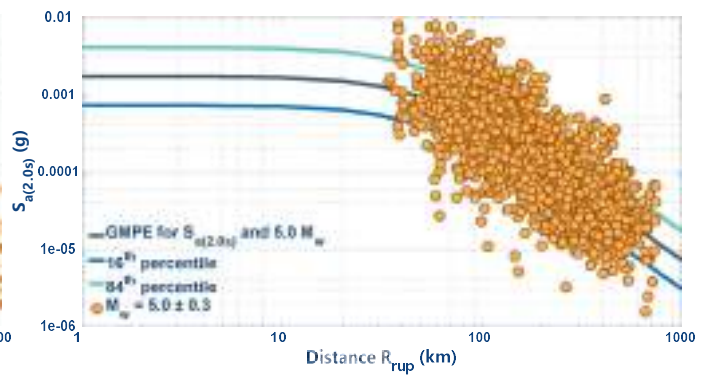
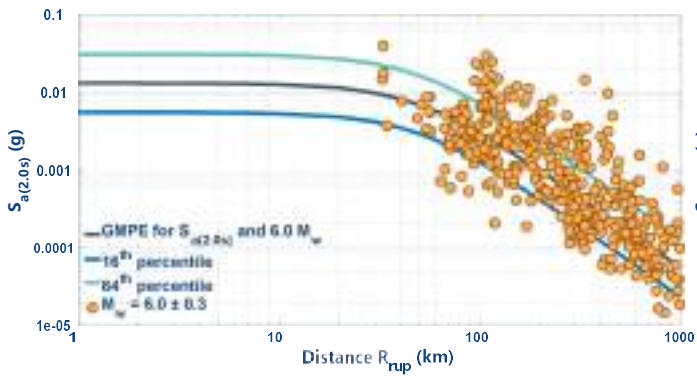


## Spectral Acceleration at 1.0s ( $S_{a(1.0s)}$ )

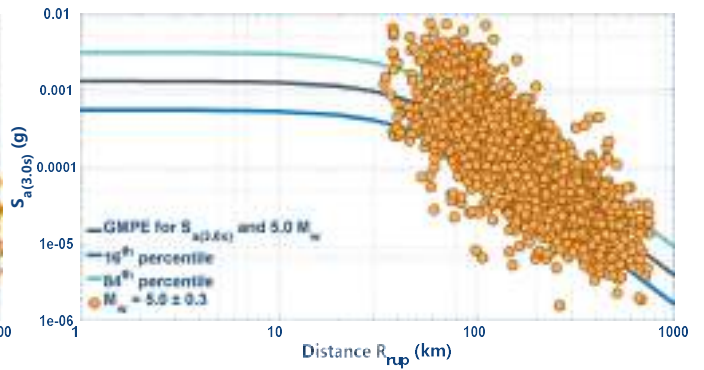
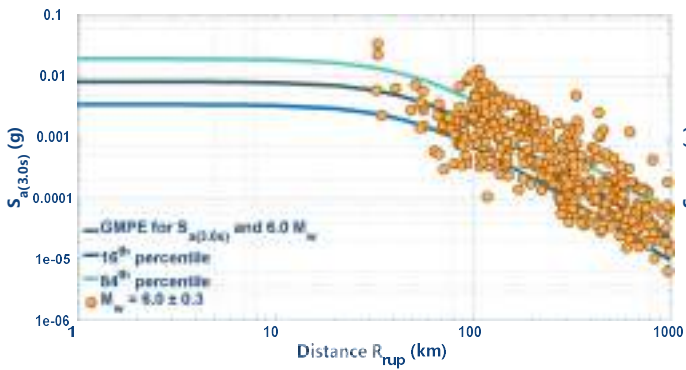
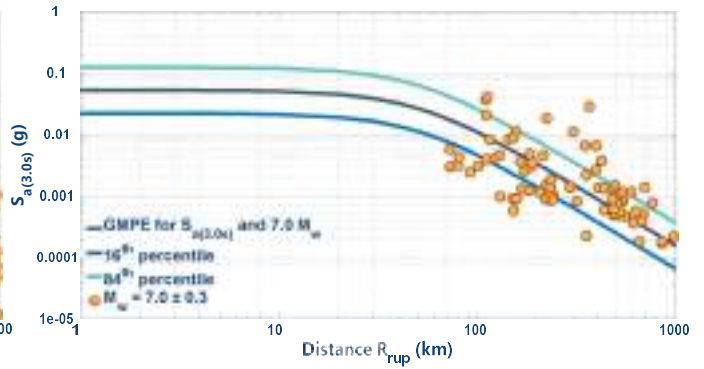
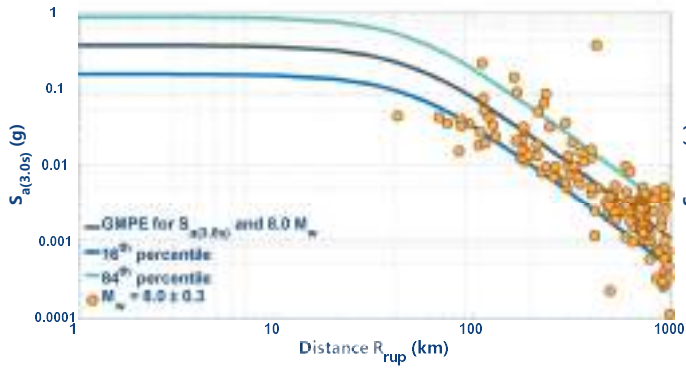


## Spectral Acceleration at 2.0s ( $S_{a(2.0s)}$ )

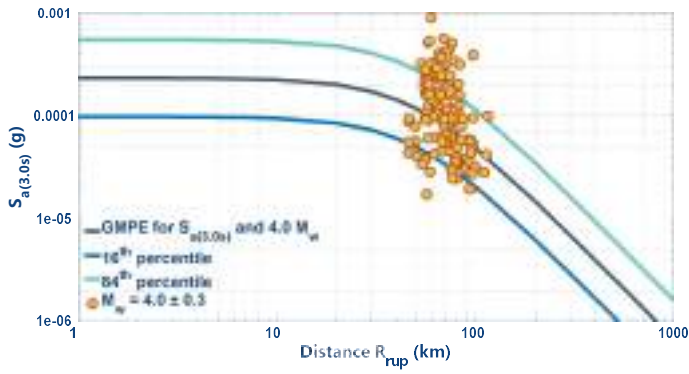




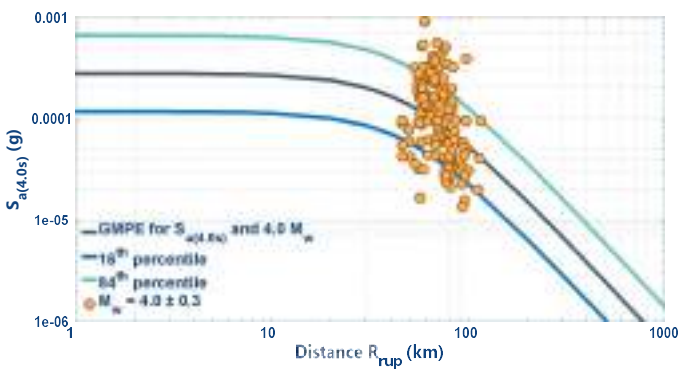
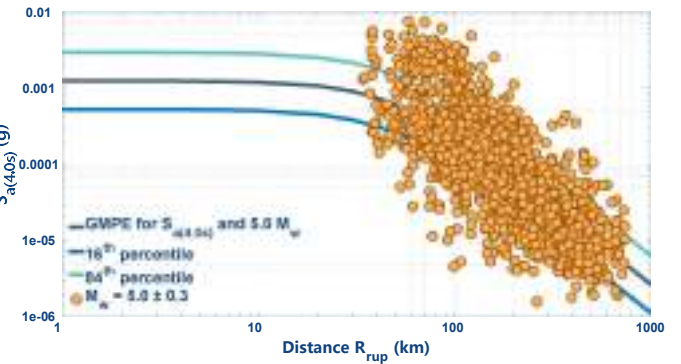
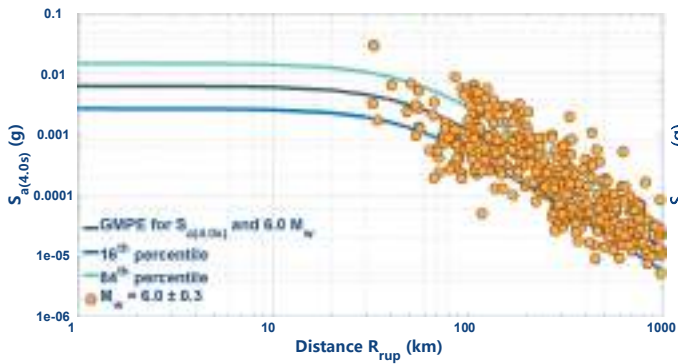
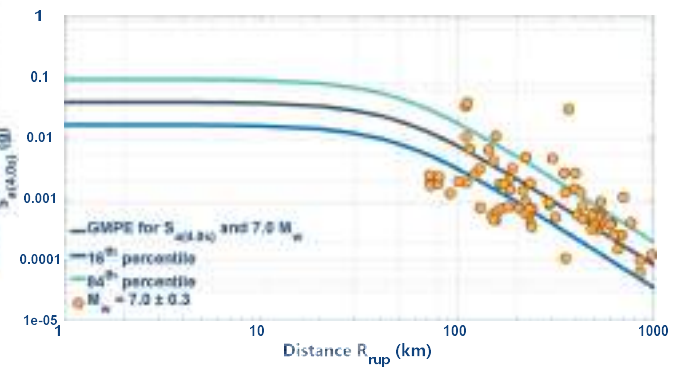
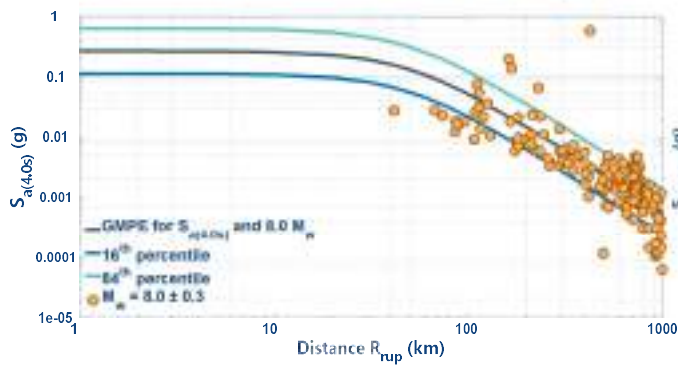
### Spectral Acceleration at 3.0s ( $S_{a(3.0s)}$ )



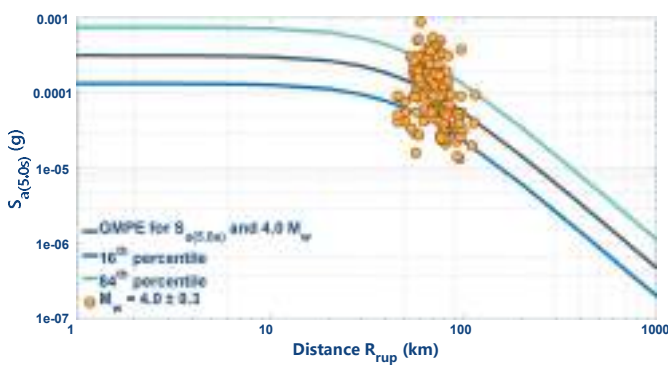
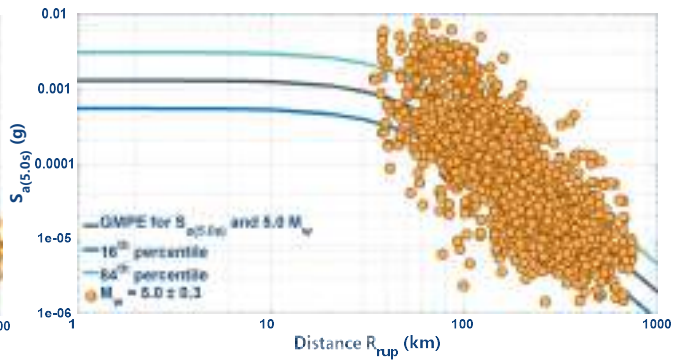
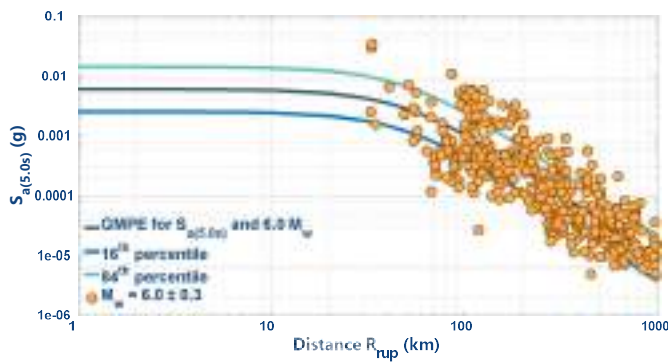
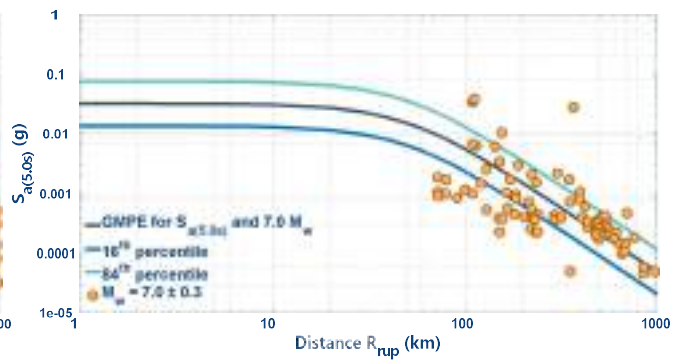
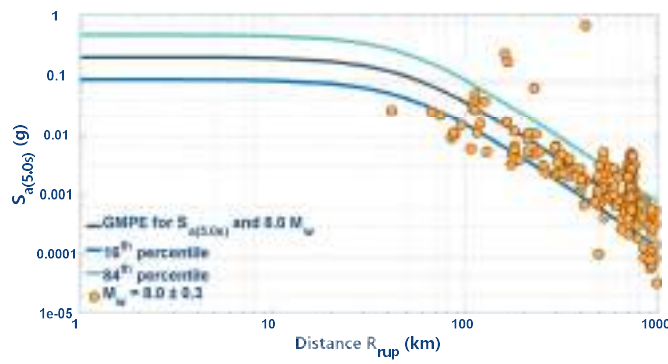




### Spectral Acceleration at 4.0s ( $S_{a(4.0s)}$ )



### Spectral Acceleration at 5.0s ( $S_{a(5.0s)}$ )

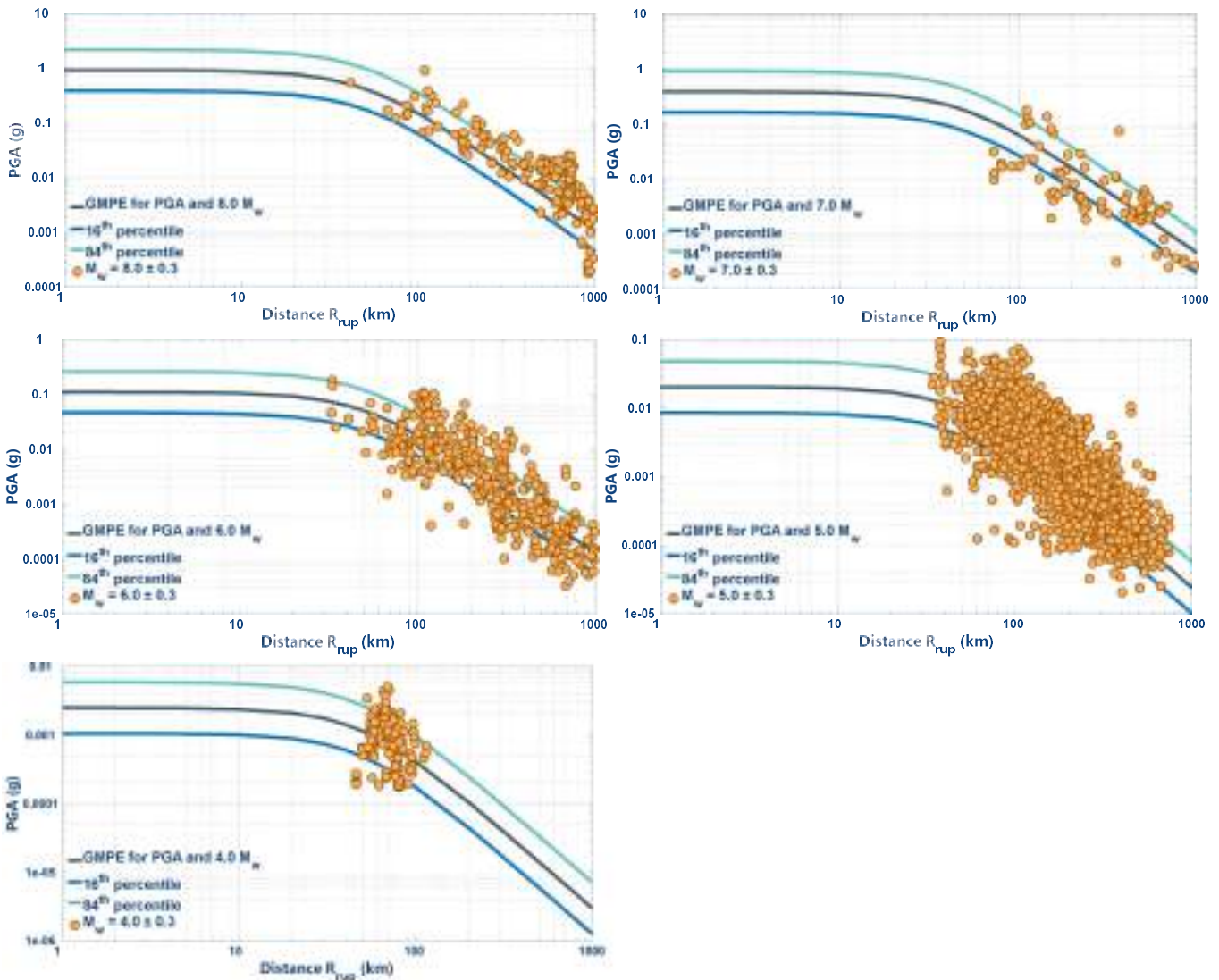




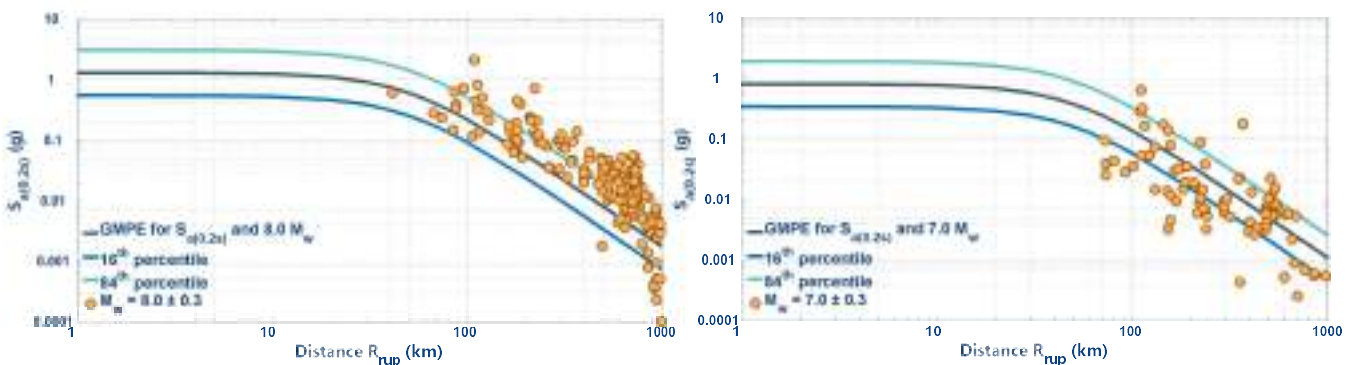
## A.6. COMPARINSON BETWEEN MODEL FITTED WITH ALL DATA CONSIDERING DIFFERENT MOMENT MAGNITUDES AND DIFFERENT IMs FOR VERTICAL GMs:

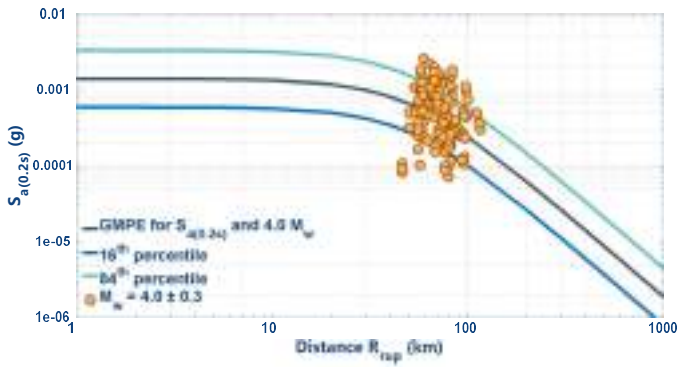
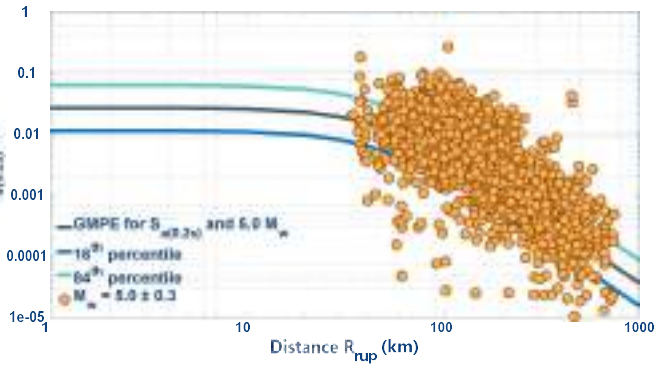
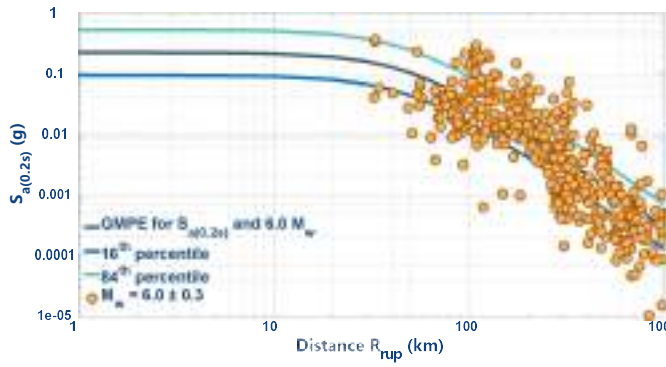
The main model mean of the GMPEs for a reference rock site ( $V_{s30} = 1200m/s$ ) and their standard deviations for each IM are plotted considering the compiled dataset for different  $R$  magnitudes used for their regression.

### Peak Ground Acceleration (PGA)

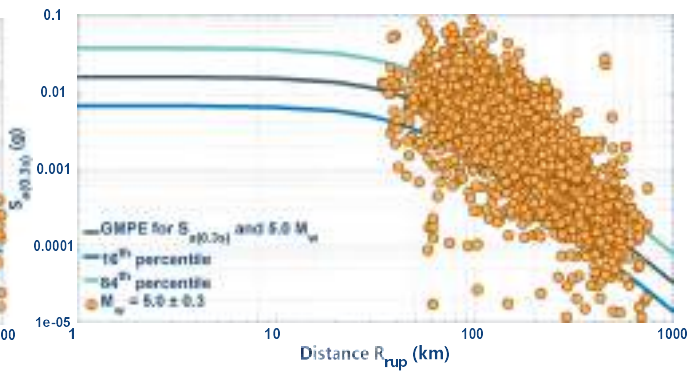
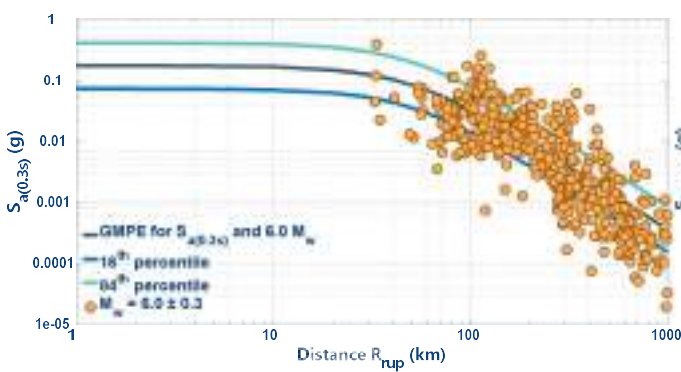
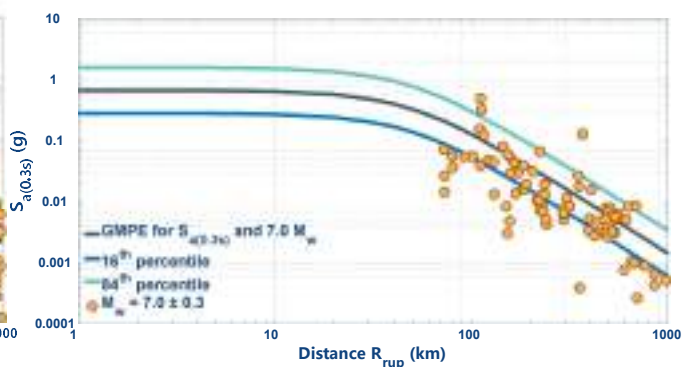
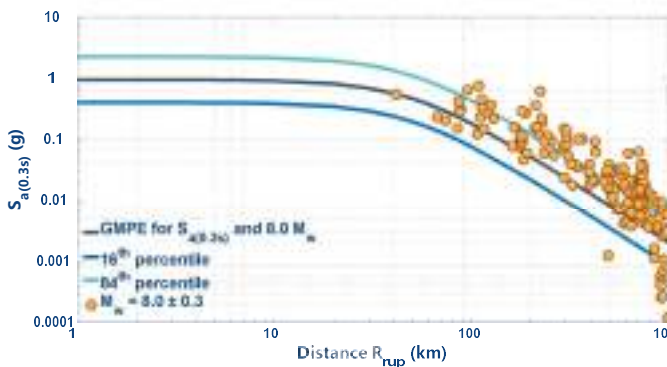


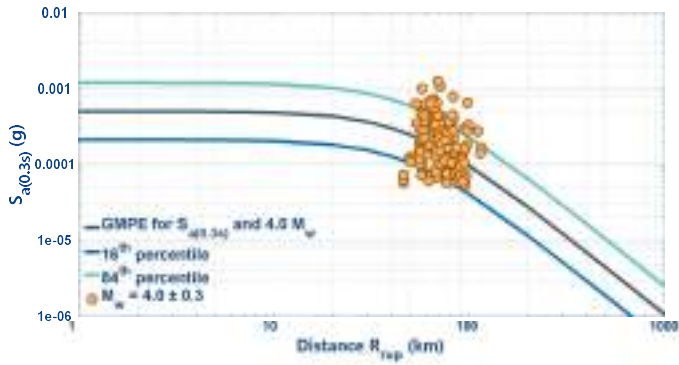
### Spectral Acceleration at 0.2s ( $S_{a(0.2s)}$ )



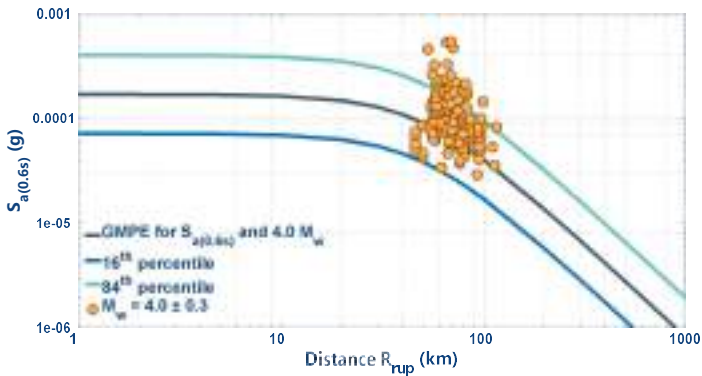
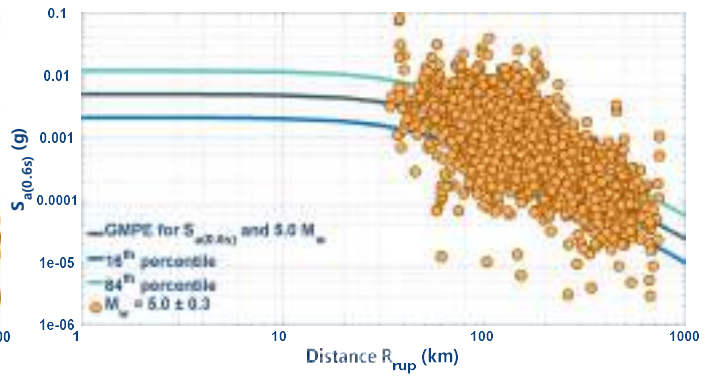
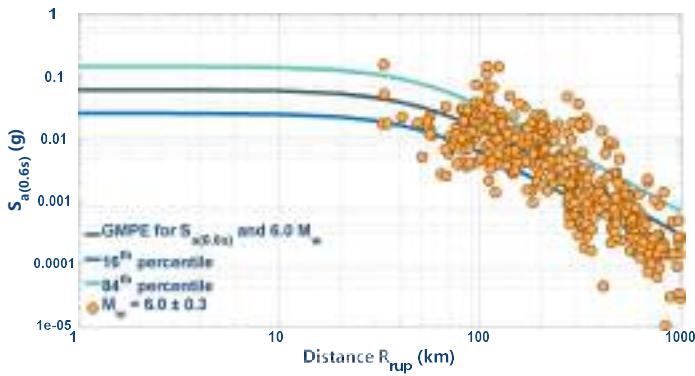
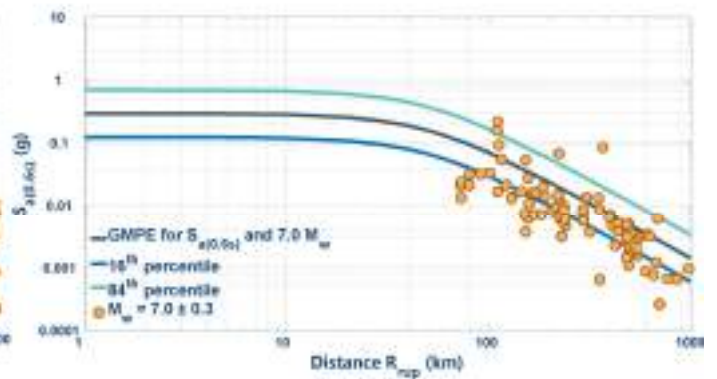
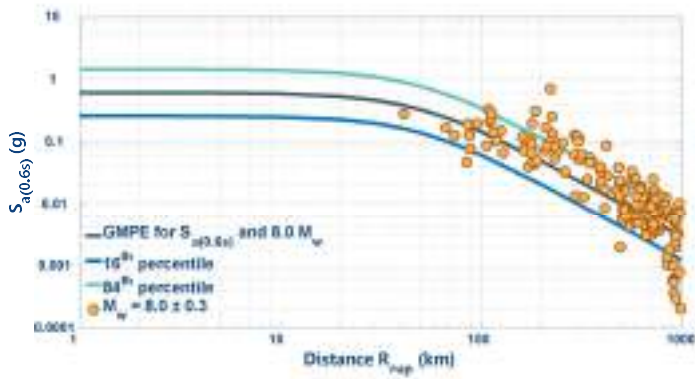


### Spectral Acceleration at 0.3s ( $S_{a(0.3s)}$ )



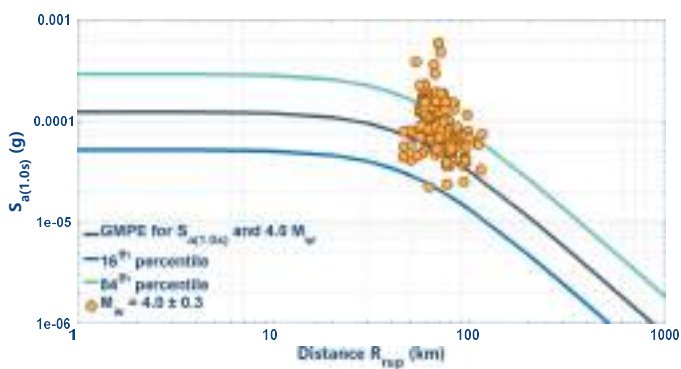
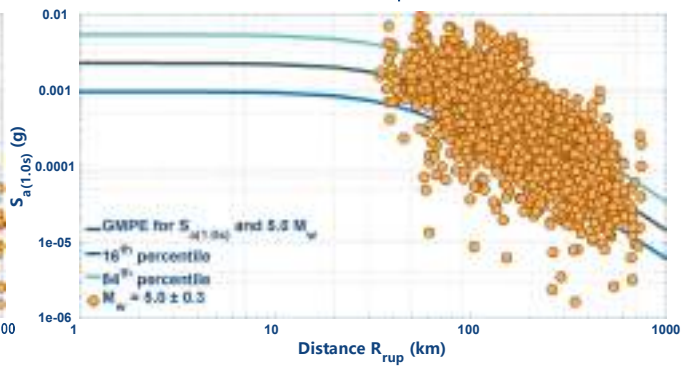
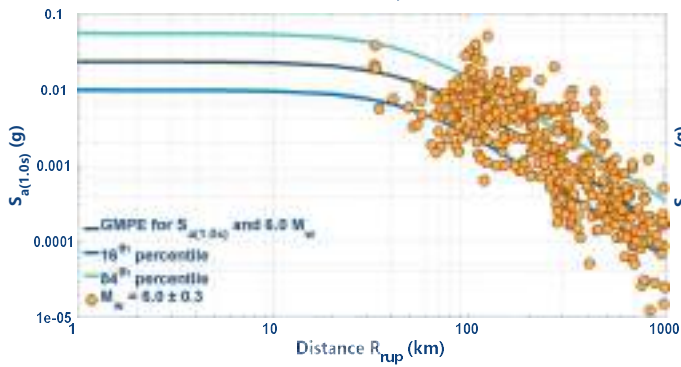
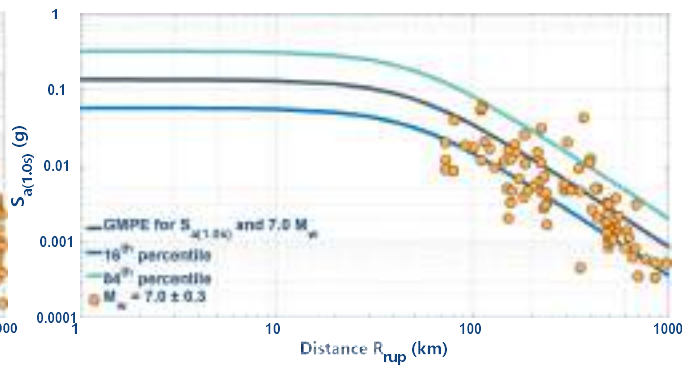
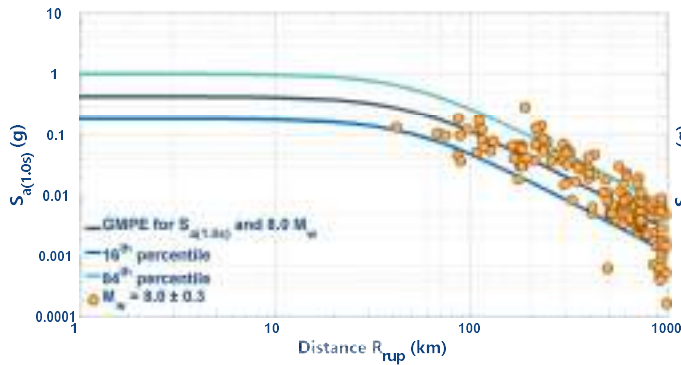


### Spectral Acceleration at 0.6s ( $S_{a(0.6s)}$ )

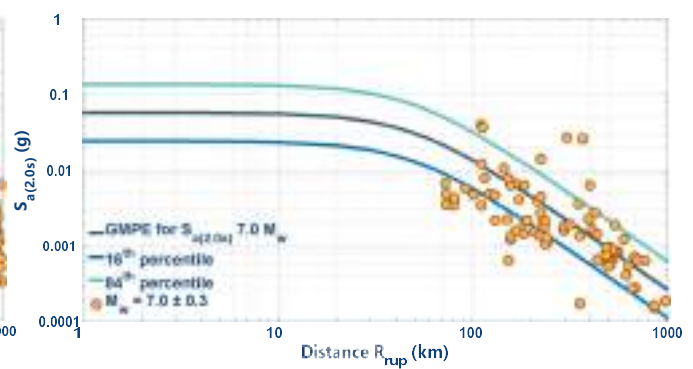
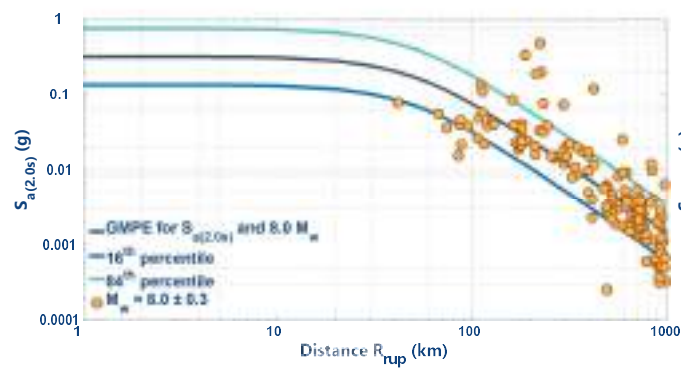


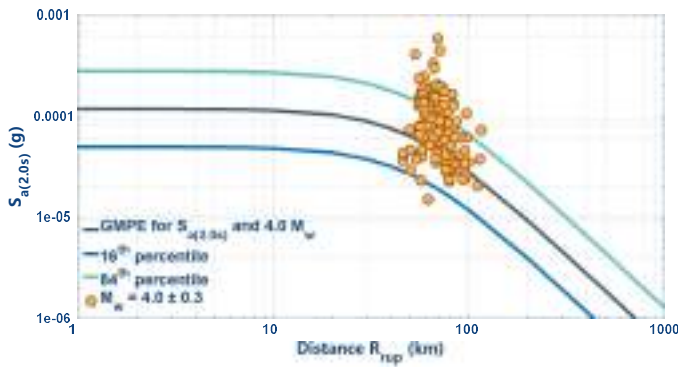
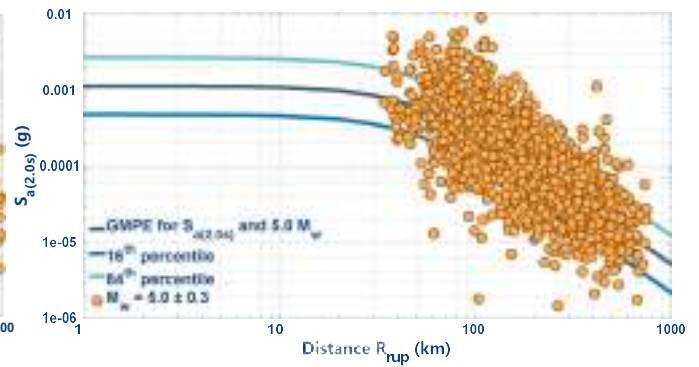
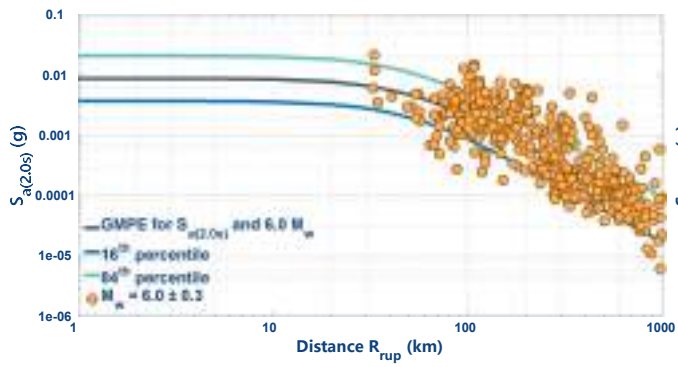


### Spectral Acceleration at 1.0s ( $S_{a(1.0s)}$ )

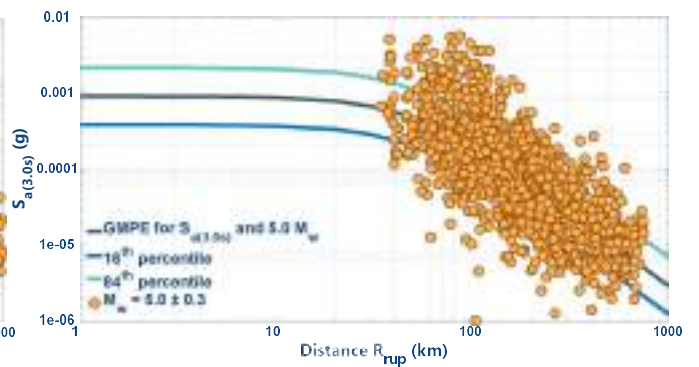
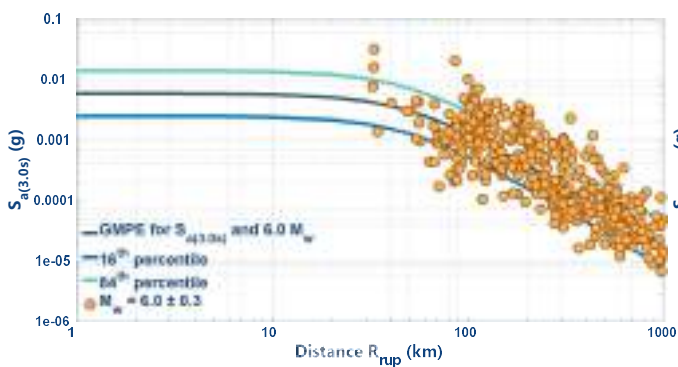
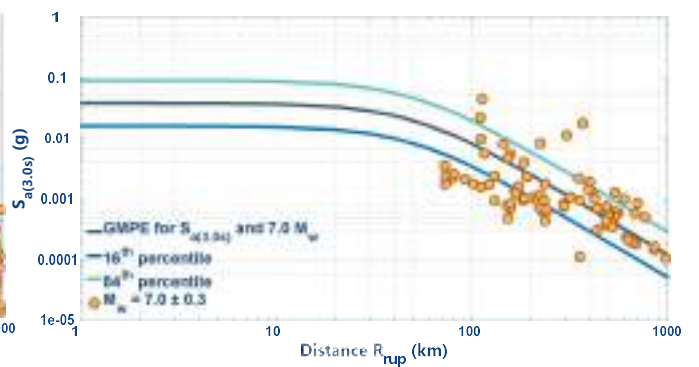
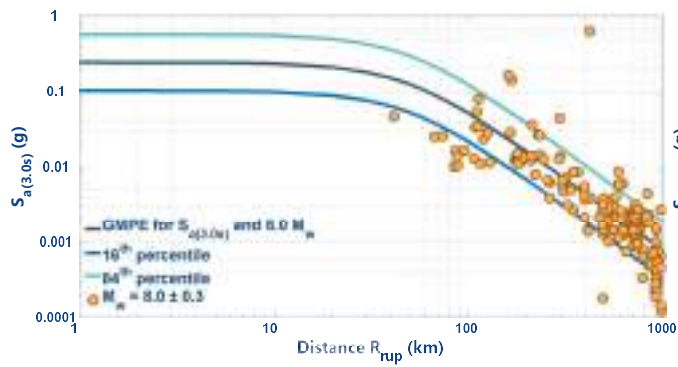


### Spectral Acceleration at 2.0s ( $S_{a(2.0s)}$ )

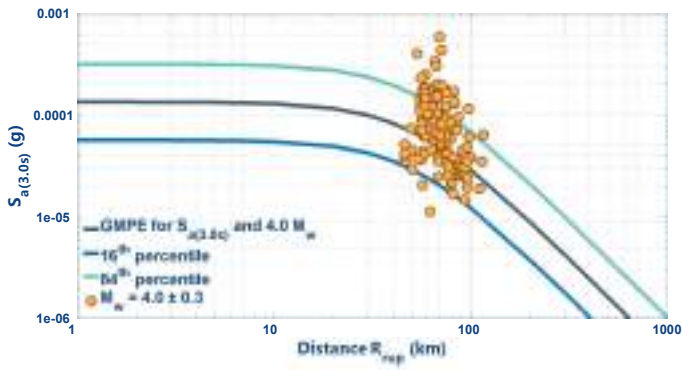




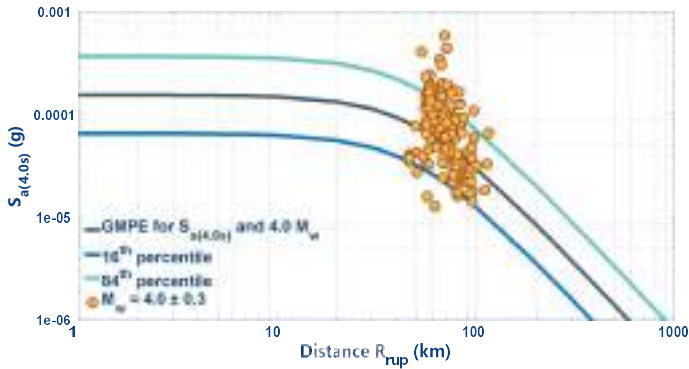
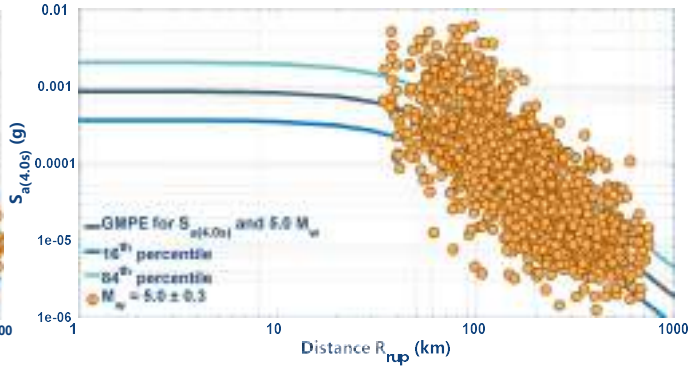
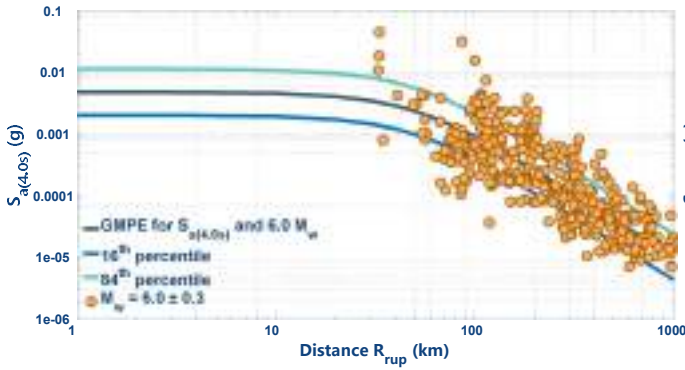
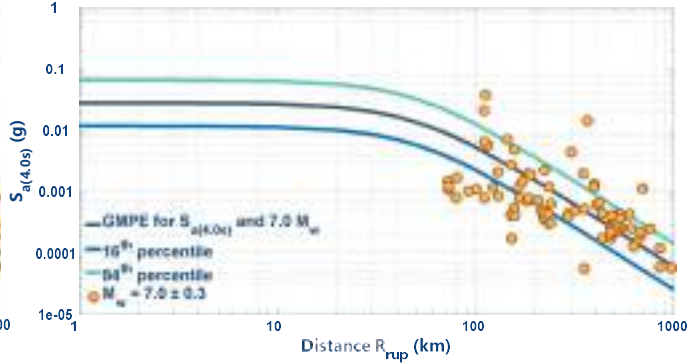
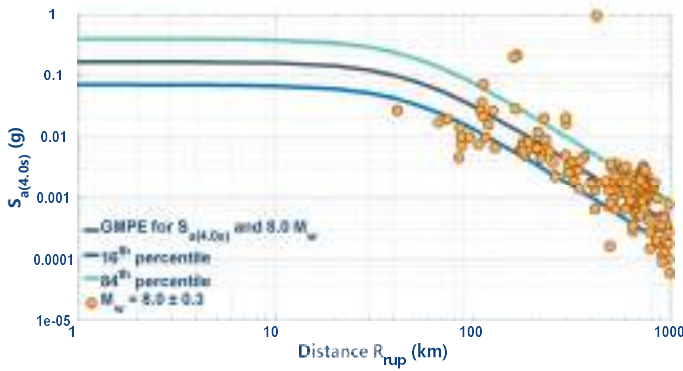
### Spectral Acceleration at 3.0s ( $S_{a(3.0s)}$ )



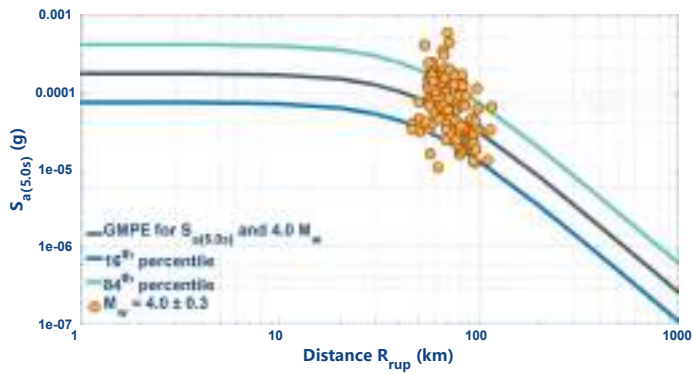
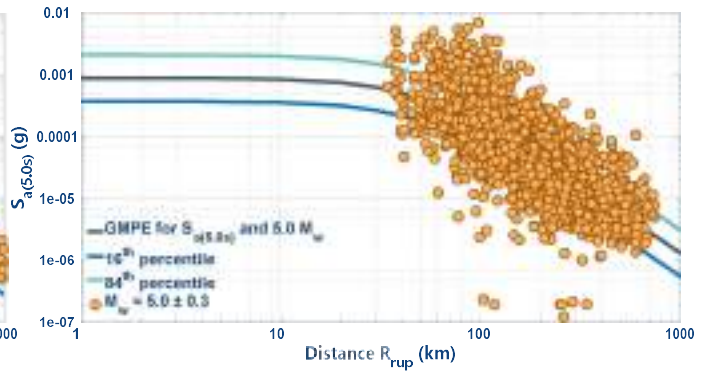
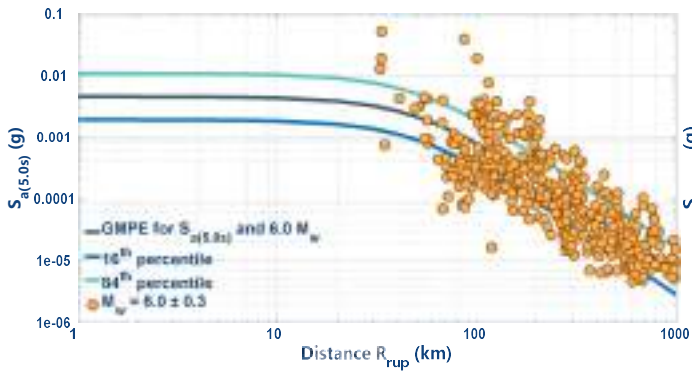
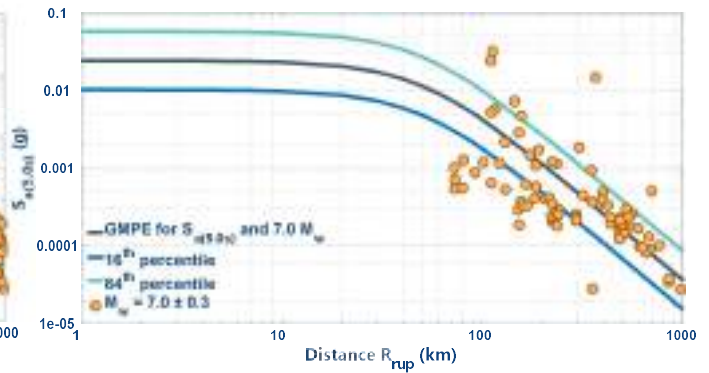
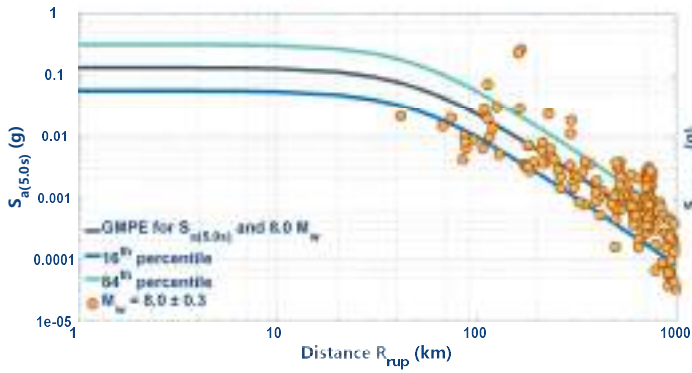




### Spectral Acceleration at 4.0s ( $S_{a(4.0s)}$ )

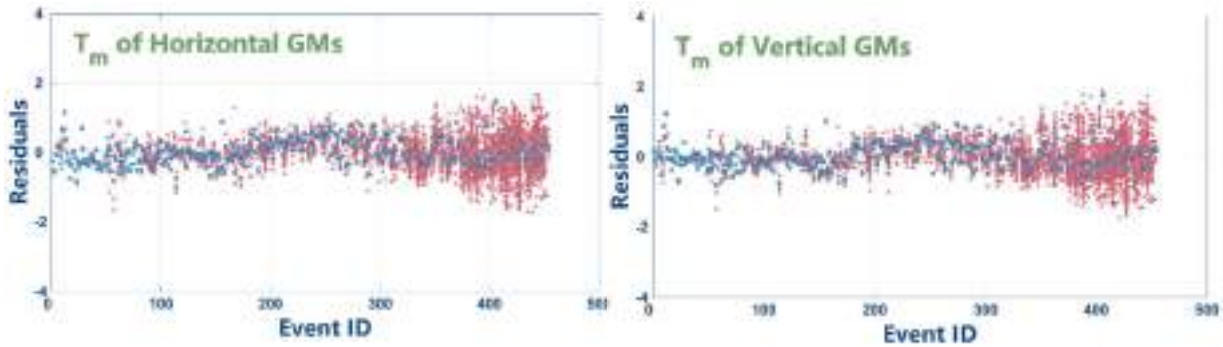


Spectral Acceleration at 5.0s ( $S_{a(5.0s)}$ )

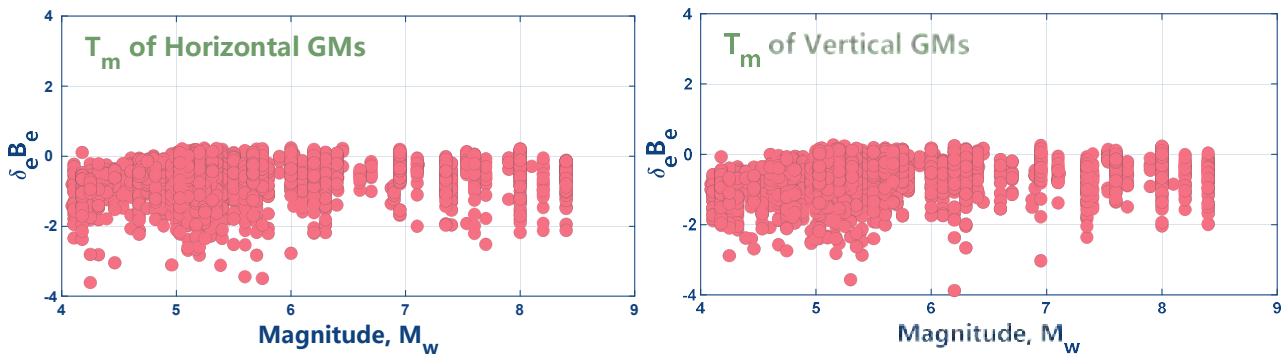


### A.7. RESIDUAL PLOTS FOR THE $T_m$ FOR BOTH HORIZONTAL AND VERTICAL GMs:

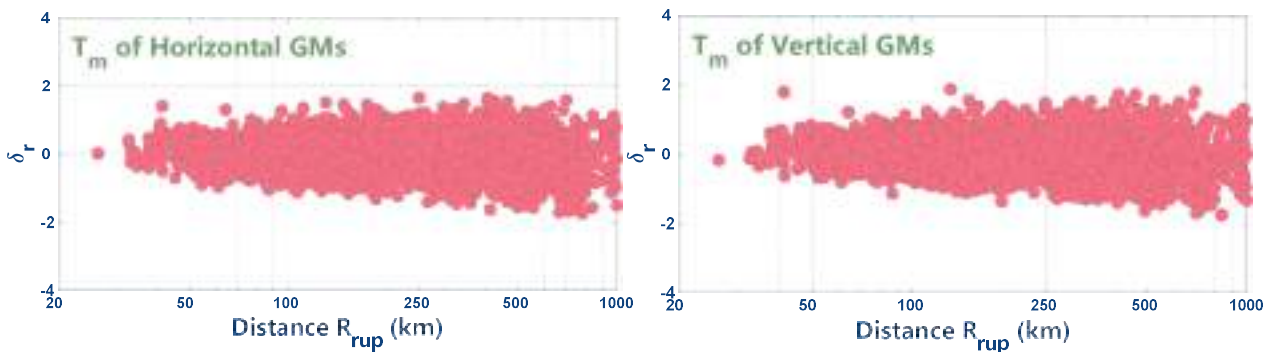
The residual plots of the  $T_m$  for the 454 events are presented. To do so, the geometric mean for the horizontal IMs was assessed for each GM. Herein the blue points are the residuals for each event respect to the median (0.0 residual value), and the red points are the number of observed IMs for each event. These plots are shown as follows:



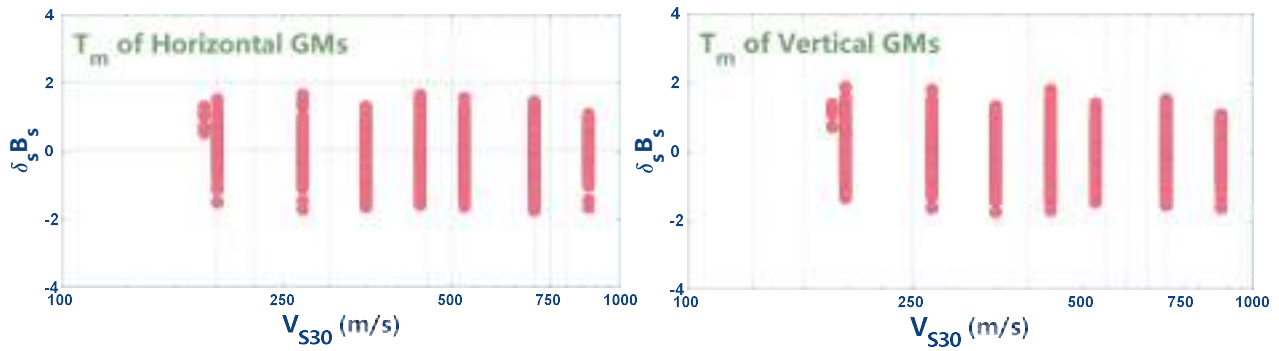
Now, the between-event ( $\delta_e B_e$ ) residual plots versus Moment Magnitude ( $M_w$ ) are presented as follows:



Also, the within-event ( $\delta_r$ ) residual plots versus Rupture Distance ( $R_{rup}$ ) are presented as follows:

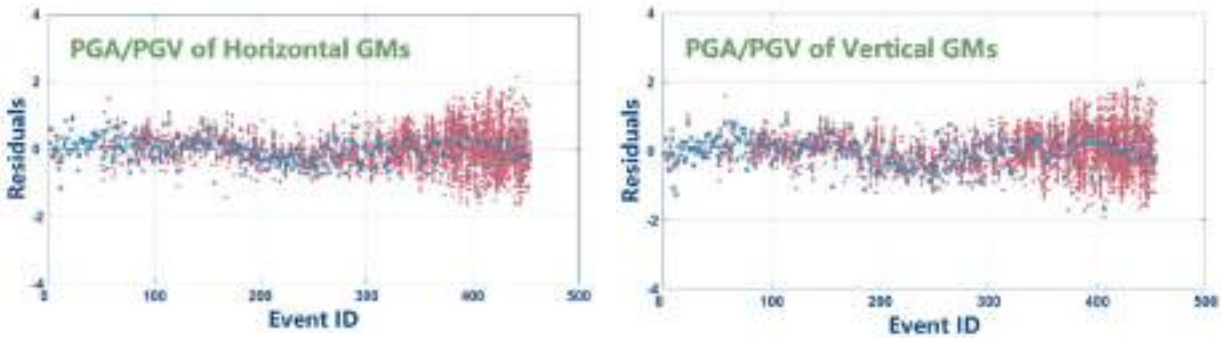


Finally, the within-event ( $\delta_s B_s$ ) residual plots versus Shear Wave Velocity of the upper 30m ( $V_{S30}$ ) for each station are presented as follows:

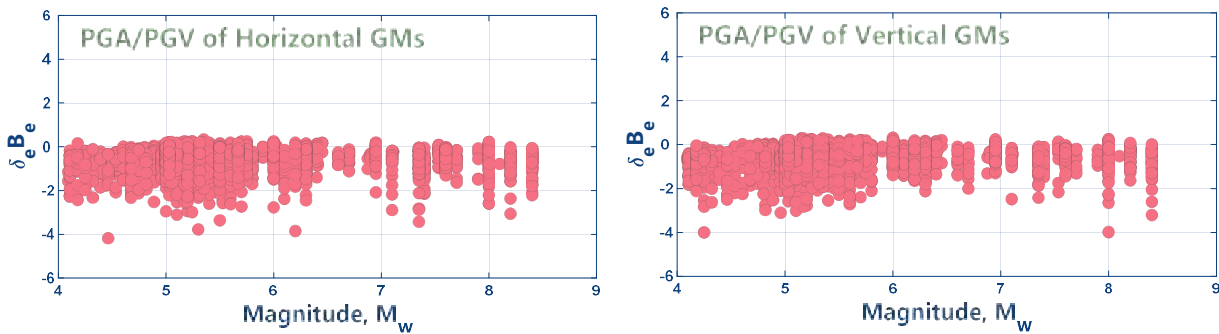


## A.8. RESIDUAL PLOTS FOR THE *PGA/PGV* FOR BOTH HORIZONTAL AND VERTICAL GMs:

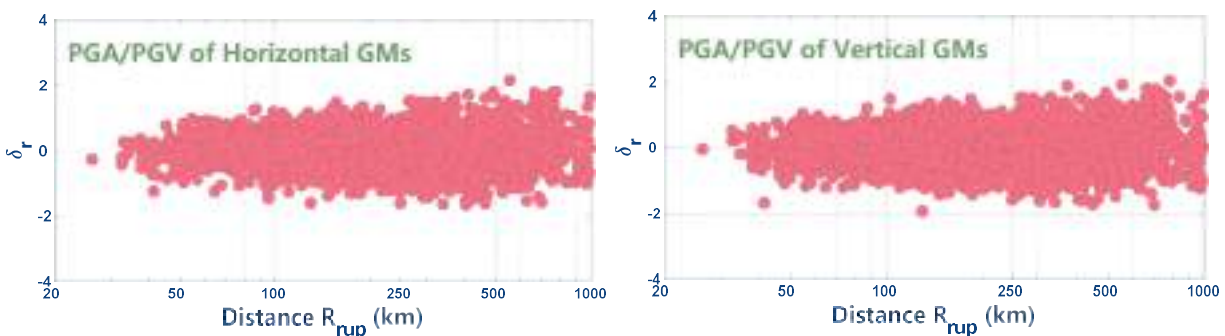
The residual plots of the *PGA/PGV* for the 454 events are presented. To do so, the geometric mean for the horizontal IMs was assessed for each GM. Herein the blue points are the residuals for each event respect to the median (0.0 residual value), and the red points are the number of observed IMs for each event. These plots are shown as follows:



Now, the between-event ( $\delta_e B_e$ ) residual plots versus Moment Magnitude ( $M_w$ ) are presented as follows:

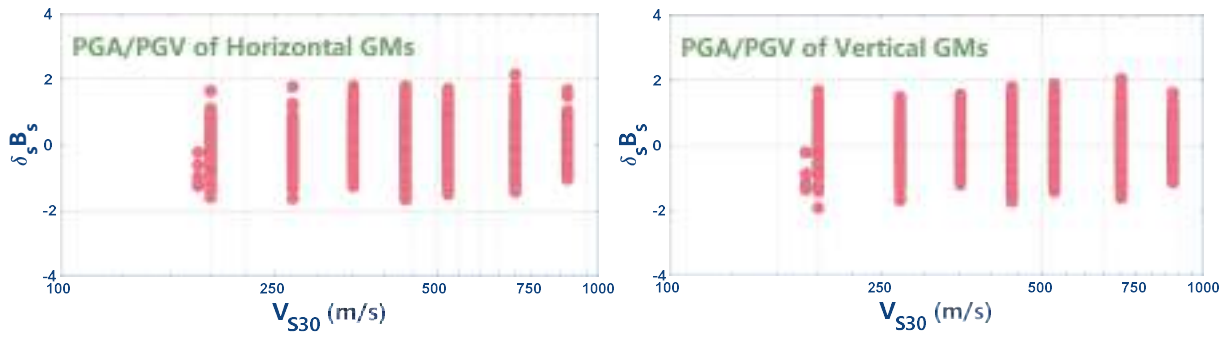


Also, the within-event ( $\delta_r$ ) residual plots versus Rupture Distance ( $R_{rup}$ ) are presented as follows:



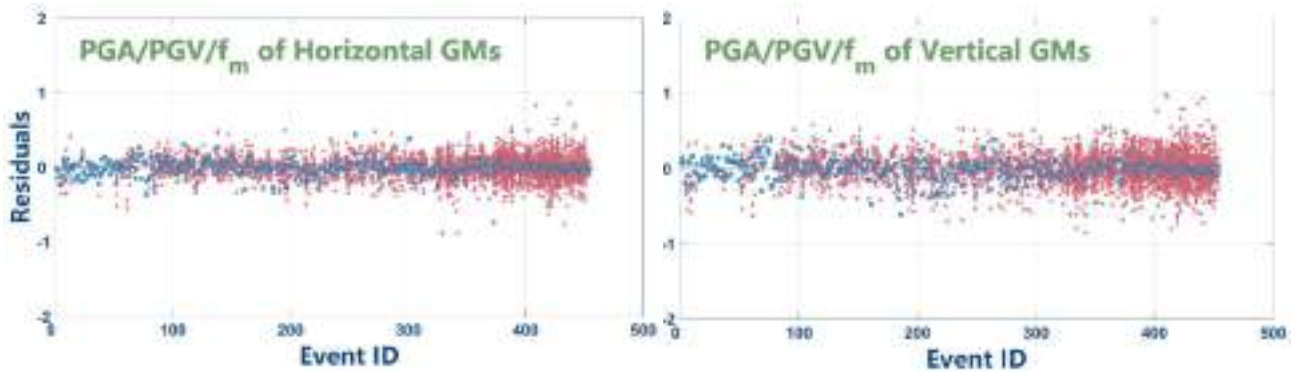


Finally, the within-event ( $\delta_s B_s$ ) residual plots versus Shear Wave Velocity of the upper 30m ( $V_{S30}$ ) for each station are presented as follows:

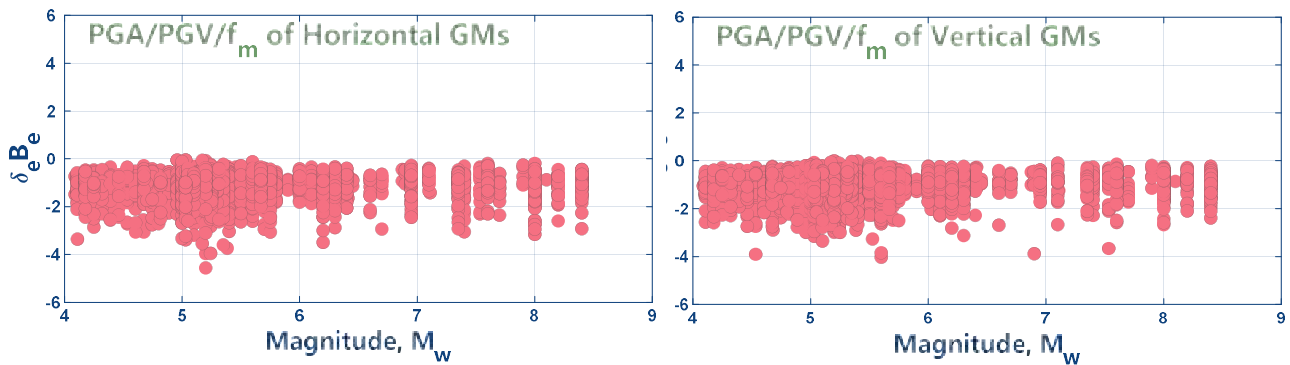


### A.9. RESIDUAL PLOTS FOR THE $PGA/(PGVf_m)$ FOR BOTH HORIZONTAL AND VERTICAL GMs:

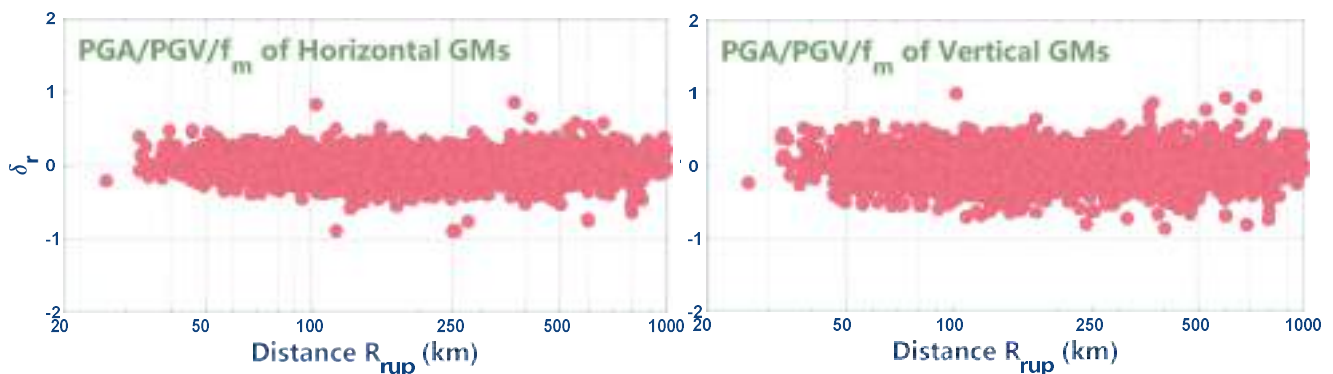
The residual plots of the  $PGA/(PGVf_m)$  for the 454 events are presented. To do so, the geometric mean for the horizontal IMs was assessed for each GM. Herein the blue points are the residuals for each event respect to the median (0.0 residual value), and the red points are the number of observed IMs for each event. These plots are shown as follows:



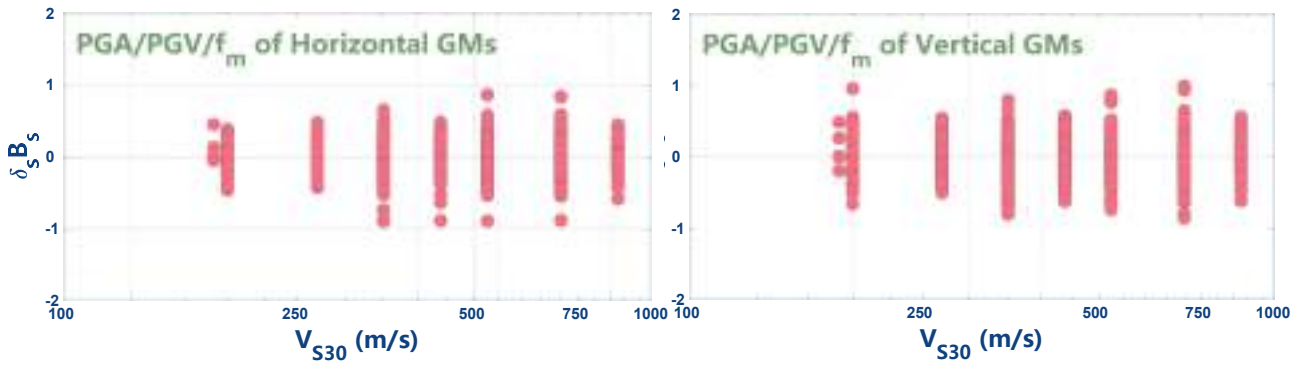
Now, the between-event ( $\delta_e B_e$ ) residual plots versus Moment Magnitude ( $M_w$ ) are presented as follows:



Also, the within-event ( $\delta_r$ ) residual plots versus Rupture Distance ( $R_{rup}$ ) are presented as follows:

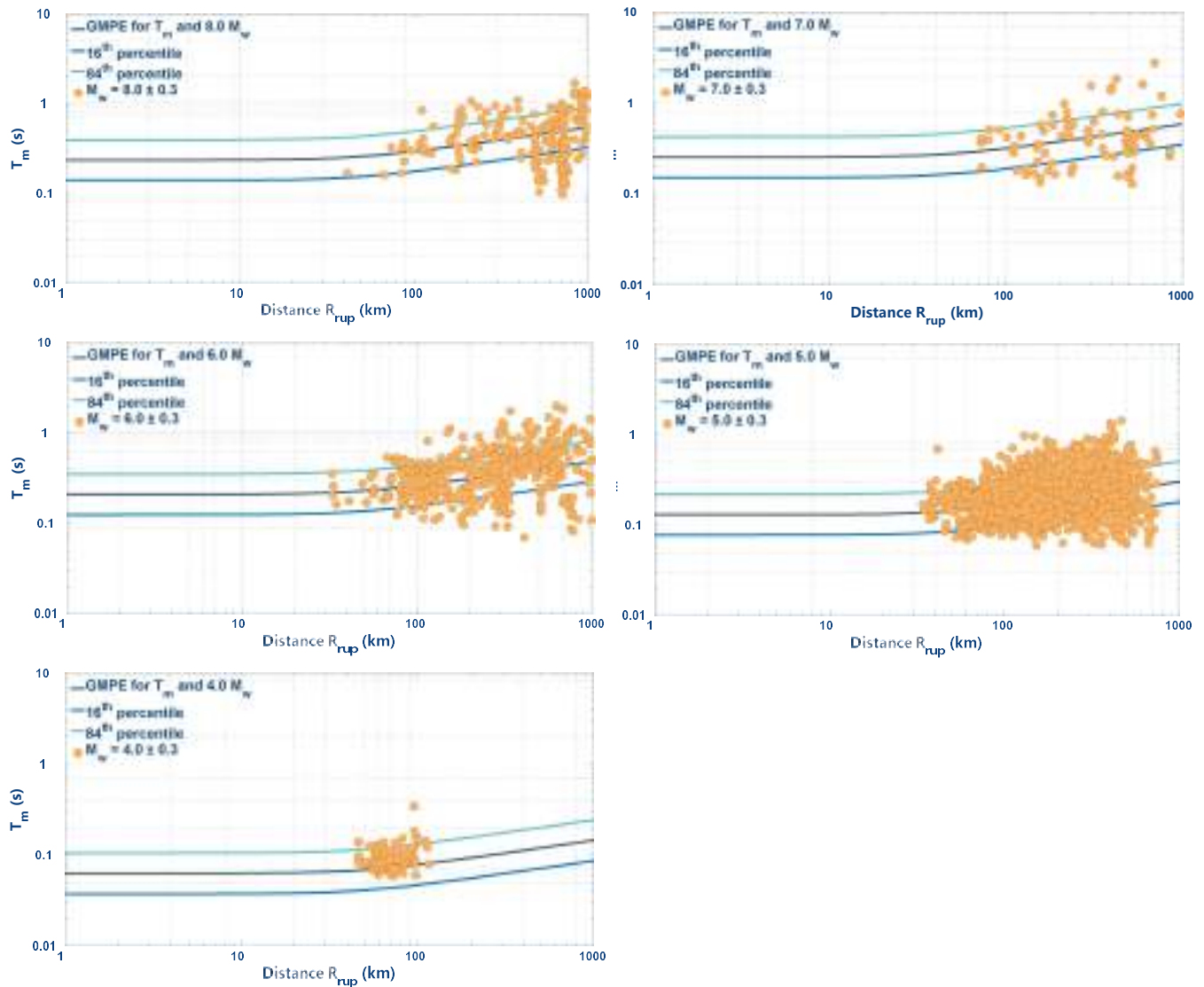


Finally, the within-event ( $\delta_s B_s$ ) residual plots versus Shear Wave Velocity of the upper 30m ( $V_{S30}$ ) for each station are presented as follows:



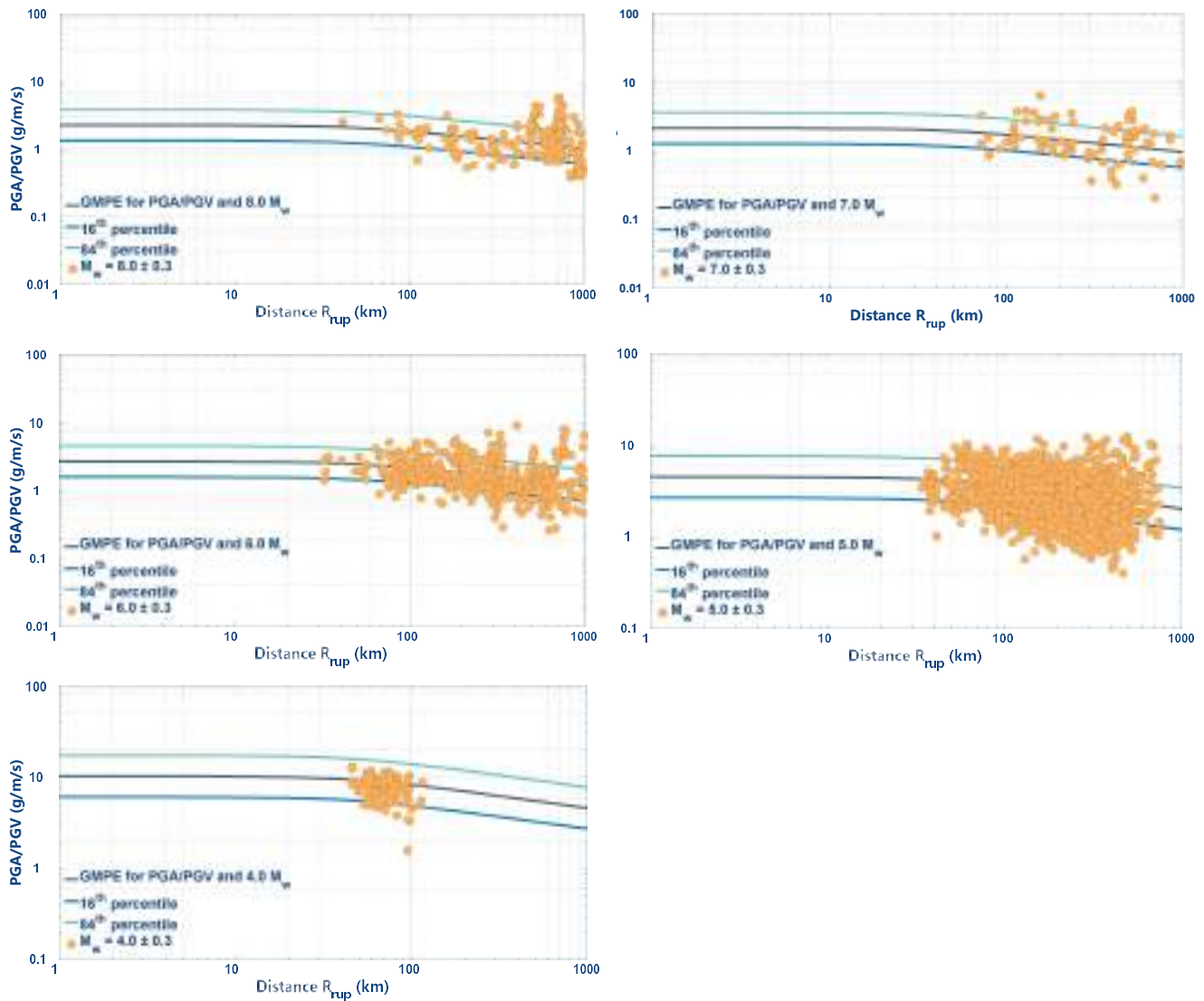
## A.10. COMPARINSON BETWEEN MODEL FITTED WITH ALL DATA CONSIDERING DIFFERENT MOMENT MAGNITUDES AND $T_m$ FOR HORIZONTAL GMs:

The main model mean of the GMPE for a reference rock site ( $V_{s30} = 1200m/s$ ) and their standard deviations are plotted considering the compiled dataset for different magnitudes used for its regression.



## A.11. COMPARINSON BETWEEN MODEL FITTED WITH ALL DATA CONSIDERING DIFFERENT MOMENT MAGNITUDES AND *PGA/PGV* FOR HORIZONTAL GMs:

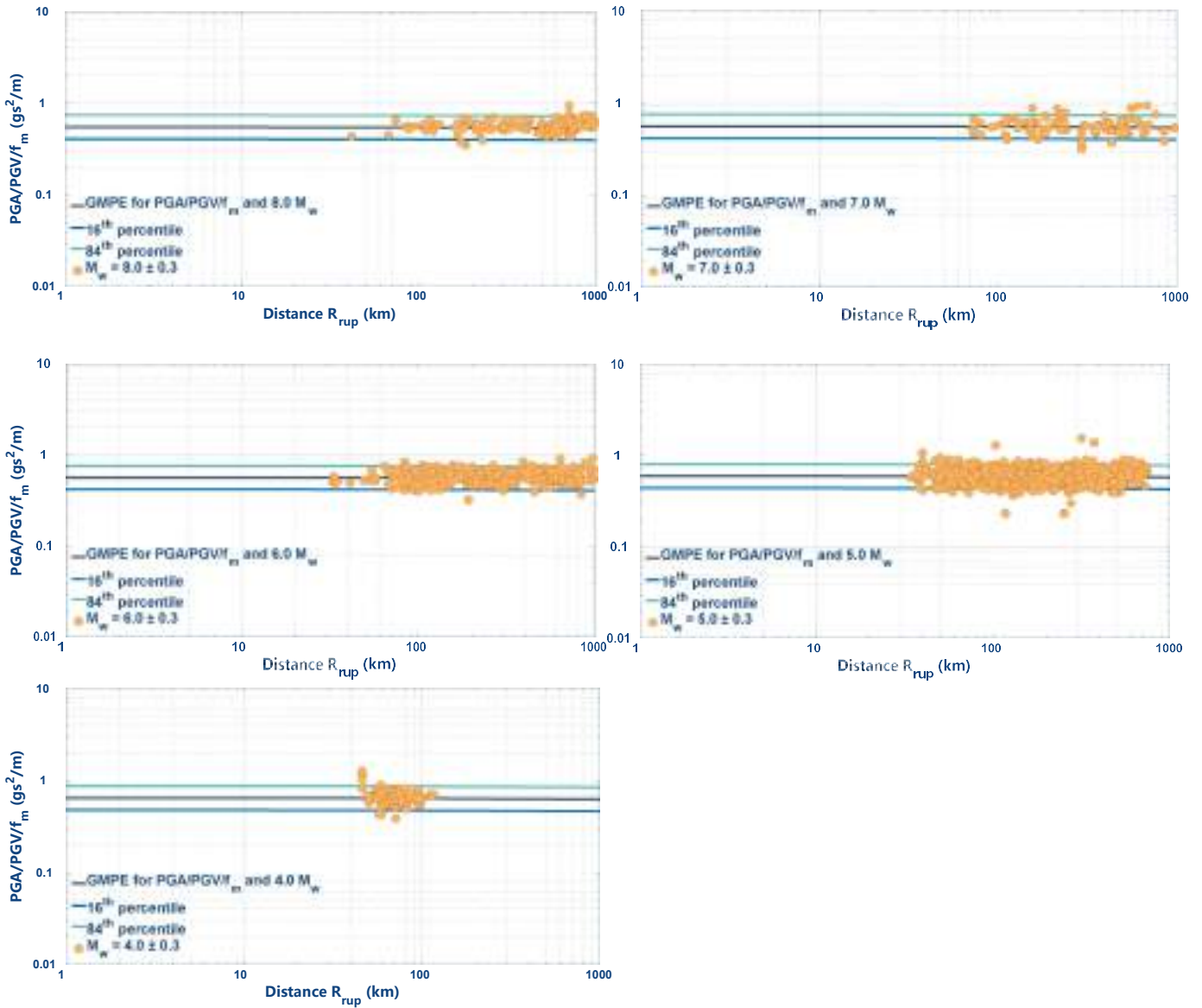
The main model mean of the GMPE for a reference rock site ( $V_{s30} = 1200m/s$ ) and their standard deviations are plotted considering the compiled dataset for different magnitudes used for its regression.





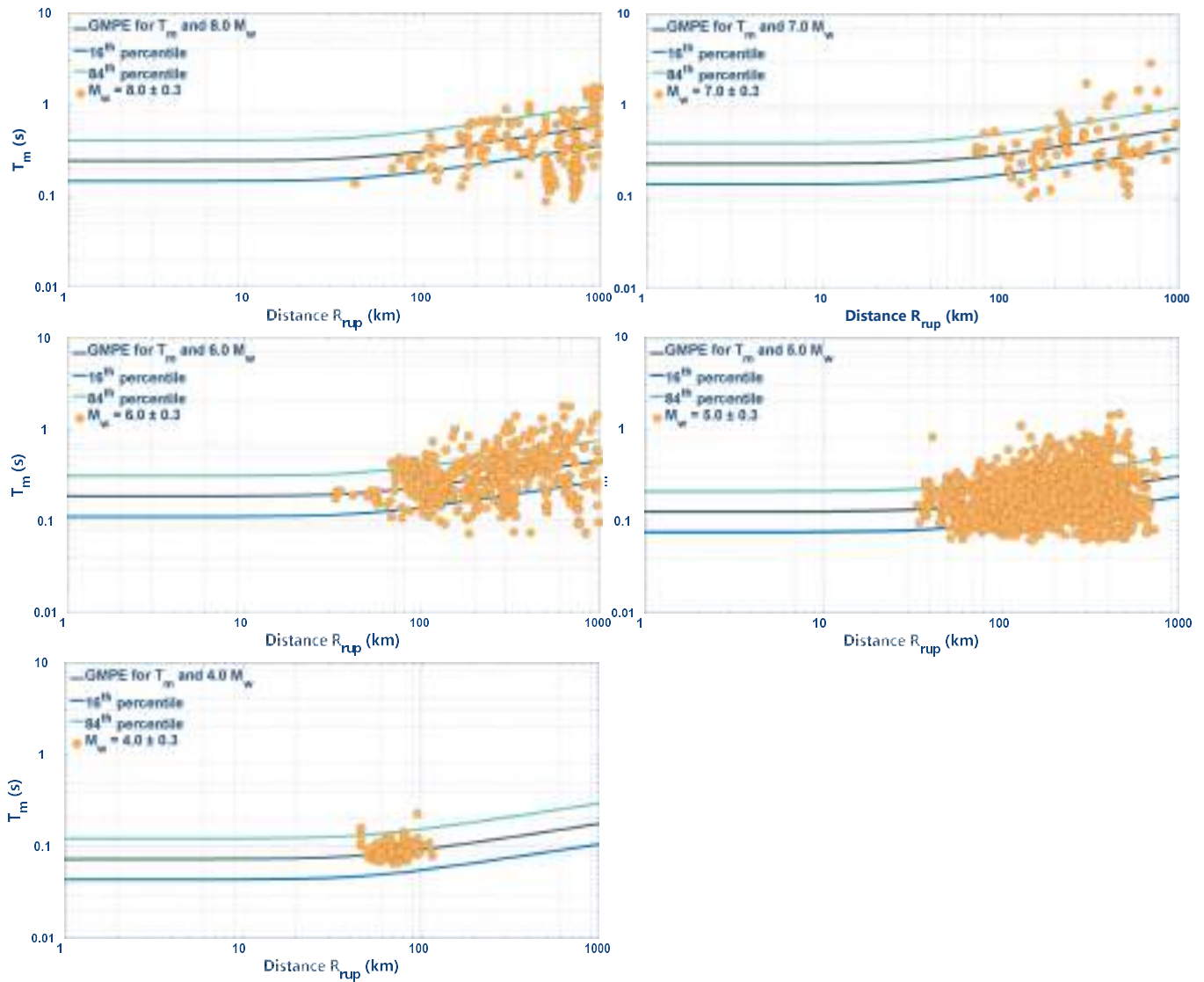
## A.12. COMPARINSON BETWEEN MODEL FITTED WITH ALL DATA CONSIDERING DIFFERENT MOMENT MAGNITUDES AND $PGA/(PGVf_m)$ FOR HORIZONTAL GMs:

The main model mean of the GMPE for a reference rock site ( $V_{s30} = 1200m/s$ ) and their standard deviations are plotted considering the compiled dataset for different magnitudes used for its regression.



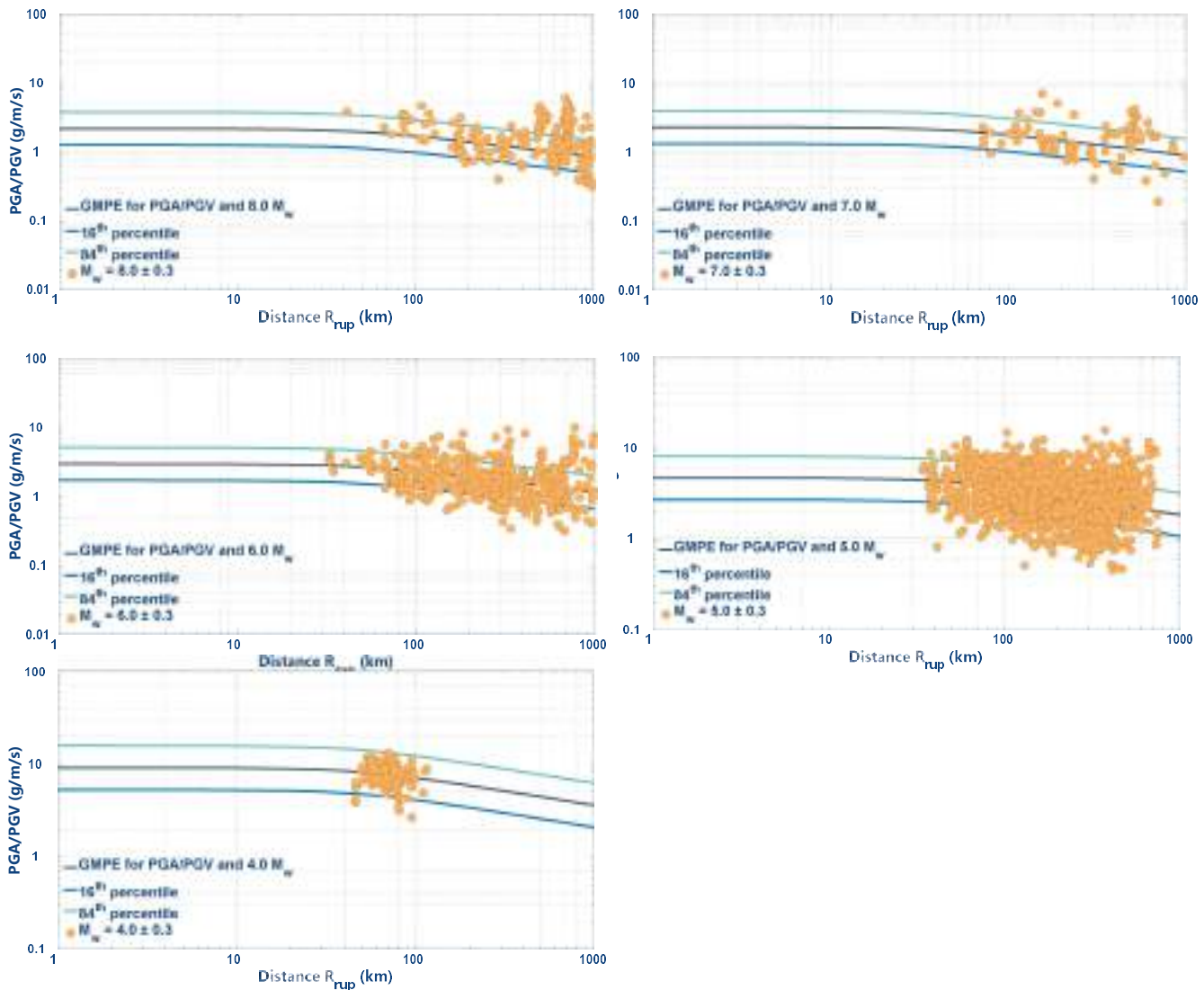
### A.13. COMPARINSON BETWEEN MODEL FITTED WITH ALL DATA CONSIDERING DIFFERENT MOMENT MAGNITUDES AND $T_m$ FOR VERTICAL GMs:

The main model mean of the GMPE for a reference rock site ( $V_{s30} = 1200m/s$ ) and their standard deviations are plotted considering the compiled dataset for different magnitudes used for its regression.



## A.14. COMPARINSON BETWEEN MODEL FITTED WITH ALL DATA CONSIDERING DIFFERENT MOMENT MAGNITUDES AND *PGA/PGV* FOR VERTICAL GMs:

The main model mean of the GMPE for a reference rock site ( $V_{s30} = 1200m/s$ ) and their standard deviations are plotted considering the compiled dataset for different magnitudes used for its regression.



## A.15. COMPARINSON BETWEEN MODEL FITTED WITH ALL DATA CONSIDERING DIFFERENT MOMENT MAGNITUDES AND $PGA/(PGVf_m)$ FOR VERTICAL GMs:

The main model mean of the GMPE for a reference rock site ( $V_{s30} = 1200m/s$ ) and their standard deviations are plotted considering the compiled dataset for different magnitudes used for its regression.

